CONDITION ASSESSMENT OF REINFORCED CONCRETE SANITARY SEWER PIPELINES USING PROBABILISTIC METHODS AND ADVANCED INSPECTION TOOLS

By

Moein Ebrahimi

DISSERTATION

Submitted in partial fulfillment of the requirements

for the degree of Doctor of Philosophy at

The University of Texas at Arlington

December, 2023

Arlington, Texas

Supervising Committee:

Himan Hojat Jalali, Supervising Professor

Mohsen Shahandashti

Suyun Ham

Yuan Zhou

ABSTRACT

Condition Assessment of Reinforced Concrete Sanitary Sewer Pipelines Using Probabilistic Methods and Advanced Inspection Tools

Moein Ebrahimi, Ph.D.

The University of Texas at Arlington, 2023

Supervising Professor: Himan Hojat Jalali

Large sanitary sewer pipelines (SSPs) are the backbone of modern infrastructure. They carry wastewater from smaller lines to treatment plans; therefore, they are critical for public health and safety. According to the ASCE report card published in 2021, the condition rate of sanitary sewage networks in the United States is D+ (i.e., poor) (ASCE 2021). Therefore, frequent inspections of SSPs are crucial for performing a proper life cycle management strategy. New inspection technologies such as LiDAR have recently been employed for rapid condition assessment of SSPs. Because of the precision of LiDAR inspection data, it can not only measure hydraulic properties but also, quantify the erosion of concrete walls in SSPs. Because of the limited available inspection data for this large aging inventory, probabilistic approaches need to be implemented into these limited inspection data to create an effective condition assessment for SSPs. Meanwhile, Reinforced concrete SSPs (RCSSPs) are commonly used for sewer mains.

In this study, an automated framework for condition assessment of RCSSPs is proposed using LiDAR inspection data and probabilistic approaches. The framework includes the procedure for filtering and alignment of the raw 3D point cloud of data, which represents the pipe's inner geometry coordinates. Then hydraulic properties (such as hydraulic radius, wetted perimeter, volumetric flow rate, and velocity of flow), ovality, and concrete erosion rate from the 2D cross

sections along the pipe length. From these outputs, probabilistic approaches will be implemented such as finding the best-fit probability density function (PDF) corresponding to the deteriorated inner concrete wall geometry of RCSSPs, and probabilistically estimating their residual service life (RSL); in addition, the Bayesian network is used to predict the erosion rates using different priors from the literature and the likelihood function which is the calculated erosion rate from the inspected SSPs at the age of 28. The results will be compared in the form of the predicted remaining service life (RSL). Lastly, statistical approaches such as single/multi-variable regression, and polynomial regression are applied to the outputs to estimate the mean concrete loss and identify underlying patterns in the data.

The overall objective of this study is to develop an innovative, automated, and rational framework for condition assessment of transportation infrastructure more specifically for RC sanitary pipelines.

DISSERTATION ORGANIZATION

This dissertation is prepared in five chapters: chapter 1 presents an overview of the concrete erosion mechanism in sewer pipes, answer to the question: of why the inspection is important? in addition to the objectives and gaps to be covered in this topic. Chapter 2 presents a summary of the literature available on inspection tools for sanitary sewer pipes (SSPs) and their limitations, different probabilistic and stochastic techniques to accommodate the scarcity of inspection data, and the limitations of inspection. Chapter 3 introduces the theory behind concrete erosion modeling. Moreover, an automated algorithm for condition assessment of reinforced concrete SSPs (RCSSPs) is presented in Chapter 3. In addition, updating concrete erosion values using Bayesian inference on the concrete erosion data is presented in Chapter 3. Chapter 4 discusses the results of the automated methodology in Chapter 3 and compares their results to the literature. Moreover, the verification results are presented in Chapter 4, as well as an evaluation of the performance of the algorithm. In addition, the results of the implementation of statistical methods on the hydraulic properties and concrete erosion are provided. Finally, chapter 5 contains a summary and concludes the dissertation.

ACKNOWLEDGEMENT

I would like to express my deep sense of gratitude to my supervising professor, Dr. Himan Hojat Jalali, for his continued support throughout my doctoral journey. This achievement would not have been completed without his valuable knowledge and advice.

My heartfelt thanks also go to my committee members, Dr. Shahandashti, Dr. Ham, and Dr. Zhou. Their astute comments have significantly enhanced the caliber of my research, enriching it from diverse perspectives.

I would like to thank the Transportation Consortium of South-Central States (Tran-SET) for providing the funding support to conduct this study. I would like to thank the Principal Investigator (PI) of this project, Dr. Hojat Jalali, and Dr. Sabatino (Co-PI) for their technical and financial support. I am also thankful to Dr. Abolmaali and the Center for Structural Engineering Research and Pipeline Inspection (CSER-PI) for providing the raw LiDAR data to carry out this research.

I am especially grateful to my first supervisor, Dr. Samantha Sabatino, for the opportunity to participate in this esteemed program at UTA. Her encouragement has been a cornerstone of my academic development.

I would like to thank my friends, Dr. Khaled Abuhishmeh, Dr. Amir Naderpour, Dr. Ashraf Daradkeh, and Erfan Ahmadzade for their companionship throughout this endeavor.

Finally, heartfelt thanks to my sister, Mahboobeh, brother-in-law, Amin, as well as my parents, and siblings. Their unwavering motivation and nurturing support have been my pillars of strength throughout my Ph.D. studies. Special gratitude to my dearest, Delaram, whose encouragement and love have been a constant source of inspiration throughout my Ph.D. journey.

Dec 15, 2023

Table of Contents

LIST OF FIGURES

LIST OF TABLES

ACRONYMS, ABBREVIATIONS AND SYMBOLS

ASTM	American Section of the International Association for Testing Materials
CCTV	Closed-Circuit Television
CIPP	Cast-in-Place Pipe
ED	Eigenvalue decomposition
LiDAR	Light Detection and Ranging
KNN	K-Nearest Neighbor
LS	Least Squares
M-M	Manhole to Manhole
MCMC	Markov Chain Monte Carlo
MSE	Mean Square Error
MSI	Multi-Sensor Inspection
PCD	Point Cloud of Data
PDF	Probability Distribution Function
RCSSP	Reinforce Concrete Sanitary Sewer Pipeline
RMSE	Root Mean Square Error
RoI	Region of Interest (5 *ft* PCD)
RSL	Remaining Service Life

SLS	Serviceability Limit State
Tran-SET	Transportation Consortium of South-Central States

CHAPTER 1. INTRODUCTION

1.1 Overview

According to the ASCE report card published in 2021, the condition rate of sanitary sewage networks in the United States is *D*+ (i.e., poor) (ASCE, 2022). The most challenging task in developing a life-cycle management for sanitary sewer systems is the maintenance of this aging infrastructure. This aging inventory, in which pipes play a major role, is reaching the end of its service life and as a result, municipalities are looking for methods for condition assessment to estimate their residual service life (RSL). Overall, the proposed decision support tool could help mitigate the risk of pipeline failure, thereby preventing detrimental societal and environmental consequences, all while saving limited resources.

Sanitary sewer mains are the most vital underground infrastructures, and it has a major role in a sustainable urban system; the sewer systems are designed to have a long service life. Thus, it is important to provide acceptable serviceability and to make a balance between the maintenance costs and the risk of failures. Failure of sanitary networks can be catastrophic and have severe consequences for people, as well as the natural and built environment. To address this issue, a $1 trillion infrastructure bill was recently signed into law to rehabilitate and improve the nation's aging infrastructure. The bill addresses 17 of the 17 categories (including sanitary sewer pipelines) outlined in the ASCE 2021 Infrastructure Report Card (Sevier, 2021). An appropriate rehabilitation and maintenance plan can be achieved only if frequent inspections of the sewer network inventory are conducted. Meanwhile, routine inspections, paired with data-driven probabilistic performance modeling, can help decision-makers and municipalities make informed choices regarding their maintenance and rehabilitation.

The biggest challenge for municipalities and decision-makers is the maintenance of infrastructures in their inventory and prioritizing limited repair funding for them. In this study, the residual service life (RSL) of large RC sanitary sewer pipelines with diameters of 60-, 54- and 30-inch RCSSPs is estimated using probabilistic and reliability-based methods on the automated data-driven framework. The inspection data includes about 8000 linear feet of sewer lines in the form of 25 different RCSSPs. To this end, the critical input information is the current erosion of pipe cross-sections, which is obtained through the inspection data in the form of LiDAR measurements. The proposed automated framework is developed to get the LiDAR raw output data and apply filtering, aligning, and obtaining the cross-section wall thickness loss. Furthermore, different probability distribution functions are fitted to the wall thickness loss data and a best fit is obtained. Moreover, based on the corrosion rate and a selected confidence level, the reliability-based residual life of the inspected pipelines is provided. In addition, the effect of different zones along pipe circumference on the concrete erosion of RCSSPs is investigated and the results of different case studies are compared with the results of the whole pipe. Furthermore, Bayesian Network (BN) is implemented on the erosion data to update the values based on the prior (which is determined from the literature). Finally, different regression analysis is utilized on the hydraulic properties (calculated from the proposed algorithm for different RCSSPs (M-M).) to estimate the mean concrete loss due to erosion and identify underlying patterns. Based on the decision makers' resources, the results could be presented at different scales, whether for small 1-inch rings, 5-*ft* sections, or even for the whole inspected line (M-M).

In the following sections, the application of sewer pipes is discussed as well as different types and shapes of SSPs. In addition, common defects of RCSSPs are investigated. The concrete erosion mechanism of RCSSPS is discussed; the main factor behind this deterioration is explained.

1.2 Sanitary Sewer Pipes

Sewer pipelines are an important part of the infrastructure that carries the wastewater out of cities. The Romans, Persians, Athenians, Macedonians, and Greeks built the early versions of sewer systems from stone and cement. Sewer systems comprise about fifty percent of the underground infrastructure in the United States (Shook 1998), which includes more than 1,300,000 miles of public and private sewer lines.

Different materials are being used for conveying the wastewater across the US. Materials such as Ductile iron, Vitrified clay, Fiberglass, Reinforced concrete, High-density polyethylene pipe (HDPE), and PVC are the different types of SSPs. Among these types, reinforced concrete (RC) is usually used in systems like sanitary sewers, storm drains, and culverts; RC pipes are manufactured in various shapes (Figure 1). Meanwhile, studies investigate the application of wastewater in industry; Soltanianfard et al., (2023) examine the use of wastewater in concrete as a sustainable resource for eco-friendly structures.

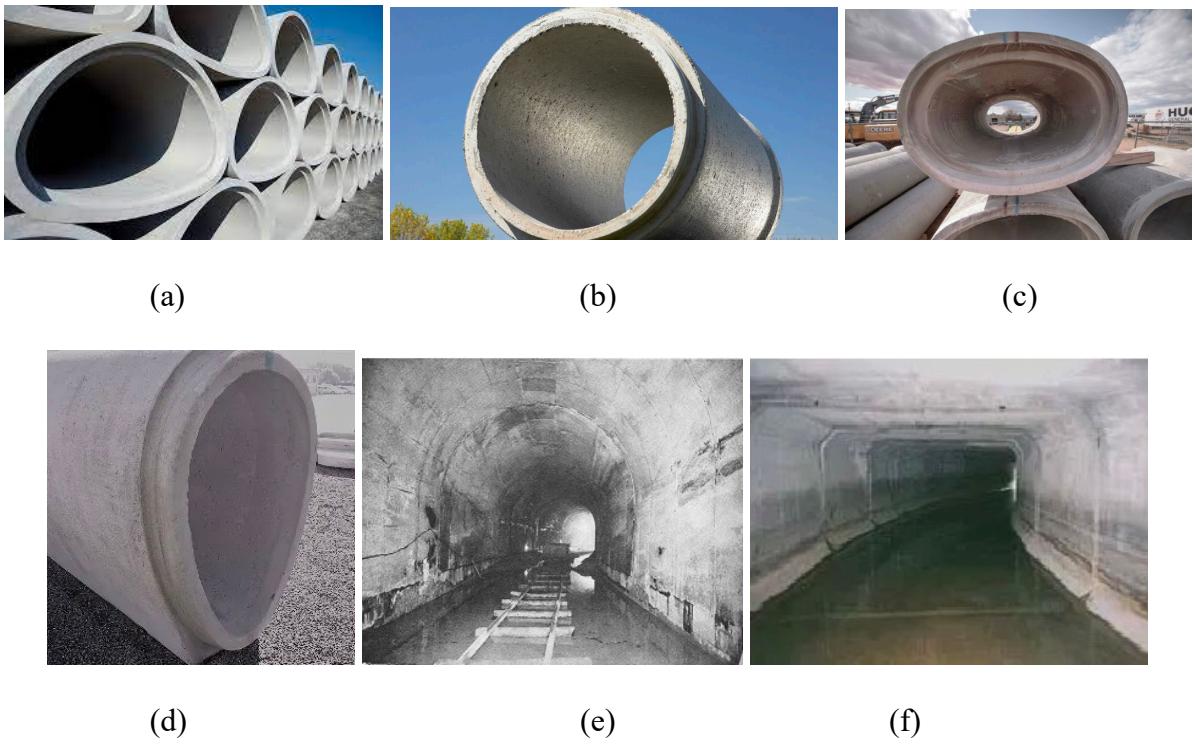

(a) (b) (c)

(d) (e) (f)

Figure 1. Different Shapes of RCSSPs (a) Arch shape, (b) Circle shape, (c) Elliptical shape, (d) Egged shape, (e) U-shaped, (f) Rectangular shape(Civil Crews, 2020)**.**

RCSSP is suitable for both gravity flow and pressure SSPs, primarily used for potable water. With a lifespan of up to 150 years, RCP's long lifespan hinges on effective design and maintenance. The serviceability of these sewer lines can be affected by structural failure, overflows, and blockages. The major benefits of RCP are its durability, strength, and long life, aided by its smooth surface that facilitates good flow. However, these pipes are vulnerable to hydrogen sulfide attacks and can erode in extremely acidic soils. Additionally, improper installation or transportation can lead to structural defects like cracks and deflection. Figure 2 shows common defects of RCSSPs.

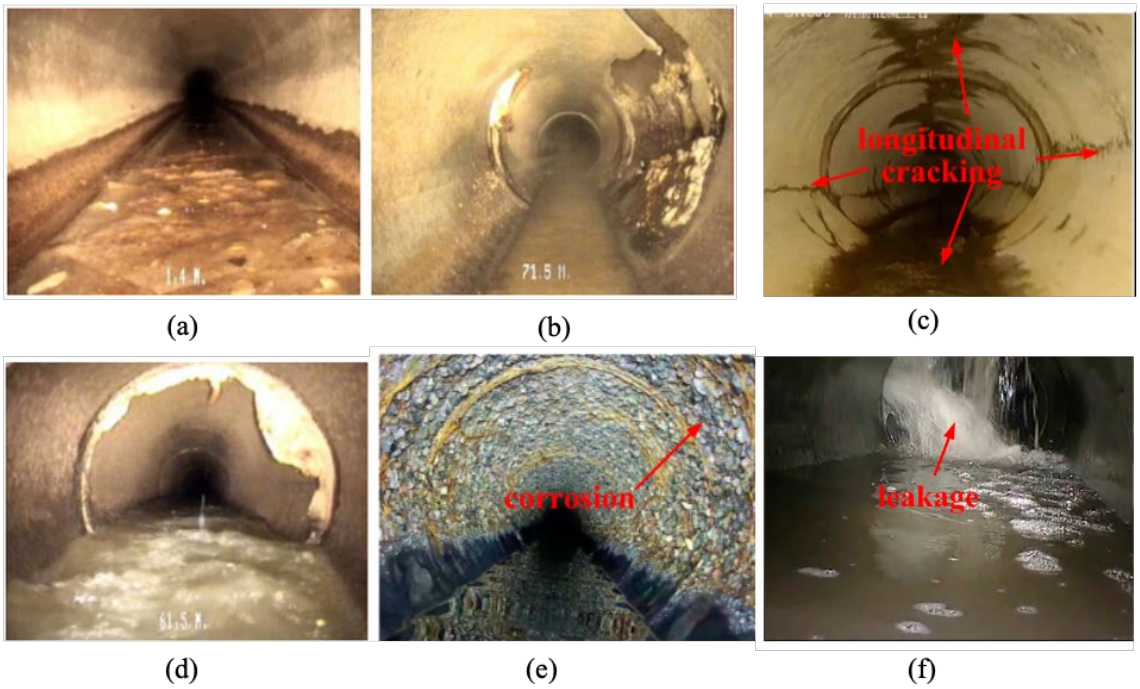

Figure 2. Major Defects in RCSSPs (a) Debris; (b) Surface Damage; (c) Cracks; (d) Connection Defect; (e) Concrete Erosion; (f) Leakage ((Bakry et al., 2016)and (Dong et al., 2023))

Different forms of structural degradation adversely affect the integrity and function of sanitary sewer pipes (SSPs) over time. Concrete erosion is the main cause of degradation in SSPs, as sewers contain corrosive elements, with hydrogen sulfide gas being the dominant one, specifically in reinforced concrete sanitary sewer pipes (RCSSPs). Biological activities of anaerobic sulfate-reducing bacteria with hydrogen sulfide gas (in the slime layer below the waterline) produce sulfuric acid that accumulates on the inner wall of the pipe above the waterline and causes concrete wall erosion over time (Bizier, 2007). This deterioration mechanism is often termed microbiologically induced corrosion (MIC), which can decrease the life of SSPs from 100 years to 30-50 years (De Belie et al., 2004). Since sewer pipes often fail abruptly without prior warning, it is necessary to properly plan for the inspection cycles to decrease the failure rates. In addition, due to the importance of these underground infrastructure, the SSPs are expected to have a longer service life than typical civil engineering structures.

The biggest challenge for municipalities and decision-makers is the maintenance of infrastructures in their inventory and prioritizing limited repair funding. Sanitary sewer mains are the most vital underground infrastructure, and they play a major role in having a sustainable urban system. Thus, it is crucial to provide an acceptable level of infrastructure serviceability and to make a balance between the maintenance costs and the risk of failures.

1.3 Concrete Erosion Mechanism

RC sanitary sewer pipes are susceptible to different types of deterioration that threaten their structural capacity and serviceability. Because sanitary sewer mains are buried underground, they could collapse without showing significant warning. Performing proper inspection cycles with highly technical methods can drastically limit collapses from happening (Papoulis & Pillai, 1991). Failure of these structures, or losing parts of their operational capabilities, may cause undesirable consequences that affect the surrounding environment, public health, and the economy. In some cases, the sewer pipe collapse could be lethal; a deputy was killed on West Side Road in San Antonio in 2016 (Bradshaw, 2017).

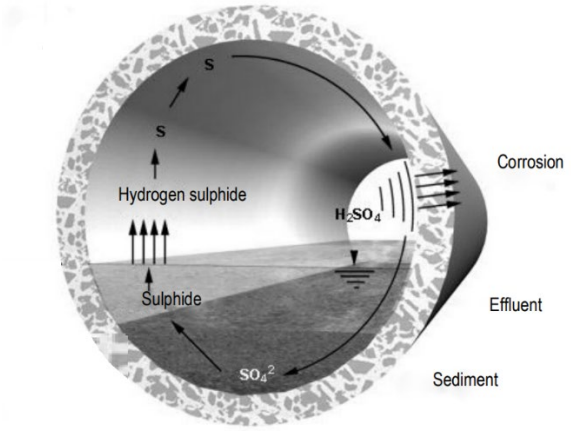

Figure 3. Mechanism of Microbially Induced Concrete Erosion in RCSSPs (Romanova et al., 2014)

Some of the most important sewer pipe damages are cracks, corrosion, root intrusion, breakage, and misaligned connections. Among these, cracks, corrosion, and breakage can result in more than half of the collapses in sewer systems (He & Koizumi, 2013). The main damage observed in RCPs is the concrete erosion due to the existence of hydrogen sulfide (H_2S)(Ribas Silva, 1995). This process is as follows:

1. Newly cast concrete has high alkalinity (a pH of 12-13) which is the result of the formation of $CaOH_2$. This hinders the formation of microorganisms. This stage is called Abiotic Neutralization. In the meantime, sulfate-reducing bacteria (SRB) exist in the biofilm along the perimeter of the submerged surface. SRB converts the sulfate (SO_4^{-2}) into hydrogen sulfide and oxidizes to form carbon dioxide (CO_2).

$$\text{Organic matter} + SO_4^{-2} \longrightarrow H_2S + CO_2$$

Some aspects such as low flow velocities, long sewage flows, and high sewage temperatures accelerate the formation of H_2S. H_2S gas and CO_2 dissolve in a biofilm to form HS^- and H^+ and a weak bicarbonate acid (H_2CO_3); then, this reacts with the alkali species in concrete (calcium hydroxide) to decrease pH down to 9. The estimated period for this process is a few months and could extended to a few years (Parker, 1951).

2. Creating of neutrophilic bacteria (sulfur-reducing bacteria NOSM): when the pH drops to 9 and due to sufficient presence of nutrients and oxygen, sulfur-reducing bacteria (Thiobacillus) initiate to colonize on the concrete surface. As NOSM grows, the oxidation of the sulfur ions (S^{-2}) is facilitated in the sulfuric acid to form hydrogen sulfate acid (H_2SO_4). This acid will further react with the concrete surface to drop the pH more. This step is called Biotic corrosion (Wells et al., 2009).

$$H_2S + 2O_2 \xrightarrow{\text{NOSM}} H_2SO_4$$

3. Colonization by Acidophilic bacteria (ASOM): ASOM starts to grow once the pH drops to 4, it has the same role as NOSM(Pomerot, 1974); it oxidizes the elemental sulfur and the thiosulfate ($S_2O_3^{-2}$). This process will further drop the pH to (1-2).

4. Initiation of loss of cover: The H_2SO_4 which results from the oxidation of the H_2S (by the ASOM) reacts with carbonate and silicate products in the concrete mix to make calcium sulfate $CaSO_4$ (gypsum). The effect of biological H_2S corrosion in RCP is bigger when the concrete contains limestone aggregate. Gypsum accumulates on the perimeter of the unsubmerged surface.

$$H_2SO_4 + CaO.SiO_2.2H_2O \longrightarrow CaSO_4 + SI(OH)_4 + H_2O$$

$$H_2SO_4 + CaCO_3 \longrightarrow CaSO_4 + H_2CO_3$$

$$H_2SO_4 + Ca(OH)_2 \longrightarrow CaSO_4 + 2H_2O$$

Gypsum will further react with the tricalcium aluminate to form ettringite ($3CaO.Al_2O_3.3CaSO_4.31H_2O$).

$$CaSO_4 + 3CaO.AL_2O_3.6H_2O + 25H_2O \longrightarrow 3CaO.AL_2O_3.3CaSO_4.31H_2O$$

This chemical process is outlined in Figure 4. In general, corrosion in concrete sewer pipes happens quickly (usually 3 to 6 months) with the constant presence of hydrogen sulfide in the sewer environment.

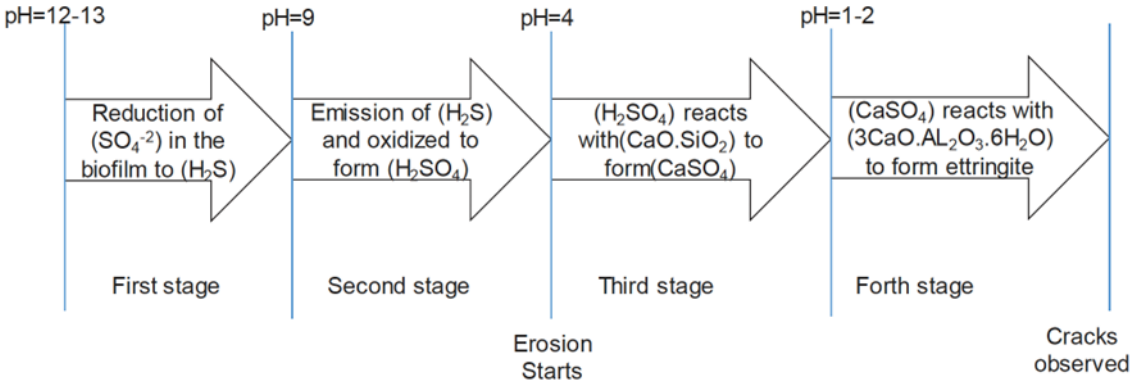

Figure 4. Chemical Process of Concrete Deterioration for Erosion due to Corrosion

Figure 4 certified that sanitary sewers that are under constant chemical deterioration caused by sulfide attacks led to excessive erosion. Reliability theory estimate the service life of pipes with a service limit state that incorporates the loss of concrete cover over steel reinforcement. From this limit state, a probability of exceedance is calculated as a time-dependent parameter.

Creating a condition assessment report from the PCD inspection data is a challenging task. The first step is to filter the noise of the inspection PCD; the raw PCD (i.e., the inspection output) contains noises such as fluid (water, sewer, etc.) and data noise, especially in partially filled pipes. Furthermore, the water level of inspected pipes is not constant throughout the length of the pipe. Therefore, developing an automated data filtering technique without user interference is not practical (Ebrahimi & Jalali, 2022a). Some studies address this issue; Al Asadi (2018) measured the sewer level of each section along the pipe length by finding the lowest PCD from the laser profiler. Abuhishmeh (2019) imported 3D inspection PCD into Cloud Compare software and manually deleted the water level noises. Hojat Jalali and Ebrahimi (Hojat Jalali & Ebrahimi, 2021) worked with 3D PCD from a LiDAR survey and eliminated the water level points by finding the ranges of the two spherical coordinate angles (∅, θ) which indicate the sewer. However, there seems to be a gap in having an automated method for filtering the inspected PCD without user

interference. This was also recognized by (Wells et al., 2009) to consider the effect of spatial variability in pipe circumference for determining wall erosion of RCSSPs as a gap in research.

1.4 Objectives

Regular inspection is vital for maintaining the integrity of underground sanitary sewer pipelines (SSPs). Since this infrastructure is typically buried, identifying defects, and performing maintenance for a large inventory of pipelines are complex and expensive tasks. In this study, LiDAR technology is used to collect the 3D point cloud of data (PCD) from the inside geometry of 3157.8 linear feet of RCSSPs and 2D point cloud of data (PCD) from the inside geometry 5000 linear feet of RCSSPs. An automated algorithm is proposed to extract robust features from these raw LiDAR PCD. The main contributions include seven aspects.

1- An automated algorithm is developed for pre-processing (which is filtering and aligning) the LiDAR inspection point cloud of data (PCD) with minimal user interventions. Previous researchers used software such as CloudCompare to filter the noises of the LiDAR PCD (Khaled Saleh Abuhishmeh, 2019; Moamaie, 2019).
2- An automated algorithm is developed for calculating hydraulic properties and concrete erosion rate of SSPs, finding best-fit distribution, and probabilistic service life prediction of the SSPs.
3- The proposed algorithm performs automatic goodness-of-fit tests for each 2D ring of LiDAR inspection data; it compares R^2 values of multiple QQ plots to determine the probability distribution that best characterizes a pipe's inner concrete wall geometry and condition.
4- Investigating the concrete cover loss for different zones of the RCSSPs circumference to check if the flow noise filtering can be eliminated.

5- Statistical methods such as the Single variable Regression model, Multi-Variables Regression model, and Polynomial Regression model were performed on the output of the proposed framework to predict the concrete erosion of the inner wall of RCSSPs using hydraulic properties.

6- Due to the scarcity of data the pipelines only have one inspection in their lifetimes. Using Bayesian inference, the mean concrete erosion for pipeline (M-M) can be "updated" based on the prior, which is determined from the literature and previous case studies; here two cases are discussed, Weibull and gamma likelihood functions.

7- Determining the remaining service life of pipeline (M-M) using different approaches such as Probability of Exceedance, X-intercept method, and Monte Carlo simulation considering the best-fit probability distribution on the mean concrete loss of the inner wall of RCSSPs. The effect of assigning different distributions for concrete degradation in estimating the service life also explored. Furthermore, the predicted service life is verified with MCS and compared to previous research that used the same LiDAR inspection data. It should be noted that remaining service life is estimated based on concrete erosion as a serviceability limit state, and it does not reflect the time to failure of the pipe. In addition, factors such as ovality and the existence of cracks, as well as operational factors such as sewer type and hydraulic condition of the pipe will affect the service life of the SSPs; however, these are excluded from the current study and need further research.

Overall, the methodology is performed with minimal user interference, using the proposed algorithm in MATLAB. Some Pipeline inspection companies have their own developed software that is proprietary and therefore, to the best of our knowledge details are not readily available to the scientific community.

1.5 Significance of Research

The following bullet points are the significance of this study.

1. The previous studies, which were working with real inspection data, imposed manual filtering using software such as CloudCompare (see Abuhishmeh, (2019); and Momani, (2019)). The LiDAR Point Cloud of Data (PCD) is filtered in the proposed automated algorithm using minimum user interference. I would like to mention that existing companies use their own software, which is a black box; there is no explanation or information about their methodology, and their data analysis team generates their final report. Therefore, underlying methodology is explained thoroughly (in Section 3. Methodology).
2. Previous studies used Weibull or Normal distribution for the degradation process of concrete due to erosion (for instance, Mahmoodian & Li, (2011), Abuhishmeh, (2019); and Moamaei, (2019)). There is no study working on fitting the best distributions for concrete degradation on real inspection data. The automated algorithm using a qualitative measure (QQ-plots) finds the best-fit distribution to the concrete erosion data. In addition, the effect of assigning different distributions in estimating the remaining service life is explored.
3. Statistical methods, including Single Variable Regression, Multi-Variable Regression, and Polynomial Regression models, are utilized on the output of a proposed algorithm to estimate concrete erosion in the inner walls of RCSSPs. The regression models can be used to understand the relationship between the "Mean Loss (mm)" (the dependent variable) and other variables in the dataset (independent variables). In addition, the Bayesian approach is utilized to update the estimated mean loss values of the proposed methodology using priors from previous studies.

1.6 Limitation of Current Research

The limitations of this study are as follows:

1. The filtering phase of the proposed methodology is done using some interference, specifically in removing the flow line noises. Since the water level of inspected pipes is not constant throughout the length of the pipe. Therefore, developing a fully automated data filtering technique without user interference is impractical.
2. LiDAR cannot capture the geometry of the pipe below the water line. Some robots integrate Sonar technology with LiDAR to capture the geometry of the pipe below the water line. Therefore, this study assumes that the pipe is free of deposits.
3. In this study, the remaining service life (RSL) is the criteria for condition assessment of RCSSPs. The RSL is estimated based on concrete erosion as a serviceability limit state, and it does not reflect the pipe's time to failure. In addition, factors such as ovality and the existence of cracks, as well as operational factors such as sewer type and hydraulic condition of the pipe, will affect the service life of the SSPs; however, these are excluded from the current study and need further research.

CHAPTER 2. LITERATURE REVIEW

The first part of this paper outlines different inspection technologies for SSPs and their limitations. Several probabilistic and stochastic models for the deterioration of reinforced concrete sanitary sewer pipelines (RCSSPs) are addressed.

2.1 Inspection tools for sanitary sewer pipes (SSPs)

Inspecting the internal geometry of SSPs is the best way to assess their condition and to identify any defects, especially those associated with the concrete erosion of RCSSPs due to the presence of hydrogen sulfide. The accuracy of an inspection system has a direct impact on the accuracy of the estimated remaining service life of SSPs, which is often used as a criterion to simplify the condition assessment of SSPs (Jackson et al., 2020). It should be noted that other factors such as root intrusion, joint failure, pipe collapse, and excessive deposits are among other factors that can affect the service life of SSPs.

A major challenge of condition assessment is translating large amounts of inspection data into meaningful results that can ultimately help municipalities make robust decisions regarding the life-cycle management of SSPs. Conventionally, municipalities across the world use Closed-circuit television (CCTV) for inspection of pipelines. It is the most frequently used, most cost-efficient, and most effective method to inspect the internal condition of a sewer for sewer lines (EPA, 1999). Like other approaches, CCTV has its advantages and disadvantages. CCTV results highly depend on image quality and inspector skills. For instance, there is a twenty-five-percentage probability that an inspector may miss existing defects (Dirksen et al., 2013). To overcome these disadvantages, statistical data analysis methods are utilized based on the CCTV inspection outputs (i.e., images). For example, some researchers have used image processing approaches along with

machine learning and artificial intelligence (AI) algorithms to supplement visual inspections. Among machine learning algorithms, convolutional neural networks (CNNs) are widely used for CCTV output; Cheng and Wang (Cheng & Wang, 2018) employed Faster R-CNN, Kumar et al. (Kumar et al., 2018) implemented deep CNN, Li et al. (D. Li et al., 2019) adopted a deep CNN with hierarchical classification approach, and Hassan et al. (Dang et al., 2018) integrated CNN with text recognition methods. Yin et al. (Yin et al., 2021) developed a real-time CCTV video interpretation algorithm and sewer pipe video assessment (SPVA) system for SSPs; it processes real-time CCTV videos by pairing it with the defect detector algorithm (developed by Yin et al. (Yin et al., 2020)) identifying defects such as crack, fracture, holes, root incursions, and deposits, etc. Despite the improvements in CCTV inspections, characterization, and quantification of the interior geometry of pipes using just the images provided by CCTV is difficult and often inaccurate. To overcome this limitation, other inspection techniques have been implemented.

For example, pipe penetrating radar (PPR), a pipe version of ground penetrating radar (GPR) (Ékes et al., 2011), is used to determine the remaining wall thickness and evaluate the bedding conditions of pipes (Najafi, 2010). Acoustic technology (Feng et al., 2012) has been used to locate blockages along the pipe and at lateral connections. Laser profiling (laser ring (2D) that is usually mounted on CCTV equipment) projects a beam of light onto the inner surface of the pipe and records it with CCTV. It has been applied for checking deformation such as ovality and defects such as cracks or deposits above the water line (Duran et al., 2003). Clemens et al. (2015) showed that laser profiling is capable of assessing the hydraulic roughness of pipes as well as evaluating remaining pipe thickness. Laser profiling is often integrated with other technologies such as sonar (Al Asadi, 2018) to quantify deposits (e.g., debris) below the flow line. However, laser profiling technology is susceptible to errors especially when it is monitoring partially filled pipes; for example, the laser

emitter is sometimes covered by water droplets resulting in noisy and/or inaccurate profiling. These MSI equipment have entered the industry as a non-destructive evaluation (NDE) technique to evaluate the pipe condition.

Light detection and ranging (LiDAR) technology has many real-world applications. It is used in today's smart devices such as smartphones and in self-driving vehicles. LiDAR collects the data by emitting a pulse or modulated light signal and calculating the time difference in the returning wavefront (Schuon et al., 2008). Lambert et al. (2020) compared the performance and accuracy of 10 commonly used LiDAR sensors in terms of scanning the environment. LiDAR allows manufacturers to obtain cost-effective and high-quality mass 3D point cloud of data (PCD) in a time-efficient way (Vogt et al., 2021). 3D LiDAR PCD can create full sections of pipe in 3D geometry of points; this makes the data size very small compared to conventional inspection techniques such as CCTV (in which the outputs are images and videos). The advantages of LiDAR technology are high precision, long perception distance, fast data collection, and robust output data sets compared to other techniques. In the pipeline industry, LiDAR is mostly used to map pipeline routes with an aircraft-mounted LiDAR system; for instance, LiDAR is used for constructing as-built maps and monitoring natural gas pipelines ((Barnwell et al., 2009), (Tao & Hu, 2002), and (Lewis et al., 2012)). Moreover, few studies have used LiDAR technology for evaluating the inner concrete wall geometry of pipes; Ékes (2021) used LiDAR inspection data for condition assessment of the inner concrete wall of 42" RC pipes. Ebrahimi and Jalali ((Ebrahimi et al., 2023; Ebrahimi & Jalali, 2022a; Hojat Jalali & Ebrahimi, 2021)) used 3D LiDAR scans of 54" RCSSPs; they developed an automated algorithm to calculate the diameter and ovality of SSPs using 3D LiDAR inspection PCD. Meanwhile, a CCTV camera is attached to the same crawler that collects LiDAR data, and stores CCTV feeds for further analysis (Feeney et al., 2009). Utilizing LiDAR

would present the actual condition of the pipeline such as how much it is corroded or whether there is any deposit. It effectively detects corrosion, debris, and ovality.

2.2 different probabilistic and stochastic techniques

Inspection of underground SSPs is more complex than above-ground infrastructure such as bridges and pavements; therefore, they are typically inspected only a few times during their service life. Meanwhile, to create an accurate stochastic model, more than one inspection data is required. This hinders the stochastic models, from capturing the true deterioration process of SSPs during their life span. There have been many studies in estimating the concrete erosion rate of RCSSPs. Among those, two common methods are used. The first method is an empirical model which was developed based on actual field test data. Islander et al. (1991) were among the first researchers to study micro-biologically influenced corrosion (MIC) of pipes (i.e., the main type of corrosion for partially filled RCSSPs); they showed that corrosion is a three-stage process, which is characterized by the PH levels of the concrete surface. Wells and Melchers (2014, 2015) supported the empirical results by monitoring concrete coupons that were mounted inside existing large SSPs throughout Australia. These studies aimed at quantifying the underlying mechanisms of corrosion processes to predict the loss of inner concrete cover due to long-term erosion. These studies led to the widely known Pomeroy model by Pomeroy and Boon (1990) which is commonly used to calculate the erosion rate of RCSSP and estimate their RSL (Liu et al., 2017). According to (Bizier, 2007), the average erosion rate is calculated as the Pomeroy model. (Li et al., 2009) suggested that the Pomeroy equation only considers some of the important factors in estimating the erosion rate. Furthermore, relevant literature indicates that three environmental factors including temperature, H_2S concentration, and relative humidity have the highest correlation with corrosion propagation

(Wells & Melchers, 2015). In addition, recent studies such as Saleh Abuhishmeh and Hojat Jalali (2023) investigated other factors such as temperature, loading, and material uncertainties on the reliability of RCSSPs. Meanwhile, according to (Makana et al., 2022) there is no real-time data available for the SSPs.

The second approach is to estimate concrete erosion rate within RCSSPs involves probabilistic or stochastic methodologies. This method integrates empirical equations with different numerical methods. The empirical models used in this approach are created for one specific environment; therefore, there is uncertainty in each dependent parameter of the erosion rate equation (Equation 23). The numerical techniques should accommodate the inherent uncertainty of the empirical models. For instance, Ahammed and Melchers (1995) proposed a simple power law to estimate the erosion rate of SSPs and determine their reliability.

The uncertainty is commonly considered by assigning a probability density function (PDF) to each of the variables (instead of deterministic values). According to the literature, the normal distribution is commonly used for modeling erosion (Foorginezhad et al., 2021a). For the dependent variables in the Pomeroy equation, Ahammed and Melchers (1995) used the normal distribution, Li et al. (2009) used the lognormal and normal distributions, Mahmoodian and Alani (2014) assigned the gamma distribution, and Teplý et al. (2018) assigned the beta, log-normal, and normal distributions. Furthermore, Ahammed and Melchers (1995) used the normal distribution for variables C and NN in the Pomeroy equation. In addition, time-dependent techniques have been implemented for modeling concrete degradation due to sulfide corrosion. For power law, Mahmoodian and Li (2011) used a stochastic process to model H2S flux (Φ) and predict the remaining service life of RCSSPs. In Equation 20, Mahmoodian and Alani (2014) developed a stochastic gamma process model to estimate the erosion rate (C). Liu et al.(2017) developed a

hybrid Gaussian (normal) process regression model and tested their method with the experimental results of laboratory chambers. Abuhishmeh (2019) and Moamaie (2019) estimated the service life of RCSSPs using the probability of exceedance method with a serviceability limit state as the inner concrete cover. Foorginezhad et al. (2021) also reviewed different data-driven approaches implemented on nondestructive (ND) inspection data for RCSSPs.

Table 1 shows the summary of studies and the estimated parameters for concrete erosion:

Table 1. Summary of Studies on Estimating the Parameters of Concrete Erosion

Reference	Distribution	Parameters	Description
Ahmad and Melcher (1991)	Normal	(0.066 * t, 0.037) (Mean(M), Standard Deviation(D))	Steel Pipe (t in year)
David and Oscar (2004)	Normal	(0.1 * t, 0.2*t) (Mean (M), COV (C))	Steel Pipe (t in year)
Li et al (2007)	Normal	(0.15 * t, 0.2 * t) (Mean (M), COV (C))	Steel Pipe (t in year)
Mahmoodian and Alani (2013)	Gamma	(0.17 * t, 0.425) (Shape (A), scale (G))	Power Law Maximum Likelihood (t in year)
Mahmoodian and Alani (2013)	Gamma	(0.094 * t , 0.235) (Shape (A) and scale (G))	Power Law Method of Moment (t in year)
Mokhtari et al. (2016)	Weibull	(1.1327 , 0.1314) (shape (B), scale (S))	Steel Pipe
Moamaei, P., (2019)	Weibull	(4.4024, 55.8223, -38.3761) (shape (B), scale (S), Location L)	Using Probability of Existance
Abuhishmeh, k (2019)	Weibull	(Normal (1.8438, 0.3323), Normal (0.00806, 0.505446)) (Fitted shape (B), Fitted Scale (S))	Fitted Normal Distrubution to the parameters which are calculated by fitting the values to 22 pipelines

This paper explores the effect of assigning different distributions to the erosion rate and examines how various deterioration models affect the service life prediction of RCSSPs. To verify the results of the proposed framework, Monte Carlo simulation (MCS) is used. The consistency of the proposed method in predicting service life is compared with a previous study (Khaled Saleh Abuhishmeh, 2019; Moamaie, 2019) that employed the same inspection data. Meanwhile, risk

assessment frameworks are also developed by researchers, Abuhishmeh (2023) and Abuhishmeh and Hojat Jalali (Forthcoming) integrates fuzzy inference systems with an adaptive neural network, enhancing interpretability and decision-making.

Bayesian Network (BN) is a probabilistic graphical model that is utilized when there is uncertainty in an existing model due to the complexity or scarcity of data. Hence, BN offers a powerful framework for predicting concrete erosion rates in SSPs. A lot of studies implement BN into the risk and reliability of pipes. Pickard (1983) was among the first researchers to use BN; Pickard predicted the failure rate of systems with Bayes' theorem. Egger et all. (Egger et al., 2013) used BN for updating the defined parameters for different concrete degradation models. Mokhtar et al. (2016) utilized the BN to update the corrosion model parameters and evaluate their dependencies between pipes in different environments. Elmasry et al. (2017) use the BN with CCTV images to develop a defect-based deterioration model. Anbari et al. (2017) used BN to develop a risk assessment model to prioritize the inspection of the sewer network. Meanwhile, researchers use BN to predict the failure of different pipe systems. Atique et al. (2018) used BN to predict the failure of water mains by considering different factors; they used BN to update the copula parameters. Li et al. (2015) and Lue and Bui (2016) utilized BN to predict water leakage/burst in the water mains. Wu et al. (2017) used BN to predict and evaluate natural gas pipeline network accidents. Dahire et al. (2018) utilized BN to predict the natural gas pipeline strength considering the mechanical properties of pipes. Bayesian Network (BN) offers a powerful framework for predicting concrete erosion rates in SSPs because it could be used when there is uncertainty in an existing model due to its complexity and large interrelated factors. Therefore, in this study, the BN is used to predict the erosion rates using different priors from the literature and the likelihood

function which is the calculated erosion rate from the inspected SSPs at the age of 28. Ultimately, the results will be in the form of the predicted RSL.

There are a couple of distributions that are used for modeling degradation. The first is Weibull distribution. The PDF function is as follows:

$$WBL(x;\lambda,k) = \begin{cases} \frac{k}{\lambda} * \left(\frac{x}{\lambda}\right)^{k-1} * e^{-\left(\frac{x}{\lambda}\right)^{k}} & x \geq 0 \\ 0 & X < 0 \end{cases} \quad \text{Equation 1}$$

Where k: is the shape parameter. λ: is the scalar parameter (λ>0).

Figure 5 shows PDFs for 2-parameter Weibull distribution with different shape factors.

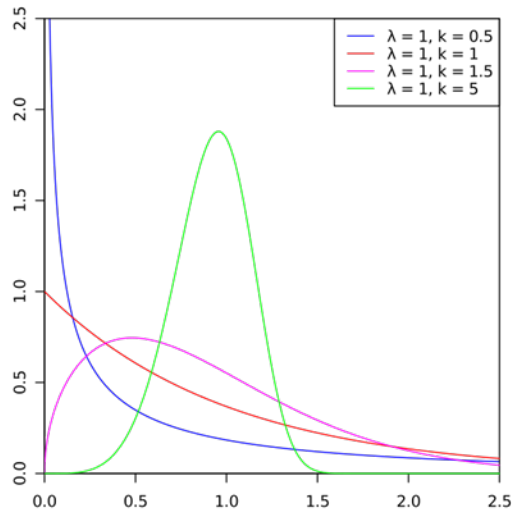

Figure 5. Probability Density Function of Weibull Distribution with Different Shape Parameters ((Papoulis & Pillai, 1991)

In this study, Half-Normal distribution will be also used to fit the loss data. Half-normal is a special case of Normal distribution (with the mean of zero). The Half-Normal is used for dealing with relationships between measurement errors and it was introduced by (Altman & Bland, 1983). The PDF for the Normal and Half-Normal distributions are shown in Figure 6. The PDF for a Half-Normal distribution is:

$$HN(x,\sigma) = \begin{cases} \frac{2}{\sqrt{2\pi}\,\sigma} * e^{-(\frac{x^2}{2\sigma^2})} & x \geq 0 \\ 0 & X < 0 \end{cases}$$ Equation 2

where: σ = Standard deviation.

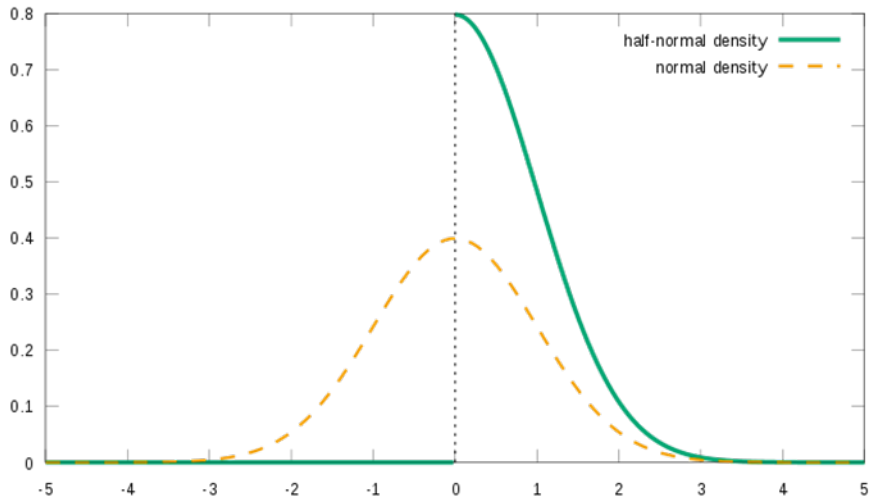

Figure 6. PDFs for Normal Distribution (with zero mean and std of 1) and Half-Normal Distribution (std of 1)(Altman & Bland, 1983)

Gamma Distribution is widely recognized for modeling concrete degradation. The mathematical representation of the gamma process can be found in Equation 3. It is important to remember that a stochastic variable x follows a Gamma Distribution with a positive shape parameter α and a positive scale parameter λ, provided its probability density function is defined accordingly.

$$Gamma\ (x|\alpha,\lambda) = \frac{\lambda^{\alpha}}{\Gamma(\alpha)}\ x^{\alpha-1}e^{-\lambda x}$$ Equation 3

Where $\alpha(t) = \alpha$ right continuous, real-value equation for $t \geq 0$, and $\alpha(0) = 0$.

Figure 7 shows PDFs for Gamma distribution with different shape factors.

Figure 7. PDF of the Gamma Distribution for values of α and λ (Pishro-Nik, 2014)

To model concrete corrosion due to a hydrogen sulfide attack using the gamma process, the expected deterioration (that increases over time) is the shape function for the gamma distribution. Different studies show that the expected corrosion depth at time *t* is often proportional to a power law (Mahmoodian & Alani, 2014):

$$\alpha(t) = C * t_i^{rate}$$

Power law will be explained in *subsection 3.4.10.1.1*

CHAPTER 3. METHODOLOGY

This dissertation includes two main parts, the first part is the automated proposed framework shown in Figure 8; the framework implements on the raw LiDAR inspection data to filter, trim the 3D raw PCD, calculate the hydraulic properties, and ultimately estimating the service life using different approaches.

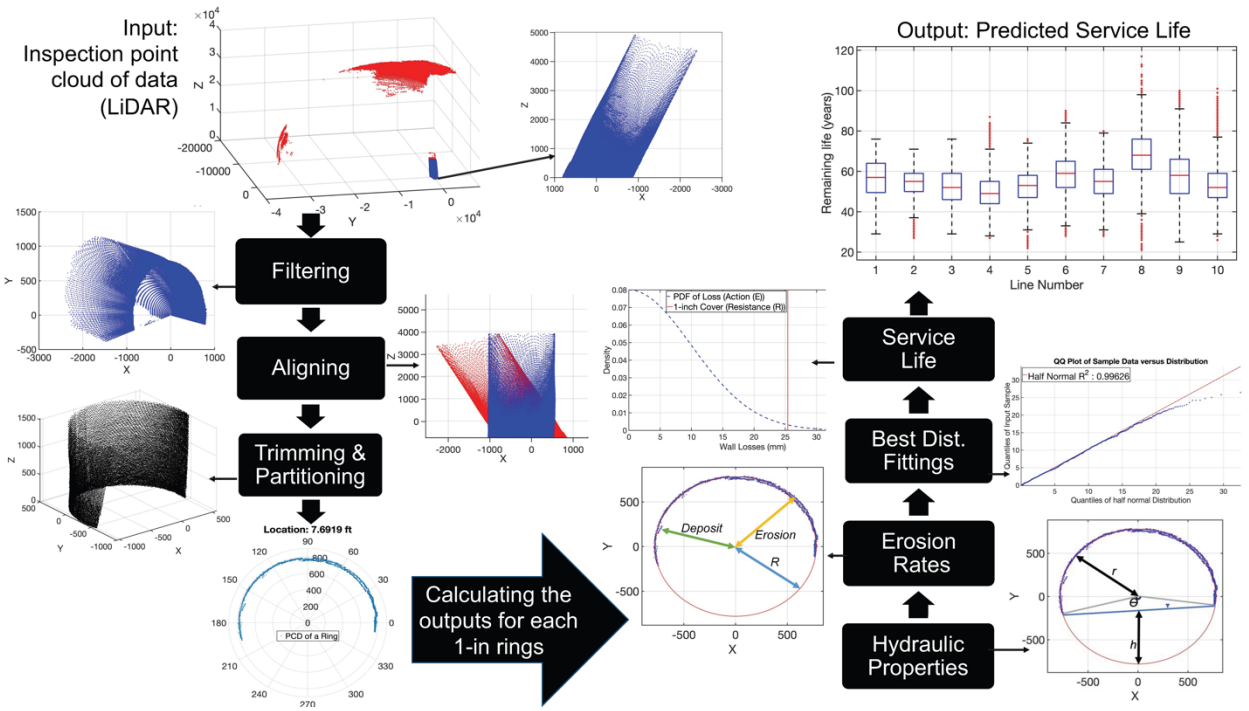

Figure 8. Summary of Proposed Automated Framework

the second part is performing regression analysis on the calculated/estimated values and performing Bayesian framework to update the estimated concrete loss of RCSSPs using two different priors.

3.1 Material Selection

In this study, the proposed algorithm probabilistically predicted the residual lives of large RC sanitary sewer pipelines (with diameters of 30, 54, and 60 inches) by incorporating inspection data for 8,000 ft of pipes. All the LiDAR raw data is borrowed from Center for Structural Engineering Research and Pipeline Inspection (CSER-PI). Table 2 shows the properties of selected materials. The age of each pipe is 28 years at the time of inspection.

For 54- and 60-inch pipes, the PCD is collected by the multi-sensor inspection (MSI) equipment from RedZone Robotics Renton (Redzone, 2021). The robot crawls into partially filled pipelines and records videos from the inside of the RCSSPs as it moves from one manhole to the adjacent manhole (M-M). To scan the 3D LiDAR data in the form of PCD, the robot stops at each 5-ft linear length and performs a 360◦ scan from the inside geometry of the RCSSPs. For a 30-inch pipe, the outputs are 2D rings of PCD scanned at different times as the crawler goes from one manhole to the other; therefore, the filtering phase is not applied to them.

All the RCSSPs are in the same geographical area, so, it is reasonable to assume that the environmental factors and deterioration rates are the same for these pipes. Table 2 shows the properties of the selected RCSSPs. To illustrate the application of the proposed methodology, the first 5-ft section of Line 1 is investigated in detail.

Table 2. Selected Materials

Line Number	Diameter; Meter(inch)	Length (M-M); Meter (ft)	Slope
1	1.524 (60)	106.7 (350)	5
2	1.524 (60)	57.9 (190)	5
3	1.524 (60)	79.4 (260.5)	5
4	1.524 (60)	67.2 (220.5)	5
5	1.524 (60)	146.3 (480)	5
6	1.372 (54)	96.9 (318)	6
7	1.372 (54)	73.2 (240)	6
8	1.372 (54)	65.8 (216)	6
9	1.372 (54)	127.1 (417)	6
10	1.372 (54)	100 (328)	6
11	0.762 (30)	161 (528.4)	-
12	0.762 (30)	7.8 (25.6)	-
13	0.762 (30)	77.9 (255.5)	-
14	0.762 (30)	22.9 (75)	-
15	0.762 (30)	78 (257)	-
16	0.762 (30)	225.2 (738.8)	-
17	0.762 (30)	107.3 (352)	-
18	0.762 (30)	145.7 (478)	-
19	0.762 (30)	30.3 (99.5)	-
20	0.762 (30)	118.1 (387.5)	-
21	0.762 (30)	82.8 (271.6)	-
22	0.762 (30)	54.4 (178.4)	-
23	0.762 (30)	175.2 (574.8)	-
24	0.762 (30)	197.6 (648.4)	-
25	0.762 (30)	52.6 (172.7)	-

Our proposed algorithm is developed to get the output of LiDAR data and apply filtering, aligning, and obtaining current corrosion levels. Based on the decision makers' decision, the results could be presented in different scales, especially for 54- and 60-inch, it could be presented as small as a 1-inch ring, or as big as a 5-foot section, or even for one whole line (M-M).


REDZONE ROBOTICS
Bellaire Boulevard Treatment Plant
BW230002 -> BW230001
Circular 60"/"
Observation Code: MWL - Water Level
Clock From Position:
Clock To Position:
Percentage of Defect: 20
In Joint?: False
Continuous:
Defect Size:
Tap Size:
Remarks:
Upstream Manhole: BW230002
Downstream Manhole: BW230001
Width of Pipe:
Material of Pipe: Reinforced Concrete Pipe
Diameter or Height if non-circular:60
Shape of Pipe: Circular
Direction of Survey: Downstream
Inspection Date: Wednesday, 11 May 2016
1.3'

(a)

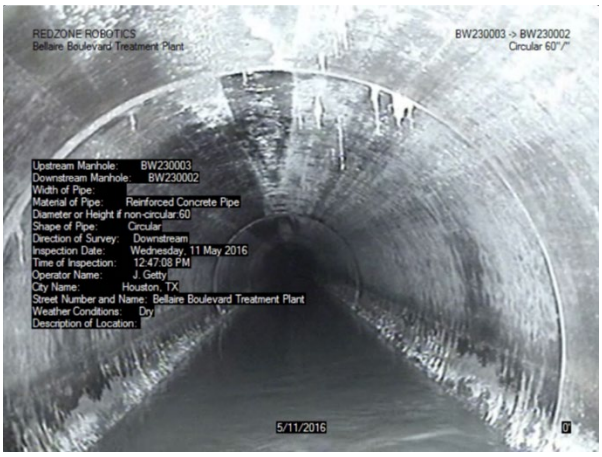
REDZONE ROBOTICS
Bellaire Boulevard Treatment Plant
BW230003 -> BW230002
Circular 60"/"
Upstream Manhole: BW230003
Downstream Manhole: BW230002
Width of Pipe:
Material of Pipe: Reinforced Concrete Pipe
Diameter or Height if non-circular:60
Shape of Pipe: Circular
Direction of Survey: Downstream
Inspection Date: Wednesday, 11 May 2016
Time of Inspection: 12:47:08 PM
Operator Name: J. Getty
City Name: Houston, TX
Street Number and Name: Bellaire Boulevard Treatment Plant
Weather Conditions: Dry
Description of Location:
5/11/2016
0'

(b)


REDZONE ROBOTICS
Bellaire Boulevard
BW230045 -> BW230044
Circular 60"/"
Upstream Manhole: BW230045
Downstream Manhole: BW230044
Width of Pipe:
Material of Pipe: Reinforced Concrete Pipe
Diameter or Height if non-circular:60
Shape of Pipe: Circular
Direction of Survey: Downstream
Inspection Date: Friday, 06 May 2016
Time of Inspection: 8:30:01 AM
Operator Name: J. Getty
City Name: Houston, TX
Customer: Cleanserve
Street Number and Name: Bellaire Boulevard
Weather Conditions: Dry
Description of Location:
5/6/2016
0'

(c)


REDZONE ROBOTICS
Bellaire Boulevard
BW230046 -> BW230045
Circular 60"/"
Observation Code: AMH - Manhole
Clock From Position:
Clock To Position:
Percentage of Defect:
In Joint?: False
Continuous:
Defect Size:
Tap Size:
Remarks: BW230046
Upstream Manhole: BW230046
Downstream Manhole: BW230045
Width of Pipe:
Material of Pipe: Reinforced Concrete Pipe
Diameter or Height if non-circular:60
Shape of Pipe: Circular
Direction of Survey: Downstream
Inspection Date: Friday, 06 May 2016
0'

(d)


REDZONE ROBOTICS
Bellaire Boulevard
BW230066 -> BW230065
Circular 54"/"
Observation Code: AMH - Manhole
Clock From Position:
Clock To Position:
Percentage of Defect:
In Joint?: False
Continuous:
Defect Size:
Tap Size:
Remarks: BW230066
Upstream Manhole: BW230066
Downstream Manhole: BW230065
Width of Pipe:
Material of Pipe: Reinforced Concrete Pipe
Diameter or Height if non-circular:54
Shape of Pipe: Circular
Direction of Survey: Downstream
Inspection Date: Monday, 09 May 2016
0'

(e)


REDZONE ROBOTICS
Bellaire Boulevard
BW230111 -> BW230110
Circular 54"/"
Upstream Manhole: BW230111
Downstream Manhole: BW230110
Width of Pipe:
Material of Pipe: Reinforced Concrete Pipe
Diameter or Height if non-circular:54
Shape of Pipe: Circular
Direction of Survey: Upstream
Inspection Date: Tuesday, 10 May 2016
Time of Inspection: 10:27:00 AM
Operator Name: J. Getty
City Name: Houston, TX
Street Number and Name: Bellaire Boulevard
Weather Conditions: Dry
Description of Location:
5/10/2016
0'

(f)

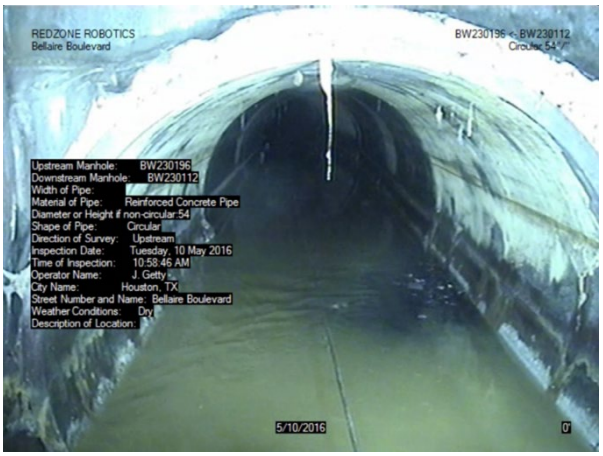

(g)

(h)

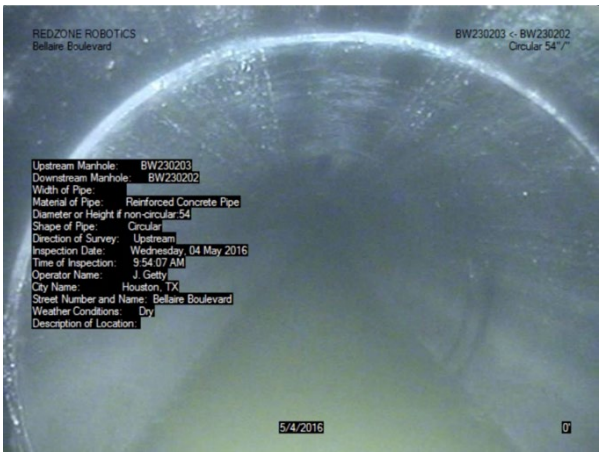

(i)

(j)

Figure 9. Screenshots of CCTVs from the 10 different RC sanitary pipelines; a-e are 60 inch and f-j are 54 inches pipes.

The MSI equipment is RedZone Robotics (Redzone, 2021). The robot crawled into a partially filled pipeline and recorded videos from the inside of the RC pipeline as it went from one manhole to the other manhole. Figure 10 shows the MSI robot used in this research. At each 5-ft section, the robot scans the inside wall of the RC pipeline using LiDAR measurements. The collected point cloud of data (raw data) is in spherical coordinates (r, θ, φ). This output is for 54- and 60-inch SSPs; however, for the inspection of 30-inch SSPs, the inspection outputs are provided as 2D rings along the length of pipes.

All the procedures for processing LIDAR information, obtaining current corrosion levels, and performing the probabilistic service life prediction are performed using the code of the proposed algorithm written in MATLAB software. The algorithms will be explained thoroughly in the following sections. In addition, the BN algorithm and regression analysis are done using Python Libraries: NumPy and SciPy, and the plots using Matplotlib dictionary.

Figure 10. MSI RedZone Robot

3.2 Properties of Collected Data

The inspection PCD (i.e., the outputs of MSI robot) are collected for each 5-ft section of every pipeline (M-M). For instance, since Line 1 is 369 ft in length and 369/5 ≈ 74, there are 74 sets of 3D PCD collected for this pipeline. These PCDs are in the spherical coordinate systems (i.e., ρ, θ, φ). In other words, each point of the PCD has three parameters: radial distance ρ (in, mm), inclination angle ($0^{\circ} < \varphi < 180^{\circ}$), and azimuth angle ($0^{\circ} < \theta < 360^{\circ}$). Figure 11 shows the relationship between the spherical (ρ, θ, φ) and Cartesian coordinate systems (x,y,z).

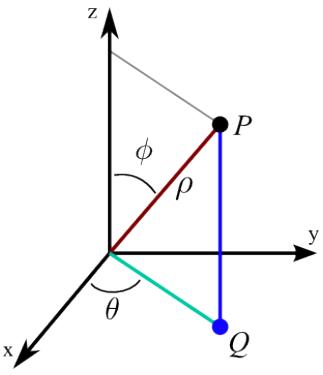

Figure 11. Spherical Coordinate Space and Cartesian Coordinate Space

3.3 Assumptions

- Inner wall concrete cover is assumed to be uniform for all pipelines. It is expressed as a single value of 1 inch by referring to (ASTM C76.8.3.1); or 1.5 in some special cases.
- The corrosion rate is assumed to be constant throughout the life span of RCSSPs.

3.4 Proposed Algorithms

This study elaborates automated algorithm for pre-processing the 3D LiDAR PCD. There are minor user-intervention in finding the constraints for parameters (ρ, θ, φ), which can be a function of pipe diameter, flow capacity, flow rate, and slope of pipe among other factors; however, the constraints are predefined to the program and pre-processing is performed automatically.

In this section, the proposed automated algorithm is explained. To illustrate the process, the first 5 *ft* section of Line 1 is used. It should be noted that the data for 30-inch pipes are excluded from the following sections since the output of the inspection data is 2D rings. Furthermore, the proposed data-driven methodology is discussed in detail, including data processing, calculating hydraulic properties of RCSSPs, finding the best-fit probability density function (PDF)

corresponding to the deteriorated inner concrete wall geometry of RCSSPs, and probabilistically estimating their residual service life.

3.4.1 Data Filtering

First, the raw data from the inspection robot is in the spherical coordinate system (ρ,θ,φ); The first step of the proposed algorithm is to convert the PCD from spherical to Cartesian coordinate using Equation 4 (Sokolov, 2020).

data is converted to cartesian coordinate (x,y,z) using following Equation:

$$x = \rho\, cos(\theta)\, sin(\boldsymbol{\varphi})$$

$$\mathrm{Y} = \rho\, sin(\theta)\, sin(\boldsymbol{\varphi}) \qquad \text{Equation 4}$$

$$z = \rho\, cos(\boldsymbol{\varphi})$$

where:

ρ = the radial distance (mm);

θ = the azimuth angle (Degree);

φ= the inclination angle (Degree);

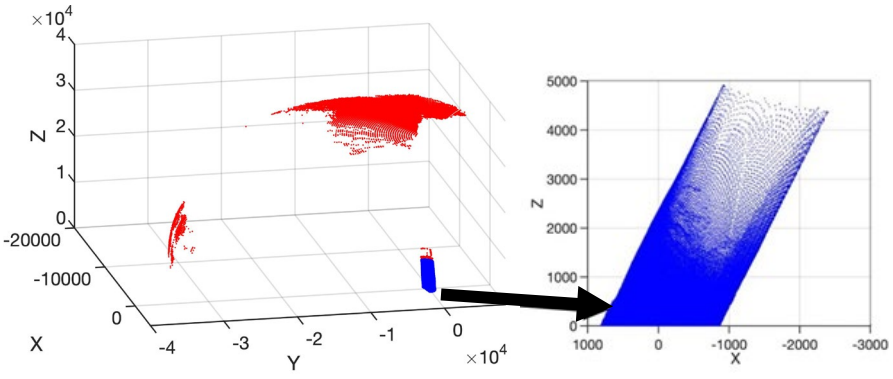

Figure 12. Unfiltered Data after Converting to Cartesian Space

Figure 12 shows the raw PCD after conversion to Cartesian coordinates; the blue PCD at the center of the spherical PCD is the cylindrical PCD representing the inner concrete wall geometry of a 5-ft section. The red points are outliers and are the noise. Figure 12 illustrates that, in addition to the noise collected from the sewer flow, the LiDAR scanner also collects noise outside the pipeline geometry. Therefore, the proposed algorithm should impose filtering by constraining the spherical parameters in converting to Cartesian coordinates (Equation 4). To capture the PCD from the internal geometry of the pipes (i.e., the blue cylindrical PCD in Figure 12), two constraints are imposed: global filtering and water noise filtering, as described in the next two sections.

3.4.1.1 Global Filtering

The MSI robot stops at the beginning of each 5-*ft* section and the LiDAR scanner (which is located at the center of the spherical shape in Figure 12) collects the PCD; to remove the outliers (red PCD in Figure 12), ρ (radial distance) values must be limited in the conversion process (in Equation 4). The maximum diameter of the pipe is 60 inches (1524 *mm*), and the region of interest (RoI) is 5 ft (1524 *mm*). Therefore, points with radial distance $500 < \rho < 2000$ mm are included in the transformation of Equation 4. The result is shown in Figure 13.

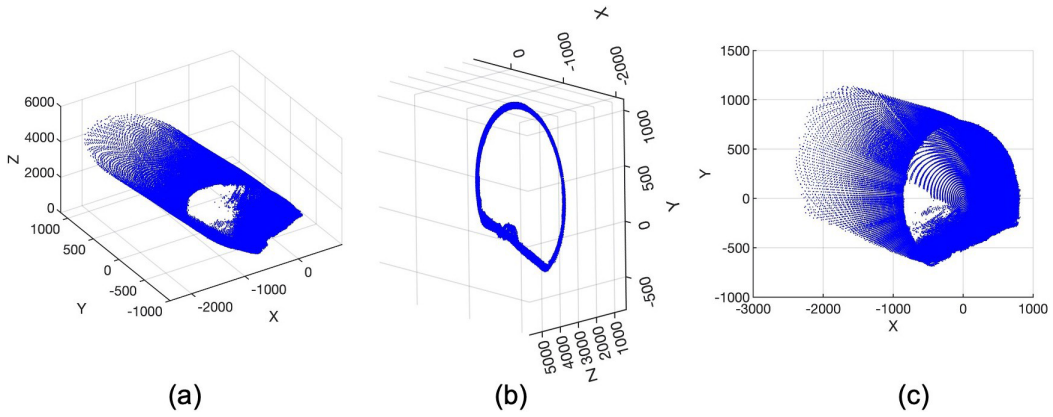

Figure 13. Result of the Global Filtering (unit: mm): (a) Isometric View, (b)3D Cross Sectional View, and (c) Y-X Plane View

3.4.1.2 Water Level Filtering

The inspected RCSSPs are partially filled pipes and the sewer flow noise exists in all the 5-ft sections' PCD. Therefore, the flow noise is filtered by excluding the flow (sewer) PCDs from Equation . This is done by finding the range of azimuth angle (θ) which indicates the water PCDs at the bottom portion of the pipe. This range is defined as follows:

$$\begin{cases} \theta_{min} < \theta < \theta_{Max} & if\ \boldsymbol{\varphi} \leq 0 \\ \theta_{min} + 180 < \theta < \theta_{Max} + 180 & if\ \boldsymbol{\varphi} > 0 \end{cases} \qquad \text{Equation 5}$$

By trial and error and visual inspection, these ranges are defined as $0^{\circ} < \theta_{min} < 15^{\circ}$ and $155^{\circ} < \theta_{Max} < 170^{\circ}$. These ranges (which are found for the first 5-ft section) are applicable for all the following 5-ft sections within a line(M-M). The PCDs that meet the constraint in Equation are included in the conversion process (Equation 4). For our inspection data, the angles are predefined to the program and filtering is performed automatically. Figure 14 shows the final (filtered) PCD after imposing the two phases of filtering.

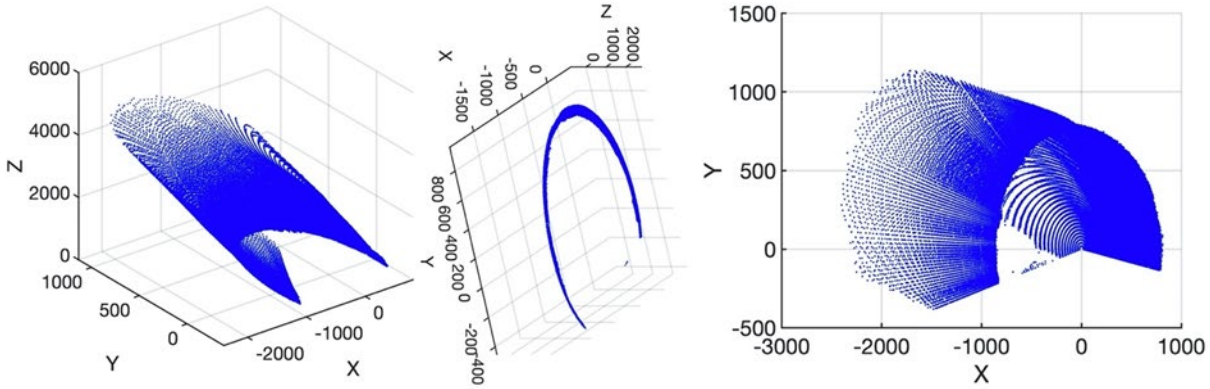

(a) (b) (c)

Figure 14. Data after Filtering of Water Level Noise (unit: mm): (a) Isometric view, (b) Z-Y view, and (c) Z-X view

It is worth mentioning that in each scan of the so-called 5-ft section, more than 5-ft length of the pipe is scanned (it is about 15-ft). So, after aligning the PCD, the data will be trimmed into a 5-ft length of pipe.

3.4.2 Alignment of PCD

Typically, the orientation of the filtered PCD (in the Cartesian space) is unknown. Therefore, to restore the filtered PCD to a correct alignment (which is the Z-axis herein), the principal axes of the cylindrical PCD are determined by estimating the center of the rotation and shifting it to the origin of the Cartesian coordinate system (0,0,0). Finally, the PCD is rotated so that the direction of flow is aligned with the Z-axis. This alignment allows for the calculation of the hydraulic properties and erosion rate. The following numbered list discusses the algorithm for finding the orientation of the cylindrical PCD and rotating them in a certain direction. Alignment is implemented in the following two steps:

3.4.2.1 Finding the Reference Line

For each 5 *ft* section, a reference line is found by selecting the points along the length of the pipe. By trial and error, the line PCD is selected when the following constraints are applied in conversion Equation 4:

$$340 < \theta < 341 \quad \& \quad \boldsymbol{\varphi} \leq -30$$

This constraint is the same for all the 5-ft sections of the 10-line pipelines (i.e., 54- and 60-inch pipes). For our inspection data, the angles are predefined to the program, and aligning is performed automatically.

Figure 15 shows the reference line for the first 5-ft section of line 1, where the direction of the reference line is indicated by the red arrow.

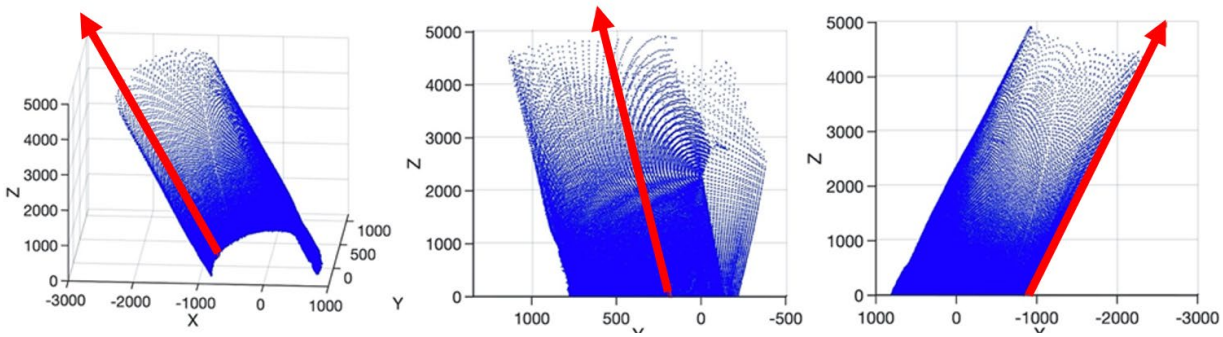

(a) (b) (c)

Figure 15. Reference Line PCD for Line 1, Section 1 (unit: mm): (a) Isometric View, (b) Z-Y View, (c) Z-X View

3.4.2.2 Eigenvalue Decomposition

Eigenvalue decomposition (ED) is the best tool for calculating the direction of an arbitrary line in 3D space. The ED is performed on covariance matrix of the reference line PCD. The outputs of ED are eigenvectors (representing the directions of the PCD), and eigenvalues (representing the amount of stretch of PCD in each of the three axes). The covariance matrix of the selected reference PCD is calculated as follows:

1- In a matrix form, the reference PCD in Cartesian space is expressed as shown in the following:

$$P=\begin{bmatrix} x_1 & y_1 & z_1 \\ x_2 & y_2 & z_2 \\ x_3 & y_3 & z_3 \\ \vdots & & \\ x_N & y_N & z_N \end{bmatrix}_{NX3}$$

where N is the number of points in the reference line PCD.

2- Determine the mean of each axis (i.e., each column): $[\bar{X}\ \bar{Y}\ \bar{Z}]$

3- Subtract each dimension (columns) from its means to create centered data:

$$\begin{bmatrix} (x_1 - \bar{X})(y_1 - \bar{Y})\ (z_1 - \bar{Z}) \\ (x_2 - \bar{X})(y_2 - \bar{Y})\ (z_2 - \bar{Z}) \\ (x_3 - \bar{X})(y_3 - \bar{Y})\ (z_3 - \bar{Z}) \\ \vdots \\ (x_N - \bar{X})(y_N - \bar{Y})\ (z_N - \bar{Z}) \end{bmatrix}$$

where $\boldsymbol{N}$ is a total number of PCD, $\overline{\boldsymbol{X}}, \overline{\boldsymbol{Y}}, \overline{\boldsymbol{Z}}$ are mean values of all $\boldsymbol{x}, \boldsymbol{y}, \boldsymbol{z}$.

4- Variance/Covariance matrix of centered data is formed as Equation 6.

$$A = \begin{bmatrix} \sum_{i=1}^{N}(x_i - \overline{X})^2 & \sum_{i=1}^{N}(x_i - \overline{X})(y_i - \overline{Y}) & \sum_{i=1}^{N}(x_i - \overline{X})(z_i - \overline{Z}) \\ \sum_{i=1}^{N}(y_i - \overline{Y})(x_i - \overline{X}) & \sum_{i=1}^{N}(y_i - \overline{Y})^2 & \sum_{i=1}^{N}(y_i - \overline{Y})(z_i - \overline{Z}) \\ \sum_{i=1}^{N}(z_i - \overline{Z})(x_i - \overline{X}) & \sum_{i=1}^{N}(z_i - \overline{Z})(y_i - \overline{Y}) & \sum_{i=1}^{N}(z_i - \overline{Z})^2 \end{bmatrix} \quad \text{Equation 6}$$

Eigenvalue decomposition is done using built-in function in MATLAB (*eig*). The output of the eigenvalue decomposition is: *[V,D] = eig(A)*.

Where *D* is a 3x3 diagonal matrix of eigenvalues and a *V* is a 3x3 full matrix whose columns are the corresponding eigenvectors so that *A*V = V*D*.

The column corresponding to the larger eigenvector (*D*) is the orientation that has the maximum variation which is the trajectory of the pipe in 3D space (the red arrow in Figure 14). v is the column vector of *V* showing the larger eigenvector represents the direction of the *5-ft* cylinder in 3D space.

$$v = \begin{bmatrix} \mathrm{v}_{3,1} \\ \mathrm{v}_{3,2} \\ \mathrm{v}_{3,3} \end{bmatrix}_{3\mathrm{x}1}$$

After estimating the eigenvector (v), the cross product of the unit vector of v (i.e., v /norm(v)) and the Z-axis ($\hat{k} = [0,0,1]'$) is calculated as Equation 7.

$$\boldsymbol{U} = \frac{v_{3\times 1}}{Norm(v)} \times [\mathbf{0}, \mathbf{0}, \mathbf{1}]' \quad \text{Equation 7}$$

The rotation of the PCD is done using rotation matrices. The rotation angles ($\emptyset_x$,$\emptyset_y$) are then calculated from the eigenvectors. In Equation 7, *U* is in the form of $[\emptyset_x, \emptyset_y, 0]$. Using the alignment algorithm, counter rotation is applied by multiplying the PCD to the rotation matrices (Alzuhiri et al., 2021) as shown in Equation 8 through 10. It creates a roto-translation matrix that rotates vector v to the constant direction which is *i=[0,0,1]'* (i.e., the unit vector of Z-direction).

$$\boldsymbol{R_x} = \begin{pmatrix} \mathbf{1} & \mathbf{0} & \mathbf{0} \\ \mathbf{0} & \boldsymbol{cos}(\emptyset_x) & -\boldsymbol{sin}(\emptyset_x) \\ \mathbf{0} & \boldsymbol{sin}(\emptyset_x) & \boldsymbol{cos}(\emptyset_x) \end{pmatrix} \quad \text{Equation 8}$$

$$\boldsymbol{R_y} = \begin{pmatrix} \boldsymbol{cos}\,(\emptyset_y) & \mathbf{0} & \boldsymbol{sin}\,(\emptyset_y) \\ \mathbf{0} & \mathbf{1} & \mathbf{0} \\ -\boldsymbol{sin}(\emptyset_y) & \mathbf{0} & \boldsymbol{cos}\,(\emptyset_y) \end{pmatrix} \quad \text{Equation 9}$$

$$\boldsymbol{AP} = \boldsymbol{R_x R_y P} \quad \text{Equation 10}$$

where *P* is the coordinate of original PCD with *X*, *Y*, *Z* coordinates; R_x and R_y are the rotation matrices around *x*-axis and *y*-axis respectively. *AP* is coordinate of aligned PCD. $\emptyset_x$ and $\emptyset_y$ are the rotation angles around *x* and *y* axes which are calculated in Equation 7.

The result is shown in Figure 16, the red points are the original data, and the blue points are the aligned data.

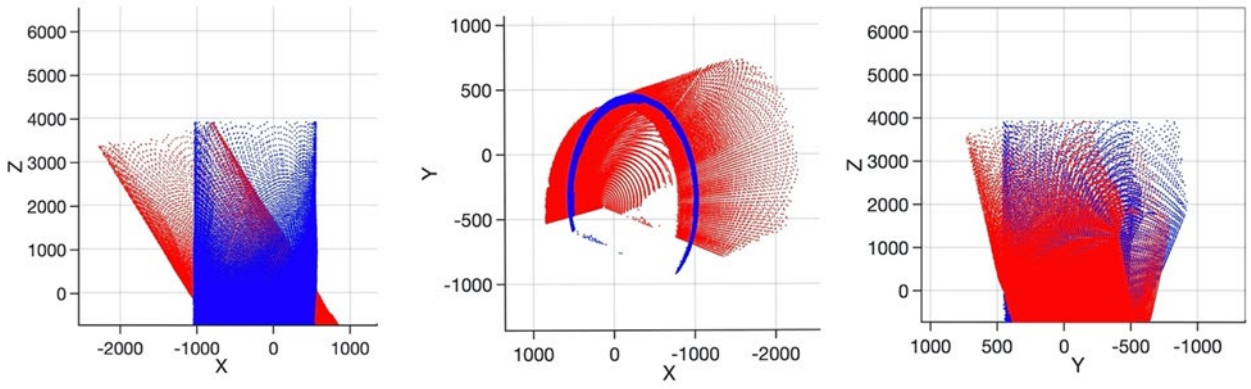

(a) (b) (c)

Figure 16. Rotating the PCD in a Constant Direction: (a) Z-Y view, (b) Y-X view, (c) Z-Y view

The last step of the data processing is to trim the PCD into a 5-ft length region along the Z-axis (i.e., the RoI), since the LiDAR scanner provides PCD for more than the 5-ft length of the pipe (it is about 15-ft, but the data shows scattering beyond 5ft, and is cut-off herein). The 5-ft length is predefined to the program and trimming is performed automatically. The final PCD of the pipe for each 5-ft section is shown in Figure 17.

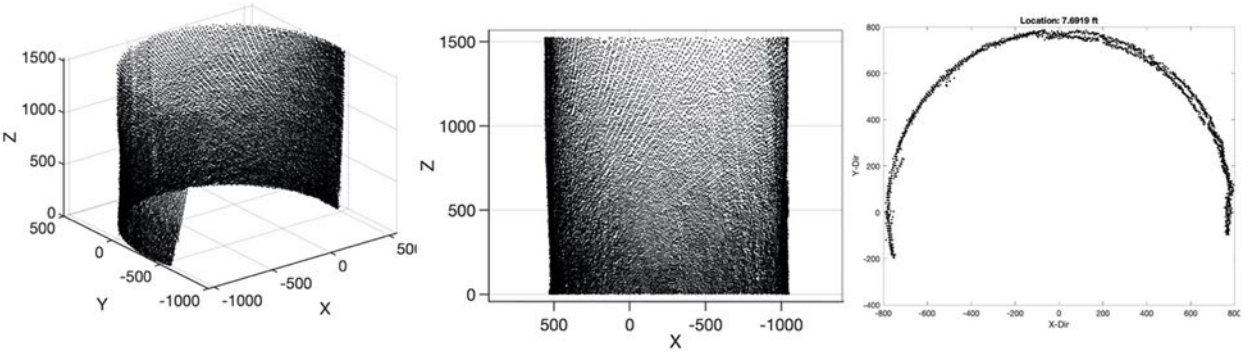

(a) (b) (c)

Figure 17. Filtered, Aligned, and Trimmed PCD: (a) isometric view, (b) Z-X view, (c) 2D PCD (i.e., Ring)

After processing the PCD (i.e., the filtering, aligning, and trimming), each 3D PCD is divided into several discrete 2D rings with 1 inch length, measured along the Z-axis; each 5 ft segment of pipe

consists of 60 1-inch wide 2D rings. 1-inch thickness (Z direction) is negligible comparing to a diameter of the pipe (54”-60”); therefore, it is safe to assumed that the 3D space (X-Y-Z) of rings is equivalent to 2D space (X-Y) (Figure 17). Determining the properties from these 2D rings is more accurate and less time-consuming than cylinder-fitting of the 3D PCDs. So, instead of using a time-consuming cylinder-fitting method in 3D space that is subject to user error, a circle fitting method in 2D space can be used instead. It should be noted that for 30 inches data, the inspection outputs are provided as 2D rings; however, the inspection outputs for 54- and 60-inches pipe are 3D PCD for 5 ft sections of each pipeline (M-M).

After rotating a cylindrical PCD into a correct alignment, its center of rotation is shifted. Since the center of these 2D rings are not located at the origin (0,0), a final re-centering is performed on the 2D rings. The initial location of each ring and its radius are calculated using the circle fitting Landau algorithm provided by (Sumith, 2023). Figure 18 illustrates this step, where the blue points are centered to the red points.

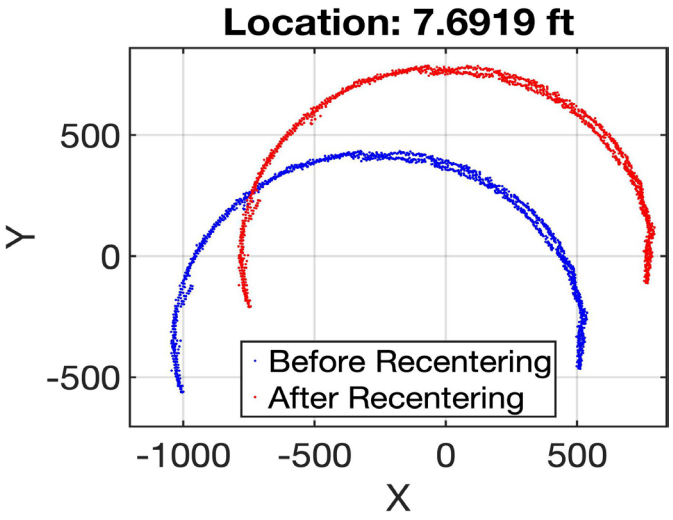

Figure 18. Recentered 2D Ring of PCD

3.4.3 Evaluating Diameter and Deflection

In practice, the deflection test is conducted for monitoring the quality of installations and verifying the minimum size requirements of the pipe (of any material). The traditional method for assessing pipe deflection is mandrel testing. Although mandrel testing is a simple approach, it has some limitations. The mandrel must be designed for a specific pipe size. Additionally, mandrel gauge could damage the pipe inner surface, particularly for pipes with linings. Also, there is a possibility that mandrel gets stuck inside the pipe. Therefore, video inspection must be performed before and after the mandrel test, which makes it more costly. The 2D PCD can provide more accurate and effective profile data for the pipeline inspection. Here the diameter and Ovality of the pipe cross section is calculated. Two methods are used to calculate the diameter of each ring:

3.4.3.1 Calculating the Diameter using K-Nearest Neighbor (KNN) Method.

For each ring, the actual diameter is calculated using k-nearest neighbors' algorithm (KNN) (Kramer, 2013). In this method, the Euclidean distance of each point with respect to other points (within the points of each ring) are calculated. The "diameter" of each point determines as the largest value among the pair-wise Euclidian distances within a vector set (see Figure 19). Here, some points that is located at the bottom of the haunches might bias the results; therefore, the two most selected points which is identified as the largest diameter are (automatically) omitted for the sake of consistency.

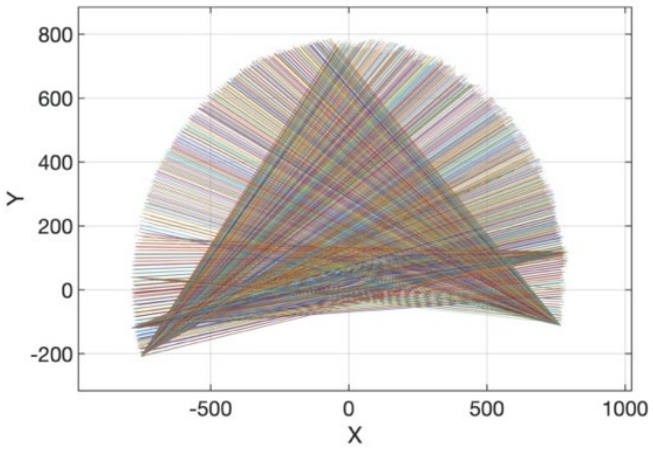

Figure 19. Determining the diameter of a ring using KNN Method

3.4.3.2 Calculating the Diameter using Least Square (LS) Method

Using least square (LS) method, a circle is fitted to the points of each ring. This study borrows the MATLAB function provided by (Sumith, 2023); the results is shown in Figure 20.

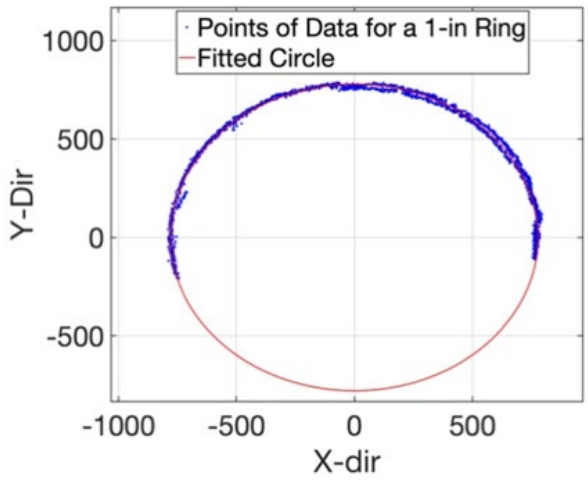

Figure 20. Determining the diameter of a ring using Circle Fitting (LS)

3.4.4 Calculating the Ovality (deflection)

The ovality is calculated based on ASTM F-1216 (ASTM, 2016). Finally, the deflection of each 5 *ft* section is calculated by averaging the ovality values of these 60 rings (using Equation 11). The

KNN output (i.e., the vector including the diameter values for each ring) is set as the input values of Equation 11. This procedure is performed for all *60* rings, and the mean value is reported for the inspected *5-ft* section of the RCSSP.

$$Ovality\ (\%) = \frac{Mean\ Inside\ Diameter - Minimum\ Inside\ Diameter}{Mean\ Inside\ Diameter} \times 100 \quad \text{Equation 11-a}$$

$$Ovality\ (\%) = \frac{Maximum\ Inside\ Diameter - Mean\ Inside\ Diameter}{Mean\ Inside\ Diameter} \times 100 \quad \text{Equation 11-b}$$

It should be emphasized that this whole procedure is performed automatically without any user interference after providing the input LiDAR inspection data.

3.4.5 Calculating the Hydraulic Properties of Pipes

The hydraulic properties, such as cross-sectional area of flow, wetted perimeter, hydraulic radius, and volumetric flow are determined using Manning's Equation. According to Figure 21, the depth of the flow is less than the radius of the pipe; for this case, the procedure to calculate the properties is outlined below(Water Management Manual, 2001):

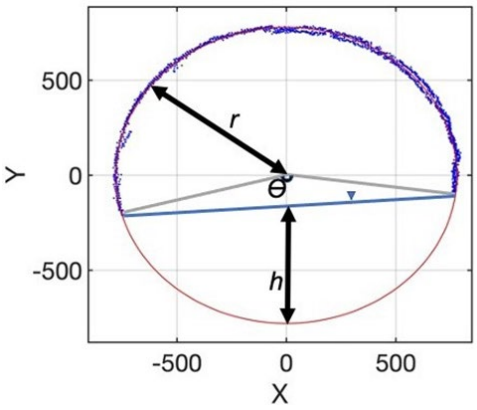

Figure 21. Calculating Hydraulic Properties (unit: mm)

From Figure 21:

$$\Theta = 2 * \arccos\left(\frac{r-h}{r}\right)$$ Equation 12

$$WP = r\,\Theta$$ Equation 13

$$AF = \frac{r^2(\theta - sin\theta)}{2}$$ Equation 14

$$R_h = \frac{AF}{WP}$$ Equation 15

where Θ is in degrees, AF is cross-sectional area of flow (mm^2), h is flow height (mm), WP is wetted perimeter (mm), R_h is Hydraulic Radius (mm).

Finally, the volumetric flow rate (Q) and velocity of the flow (VF) are calculated using Manning's Equation (Bizier, 2007):

$$Q = \left(\frac{1}{n}\right) * AF * R_h^{\frac{2}{3}} * S^{1.2}$$ Equation 16

$$VF = Q/AF$$ Equation 17

where n is the Manning's roughness coefficient, which is typically 0.013 for RCSSP (Water Management Manual, 2001), Q is the volumetric flow rate passing through the pipe (m^3s), and S is the slope of the pipe (ft/ft). It should be noted that in case of erosion below the flow line, the manning coefficient will be impacted, which is neglected in this study due to the lack of sonar data. Since the LiDAR data could not capture the geometry of pipe below the flow line, it is assumed that the pipe is free of deposits. This is a limitation of the proposed method; Equation 16

does not apply for RCSSPs with deposits. meanwhile, to accommodate this uncertainty, a PDF is assigned to some parameters of Equation 16 (see Table 5).

3.4.6 Evaluating Corrosion Rate

The blue points presented in Figure 18 are used for calculating the inner wall thickness loss of each section. As mentioned earlier, each 5-ft length of the cylinder is divided into 60 rings with a thickness of 1-in (25.4 mm). One inch thickness (Z direction) is negligible compared to the diameter of the pipe (54 and -60 inches); therefore, instead of working in 3D space (X-Y-Z), each ring can be analyzed in 2D space (X-Y) (Figure 18). The corrosion rate is calculated for each 1-in ring as follows:

3.4.6.1 Fitting a circle to each ring.

To ensure that our data is centered at (x=0, y=0) and completely alighted, each ring will recentered. Figure 20 shows the PCD and the fitted circle for the first 1-in ring of line 1, section 1. A circle is then fitted to the ring using Landau method provided by (Sumith, 2023). Figure 22 shows the fitted circle along with the filtered data.it is also shown in cylindrical coordinates to have a better presentation for diameter of the pipe.

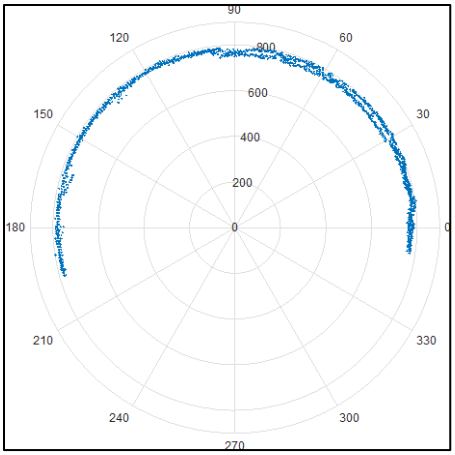

Figure 22. 1-in Ring of Point Cloud PCD in Cylindrical Coordinate (Degree, mm)

3.4.6.2 Calculating Mean Inner Concrete Loss

The mean inner concrete wall loss of each 2D ring is calculated by measuring the Euclidean distance of each point (i.e., the centered blue points of Figure 20) and subtracting them from the radius which could be the estimated radius by the fitted circle (using MATLAB Code by (Sumith, 2023), or from *KNN* method or the map value from Table 2.

$$\boldsymbol{L} = \sqrt{(\boldsymbol{x_i} - \boldsymbol{0}) + (\boldsymbol{y_i} - \boldsymbol{0})} - R \qquad \text{Equation 18}$$

where L is the loss/deposit value, x and y are the coordinate of the point in Cartesian coordinate and R is the radius. Points with positive (+) L are indicated as the loss PCD, and negatives (-) are deposits. Figure 23 illustrates the loss/deposits concept.

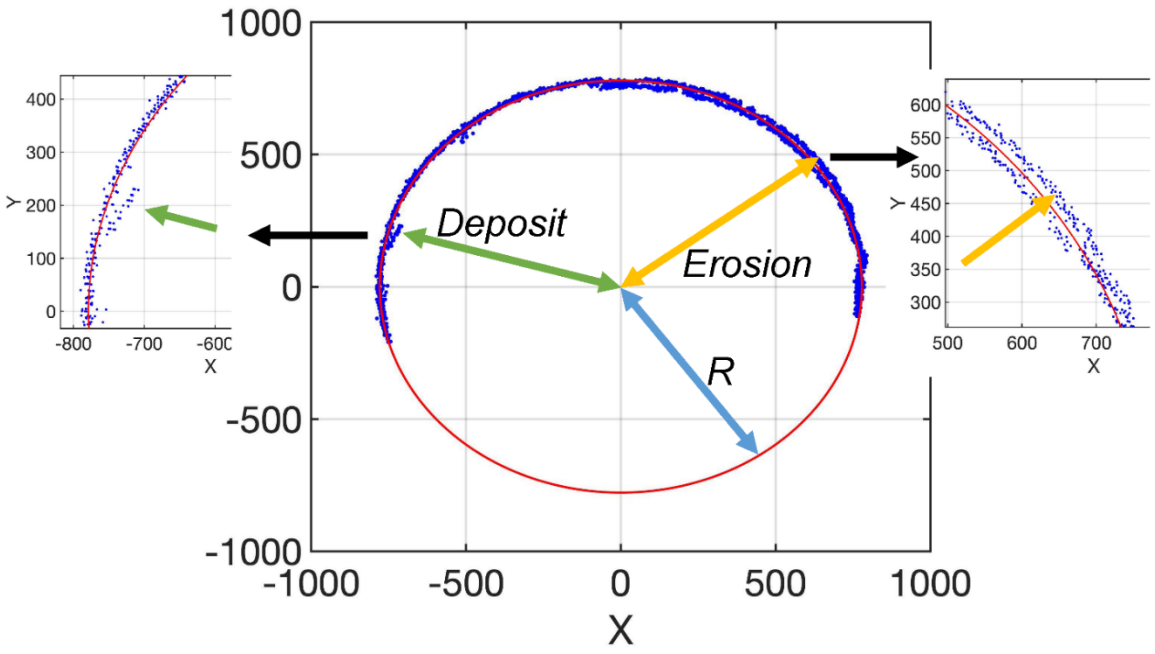

Figure 23. Definition of Loss and Deposit

The properties for each RoI (i.e., 5-ft section) are the mean value of all the properties of these 60 2D rings. After collecting the PCDs of the inner concrete wall loss (positive L), the erosion rate is calculated as Equation 19:

$$\text{Er}\left(\frac{\text{mm}}{\text{year}}\right) = \frac{\text{Erosion for each point from ring PCD (at the time of inspection)}}{\text{Age of the RCSSP at the time of inspection (i.e.,28 years)}} \qquad \text{Equation 19}$$

The erosion rate (Er) is calculated for each point identified as loss, to form a vector for all the erosion rates (for each 2D ring).

3.4.7 Considering the Spatial Variability of Pipeline Circumference.

The literature shows that quantifying the wall cover erosion is one of the well-known methods to develop a proactive condition assessment of RCSSPs at the serviceability level. In addition, as mentioned in the Chapter 1 (Introduction Section), filtering of the inspection PCD is a challenging task. Therefore, this study also investigates the concrete cover loss for different zones of the

RCSSPs circumference to check if the flow noise filtering can be eliminated. The PCD of the cross-section of the pipe (0°-360°) is divided into five different sectors: top-half (0°-180°), (15°-165°), (30°-150°), (45°-135°), and (60°-120°). For each sector, the concrete wall erosion is calculated and compared with the results from the whole circumference of pipe (Ebrahimi & Jalali, 2022b).

In order to consider the effect of spatial variation of pipeline circumference, points of each 2D rings are divided into five different cases (which are different sectors of the pipes): top-half (0°-180°), (15°-165°), (30°-150°), (45°-135°), and (60°-120°) as shown in Figure 24. For each case, the concrete erosion is calculated using the method discussed in (3.3.4.6.2 Calculating Mean Inner Concrete Loss)

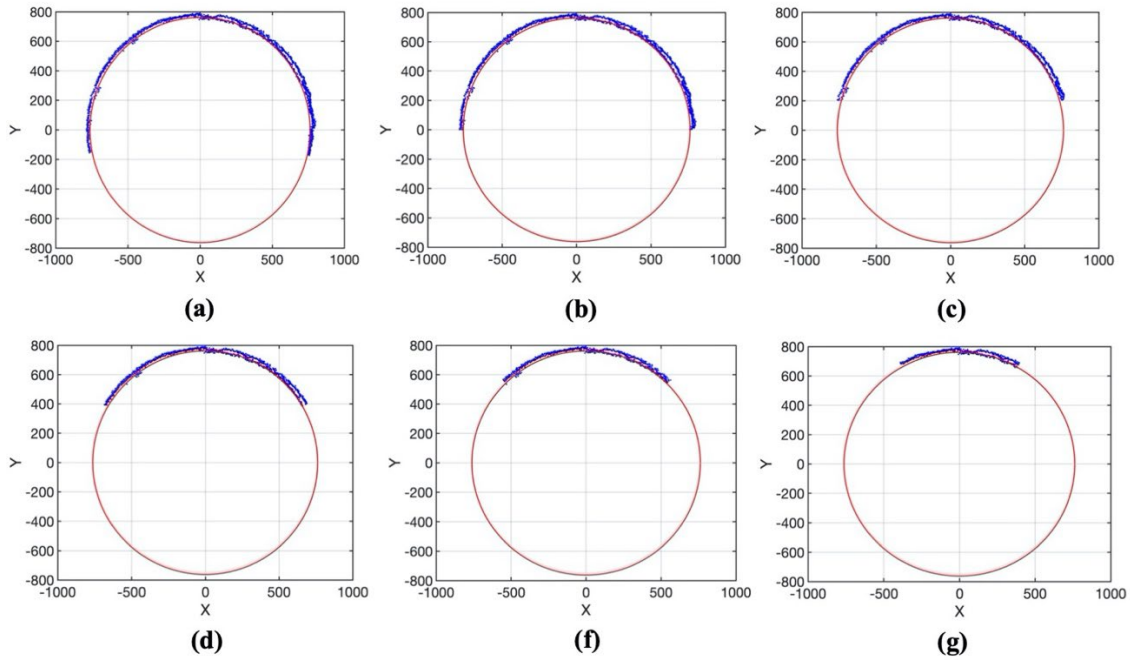

Figure 24. Spatial Variation of Pipeline Circumference; (a) Whole Ring (0º-360º), (b) 0º-180º, (c) 15º-135º, (d) 30º-150º, (e) 30º-150º, (f) 45º-135º, (g) 60º-120º

It should be noted that the mean concrete loss for each 5-*ft* section is the mean loss of the 60 rings. Next section provides the results of mean inner concrete loss for selected zones of the pipe circumference (i.e., different cases) and compares them with the results of the whole pipe; three different methods are used for comparison, i.e., boxplots, probability plots, and chi-square

goodness-of-fit test. Method 1 and 2 are graphical techniques and method 3 is a more accurate statistical approach.

3.4.8 Finding the Best-Fit-Distribution

The erosion rate (*Er*) is calculated for each point identified as loss, to form a vector for all of the erosion rates (for each 2D ring). The proposed algorithm fits 6 different distributions to the erosion rate data; the selected PDFS are:

1. Normal distribution.

2. Lognormal distribution.

3. Half Normal distribution.

4. Exponential distribution.

5. Gamma distribution.

6. Weibull distribution.

These distributions are selected considering relevant literature (Ahammed & Melchers, 1995; Foorginezhad et al., 2021b; S.-X. Li et al., 2009; Mahmoodian & Alani, 2014; Teplý et al., 2018). Goodness-of-fit is measured by comparing R^2 values for fitted line to QQ-plots of each 1-inch rings. The algorithm uses a qualitative measure for interpreting and evaluating these distributions using quartile/quartile, or QQ-plot. For each distribution, the goodness-of-fit is measured by R^2 values from the fitted first-order regression line on these QQ-plots (Pleil, 2016).

3.4.9 Updating the Mean Concrete Loss Values using Bayesian Network (BN)

Duo to the scarcity of data the pipelines does not have multiple inspections in their lifetimes. Using Bayesian inference the mean concrete erosion for pipeline (M-M) can be "updated" based on the prior which is determined from the literature and previous case studies. Bayesian Network (BN) is a statistical method that updates the probability for a hypothesis (i.e., the Prior) as more information becomes available as the observed data (i.e., the calculated Mean Loss for each Pipeline #). Bayesian methods with appropriate prior distributions provide an alternative approach for estimating parameters of a complicated degradation model. It's based on Bayes' theorem, which relates the conditional and marginal probabilities of stochastic events. Here two cases are discussed, Weibull and gamma likelihood functions.

The basic formula for Bayes' theorem is as Equation 20.

$$P(H|E) = \frac{P(E|H).\ P(H)}{P(E)} \qquad \text{Equation 20}$$

Where:

P(H|E) is the probability of hypothesis H given the evidence E (posterior probability).

P(E|H) is the probability of evidence E given that hypothesis H is true (likelihood).

P(H) is the probability of hypothesis H being true (prior probability).

P(E) is the probability of the evidence E (marginal probability).

To perform BN, you start with a prior belief about the probability of the hypothesis (prior probability), and the observed data (i.e., the calculated Mean Loss for each Pipeline #). The updated belief is the posterior probability.

The BN updating has the following steps:

1-Define the model which would be related to the "Mean Loss (mm)" for all the pipelines.

2-Establish a prior distribution for the parameters of our model. This could be based on previous knowledge or assumptions about the "Mean Loss (mm)"; two priors are defined in this study. Table 3 shows two distributions to be assigned for BN according to Table 1. The first one follows the Gamma distribution obtained by (Mahmoodian & Alani, 2014); this study estimated the Gamma parameters using maximum likelihood methods (MLE). The second priors follow Weibull distribution; Abuhishmeh, (2019) estimated Weibull parameters for all sections of 22 different RCSSPs; the Weibull parameters were determined by averaging all the parameters of the 22 different RCSSPs.

Table 3. Different Priors from Literature for Bayesian Network

Reference	Distribution	Parameters	Description
Mahmoodian and Alani (2013)	Gamma	(0.17*t,0.425) (Shape(A) and scale(G))	Power Law Maximum Likelihood (MLE) (t in year)
Abuhishmeh, k. (2019)	Weibull	(Normal(1.8438,0.3323), Normal(0.00806,0.505446)) (Fitted shape(B), Fitted Scale(S))	Fitted Normal Distrubution to the parameters which are calculated by fitting the values to 22 pipelines

3-Determine the likelihood function, which describes how probable the observed data is given certain values of our model parameters; Here the likelihood would be Gamma and Weibull PDF.

4-Calculate the posterior distribution, which updates our belief about the model parameters after considering the observed data; in this case since it is not conjugate prior for the Gamma and Weibull likelihood, and hence, the posterior distribution cannot be obtained analytically. This process typically requires a numerical approach, such as Markov Chain Monte Carlo Metropolis-Hastings (MCMC-MH) or other sampling methods, to approximate the posterior distributions.

In order to compare the updated values by BN with the prior and observed data, RSL values is calculated for all the update values (posterior), prior and observed data; Monte Carlo simulation (MCS) is utilized for this purpose (discussed in subsection 3.4.8.3)

3.4.10 Calculating Residual Service Life (RSL)

Many factors are involved in degradation process of RCSSPs such as temperature, H_2S concentration, and relative humidity (Wells & Melchers, 2015); however, these data are generally not readily available which makes the degradation models limited (Makana et al., 2022). On the other hand, Wu et al. (2018) reported that deterioration due to MIC of concrete are responsible for 50 percent reduction in the service life of concrete sewers. Therefore, concrete erosion is the main factor considered in this study. In this study the serviceability limit state (SLS) (i.e., remaining inner concrete cover) is utilized for predicting the RSL (life expectancy) of RCSSPs. The serviceability limit state does not reflect the failure/collapse of RCSSPs. In addition, it is assumed that the concrete erosion changes linearly w.r.t time; this assumption is used in other studies (Andrade, 2020; Khaled Saleh Abuhishmeh, 2019; Teplý et al., 2018; Wells & Melchers, 2014). Two different methods are discussed for calculating life expectancy (service life) of RCSSPs as follows:

3.4.10.1 Probability of Exceedance

This method utilizes the concrete erosion rates (result of Equation 19). In the proposed algorithm, it is assumed that erosion rate *Er* increases in a constant rate (Andrade, 2020; Khaled Saleh Abuhishmeh, 2019). This concept is integrated by the concept of SLS (*G*) described in the Equation 21 (Ahammed & Melchers, 1995) :

$$G(t) = R_e(t)-E(t) \qquad \text{Equation 21}$$

Where R_e is resistance defined as inner concrete cover of 1 inch (25.4 mm) (Bizier, 2007); the concrete cover protects the reinforcements from corrosion by isolating them from the surrounding environment and sewage. *E* is action considered as corrosion rate; *t* is time as year. Failure is occurred when the action *E* overcomes the resistance R_e. *E* at each point of the ring is different, so the erosion at *t* is presented as a random variable follows the best fit distribution function (e.g., Half Normal, Weibull or Gamma).

Action *E* can be assumed to follow any function that represents concrete erosion rate. In this study two different functions are used. Power law and Pomeroy model is discussed in following sections:

3.4.10.1.1 Power law

Equation 22 shows the power law formulation.

$$d_i = C * t_i^{rate} \quad \text{Equation 22}$$

Where:

d: erosion depth at time i (in mm),

C: erosion rate (mm/year).

rate: the constant reflecting the nonlinear trend of degradation law. *rate* is typically assumed to be 1, which shows that the erosion rate is assumed to be linear with respect to time (van Noortwijk et al., 2007)

3.4.10.1.2 Pomeroy Model

Equation 23 -24 shows the well-known Pomeroy model for concrete degradation modeling.

$$\Phi = 0.7 * (S*VF)^{3/8} * j * [DS] * (b/WP) \quad \text{Equation 23}$$

$$C = 11.5 * K * \Phi * (1/AC) \quad \text{Equation 24}$$

Where:

t: age of pipe at time i (year),

Φ: the average flux of H_2S to the wall,

S: slope of the pipeline (m/m),

VF: velocity of the stream(flow) (m/sec),

j: the pH-dependent factor for the proportion of H_2S,

DS: dissolved sulfide concentration (mg/l),

b: stream width (mm),

WP: perimeter of the exposed wall to atmosphere (mm),

C: the average erosion rate (mm/year),

K: the Acid reaction factor ranging from 0.3 to 1,

AC: the acid-consuming capability of the wall material; AC is defined based on material types; for granite aggregate: $0.17<AC<0.24$, calcareous aggregates: $0.9<AC<1.1$, mortar-lined pipe: $AC=4$, and asbestos cement pipe: $AC=0.5$.

The so-called failure occurs when the action E, exceeds the resistance R_e; in other words, G (SLS) becomes negative. There is an uncertainty in evaluating the concrete erosion rate, since there is not any real data available for these properties to predict the erosion rate; therefore, probabilistic methods are employed to overcome this challenge (Khaled Saleh Abuhishmeh, 2019; Mahmoodian & Li, 2011; Teplý et al., 2018) by assigning random variables to these properties.

Here, the best distribution (which is the result of the proposed distribution- fitting algorithm) is assigned to the erosion rate. The concrete erosion at time *t* (i.e., the action *E*) is calculated by multiplying the time (in years) by the erosion rate (*mm/year*). This is the manifestation of the constant erosion rate assumption. This is a reasonable assumption since there is no second inspection data available for these pipes up to date. It is worth mentioning that the BN method is used in this study to accommodate the uncertainties to some extent.

The probability of failure is the area bounded by the probability density function (the action, *E*) and the concrete cover (i.e., the vertical line); this area is highlighted in Figure 24 by green hatched area.

The probability of failure of each ring at *t* is the area bounded by the probability density function (action) and the concrete cover in which the action is greater than the resistance. According to the basic definition of probability, probability of failure is the area under the probability density function. Probability of failure is the area under the curve beyond 1 toward infinity as in the Equation 25.

$$P_f = \int_{25.4}^{\infty} f(x)dx \qquad \text{Equation 25}$$

Finally, the RSL is estimated as the time at which the structure requires maintenance, however this does not reflect failure of that structure. The degradation of concrete is not included in this study; This is the limitation of this method. In this study the erosion rate (Equation 19) is used along with probability of failure concept (Equation 25) to estimate the RSL of RCSSPs. Using the age of the pipe at time of inspection, the residual service life of the pipe is calculated as Equation 26.

$$P_f\,(G(t)>1) \qquad \text{Equation 26}$$

Equation 26 is the area between the vertical line (Resistance R_e) and the PDF curve (Action E) illustrated in Figure 25.

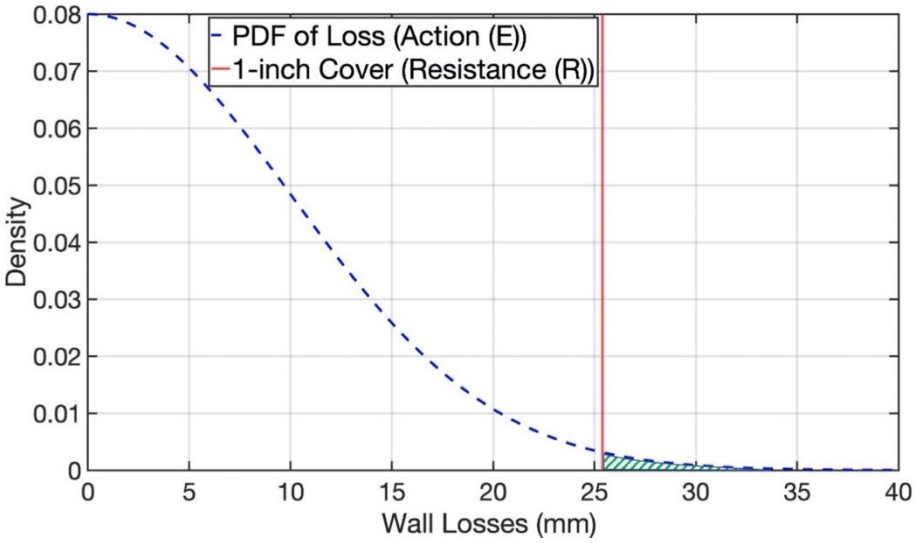

Figure 25. Probability of Exceedance for Erosion (Half Normal Distribution) at t

For each 2D ring, this process is repeated for the next following years (up to year 300) in Equation 25. For instance, the PDF in Figure 25 is the erosion PDF for the 30th year after inspection (for ring 1, section 1, line 1). The results of Equation 25 for each t forms a vector, and the service life is defined as a year in which p_f is 0.10 or 0.05 and larger. In other word, this is the remaining life (year of maintenance) of ring with 90-95 percent confidence interval respectively; this is assumed as the maximum acceptable risk in terms of probability of failure. In other word, this indicates the year of which the RCSSP becomes unsafe and needs maintenance. It should be noted that the accurate acceptable risk should be determined from a risk-cost optimization of pipe system during its service life (Mahmoodian & Li, 2011). This remaining service life shows the time when the RCSSP requires maintenance. It does not reflect actual structural failure of the pipe; however, it helps the pipe network manager implement a proactive asset management strategy by prioritizing repair and rehabilitation of pipes.

3.4.10.2 X-intercept Method

This method is a simplistic approach for estimating RSL. This method uses the average of concrete wall losses for each Section at the time of inspection. this method considers the average inner concrete wall loss of RCSSPs at the time of inspection. It is also assumed that rate of concrete erosion is constant throughout the lifespan of the pipe (Teplý et al., 2018; Wells & Melchers, 2014). Assuming that corrosion rate is constant.

From Figure 26, initial cover (C_0) is assumed to be 1 inch (25.4 mm) (according to ASTM C76.8.3.1); the service life (t_{SL}) is calculated by finding the x-intercept of a line which passes through initial cover (point (0 , 25.4)) and mean remaining cover (μ_c) at time of inspection (i.e., point (t_{insp} , μ_c)).

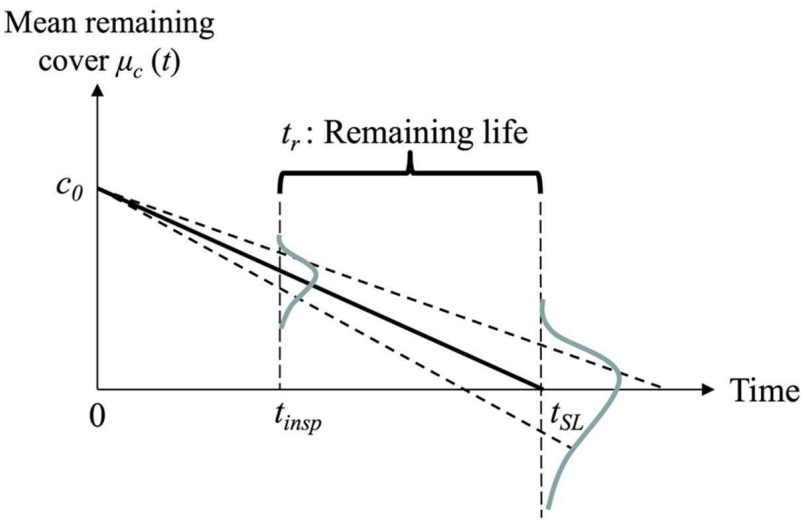

Figure 26. Calculation Remaining Life Using X-Intercept Method

3.4.10.3 Applying Monte Carlo Simulation (MCS) on the Basic Reliability Problem

In order to calculate RSL basic reliably problem is defined. This problem considers only concrete erosion *D* and the threshold as initial cover C_0. Each is described by a known Probability density function, $f_D()$ and $f_{C0}()$. Both units are in mm. The pipe will be considered to failed if the initial cover which is the inner wall concrete cover that is assumed to be 1 inch (25.4 mm), is less than concrete erosion D. The probability of exceedance of each pipe can be calculated Equation 27.

$$p_e = P[E(D, C_0) \leq 0] \quad \text{Equation 27}$$

where *E()* is termed the "serviceability limit state problem" and *D* and C_0 are erosion and initial cover respectively.

The failure probability may be written as Equation 28 Since the *D* and C_0 are independent, the joint (bivariate) density function f_{D,C_0} (*D*, C_0) is formed the area calculated by Equation 28.

$$p_e = P(C_0 - D \leq 0) = \int_{-\infty}^{\infty} \int_{-\infty}^{D \geq C_0} f_{C_0}(c_0) f_D(d)\, d_d\, d_{C_0} = \int_{-\infty}^{\infty} F_{C_0}(x) f_D(x)\, dx \quad \text{Equation 28}$$

This is the 'convolution integral.' $F_{C_0}(x)$ is the probability that $C_0 \leq x$ or the probability that the actual resistance C_0 is less than some value *x*. This represents failure if the remaining cover D is larger or equal to *x*. This is also shown in Figure 27, where the (marginal) density functions f_{C0} and f_D have been illustrated along the same axis.

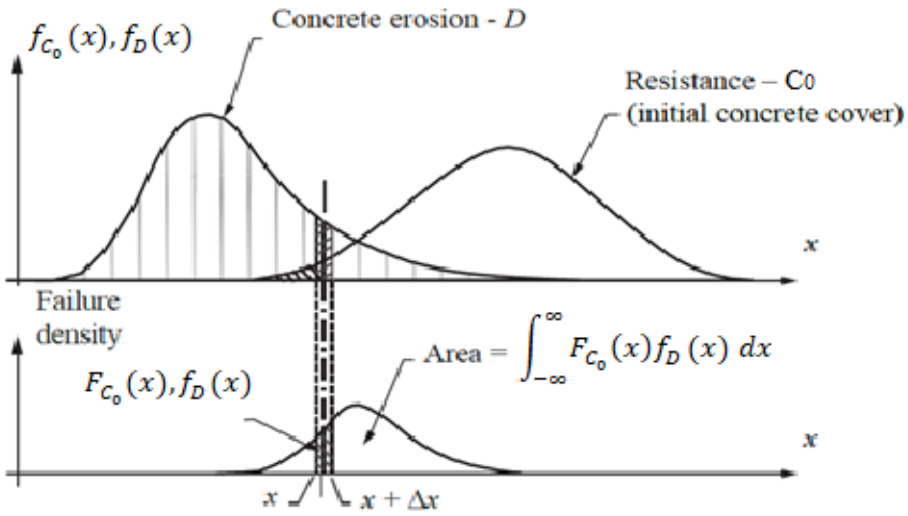

Figure 27. Basic C_0− D problem: fC_0( ) fD( ) representation.

In another words, Equation 28 can be simply calculated by the 'sum' of the failure probabilities over all cases of resistance, where concrete erosion D exceeds resistance C_0 (Melchers & Beck, 2018).

$$p_e = \frac{nn(E(x_i) \leq 0)}{NT} \qquad \text{Equation 29}$$

where $nn(E(x_i) \leq 0)$ is the number of trials when $(E(xi) \leq 0)$. NT is the total number of trials required to the desired accuracy for p_e. Here, NN=10,000 is set for BN, and 1000 for other problems. NN of trials required is related to the desired accuracy for p_e.

In the next section, the values of RSL for the different approaches will be shown. In addition, other statistical methods such as the Single variable Regression model, Multi-Variables Regression model, and Polynomial Regression model are implemented on the output of the proposed algorithm in order to estimate the concrete erosion of the inner wall of RCSSPs using the calculated parameters. The parameters are:

1-Area of Flow (mm^2),

2-Water Level (%),

3-Hydraulic Radius (mm),

4-Actual Radius (mm),

5-Ovality, and the target, Mean Loss (mm)

These parameters are provided in 3 different tables for all pipeline # of different Pipeline diameters 30-,54-, 60-inches. The statistical methods are done using *Python* Libraries: *NumPy* and *SciPy* and the plots using *Matplotlib* dictionary.

CHAPTER 4. RESULTS AND DISCUSSION

4.1 Verifying the LiDAR PCD with CCTV

As discussed in Chapter 3, the outcome of the proposed algorithm is a 3D PCD. It provides an accurate presentation of the inner wall geometry of a RCSSP at each RoI (i.e., 5-*ft*). Figure 27-b shows an overlay of the PCD and actual CCTV image corresponding to the seventh 5-*ft* section of Line 4; the yellow points are the PCD after applying the global filtering. Figure 28 certifies that the PCD is able to locate the water line, deposits at the haunches, and uneven joints accurately.

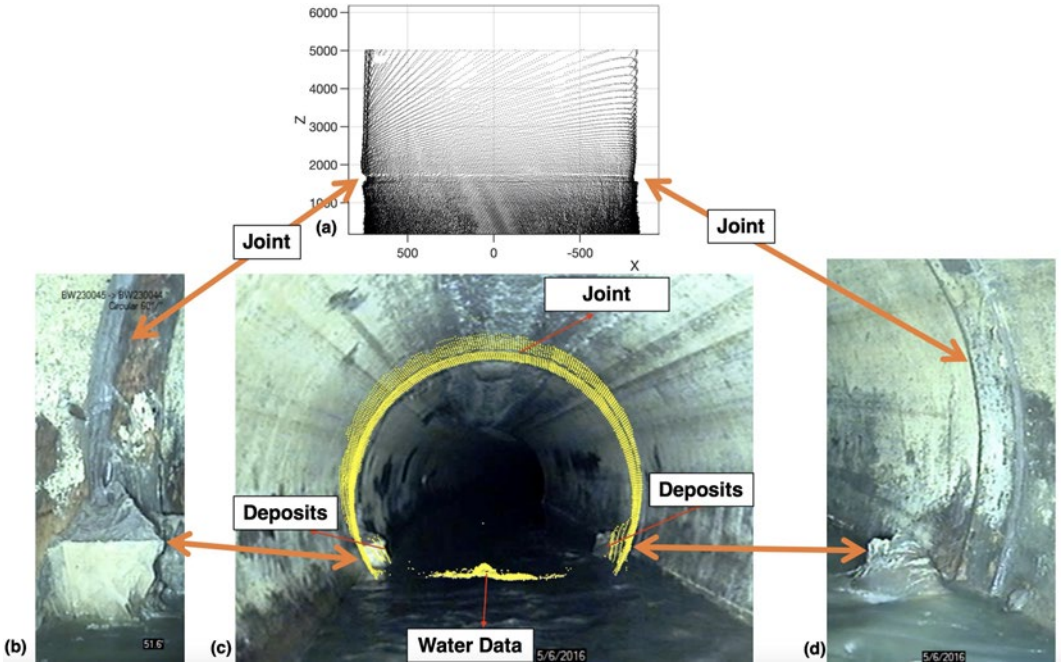

Figure 28. Overlaying the PCD on the Respective CCTV image. (a) The PCD, (b) Image of the Left Haunch, (c) Image of the Whole Section, (d) Image of the Right Haunch

4.2 Diameter Calculation

Using the proposed method, the diameter of all 5-ft sections for 54 inches pipes are computed, and the values are compared with diameter value (i.e., 54 inches). Figure 28 illustrates the consistency of results using both methods; each "dot" represents the mean diameter of a 5-ft section. Figure 28 also certifies that the actual diameter of pipes could vary from values of as-built maps (i.e., the values in Table 2); for instance, as shown in Figure 29, the diameter of Line 1 varied at the location 75 ft from the manhole. This is also visible in Figure 29 (for Line 1), where there is a drop in the measured diameter at that location. Figure 30 shows the accuracy of inspected PCD in representing the inside geometry of pipelines.

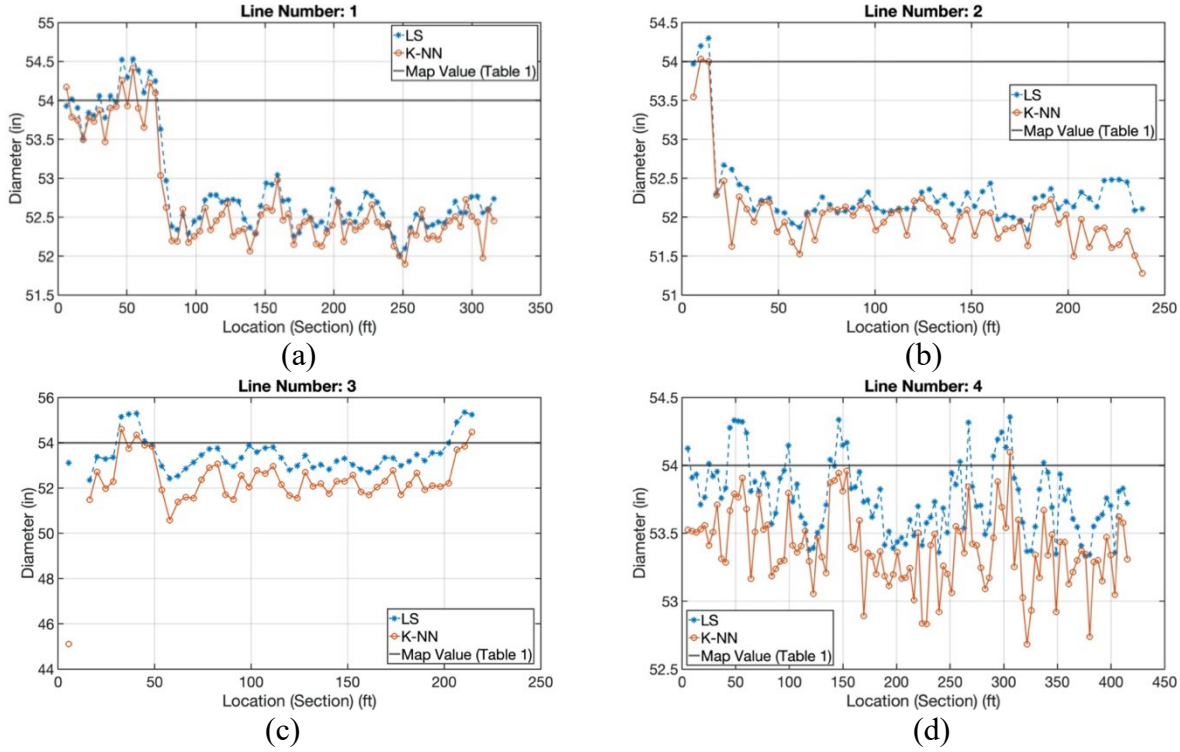

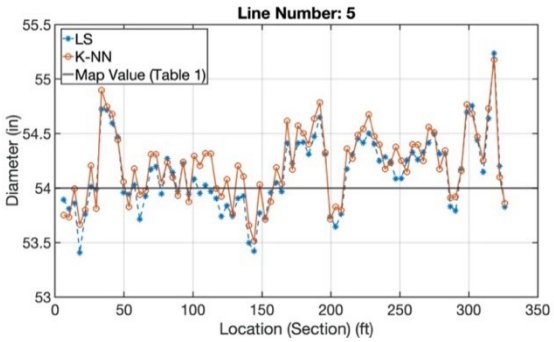

(e)

Figure 29. Comparing the calculated diameters with map values for each *5-ft* section.

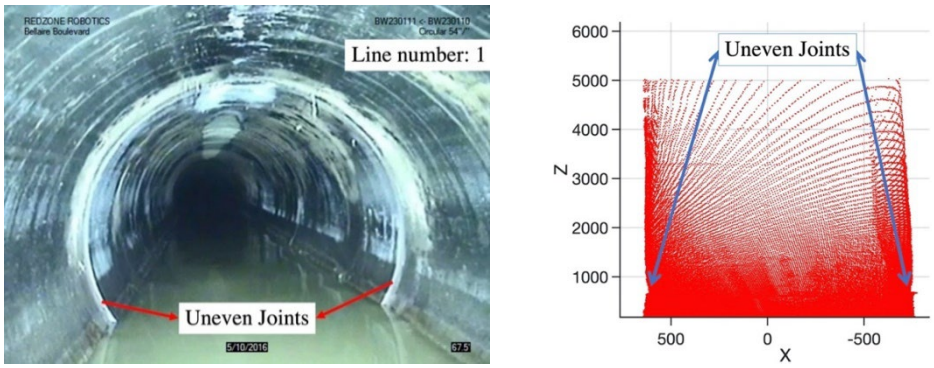

(a) **(b)**

Figure 30. Comparing CCTV image with PCD of line number 1, section: 18 (Location: 75 ft) (a) CCTV image (b) Z-X view of PCD

4.3 Ovality Calculations

The ovality (deflection) of all *5-ft* sections for the 5 selected pipelines are shown in Figure 31; it suggests that Equation 11.a provides more consistent and reasonable deflection values with the implemented proposed method.

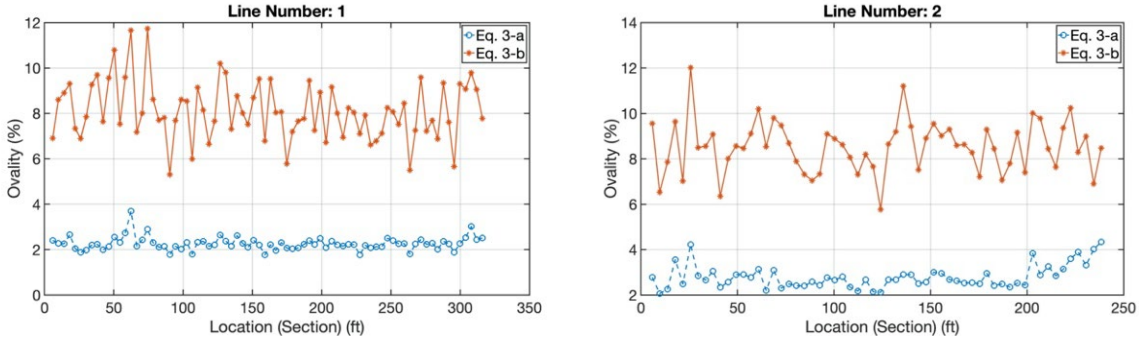

(a) (b)

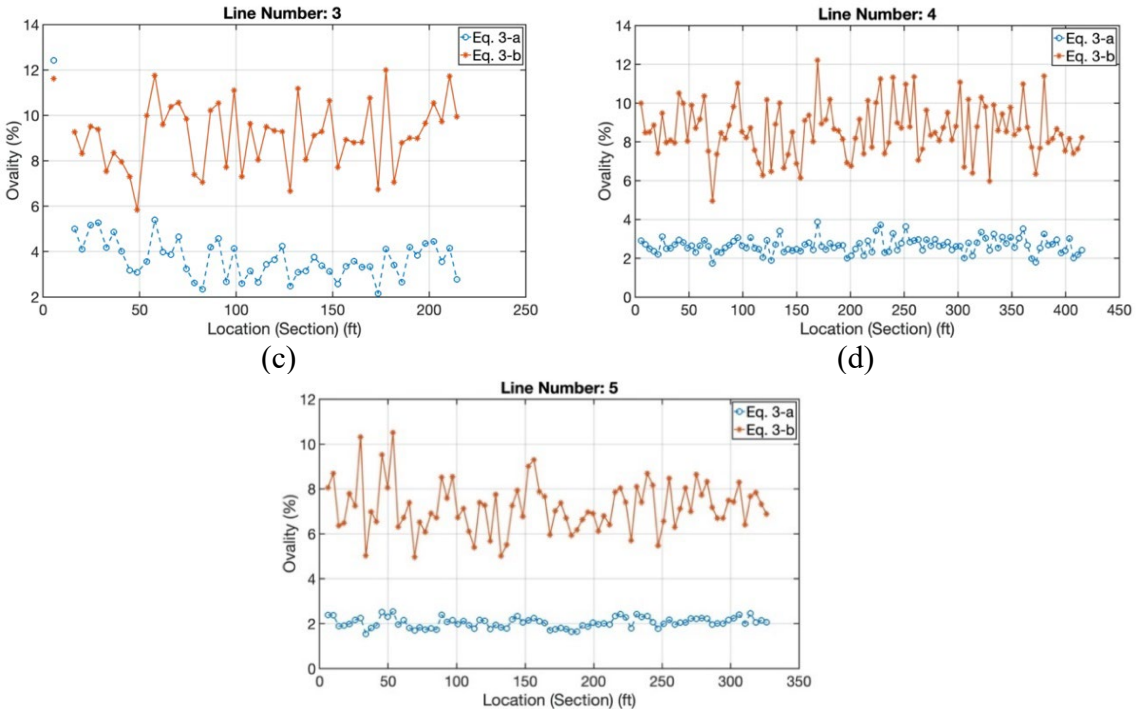

Figure 31. Comparing the Ovality (deflection) Values using Equation (11) for each *5-ft* Section

Meanwhile, Figure 31 shows the comparison between different methods on calculating the ovality of each ring. Here, one of the rings of 30-inch pipeline is used for this comparison. As mentioned in the Chapter 3 (i.e., Methodology section) for 30 inches data, the inspection outputs are the 2D rings; however, the inspection outputs for 54- and 60-inches pipe are 3D PCD for each 5-*ft* sections of each pipeline (M-M). The Ellipse fitting algorithm is borrowed from (Gal, 2023).

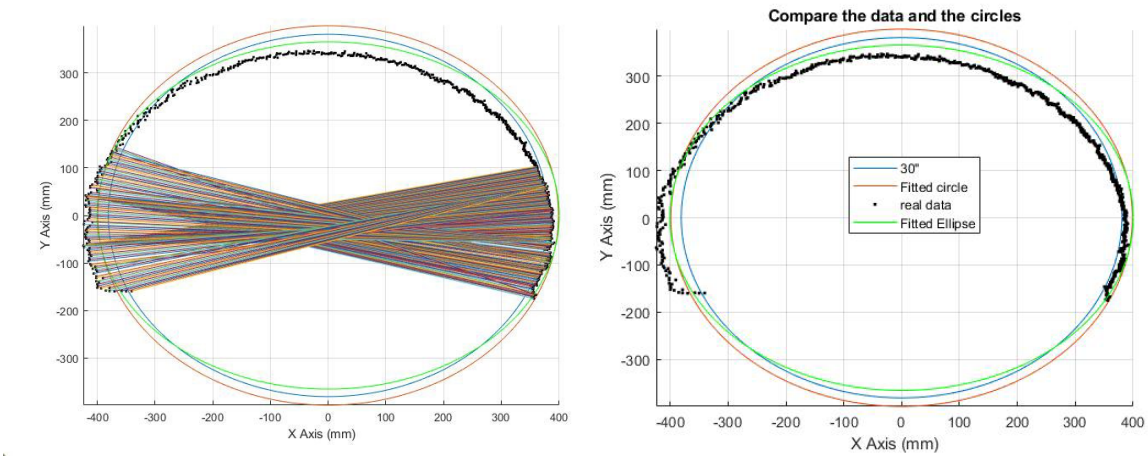

(a) (b)

Figure 32. Comparing Different methods for calculating the Ovality of pipes; (a) KNN method, (b) Other Methods

From Figure 32 it shows that the proposed KNN method calculate the diameter and ovality of 2D rings more accurately than other methods such as Circle fitting and Ellipse fitting algorithms based on LS method.

4.4 Calculating Mean Inner Concrete Wall Loss at the Time of Inspection

The proposed framework is also capable of showing the results for each 1-inch rings along the length of each pipeline (Figure 33.b -Figure 42.b). Here inspection PCD from LiDAR surveys for 1,500 linear ft of RCSSPs with 60-inch diameter and 1,500 linear ft of RCSSPs with 54-inch is used. It is assumed that the inner cover thickness is 1 inch in this comparison. To calculate the mean wall loss, radius sets as the fitted radius in Equation 18.

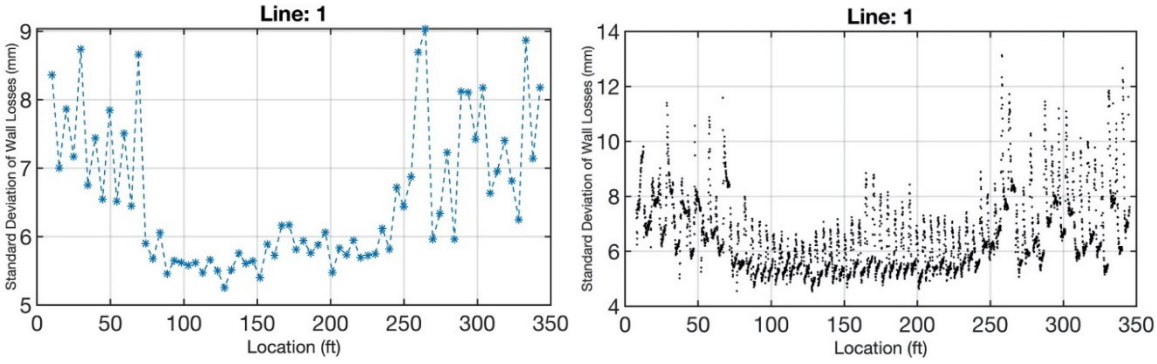

(a) (b)

Figure 33. Comparing Half Normal Standard Deviation of Losses for Line 1; (a) 5 ft, (b) 1 inch ring

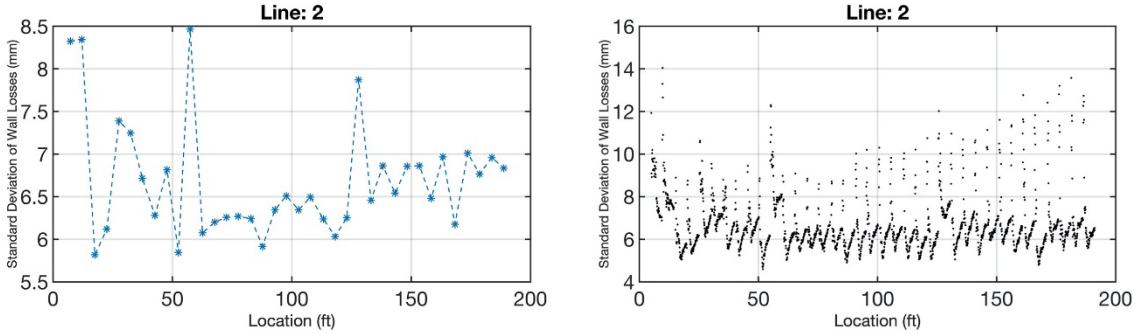

(a) (b)

Figure 34. Comparing Half Normal Standard Deviation of Losses for Line 2; (a) 5 ft, (b) 1 inch ring

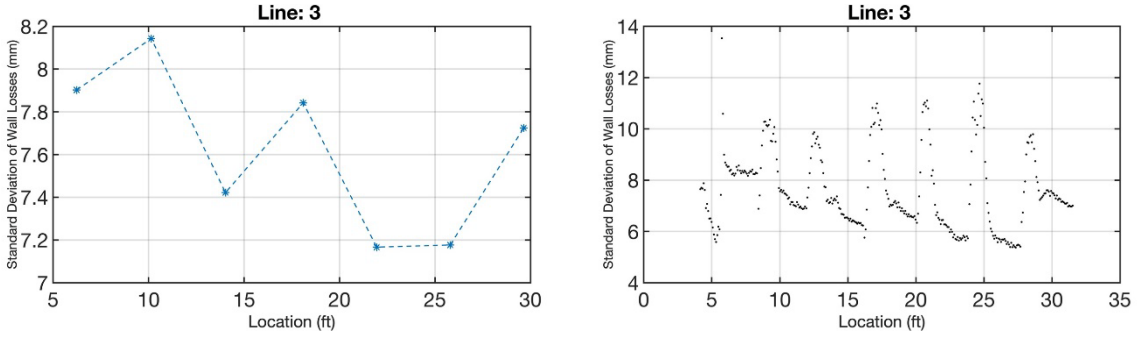

(a) (b)

Figure 35. Comparing Half Normal Standard Deviation of Losses for Line 3; (a) 5 ft, (b) 1 inch ring

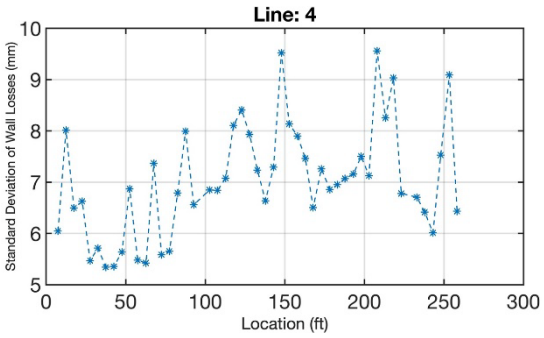

(a)

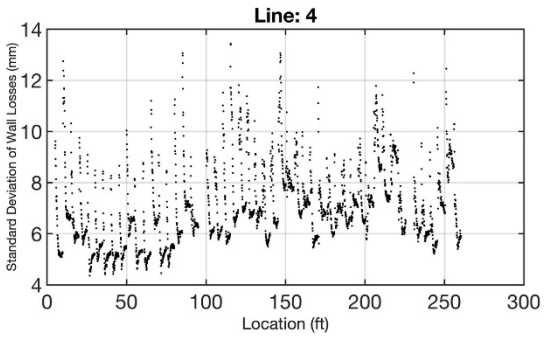

(b)

Figure 36. Comparing Half Normal Standard Deviation of Losses for Line 4; (a) 5 ft, (b) 1 inch ring

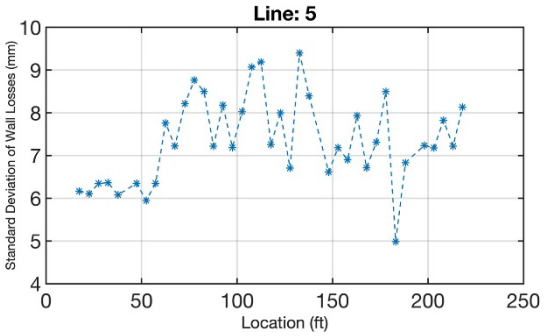

(a)

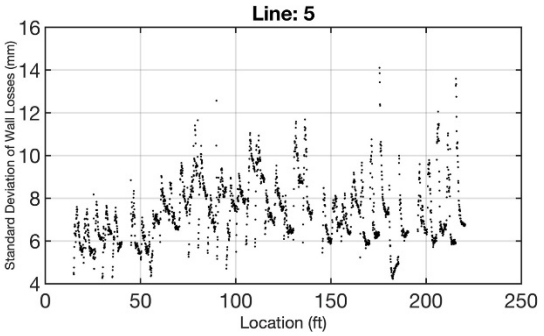

(b)

Figure 37. Comparing Half Normal Standard Deviation of Losses for Line 5; (a) 5 ft, (b) 1 inch ring

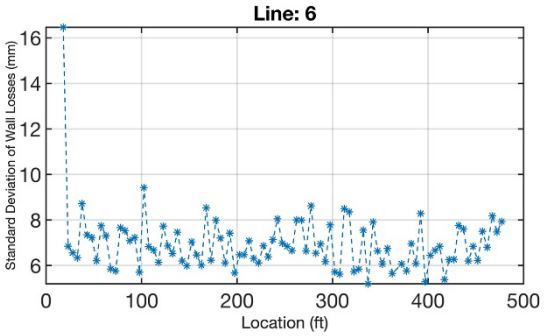

(a)

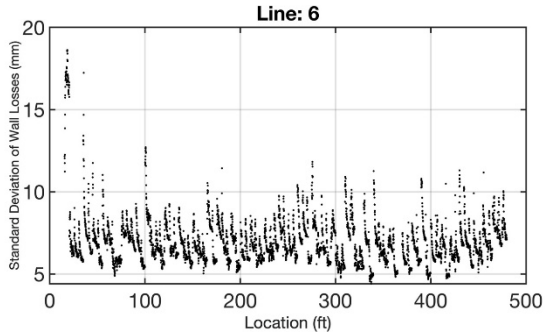

(b)

Figure 38. Comparing Half Normal Standard Deviation of Losses for Line 6; (a) 5 ft, (b) 1 inch ring

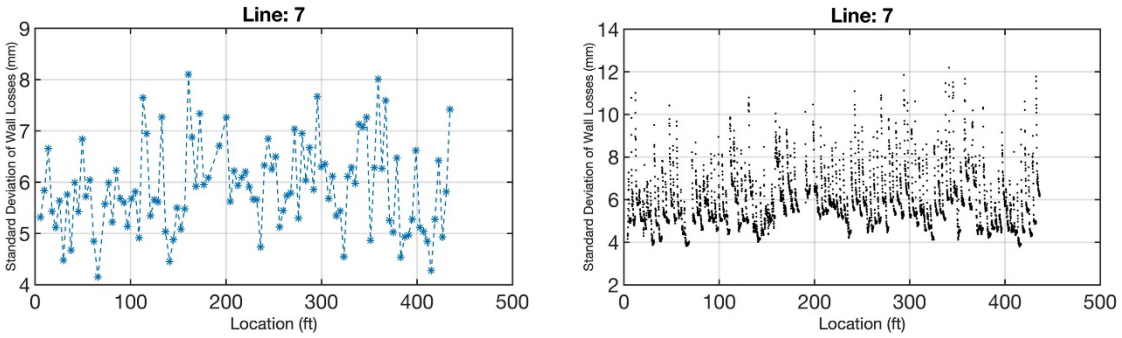

(a) (b)

Figure 39. Comparing Half Normal Standard Deviation of Losses for Line 7; (a) 5 ft, (b) 1 inch ring

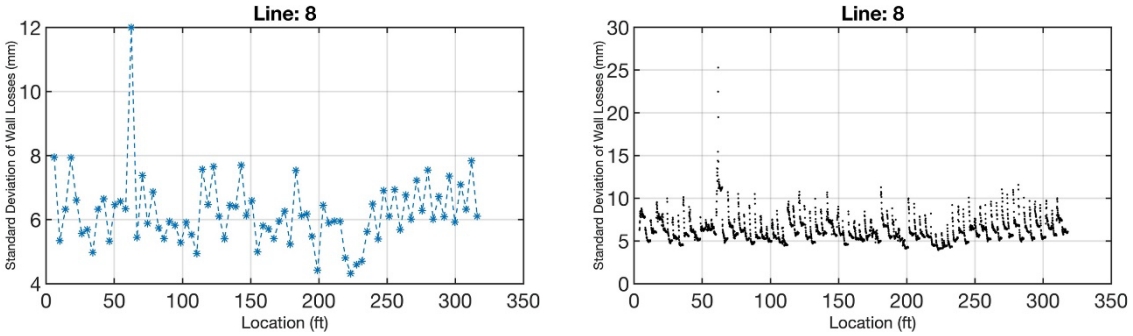

(a) (b)

Figure 40. Comparing Half Normal Standard Deviation of Losses for Line 8; (a) 5 ft, (b) 1 inch ring

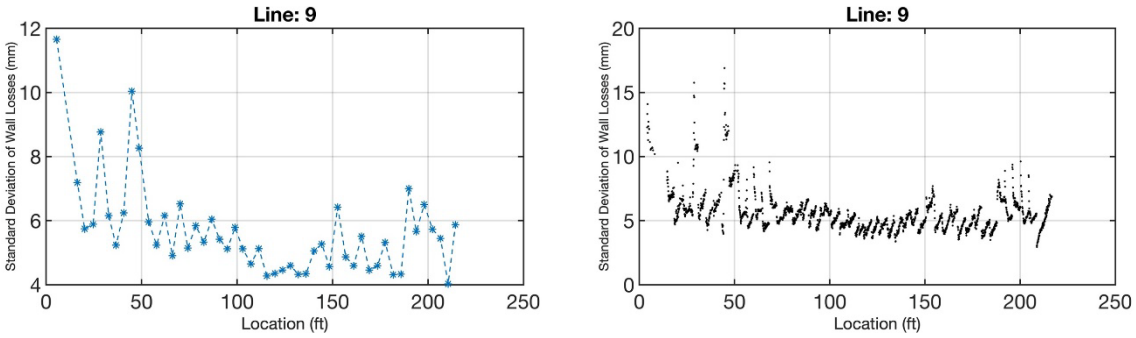

(a) (b)

Figure 41. Comparing Half Normal Standard Deviation of Losses for Line 9; (a) 5 ft, (b) 1 inch ring

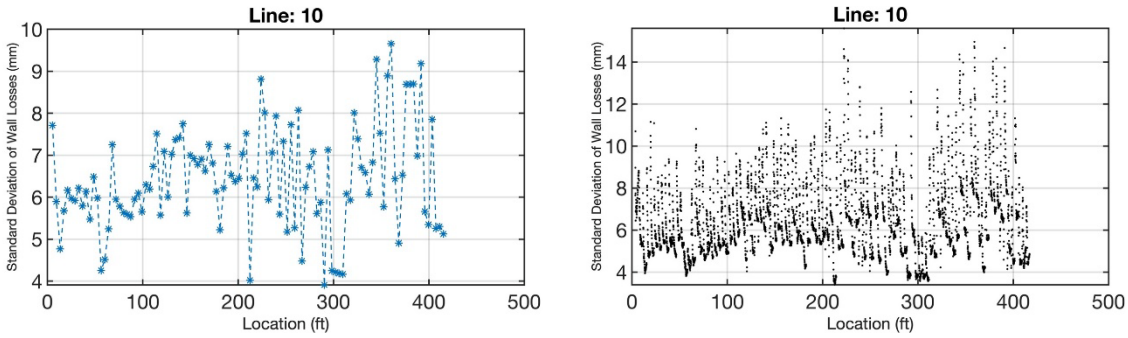

(a) (b)

Figure 42. Comparing Half Normal Standard Deviation of Losses for Line 10; (a) 5 ft, (b) 1 inch ring

Figure 43 shows the average loss of cover for all 54- and 60- inch RCSSPs as box plots.

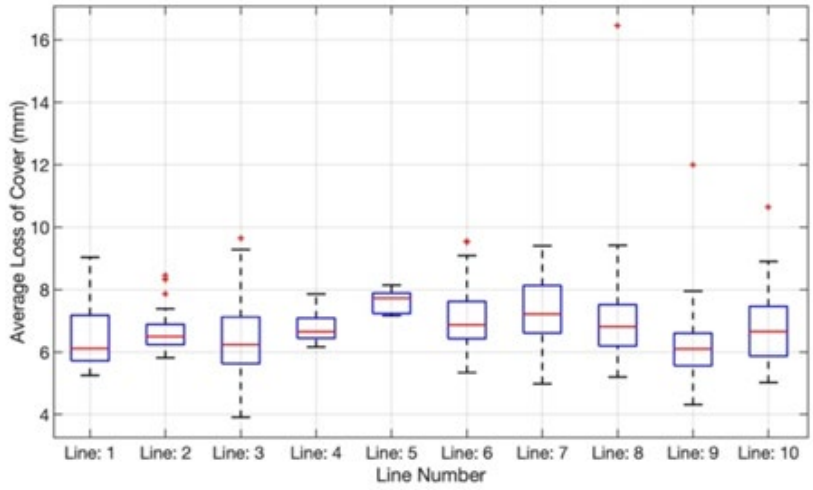

Figure 43. Box Plots of Average Loss of Cover for All Lines

4.4.1 Concrete Erosion for different Spatial Variability in Pipe Circumference

The purpose of this section is to investigate whether it is possible to eliminate some of the data in the filtering process of the inspection PCD in evaluating wall erosion of RCSSPs. Therefore, the mean concrete erosion of different cases (i.e., the different zones of pipe circumference) are compared with the result of the whole pipe circumference. To this end, the LiDAR inspection PCD of five different RCSSPs (M-M) are selected. Each data sets are consecutive 5-*ft* sections of each

line (M-M). The proposed algorithm automatically filters and aligns the cylindrical PCD and divides them into 60 different 2-D rings. Then, each ring (0°-360°) is divided into five different sectors: (0°-180°), (15°-165°), (30°-150°), (45°-135°), and (60°-120°). Lastly, the automated algorithm calculates the mean concrete loss for each case study; the results of different cases are compared using three different data assessment techniques, i.e., boxplots, probability plots, chi-square goodness-of-fit test.

In order to compare this effect of spatial variability, inspection PCD from LiDAR surveys for 1,500 linear ft of RCSSPs with 60-inch diameter is used; it is assumed that the inner cover thickness is 1.5 inch in this comparison. In order to calculate the mean wall loss, radius sets as the map value (i.e., 60 inches) for Equation 18.

The first graphical method for comparing the concrete erosion of different case studies is boxplot. Figure 44 shows the parallel boxplots (side-by-side boxplots) for six different spatial variation of pipe circumference. Each boxplot is drawn from the mean concrete erosion values of each 5-*ft* sections. The boxplots shows that the mean concrete erosion of the whole circumference of pipe is the same as the other case studies, except for the sector of 60^{o}-120^{o}.

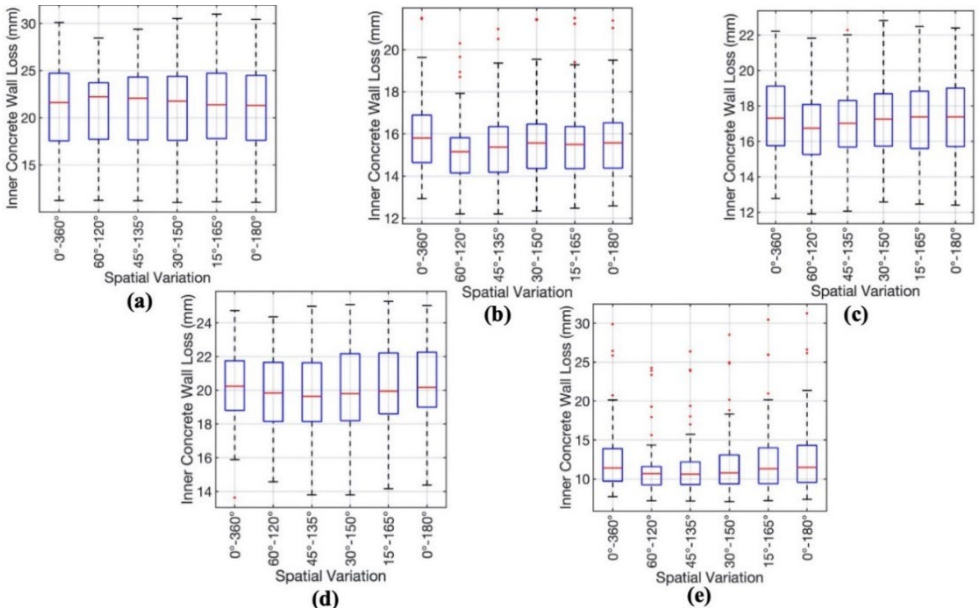

Figure 44. Box Plots of Concrete Wall Loss For Different Zones of the Pipe Circumference; (a) Line 1, (b) Line 2, (c) Line 3, (d) Line 4, (e) Line 5

To investigate if the mean concrete erosion for different cases is following the same distribution as that of the whole pipe circumference, the Weibull probability plots for each case study and the whole pipe are compared next; Weibull distribution is often used to model degradation phenomena. Figure 45 depicts the probability plots for different cases for line 1 for illustration purposes. The fitted lines to each case (one for the whole pipe shown in green and one for each case shown in red), are a good measure for comparison. Figure 45.e illustrates that for the 60°-120° case, the fitted line diverges from the whole pipe; however, all the other cases are following the same distribution and the difference is negligible. The same conclusion is also reported by (Bizier, 2007), where the concrete erosion of the crown is shown to be different from other parts of pipe circumference due to the sulfide accumulation at that location.

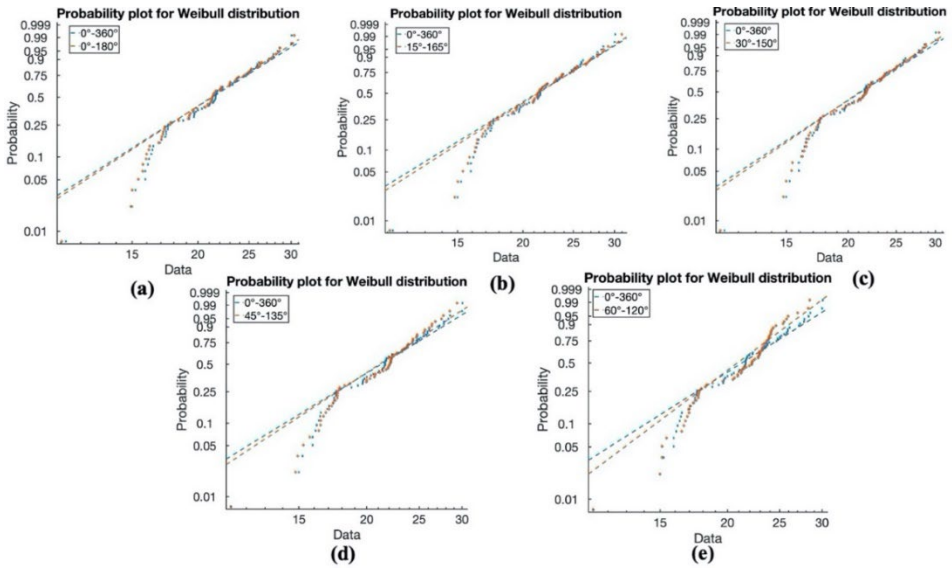

Figure 45. Weibull Probability Plots of Mean Concrete Loss of 5-ft Sections for Line 1

Besides these two visual techniques, the chi-square goodness-of-fit test are performed on different cases. The chi-square is a statistical test for evaluating if the two sets of data are following the same distribution. The null hypothesis is that the erosion data of each case study comes from the Weibull distribution (which is fitted to the concrete erosion of whole pipe circumference (0°-360°)). Table 4 shows the result of the test; *Pass* indicates that the chi-square method does not reject the null hypothesis at 1 percent significance level. Meanwhile, *Reject* indicates that Chi-square method reject the null hypothesis at 1 percent significance level.

Table 4. Results of Chi-Square Goodness-of-Fit-Test for Different Cases

Case Study / Line #	0°-180°	15°-165°	30°-150°	45°-135°	60°-120°
1	*Pass*	*Pass*	*Pass*	*Pass*	*Reject*
2	*Pass*	*Pass*	*Pass*	*Reject*	*Reject*
3	*Pass*	*Pass*	*Pass*	*Pass*	*Reject*
4	*Pass*	*Pass*	*Pass*	*Pass*	*Pass*
5	*Pass*	*Reject*	*Reject*	*Reject*	*Reject*

The results of chi-square goodness-of-fit test in Table 4 illustrates that there are statistically significant relationships between the mean concrete erosion of different cases and the whole pipe

circumference. Meanwhile, the concrete erosion data for the case: 0 º -180 º (of all five lines) has the closest results to the mean erosion of the whole circumference of the pipe. In addition, the two cases: 15 º -165 º and 30 º -150 º are the next best options. Meanwhile, the results of chi-square goodness-of-fit test matches those of the visual tests, e.g., the underlying distribution of the case: 60 º -120 º is different from other cases in line 1.

4.5 Assigning the Best-Fit Distribution to Erosion Rates

A best distribution is fitted to wall thickness loss data. The goodness of fit is calculated by comparing R^2 values from least squares (LS) for QQ-plots of 6 different distribution. Figure 46 shows that the results of the proposed distribution-fitting algorithm for the first ring (of section 1, line 1); according to Figure 46.c, the erosion rate data follows the Half-normal distribution with a coefficient of determination R^2 equal to 0.99. The results shows that the data could be following Exponential distribution or Weibull distribution too; however, it is easier to use Half Normal distribution because it is dependent on one parameter (i.e., standard deviation and the mean is zero). Figure 46 shows the results for the distribution fitting algorithm. Here, first Line is shown in Figure 46; all QQ-plots for all 10 lines are provided in *Appendix A*.

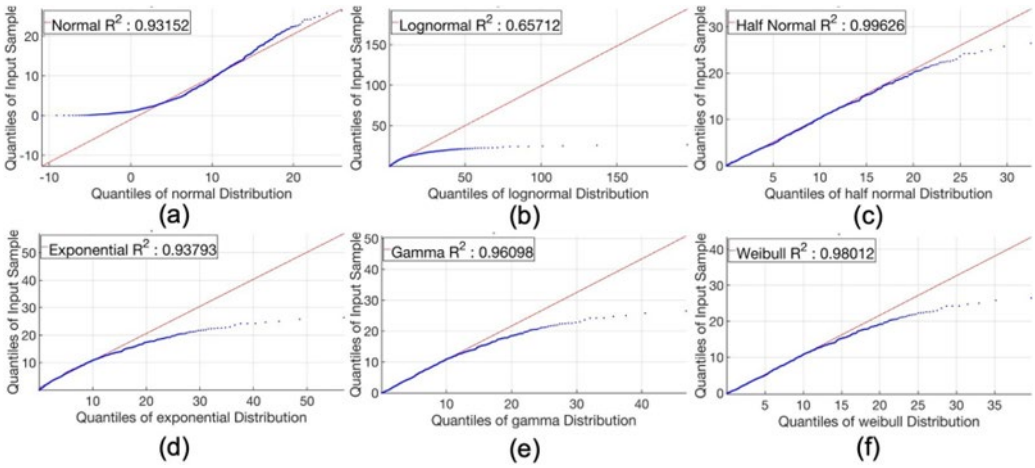

Figure 46. Results for Fitting Different Distribution to the Losses

From the QQ-plots of the distribution-fitting algorithm in Figure 46, it is shown that the right-tail of the erosion data is non-linear; it is light-tailed. According to (Pleil, 2016), these effects reflect a certain amount of error in the distribution, and ultimately must be interpreted as such.

As it is explained in *Chapter 3 Methodology*, the distribution fitting algorithm is performed on the erosion rate vector of each ring. The result of the proposed algorithm (in Figure 46) is verified by the graphical technique (histogram fitting); Figure 47 is generated by the Distribution-Fitting application (*histfit* function in MATLAB) comparing the top 4 best-fit distributions in Figure 46. Both results from Figure 46 and Figure 47 (probability plots) confirm that the underlying distribution follows Half-normal distribution

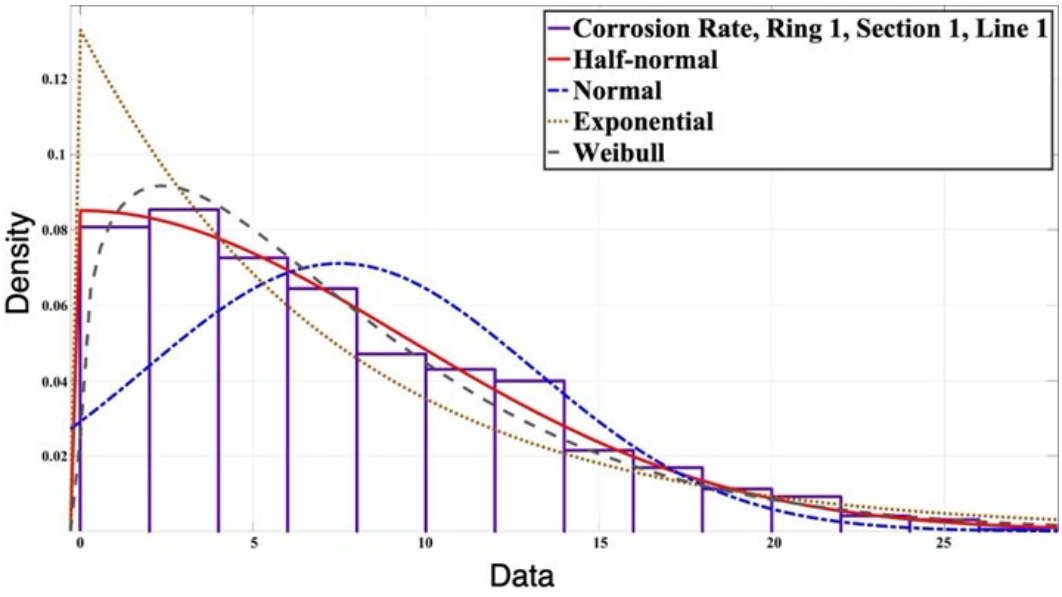

Figure 47. Comparing the Histogram Fitting of Erosion Rate Data Using 4 Different Distributions

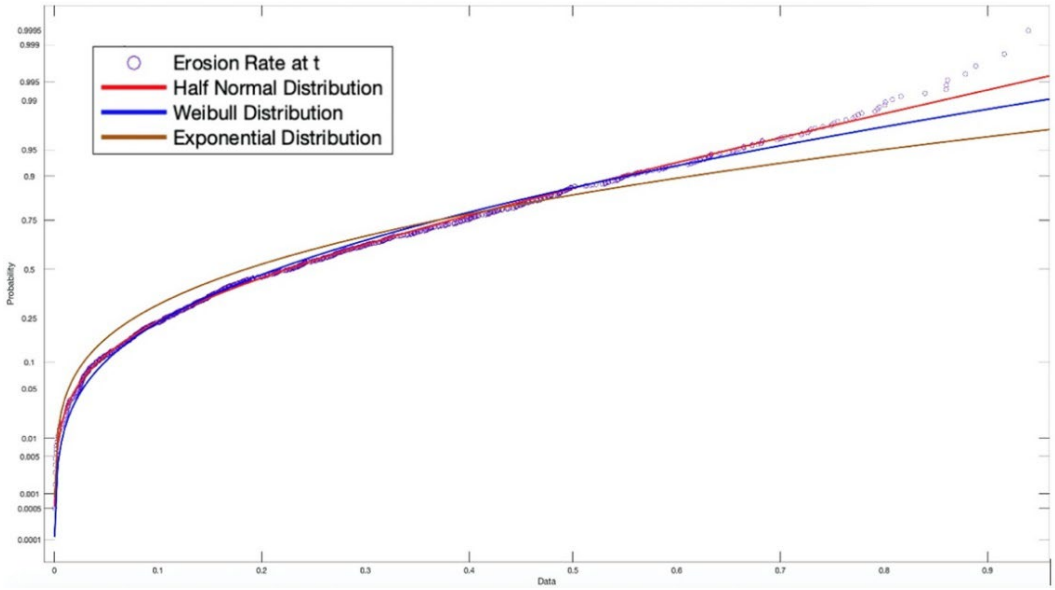

Figure 48. Probability Plots of 3 Top Best Fit Distribution on Erosion Data

The pie charts in Figure 49 shows the results of the proposed distribution-fitting algorithm for all the rings of each 10 lines (54- and 60- inch pipe). This confirms that for most of the rings, the erosion rate data follow the Half-normal distribution (with zero mean).

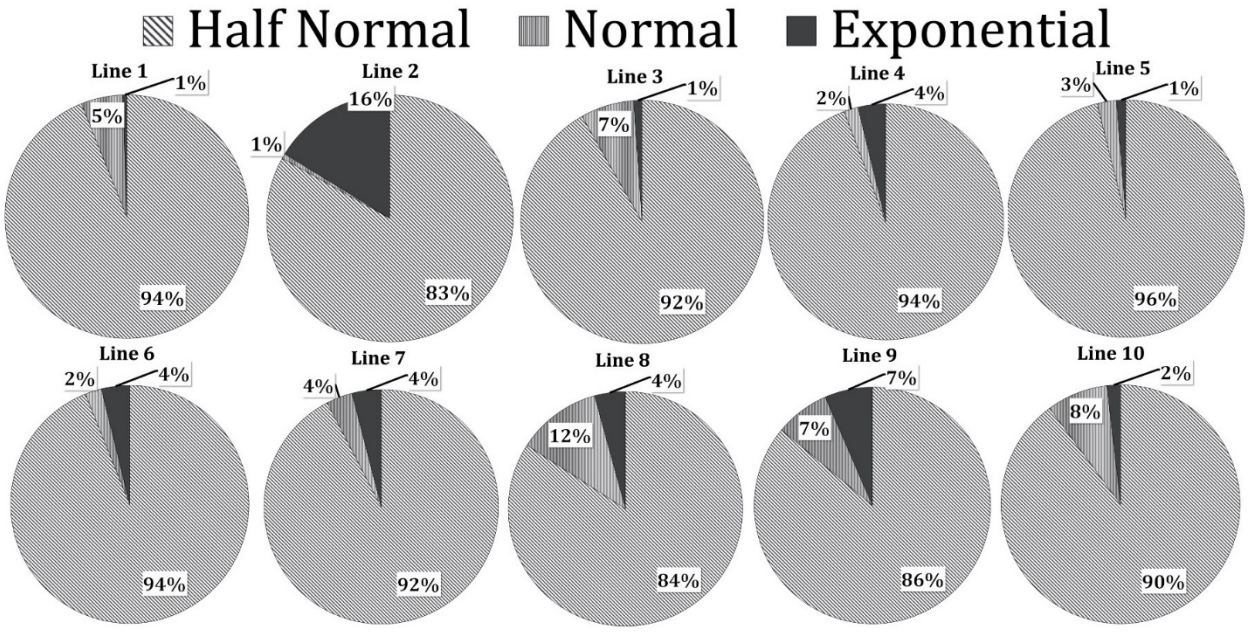

Figure 49. Pie Charts of the Results from Distribution-Fitting Algorithm for Erosion Rate Data

4.6 RSL Calculations

Once the pipe wall thickness loss is estimated using the filtered LiDAR data, corrosion rate is calculated by dividing the wall thickness loss amount to the age of the pipeline. RSL is calculated considering serviceability limit state that defines failure as the complete loss of 1-in concrete cover. Considering this limit state and a prescribed probability of exceedance threshold, a reliability-based prediction of the remaining service life is determined for 1000 linear foot of large diameter RCSSPs (54- and 60-inches).

4.6.1 Comparing RSL of two methods: Probability of Exceedance and X-intercept Method

Using the proposed framework, the residual service life (RSL) of the RCSSPs is presented for each 5-*ft* section. Figure 50-Figure 59 show the results for the first ten selected RC sanitary sewer pipelines using two different methods discussed in the previous section 3 (Section 3.4.5). It should

be noted that “Method 1” denotes the method of probability of exceedance (Section 3.4.5.1), and “Method 2” is the method of X-intercept (Section 3.4.5.2).

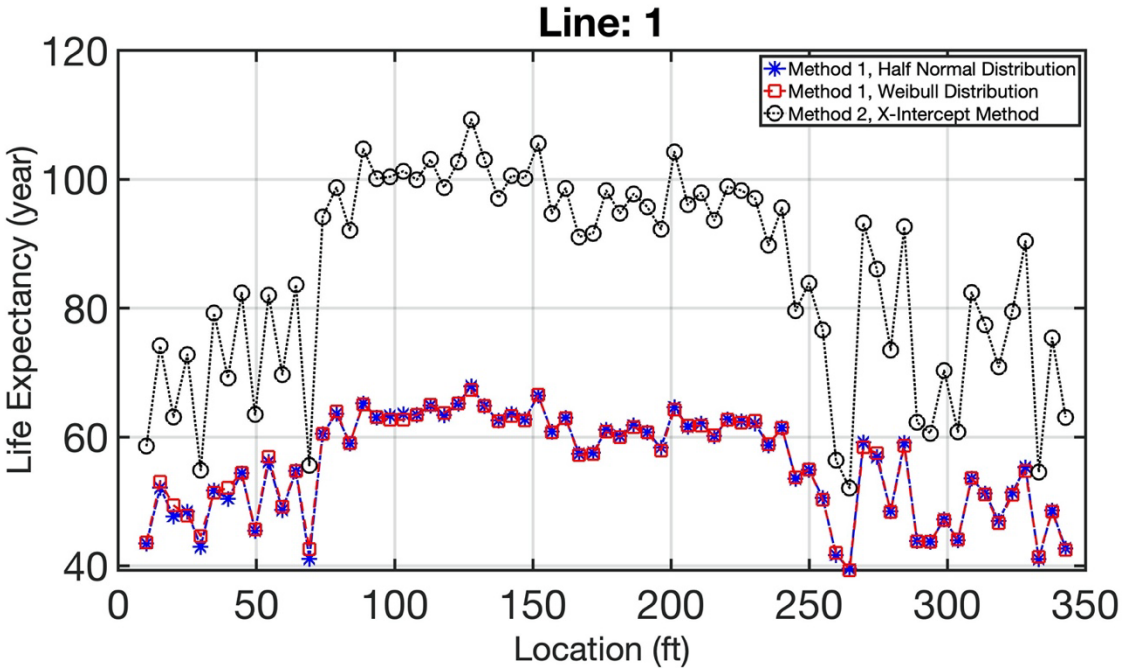

Figure 50. Comparison of RSL using X-intercept and Probability of Exceedance for Line 1

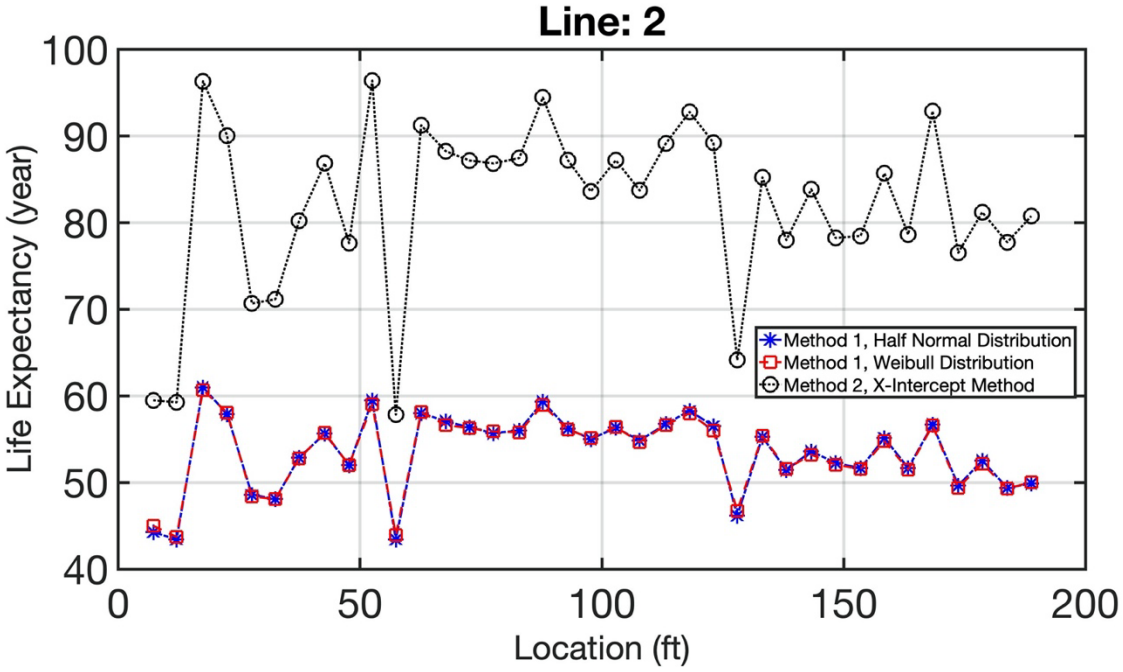

Figure 51. Comparison of RSL using X-intercept and Probability of Exceedance for Line 2

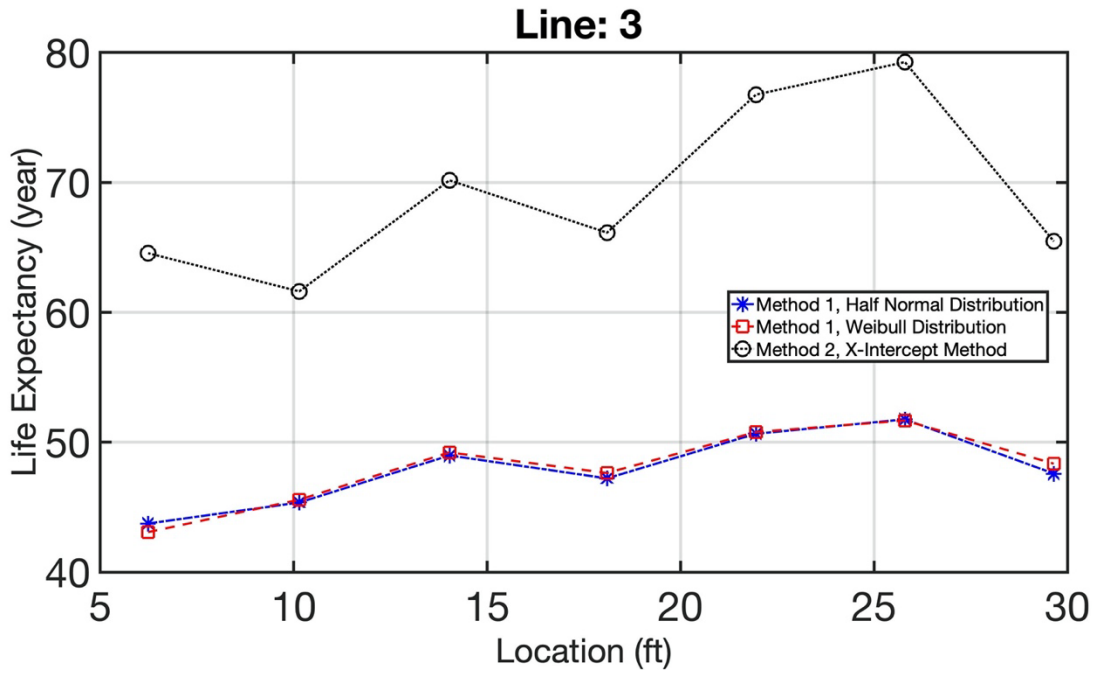

Figure 52. Comparison of RSL using X-intercept and Probability of Exceedance for Line 3

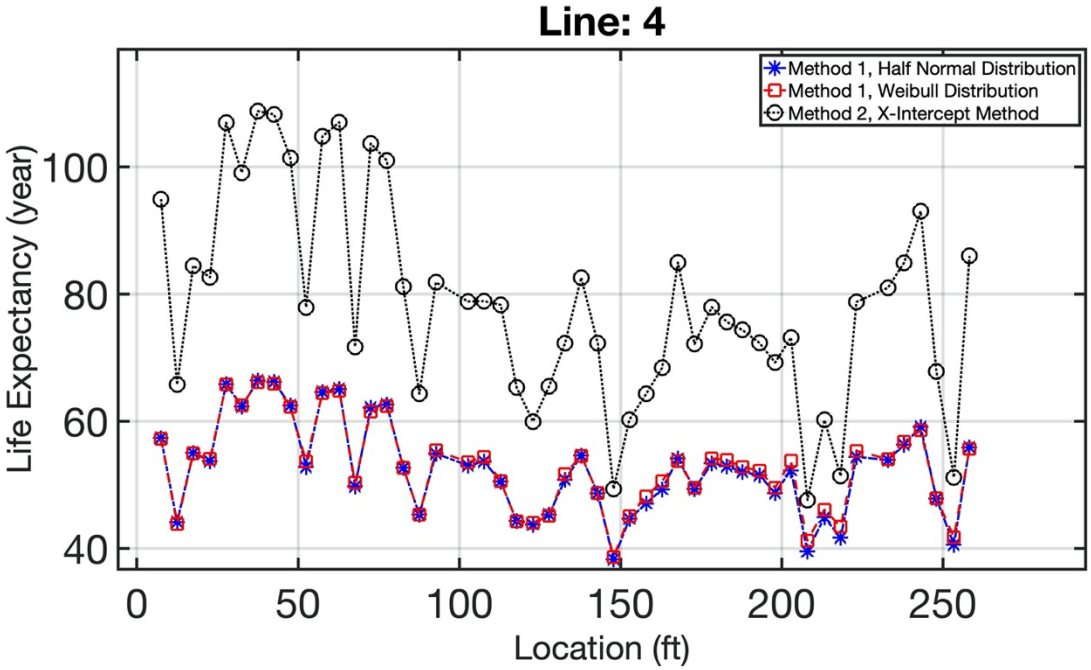

Figure 53. Comparison of RSL using X-intercept and Probability of Exceedance for Line 4

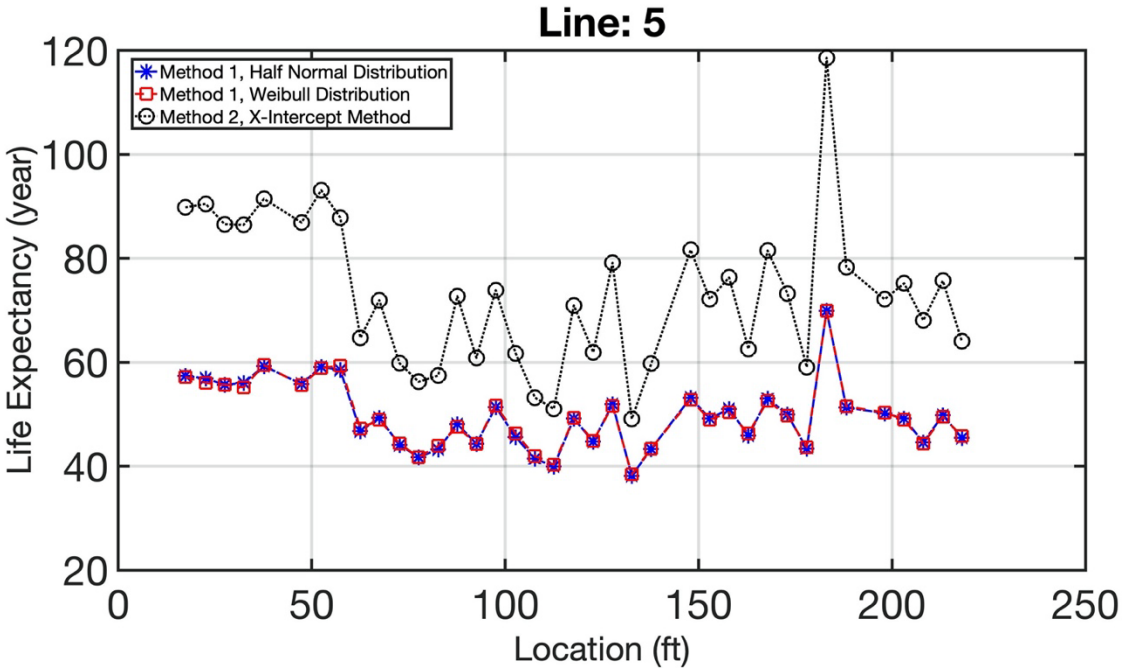

Figure 54. Comparison of RSL using X-intercept and Probability of Exceedance for Line 5

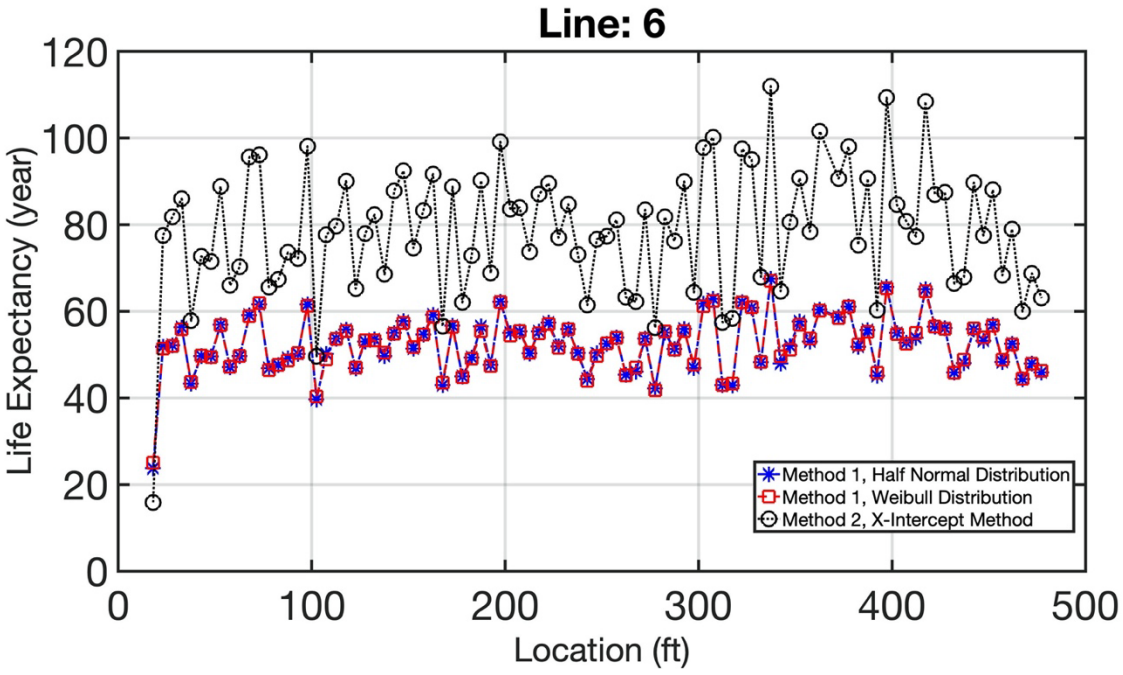

Figure 55. Comparison of RSL using X-intercept and Probability of Exceedance for Line 6

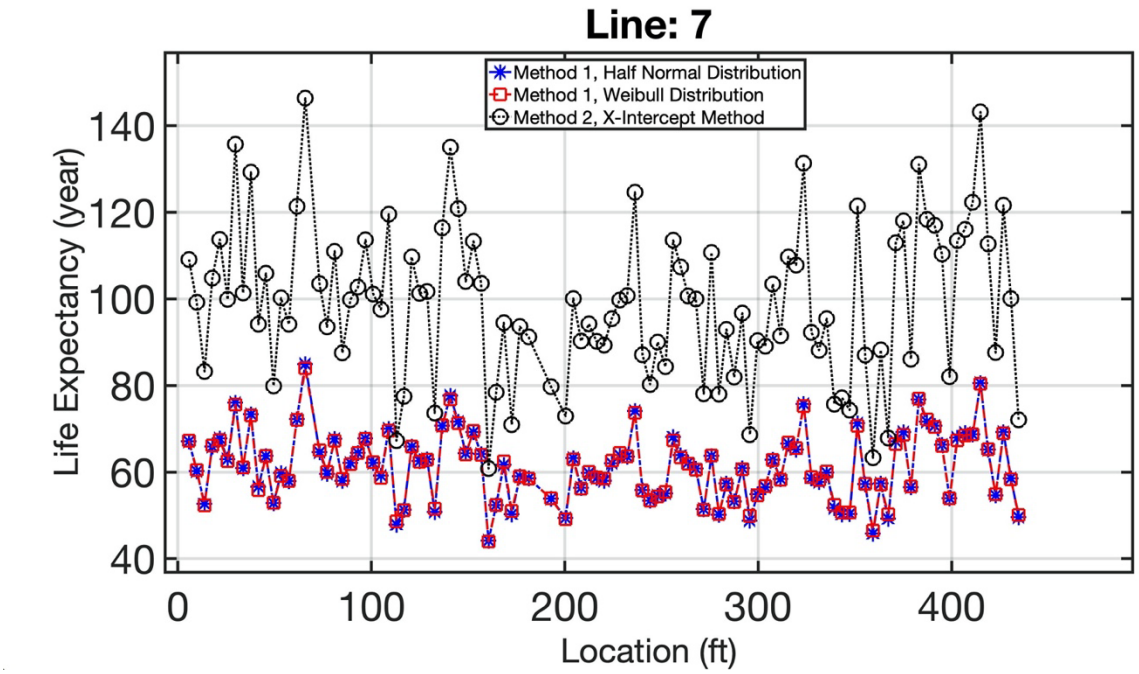

Figure 56. Comparison of RSL using X-intercept and Probability of Exceedance for Line 7

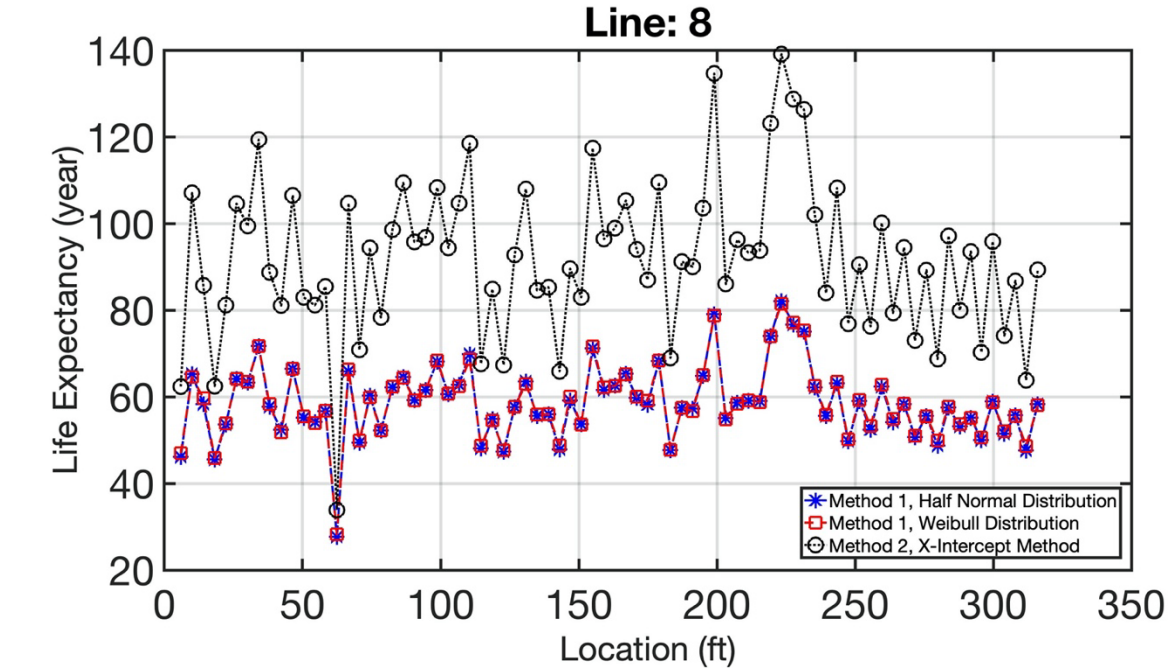

Figure 57. Comparison of RSL using X-intercept and Probability of Exceedance for Line 8

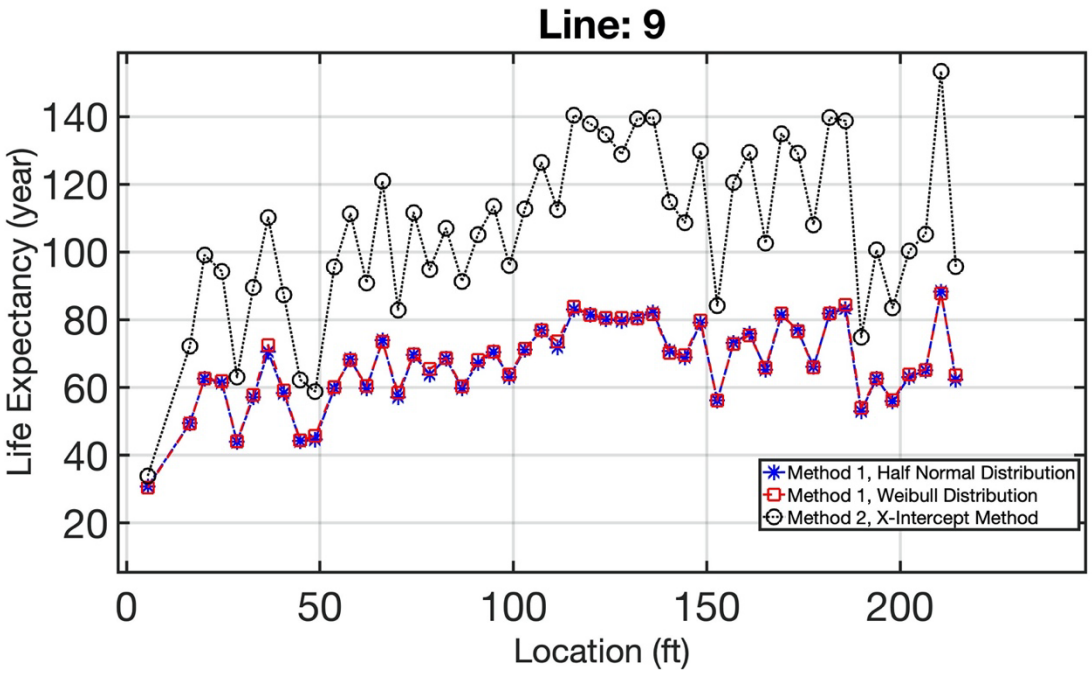

Figure 58. Comparison of RSL using X-intercept and Probability of Exceedance for Line 9

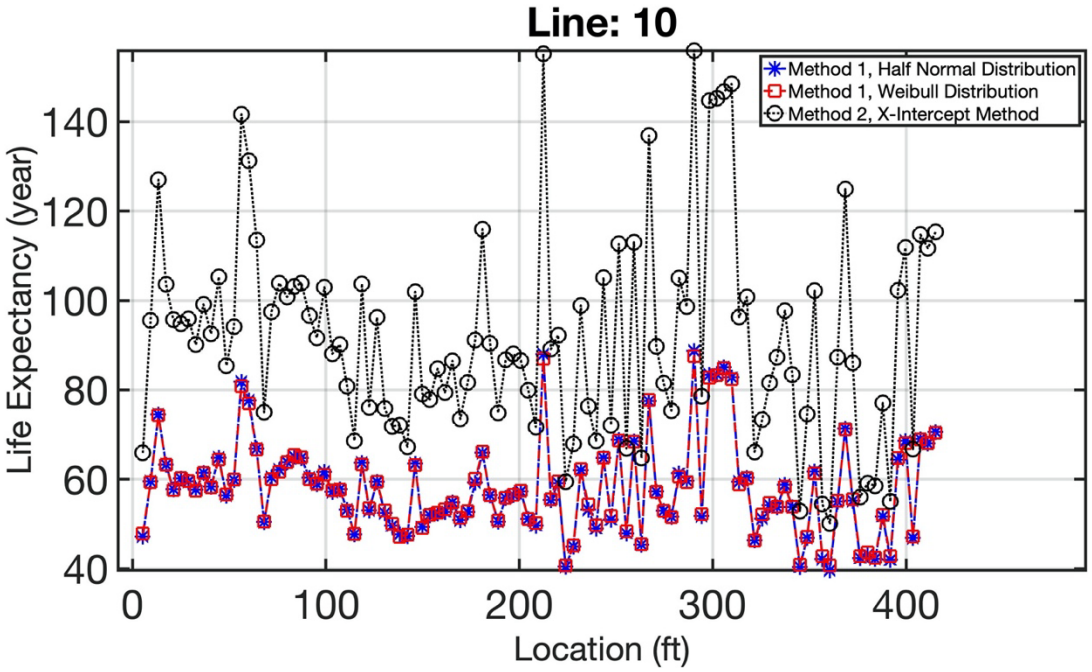

Figure 59. Comparison of RSL using X-intercept and Probability of Exceedance for Line 10

Figures 50-59 show a consistency between the Half-Normal distribution and Weibull distribution and is therefore, the best choice for modeling the erosion rate with uncertainty, since it requires knowing only the standard deviation.

Meanwhile, for the matter of simplicity, instead of working with the time consuming and long process of finding the life expectancy, the only parameter of Half Normal distribution (i.e., standard deviation) for the wall losses (not the erosion rate) can be plotted with respect to each location of each 5-ft section (Figure 33.a -Figure 42.a).

4.6.2 Investigating the Effect of Assigning Different Distributions on the Service Life of RCSSPs (using Probability-of-Exceedance Method)

The method of Probability-of-Exceedance is explained in (Section 3.4.10.1); it is a well-known method for estimating the service life of the RCSSPs. The key feature of this method is to assign the best distribution to the erosion rate so that it accurately represents the concrete degradation process of RCSSPs. Here, the top 4 best distributions are selected from Figure 46. The predicted RSL (life expectancy) for all the rings of each 10 lines are shown in the boxplots of Figure 60. The results show that assigning Exponential distribution decreases the service life about 12-13%; however, Normal distribution increases service life to 6%. More importantly, the Weibull and Half-normal distributions lead to the same values. It should be specified that these 10 RCSSPs are consecutive lines, so, their service life should be similar. Figure 60 suggests that the proposed method calculates the erosion of inner wall of RCSSPs consistently. This is confirmed with the CCTV data, as there was no root intrusion, joint failure, or pipe collapse.

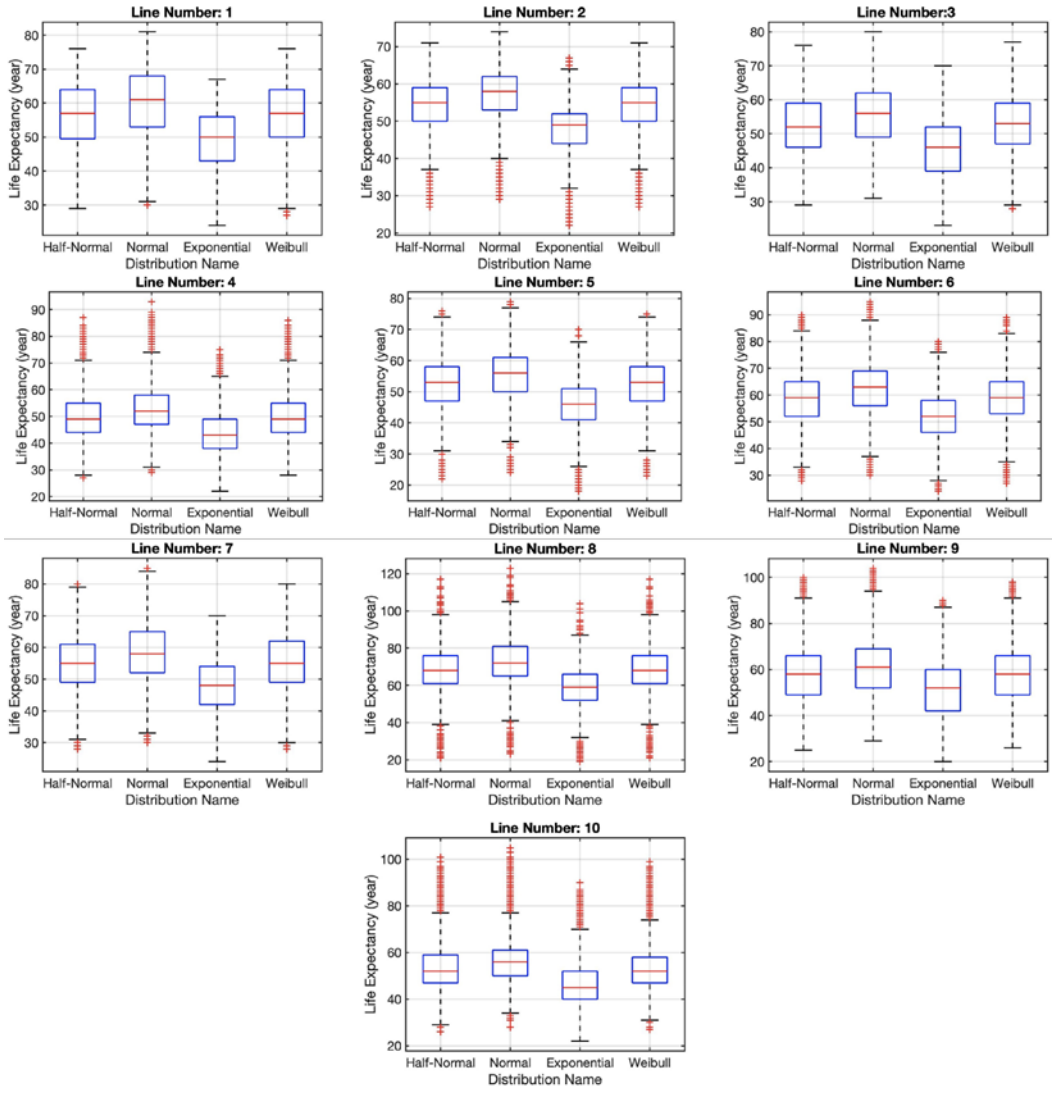

Figure 60. Comparing the Service Life of RCSSPs by Assigning 4 Different Distributions

The so-called year of maintenance could be calculated by adding the predicted RSL in Figure 60 to the inspection year.

4.6.3 Consistency of the Proposed Algorithm with Similar Study Using Manual Filtering

The uncertainty of the predicted service life is determined by constructing the confidence interval of the mean predicted RSL of all rings (with 95% confidence). To calculate the confidence interval, Equation 30 is utilized.

$$\mu_{(1-\alpha)} = \left[X + \left(\frac{\left(tz_{\left(\frac{\alpha}{2}\right),(NS-1)} \right) SD}{\sqrt{NS}} \right); \; X - \left(\frac{\left(tz_{\left(1-\frac{\alpha}{2}\right),(NS-1)} \right) SD}{\sqrt{NS}} \right) \right] \qquad \text{Equation 30}$$

where μ is the weighted average of service life, α is the significance (i.e., 5 % herein), *tz* is the z-score from the z-table, *SD* is the sample standard deviation of mean service life of all rings, and *NS* is the number of rings at each RoI.

The confidence interval of the predicted service life values (from the proposed method) is compared with the results of a previous study (Moamaie, 2019) that used the same LiDAR inspection data. (Moamaie, 2019) filtered and processed the 3D PCDs manually for each RoI; the raw LiDAR PCD of each RoI is imported into an open-source program called Cloud Compare; a cylinder was centered to the filtered PCD (knowing the radius from Table 2). In this smilar study using the same data (Moamaie, 2019) the mean inner concrete loss of each RoI was the mean Euclidean distance of each filtered PCD and the centered cylinder. Figure 61 shows the comparison between the results of the predicted service life using the proposed algorithm and the previous study with the user interference from (Moamaie, 2019). Both approaches use a Probability-of-Exceedance method (discussed in subsection 3.4.8.1) for predicting the service life of the selected RCSSPs. In contrast (Moamaie, 2019) fitted the Weibull distribution to erosion rate data and the method proposed herein used the best-fit distribution (i.e., Half-normal distribution).

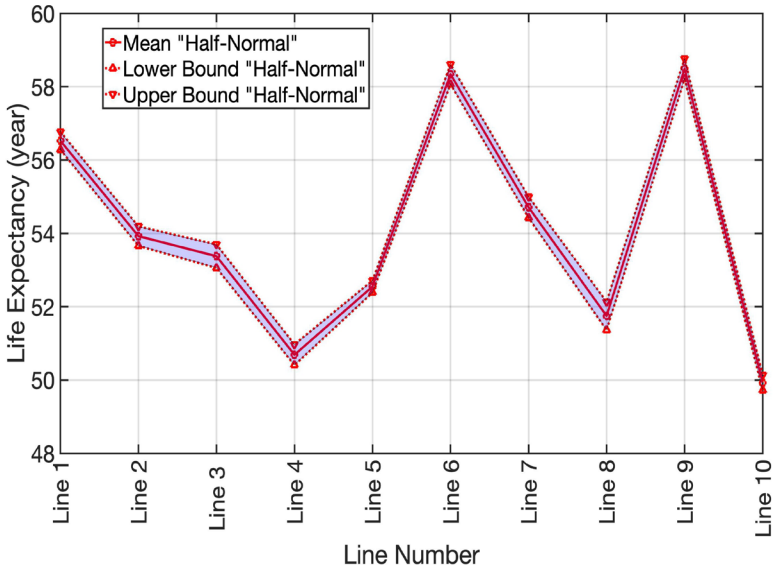

(a)

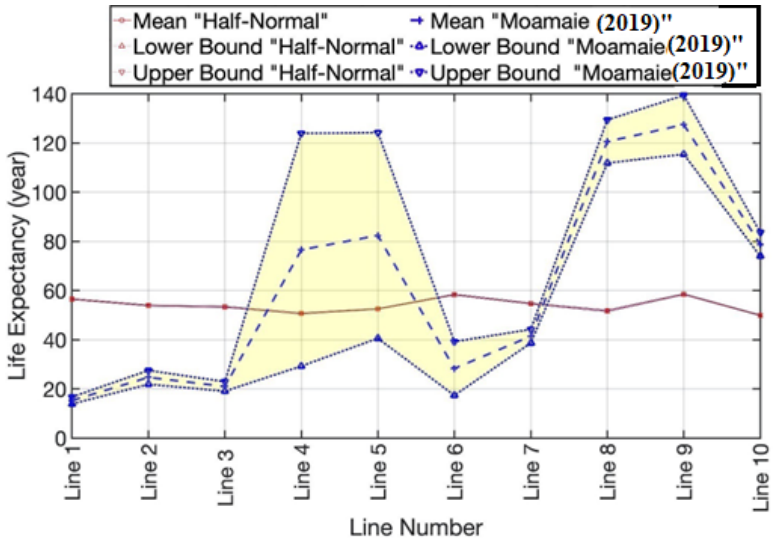

(b)

Figure 61. Comparing the Results of Predicted RSL using (a) The Proposed Method, and (b) Previous Study (Moamaie, 2019)

Figure 61 shows that the difference between each lower and upper bound is much smaller than the previous study, indicating that the results from the methodology proposed herein are more consistent.

4.6.4 Comparing the Results of Different Reliability Methods on the Predicted Service Life of RCSSPs

As it is discussed in *subsection 3.4.8*, two methods are used for predicting the service life of RCSSPs. Here, the results from the approach proposed herein are compared with different time-dependent reliability methods discussed by (Mahmoodian & Li, 2011) and (He & Koizumi, 2013); they performed Monte Carlo simulation (MCS) on Equation 22 and Equation 23. Here, MCS runs on the Equation 22 and Equation 23 with the variable inputs shown in Table 5.

Table 5. Properties of Random Variables for Monte Carlo Simulation (MCS)

Basic Variables	Distribution Name	value/Mean	Coefficient of Variation
K	Normal Distribution	0.8	0.05
j	Normal Distribution	0.2	0.04
DS	Normal Distribution	1	0.1
S	Deterministic	From Table 2	-
VF	Deterministic	Calculated using Equation 23	-
b/WP	Deterministic	Calculated using subsubsection 3.4.5	-
AC	Normal Distribution	0.45	0.18
Ψ	Standard Normal Distribution	0	$\sigma = 1$
Initial Cover	Normal Distribution (mm)	25.4 (ASTM 2007)	0.005
Er_{MC}	Deterministic (mm)	Calculated using Equation 19	-

It should be noted that the slope (*S*) is derived from the as-built drawing (from Table 2), b/WP and *VF* are calculated with the proposed algorithm (i.e., explained in subsubsection 3.4.5), Er_{MC} is the mean erosion rate of each 5-ft sections (from subsubsection 3.4.6), and Ψ is the coefficient representing the uncertainty of the model. Different distributions are assigned to the other variables as shown in Table 5. Figure 62-a shows different probability-of-failure plots for various reliability methods. Figure 62-b illustrates the bar plots of predicted RSL (service life) using different reliability methods. The results of Figure 61 are for the first 5-*ft* section of line 1. Meanwhile, based on the convergence tests, it is accurate enough for the MCS to run with 1000 populations.

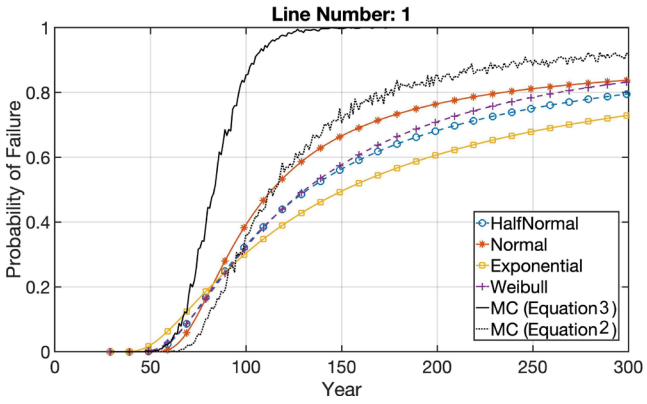

(a)

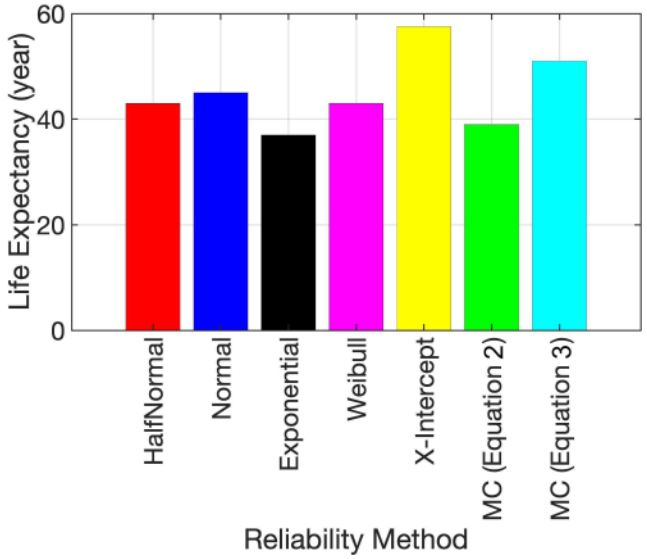

(b)

Figure 62. Comparing the Results of Different Reliability Methods: a) Probability-of-Failures Plots, b) Predicted Service Life using Different Reliability Methods

Figure 62-a shows that the probability of failure plot of MC simulation (using Pomeroy Equation 23) is similar the method proposed herein. Lastly, in order to have a thorough comparison between all the lines, the predicted life expectancy using 4 different reliability methods are shown in boxplots in Figure 63. As previously mentioned, the service life is calculated for an acceptable risk of $P_a = 0.1$.

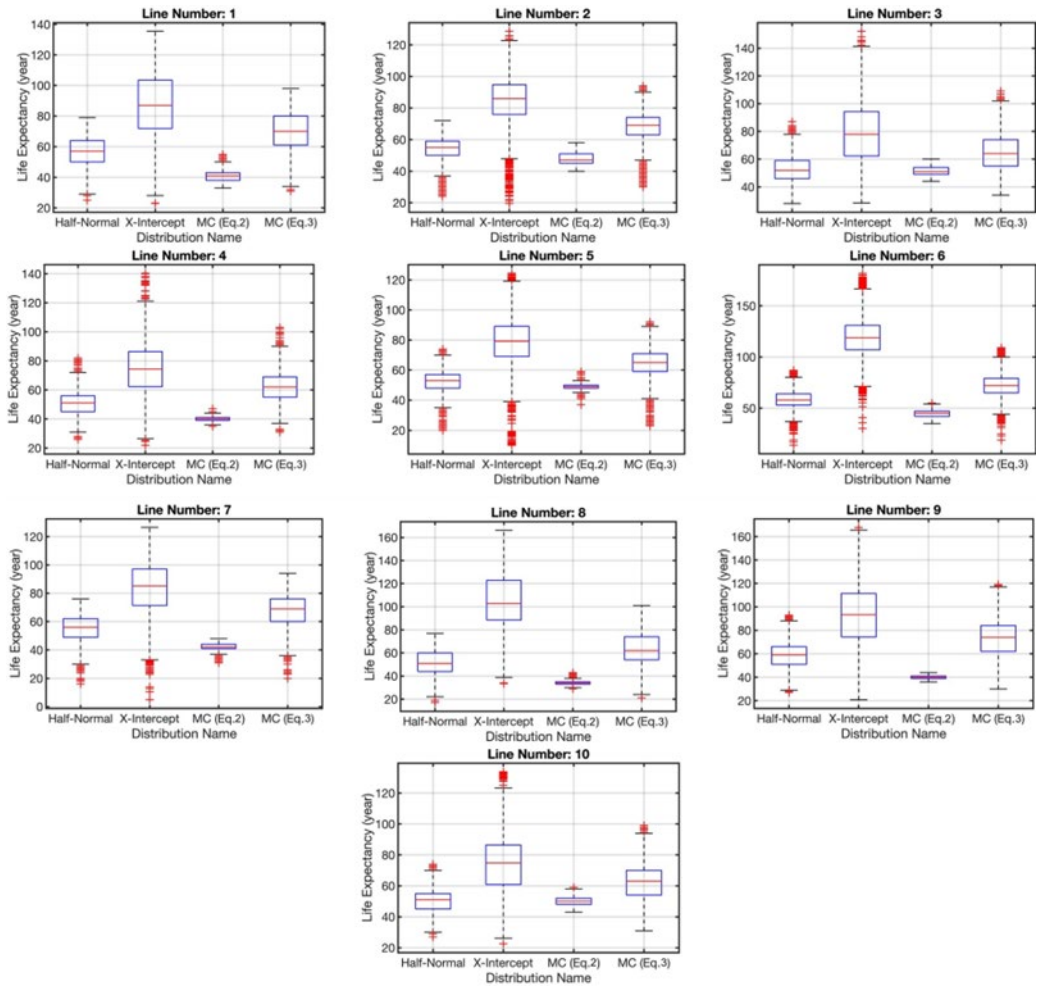

Figure 63. Results of Predicted Service Life using 4 Different Reliability Methods

The service life of all rings within each line are shown as boxplots of Figure 63; the results illustrate that the X-intercept method led to larger service life predictions than other methods; this could be the result of its underlying method which does not consider any uncertainty. Service life predictions from MCS of Power law (Equation 22) are larger than those obtained by using the Half-normal distribution; however, estimated remaining service life from MCS of Pomeroy model (Equation 23) aligns well with those obtained by using the Half-normal distribution.

4.7 Results of Statistical Methods on the Calculated Properties

statistical methods such as the Single variable Regression model, Multi-Variables Regression model, and Polynomial Regression model are implemented on the output of the proposed algorithm in order to estimate the concrete erosion of the inner wall of RCSSPs using the calculated parameters. The Regression models can be used to understand the relationship between the "Mean Loss (mm)" (the dependent variable) and other variables in the dataset (independent variables).

Figure 64 to Figure 66 show the summary of data being used for different statistical methods. The data is calculated using the proposed algorithms.

Area of Flow (mm^2)	Water Level (%)	Hydraulic Radius (mm)	Actual Radius (mm)	Ovality	Mean Loss (mm)	Pipeline #
165198.8003	0.307000181	331.7438174	498.6978753	0.120646596	28.50376846	1
118348.3071	0.286010069	249.7953327	445.0304991	0.105690522	32.14961359	1
101887.2444	0.291688815	216.397014	419.6866101	0.093577111	32.59645832	1
87689.41322	0.281576875	192.205284	402.6696061	0.081794279	28.8784331	1
87782.06498	0.276478049	193.7862093	401.2976334	0.084242695	28.69172261	1
87598.36963	0.254785383	197.6548328	404.0315607	0.077341479	28.07251137	1
86819.02659	0.269443358	192.9797858	401.8872241	0.078523578	32.11350421	1
82801.24706	0.27861687	183.0166949	394.0838002	0.079642345	32.5516113	1
77207.73088	0.279588404	172.1832319	386.1626543	0.072115541	29.96995958	1

Figure 64. Overview of 30-inches Data to Perform Different Statistical Methods (Pipeline #1-15)

Area of Flow (mm^2)	Water Level (%)	Hydraulic Radius (mm)	Actual Radius (mm)	Ovality	Mean Loss (mm)	Section #	Pipeline #
422277.088	0.498182922	256.8074633	669.3371912	0.027226669	8.750288538	1	1
420893.1457	0.496587016	257.0305876	670.0364686	0.03218617	8.563519274	1	1
428090.5647	0.501651083	259.079373	671.178302	0.024495924	8.433411284	1	1
420167.6802	0.494001675	255.5328448	672.6440715	0.020575039	8.251463728	1	1
426681.6233	0.497391063	258.2568573	674.2236134	0.018524989	8.017806486	1	1
422981.9877	0.495103827	256.3413863	674.3544595	0.019328728	8.286268405	1	1
412115.3209	0.487943124	252.9779921	673.8514951	0.022913199	8.457251718	1	1
404920.0296	0.482643526	250.0350961	674.2608224	0.025880707	9.091593736	1	1
395175.0011	0.474704104	245.8311672	675.6329956	0.02461234	8.930564221	1	1

Figure 65. Overview of 54-inches Data to Perform Different Statistical Methods (Pipeline #1-5)

Area of Flow (mm^2)	Water Level (%)	Hydraulic Radius (mm)	Actual Radius (mm)	Ovality	Mean Loss (mm)	Section #	Pipeline #
723048.9003	0.560630014	336.855963	778.8140289	0.066474613	8.989317368	1	1
720420.6684	0.560912509	335.8277236	778.1661727	0.030198017	8.832950229	1	1
705449.7767	0.554189133	332.0601736	776.8526848	0.052483633	8.646398561	1	1
702113.9501	0.553980709	331.3586661	775.8508754	0.017712085	8.732907516	1	1
706888.057	0.558462121	333.7777047	774.5785417	0.037261299	8.069564449	1	1
698956.1031	0.553399092	330.0820124	776.0179785	0.012842965	7.715089177	1	1
700418.7842	0.555990873	330.608259	774.8937723	0.059257691	7.598156852	1	1
680500.505	0.54519811	325.5316296	774.3200668	0.014552328	7.456227406	1	1
684768.7304	0.548243799	328.1913518	773.7439483	0.020323177	7.714967191	1	1

Figure 66. Overview of 60-inches Data to Perform Different Statistical Methods (Pipeline #1-5)

Properties shown in Figure 64 to Figure 66 are described as follows:

Area of Flow: Represents the cross-sectional area of the flow (calculated using Equation 14).

Water Level: Indicates the percentage of water in the sewer pipe (calculated using Equation 15).

Hydraulic Radius: A measure of the pipe's efficiency in conveying fluid (calculated using Equation 15).

Actual Radius: The measured radius of the RCSSPs (calculated by circle fitting algorithm).

Ovality: Represents the deviation from a perfect circle, based on the ASTM equation (calculated using Equation 11.a).

Mean Loss (Fitted Circle): The average loss based on a fitted circle representation (calculated using Equation 9).

Section #: Indicates the number of 5-ft section for each pipeline # (For 54- and 60-inches pipes).

Pipeline #: Indicates the pipeline number (M-M).

4.7.1 Single Variable Regression Model

Results from Single-variable regressions on the data for 30-, 54- and 60-inches are presented in the following steps:

First, dataset in slitted into training and testing sets (80-20) method. Then the regression models are build using different independent variables. Finally, the performance of each model on the is evaluated on testing set.

Table 6-Table 8 show the results from the Single variable regression for 30-, 54-, and 60-inch data respectively. In addition, fitted regression line and the corresponding mean square error (MSE) and root mean square error (RMSE) are provided.

Figure 67-Figure 69 show the scatter plots from the Single variable regression analysis for 30-, 54-, and 60-inch data respectively. The blue points are training data and red points are test data. The scatter plots visualize the data points and the regression line fitted by the model.

Table 6. Results of Single Variable Regression Model on 30-inches Data

30 Inches Pipe			
Variable	**Regression Line**	**MSE**	**RMSE**
Area of Flow (mm^2)	$y = 0.00010\,x + 45.83$	41.38	6.43
Water Level (%)	$y = 186.34\,x + 18.47$	14.36	3.79
Hydraulic Radius (mm)	$y = 0.46\,x + 50.33$	91.93	9.59
Actual Radius (mm)	$y = 0.09\,x + 13.19$	114.64	10.71
Ovality	$y = 574.82\,x + 7.73$	28.63	5.35

Table 6 shows that *Water Level* data can better predict the Mean loss for 30-inches data.

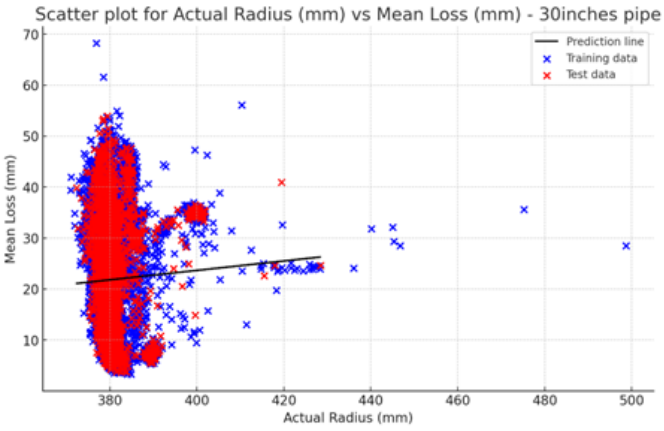

(a)

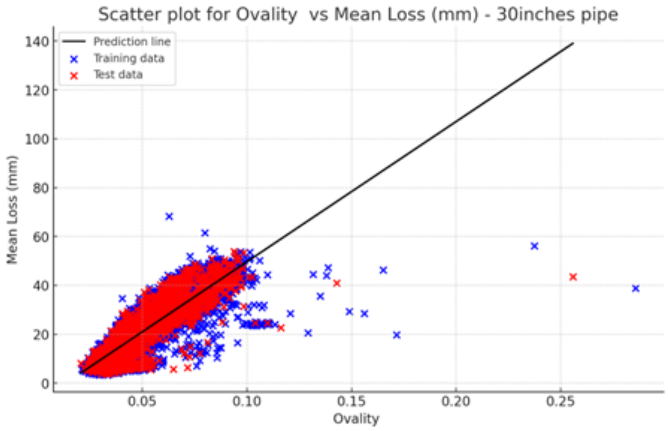
Scatter plot for Ovality vs Mean Loss (mm) - 30inches pipe
Prediction line
Training data
Test data
Mean Loss (mm)
Ovality
0
20
40
60
80
100
120
140
0.05
0.10
0.15
0.20
0.25

(b)

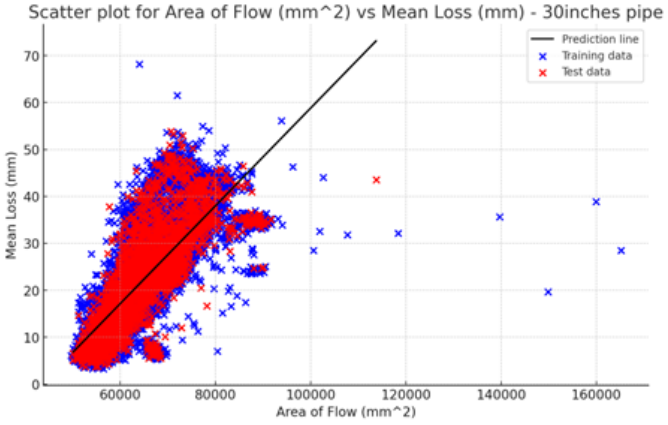
Scatter plot for Area of Flow (mm^2) vs Mean Loss (mm) - 30inches pipe
Prediction line
Training data
Test data
Mean Loss (mm)
Area of Flow (mm^2)
0
10
20
30
40
50
60
70
60000
80000
100000
120000
140000
160000

(c)

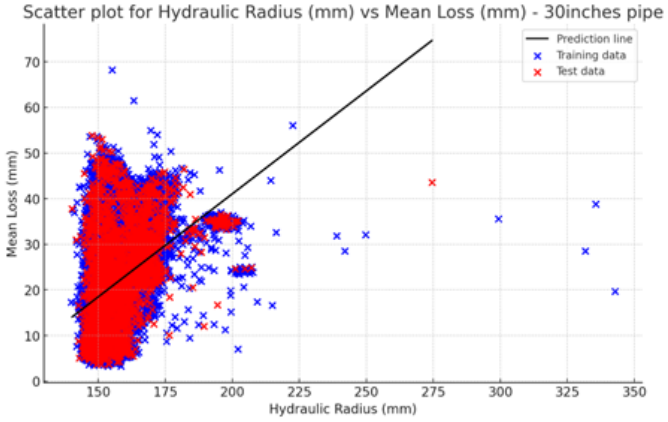
Scatter plot for Hydraulic Radius (mm) vs Mean Loss (mm) - 30inches pipe
Prediction line
Training data
Test data
Mean Loss (mm)
Hydraulic Radius (mm)
0
10
20
30
40
50
60
70
150
175
200
225
250
275
300
325
350

(d)

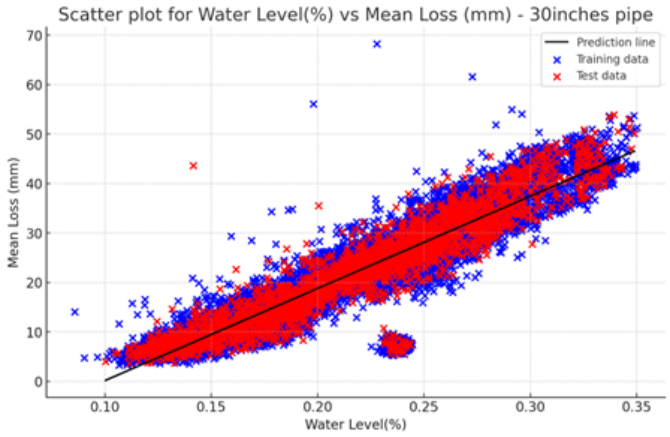

(e)

Figure 67. The Scatter Plots from the Outputs of Single Variable Regression for 30-inches Data

Table 7. Results of Single Variable Regression Model on 54-inches Data

54 Inches Pipe			
Variable	**Regression Line**	**MSE**	**RMSE**
Area of Flow (mm^2)	$y = 0.01 * 10^{-6}x + 5.92$	2.51	1.58
Water level (%)	$y = 4.81\,x + 4.30$	2.48	1.58
Hydraulic Radius (mm)	$y = 0.01\,x + 5.31$	2.51	1.58
Actual Radius (mm)	$y = -0.04\,x + 30.86$	2.35	1.53
Ovality	$y = 15.00\,x + 6.26$	2.4	1.55

Table 7 shows that *Actual Radius* is the best property to predict the Mean loss for 54-inch data. Meanwhile, difference between other regression models is small for other properties. It is the same for 60-inch results (Table 8).

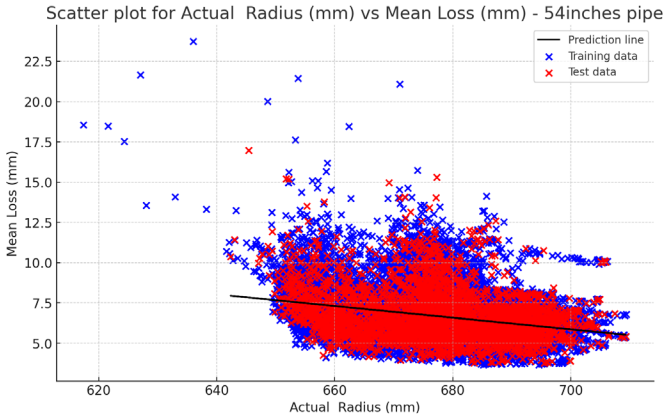
Scatter plot for Actual Radius (mm) vs Mean Loss (mm) - 54inches pipe
Prediction line
Training data
Test data
Mean Loss (mm)
Actual Radius (mm)

(a)

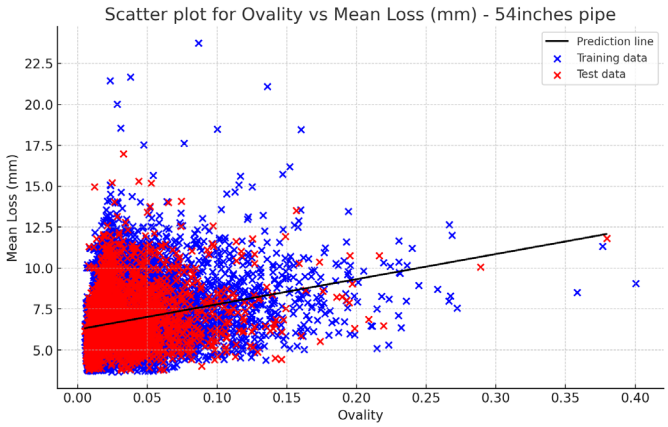
Scatter plot for Ovality vs Mean Loss (mm) - 54inches pipe
Prediction line
Training data
Test data
Mean Loss (mm)
Ovality

(b)

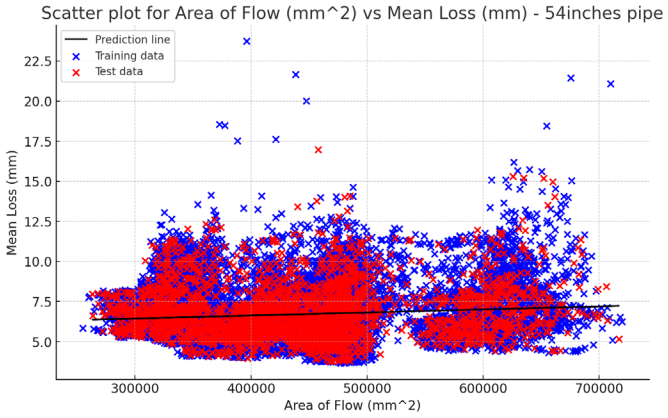
Scatter plot for Area of Flow (mm^2) vs Mean Loss (mm) - 54inches pipe
Prediction line
Training data
Test data
Mean Loss (mm)
Area of Flow (mm^2)

(c)

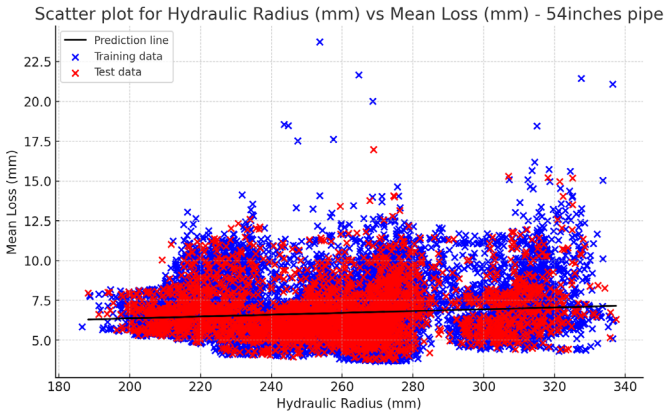

(d)

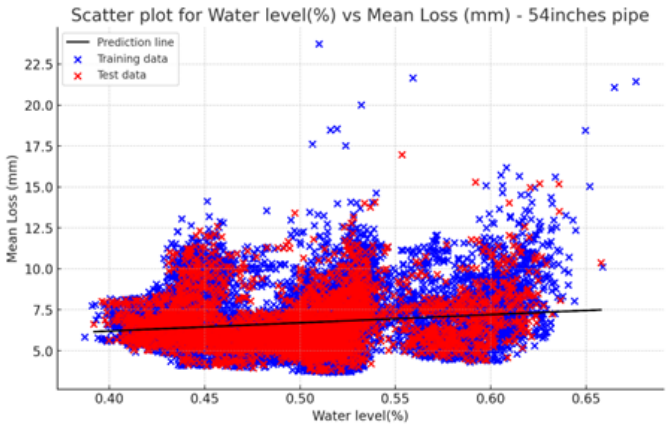

(e)

Figure 68. The Scatter Plots from the Outputs of Single Variable Regression for 54-inches Data

Table 8. Results of Single Variable Regression Model on 60-inches Data

60 Inches Pipe			
Variable	**Regression Line**	**MSE**	**RMSE**
Area of Flow (mm^2)	$y = 0.01 * 10^{-5} x + 6.22$	1.87	1.37
Water level (%)	$y = 3.88 x + 4.88$	1.85	1.36
Hydraulic Radius (mm)	$y = 0.00 x + 5.48$	1.86	1.36
Actual Radius (mm)	$y = -0.06 x + 50.76$	1.62	1.27
Ovality	$y = 13.39 x + 6.45$	1.8	1.34

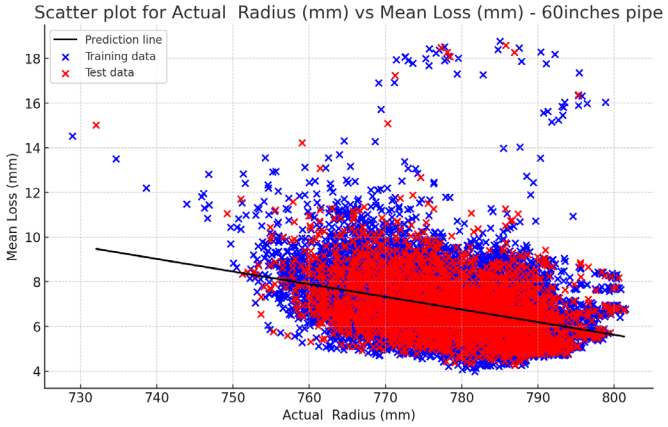
Scatter plot for Actual Radius (mm) vs Mean Loss (mm) - 60inches pipe
Prediction line
Training data
Test data
Mean Loss (mm)
Actual Radius (mm)

(a)

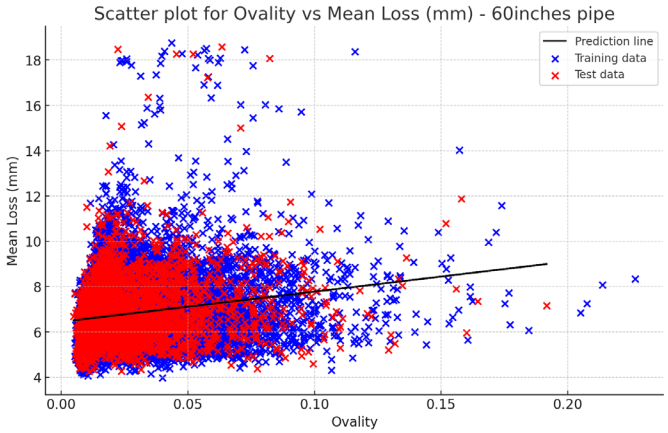
Scatter plot for Ovality vs Mean Loss (mm) - 60inches pipe
Prediction line
Training data
Test data
Mean Loss (mm)
Ovality

(b)

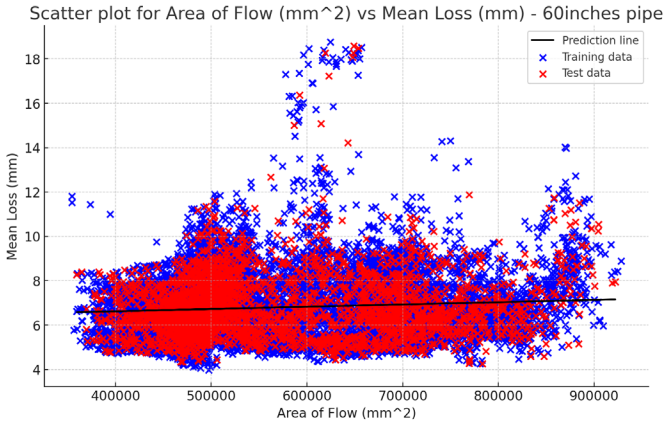
Scatter plot for Area of Flow (mm^2) vs Mean Loss (mm) - 60inches pipe
Prediction line
Training data
Test data
Mean Loss (mm)
Area of Flow (mm^2)

(c)

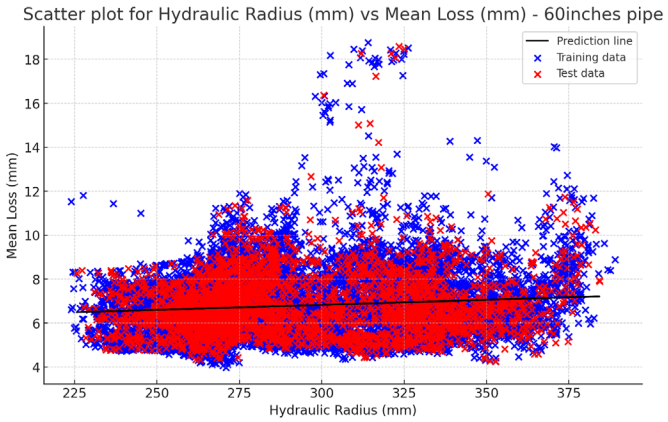

(d)

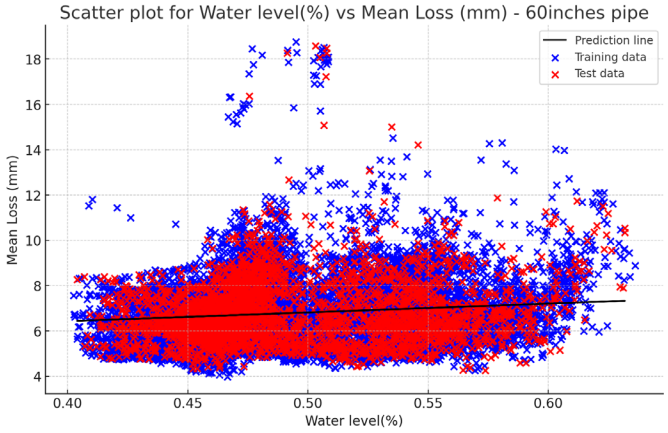

(e)

Figure 69. The Scatter Plots from the Outputs of Single Variable Regression for 60-inches Data

From the results of single variable regression, the following bullet points are concluded:

- Results of Single variable regression model (Table 6-Table 8) shows that *Ovality* is the best variable to predict the *Mean concrete loss* with RMSE of 5.35,1.55,1.34 for 30-54-, and 60-inches data. For instance, for 30-inch data the predictions using Ovality have an average error of 1.55 *mm* from the actual values.
- Results of Single variable regression on the properties of 30-inch pipes are more diverse than 54- and 60-inch pipe; this could be due to filtering phase of 54-60-inch data. The 30-inch inspection data are different 2D rings along the length of the pipe, however, the output of 54-

60-inch inspection data are 3D PCDs for each 5-*ft* along the length of the pipe; the 2D rings are extracted from the 3D PCD using the proposed methods.

Figure 70 shows the heatmaps representing the correlation matrices for the three different pipe diameters: 30-inches, 54-inches, and 60-inches. The values on the heatmap are the correlation coefficients between each pair of variables. These heatmaps provide a visual representation of how each variable is associated with the others. Strong correlations (closer to 1 or -1) suggest a more significant linear relationship between two variables, while values closer to 0 indicate a weaker or non-linear relationship. This information is valuable for understanding the relationships within the data and for feature selection in predictive modeling.

In each heatmaps, positive correlations are displayed in warmer colors (towards red), and negative correlations are in cooler colors (towards blue).

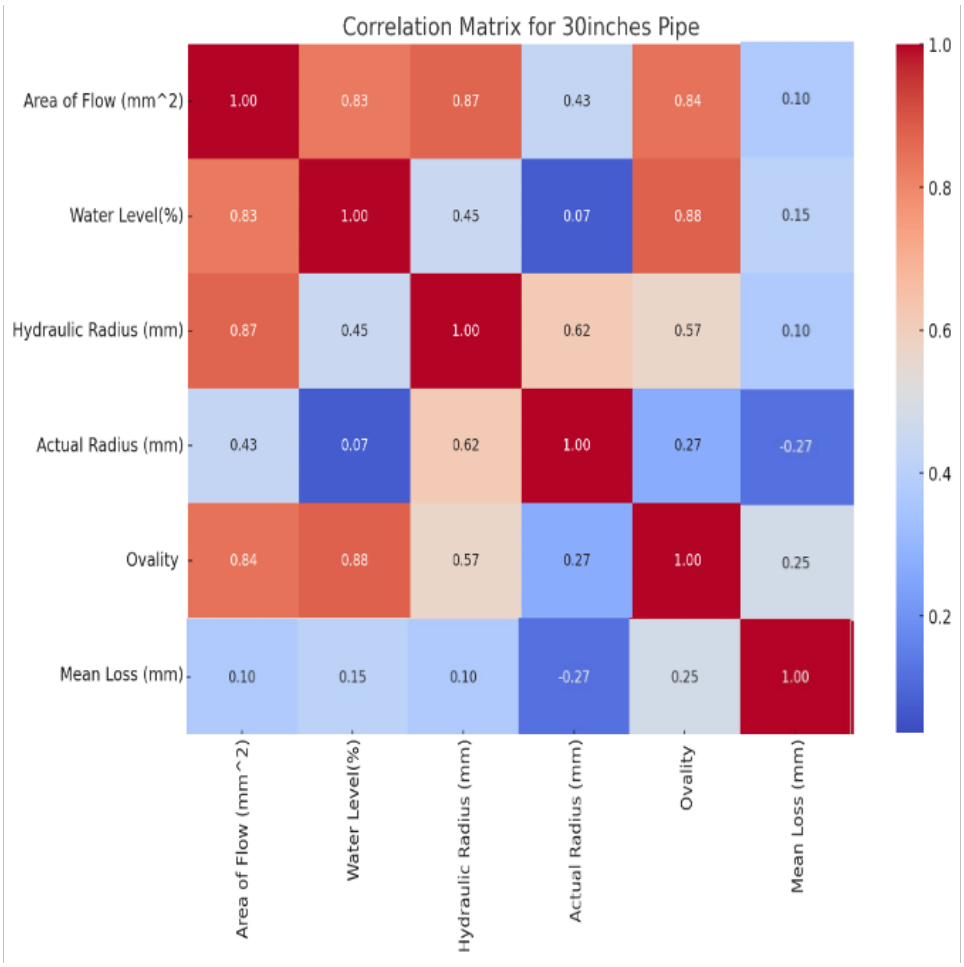
Correlation Matrix for 30inches Pipe
Area of Flow (mm^2)
Water Level(%)
Hydraulic Radius (mm)
Actual Radius (mm)
Ovality
Mean Loss (mm)
1.00 0.83 0.87 0.43 0.84 0.10
0.83 1.00 0.45 0.07 0.88 0.15
0.87 0.45 1.00 0.62 0.57 0.10
0.43 0.07 0.62 1.00 0.27 -0.27
0.84 0.88 0.57 0.27 1.00 0.25
0.10 0.15 0.10 -0.27 0.25 1.00
1.0
0.8
0.6
0.4
0.2

(a)

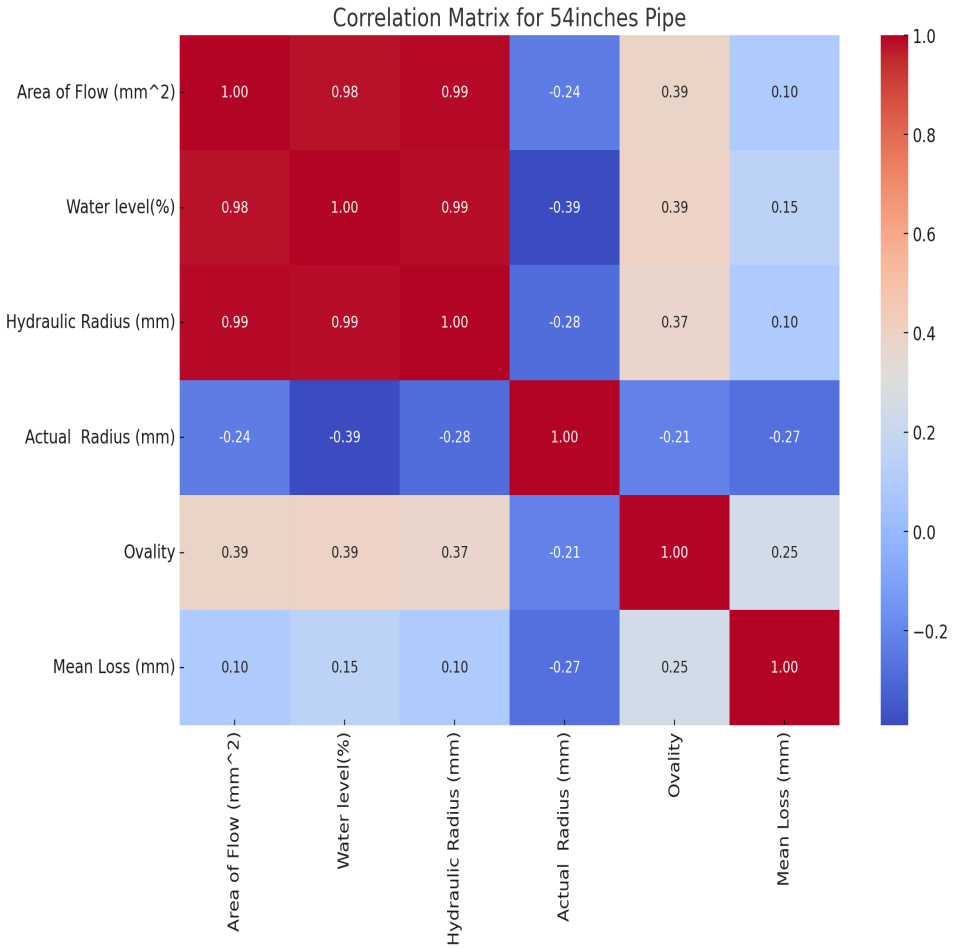
Correlation Matrix for 54inches Pipe
Area of Flow (mm^2)
Water level(%)
Hydraulic Radius (mm)
Actual Radius (mm)
Ovality
Mean Loss (mm)
1.00 0.98 0.99 -0.24 0.39 0.10
0.98 1.00 0.99 -0.39 0.39 0.15
0.99 0.99 1.00 -0.28 0.37 0.10
-0.24 -0.39 -0.28 1.00 -0.21 -0.27
0.39 0.39 0.37 -0.21 1.00 0.25
0.10 0.15 0.10 -0.27 0.25 1.00
Area of Flow (mm^2)
Water level(%)
Hydraulic Radius (mm)
Actual Radius (mm)
Ovality
Mean Loss (mm)
1.0
0.8
0.6
0.4
0.2
0.0
−0.2

(b)

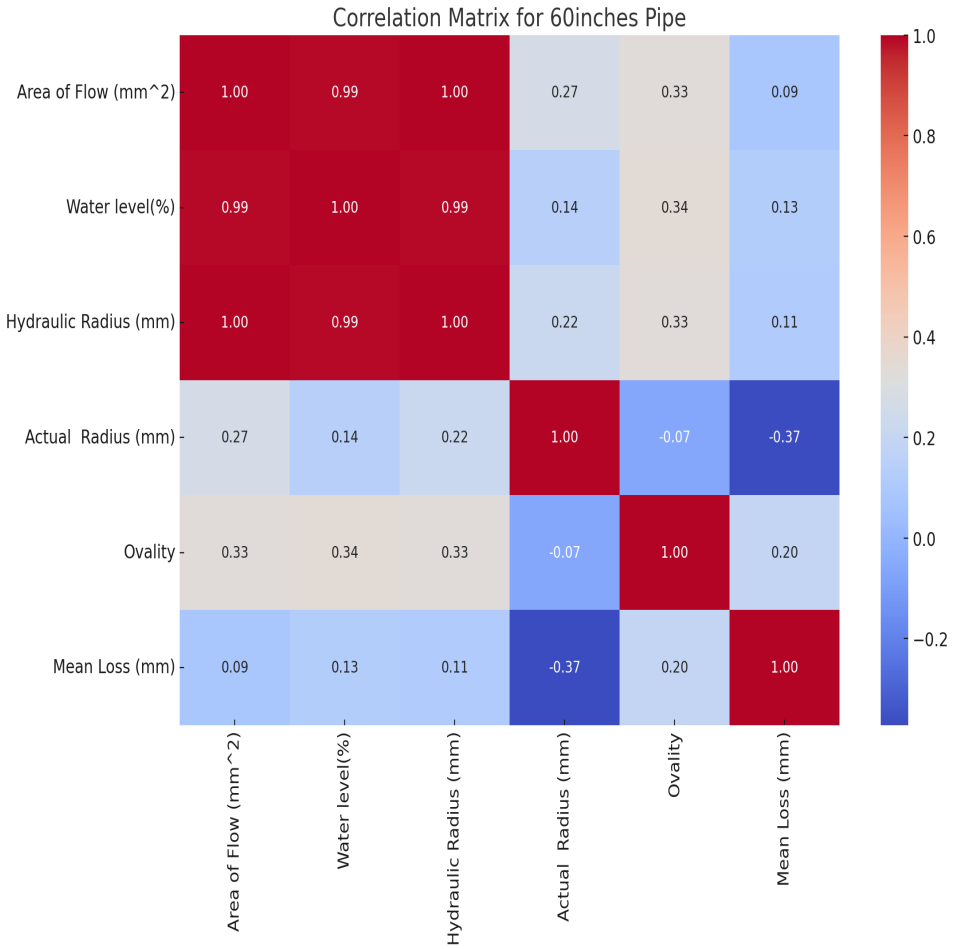

(c)

Figure 70. Heatmaps Showing the Correlation Matrices for (a) 30-inch data, (b) 54-inch data, (c) 60-inch data

From the heatmaps (correlation Matrices) of Figure 70, it is certified that the Mean loss does not have underlying correlation with the hydraulic parameters.

4.7.2 Multi Variable Regression Model

In order to simplify the equation for the fitted regression lines, a unique letter is assigned to different parameters as follows. Area of Flow (mm^2): (*A*), Actual Radius (mm): (*B*), Hydraulic Radius (mm): (*C*), Ovality: (*D*), Water Level (%): (*E*).

Here, for each diameter, different permutations of three-feature combinations are created; then, Multi variable regression is performed on these combinations. Finally, the best three combinations with the lowest MSE/RMSE for each diameter are provided Table 9-Table 11.

Table 9-Table 11 show the results from the Multi variable regression for 30-, 54-, and 60-inch data, respectively. In addition, calculated Mean Squared Error (MSE) and Root Mean Squared Error (RMSE) for each feature are provided. These summaries provide comprehensive insights into which sets of variables most effectively predict "Mean Loss (mm)" for different pipe diameters, as indicated by the lowest MSE/RMSE values.

In addition, a unique combination is selected based on the least correlated parameters obtained from the heatmaps (Figure 70). In order to have a clear comparison between different data sets, the result from the selected combination is shown as highlighted rows in Table 9-Table 11. The results show the combination "*Water Level* (%): (*E*), *Actual Radius* (mm): (*B*), *Hydraulic Radius* (mm): (*C*)" can predict the Mean Loss with 3.84, 1.5, and 1.23 *RMSE* for 30-, 54-, and 60-inch data respectively.

Table 9. Results of Multi Variable Regression Model on 30-inches Data

30 Inches Pipe				
Rank	**Variables**	**Regression Equation**	**MSE**	**RMSE**
1	Water Level (%)(E), Actual Radius (mm) (B), Ovality (D)	y = 141.56 E - 0.2067 B + 174.571 D + 60.97	12.6	3.55
2	Area of Flow(mm^2)(A), Hydraulic Radius (mm) (C), Actual Radius (mm) (B)	y = 0.00218 A - 0.9894 C - 0.2264 B + 122.046	13	3.6
3	Area of Flow (mm^2) (A), Hydraulic Radius (mm)(C), Ovality (D)	y = $1.9122 * 10^{-3}$ A - 0.09667 C + 113.521 D + 44.89	13.1	3.62
4	Water level (%) (E), Hydraulic Radius (mm) (C), Actual Radius (mm) (B)	y = 181.22 E + 0.07 C - 0.18 B + 38.37	14.8	3.84

Table 9 shows the best three-combination to predict the Mean Loss of 30-inch pipe is "Water Level (%): (*E*), *Actual Radius* (mm): (*B*), and *Ovality* (*D*)" with MSE and RMSE of 12.61 and 3.55 respectively.

Table 10. Results of Multi Variable Regression Model on 54-inches Data

54 Inches Pipe				
Rank	**Variables**	**Regression Equation**	**MSE**	**RMSE**
1	Water Level (%) (E), Hydraulic Radius (mm) (C), Ovality (D)	y = 59.79 E - 0.1014 C + 11.525 D + 2.65	2.2	1.48
2	Area of Flow (mm^2) (A), Hydraulic Radius (C) , Actual Radius (mm) (B)	y = - $2.4519 * 10^{-5}$ A + 44.53 C - 13.449 B + 2.236	2.24	1.49
3	Water Level (%) (E), Hydraulic Radius (mm) (C), Actual Radius (mm) (B)	y = 60.40 E - $9.92 * 10^{-2}$C - $5.698 * 10^{-3}$ B + 5.98	2.26	1.5

Table 10 shows the best three-combination to predict the Mean Loss of 54-inch pipe is "*Water Level* (%): (*E*), *Hydraulic Radius* (mm): (*C*), and *Ovality* (*D*)" with *MSE* and *RMSE* of 2.2 and 1.48 respectively.

Table 11. Results of Multi Variable Regression Model on 60-inches Data

60 Inches Pipe				
Rank	**Variables**	**Regression Equation**	**MSE**	**RMSE**
1	Water level (%) (E), Hydraulic Radius (mm) (C), Actual Radius (mm) (B)	$y = -58.204\,E + 0.086\,C - 0.0864\,B + 77.63$	1.51	1.23
2	Area of Flow (mm^2)(A), Water Level (%) (E), Actual Radius (mm) (B)	$y = 3.1205 * 10^{-5}\,A - 73.138\,E - 0.1214\,B + 112.62$	1.52	1.23
3	Hydraulic Radius (mm) (C), Actual Radius (mm) (B), Ovality (D)	$y = 6.578 * 10^{-3}\,C - 6.093 * 10^{-2}\,B + 7.97\,D + 52.1523$	1.53	1.236

Table 11 shows the best three-combination to predict the Mean Loss of 60-inch pipe is "Water Level (%): (*E*), Actual Radius (mm): (*B*), Hydraulic Radius (mm): (*C*)" with MSE and RMSE of 1.51 and 1.23 respectively.

4.7.3 Polynomial Regression Model

The polynomial regression analysis (of degree 2) for three datasets are performed as follows:

1-polynomial (degree of 2) features for the selected independent variables,

2- Split the data into training and testing sets; 12,946 samples in the training set and 3,237 samples in the testing set.

3-Train a polynomial regression model using the training set.

4-Predict the target variable "Mean Loss (mm)" using the testing set.

5-Evaluate the model's performance by calculating the MSE, RMSE, and R^2 values. The following tables summarize the evaluation metrics.

Here, for each diameter different permutations of three-feature combinations are created; then, Polynomial regression (degree of 2) is performed on these combinations. Finally, the best three combinations with the lowest MSE/RMSE for each diameter are provided in Table 12. It shows the results from the Polynomial regression for 30-, 54-, and 60-inch data respectively. In addition, calculated Mean Squared Error (*MSE*) and Root Mean Squared Error (*RMSE*) and R^2 for the best combination.

Table 12. Results of Polynomial Regression Model Showing the Best Combination for all Data Sets

Diameter	Variables	MSE	RMSE	R-squared
30 inches	Water Level (%), Actual Radius (mm), Ovality	16.517087	4.064122	0.856553
54 inches	Water Level (%), Hydraulic Radius (mm), Ovality	2.136504	1.461678	0.216745
60 inches	Water Level (%), Hydraulic Radius (mm), Actual Radius (mm)	1.096849	1.047306	0.39764

Table 12 show the best three-combination to predict the Mean Loss of all pipe diameters. For instance, for 30 inches data, the model has an R^2 value of 0.8566, indicating that approximately 85.66% of the variance in the "*Mean Loss* (mm)" can be explained by the model. In addition, the unique combination which is selected based on the least correlated parameters obtained from the heatmaps (Figure 69). In order to have a clear comparison between different data sets, the result from the selected combination is shown in Table 13.

Table 13. Results of Polynomial Regression Model for the Same Combination for all Data Sets

Diameter	Variables	MSE	RMSE	R-squared
30 inches	Water Level (%), Hydraulic Radius (mm), Actual Radius (mm)	21.316612	4.616992	0.81487
54 inches	Water Level (%), Hydraulic Radius (mm), Actual Radius (mm)	2.144836	1.464526	0.21369
60 inches	Water Level (%), Hydraulic Radius (mm), Actual Radius (mm)	1.096849	1.047306	0.3976

Table 13 shows the combination "*Water Level* (%), *Actual Radius* (mm), *Hydraulic Radius* (mm)" can predict the Mean Loss with R^2 of 0.81, 0.21, and 0.39 for 30-, 54-, and 60-inch data respectively. From the results of Polynomial regression model, it is concluded that Polynomial regression model does not improve the accuracy of the predictions comparing to Multi variable regression model. Table 13 shows the combination "*Water Level* (%), *Actual Radius* (mm), *Hydraulic Radius* (mm)" can predict the Mean Loss with *RMSE* of 4.6, 1.4, and 1.04 for 30-, 54-, and 60-inch data respectively. Meanwhile for 60-inches data the predictions are improved by 15%.

4.8 Results of BN Framework

The datasets for each Pipeline # and the corresponding Mean Loss (mm) is selected for implementation of BN. based on the literature two different case studies are investigated for the BN. In the following two cases are discussed:

4.8.1 Weibull Distribution

In this case study, the likelihood is calculated from the data collected from 22 RCSSPs from (Abuhishmeh, 2019). Table 14 shows the parameters of Weibull distribution. In this case, Normal distribution is fitted to all the parameters of Weibull for all 22 sections of RCSSPs. In addition, the criteria for fitted values are provided in Table 14 as P-Values. Here, Kolmogorov–Smirnov goodness of fit test is used.

Table 14. Calculating the Prior for Weibull Distribution

Pipeline #	Mean_Scale	COV_Scale	P_Value_Scale	Mean_Shape	COV_Shape	P_Value_Shape
1	0.00535606	0.526860308	2.39E-21	1.677810967	0.332734052	1.03E-19
2	0.00385281	0.371089559	0.001656391	1.56109651	0.223099482	0.000733798
3	0.00550442	0.495079539	5.04E-08	1.844537336	0.388490471	5.23E-13
4	0.00497496	0.299922568	0.031650551	1.743399339	0.255393018	2.67E-06
5	0.005636777	0.382010287	0.000434422	1.986836374	0.341139132	7.55E-10
6	0.007270541	0.255243771	0.140404373	3.355205732	0.331941452	0.000283648
7	0.006556424	0.220441872	0.437844366	2.49647212	0.248423552	2.22E-05
8	0.009318599	0.397925944	9.01E-10	1.466240445	0.259603364	2.00E-05
9	0.006695864	0.939791626	1.48E-27	1.243825721	0.22184698	3.22E-08
10	0.008387825	0.414548835	0.00092892	1.254278234	0.232112111	0.000332063
11	0.010983015	0.510195	3.19E-10	1.721002941	0.391294612	2.72E-16
12	0.00991498	0.552258789	5.74E-14	1.714950565	0.375396052	1.38E-15
13	0.016890779	1.80341928	2.59E-12	1.833538053	1.143871797	2.72E-12
14	0.011985396	0.196996297	1.46E-09	1.435461203	0.242125149	4.69E-17
15	0.009837751	0.216464961	0.584162772	2.179418294	0.227888588	0.307359576
16	0.007892338	0.222791003	0.137336403	2.12066497	0.278418057	0.038861297
17	0.008421407	0.67560432	3.99E-26	1.869347247	0.344276018	5.12E-17
18	0.005835214	0.282222914	0.002058279	2.020560525	0.31323829	3.41E-10
19	0.006652145	0.402920904	1.27E-13	2.061325766	0.296294529	1.54E-08
20	0.009142053	0.394999759	0.177176103	1.890516452	0.311638546	2.15E-08
21	0.006852151	0.486719766	0.063893653	1.480833713	0.260062812	0.001053782
22	0.009427412	1.072323596	1.40E-35	1.606990923	0.292707623	9.89E-16
Mean Values	**0.008063133**	**0.505446859**		**1.843832429**	**0.33236344**	

According to Table 14 the prior is set as Weibull distribution with each parameter as following

Shape = Normal (1.8438,0.332)

Scale = Normal (0.00806,0.505)

Posterior distribution is calculated using MCMC-MH algorithm with the following properties:

Iteration: 4000 with burn-in 25%.

Figure 71 shows the trace plots for the first pipeline # of 30-, 54-, and 60-inch pipes using 3 chains. It shows that 3 chains converge and mix well, indicating a good sampling of the posterior distribution. The trace plots indicate the progression of the MCMC-MH samples over iterations for both the shape and scale parameters. All the trace plots for the rest of pipeline # are provided in *Appendix B* with 1 chain.

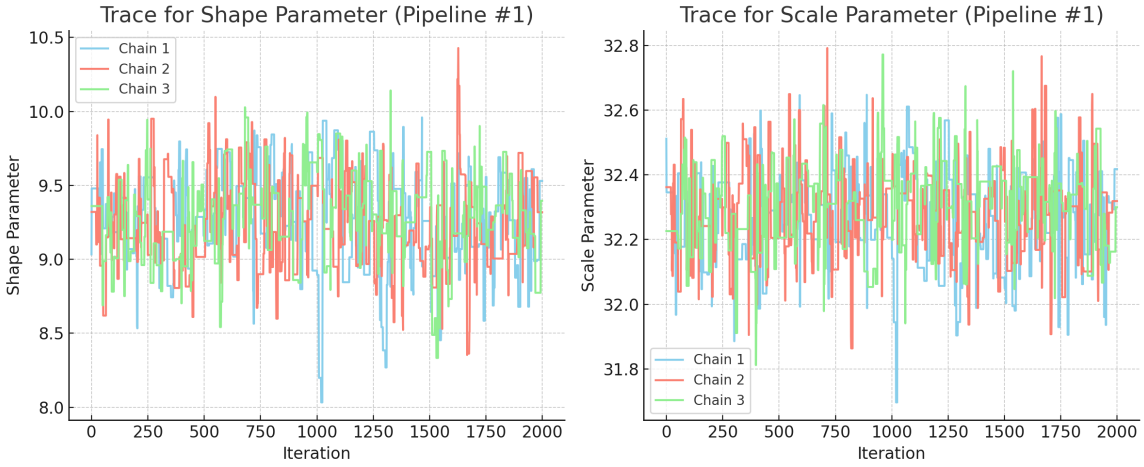

(a)

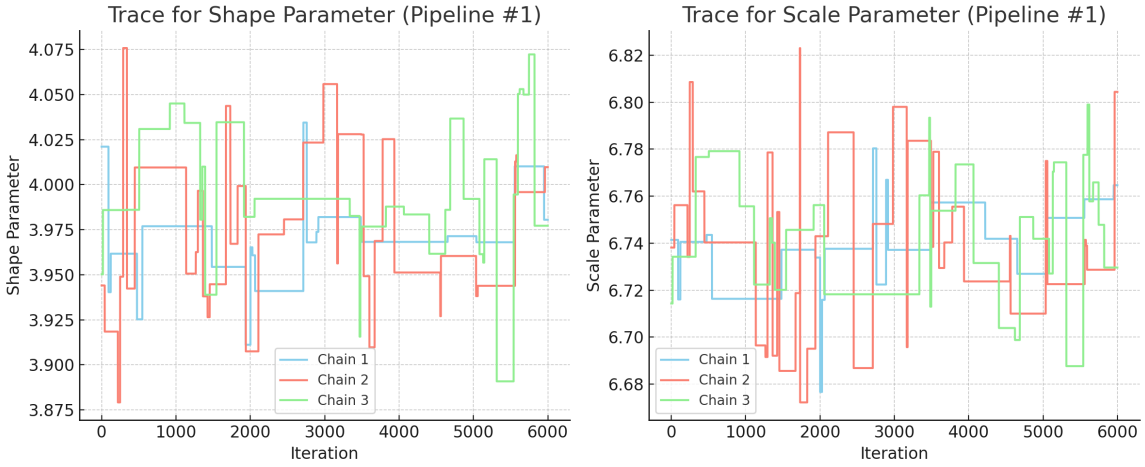

(b)

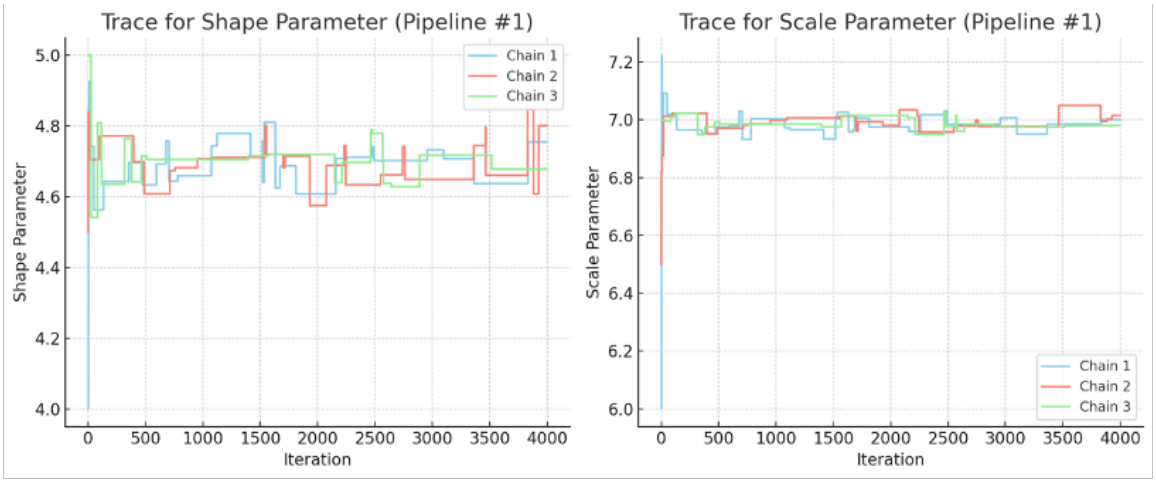

(c)

Figure 71. Trace Plots for Updated Posterior for the Weibull parameters Using BN for (a)30-inches, (b) 54-inches, (c) 60-inches.

Figure 72 shows the histograms for the posterior distributions of the of the shape and scale parameters. All the histograms for the rest of pipeline # are provided in *Appendix B*.

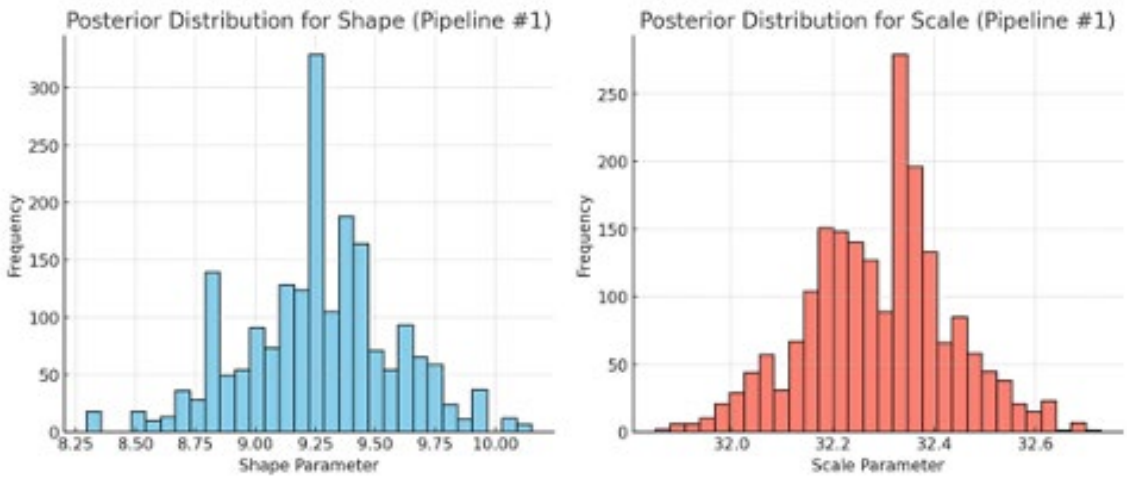

(a)

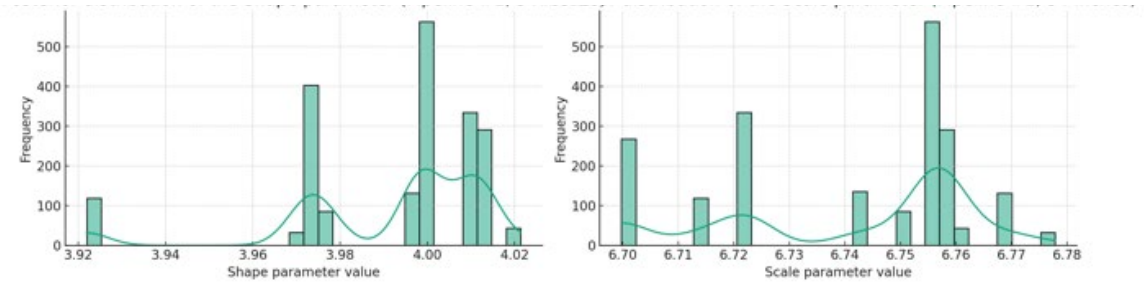

(b)

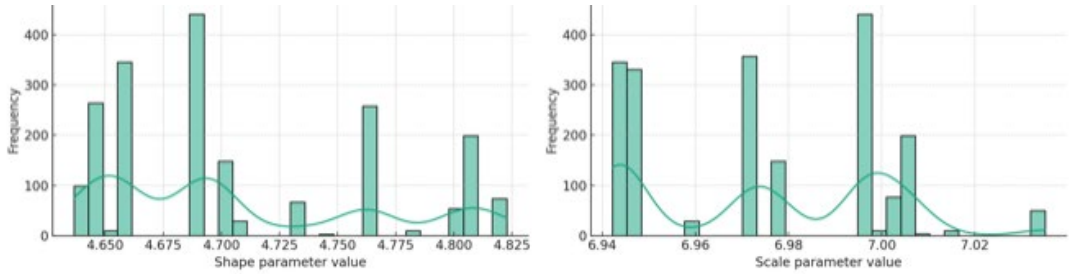

(c)

Figure 72. Histograms of Posterior Weibull Parameters Using BN for (a)30-inches, (b) 54-inches, (c) 60-inches.

Table 15-Table 17 show the results of the BN for posterior Weibull parameters for 30-, 54-, and 60-inch data respectively.

Table 15. Summary of Posterior Weibull Values for 30-inches RCSSPs

Pipeline #	Posterior Shape	Posterior Scale
1	9.232731811	32.28485741
2	5.105897914	27.76217513
3	3.811839918	29.03092073
4	1.088014016	11.39237178
5	3.709175695	22.38500831
6	2.547240544	14.12685882
7	2.519292533	13.4198928
8	3.030783052	30.18489555
9	1.670518829	14.36270794
10	4.912510855	22.71727968
11	1.857702217	12.95668034
12	2.625672791	13.24409074
13	2.587921302	11.64018511
14	2.958916916	22.07755947
15	5.439845556	34.68896217

Table 16.Summary of Posterior Weibull Values for 54-inches RCSSPs

Pipeline #	Posterior Shape	Posterior Scale
1	3.981791267	6.74696685
2	3.906449187	7.256307802
3	3.53363567	8.013851651
4	3.811753712	6.879845718
5	4.751915584	7.930668652

Table 17. Summary of Posterior Weibull Values for 60-inches RCSSPs

Pipeline #	Posterior Shape	Posterior Scale
1	4.727087147	6.983164055
2	4.288957182	7.096861803
3	4.831012552	7.549541175
4	5.419597655	7.674908509
5	3.718709534	7.475095803

These visualizations aid in understanding the behavior of the MCMC sampling and the resulting posterior distributions for the parameters of Weibull.

4.8.1.1 RSL Comparisons for Update Weibull Distribution

RSL values of (from BN) are determined using MCS method (discussed in subsection 3.4.10.3). Figure 73 shows the probability of failure plots using probability of exceedance method and MCS (using Pomeroy Equation 23) similar to the comparison shown in Figure 62-a. Figure 73 shows the comparison of the probability of exceedance curves using the MCS for 30-, 54-, and 60-inches data. *Appendix C* provides probability of exceedance plots for the remaining pipelines of for 30-, 54-, and 60-inches data.

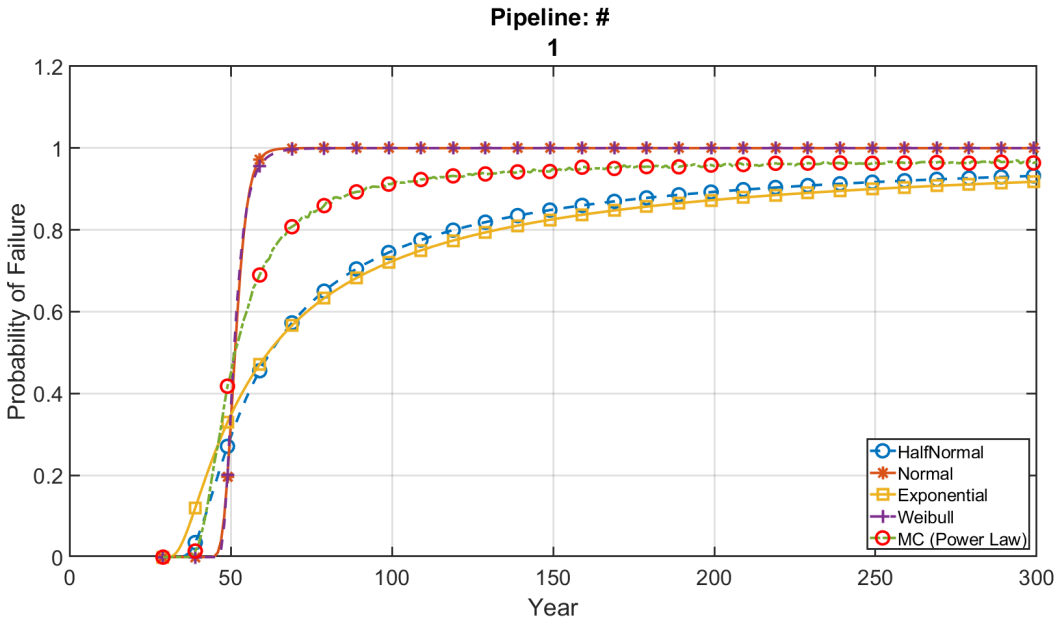
Pipeline: #
1
Probability of Failure
Year
HalfNormal
Normal
Exponential
Weibull
MC (Power Law)

(a)

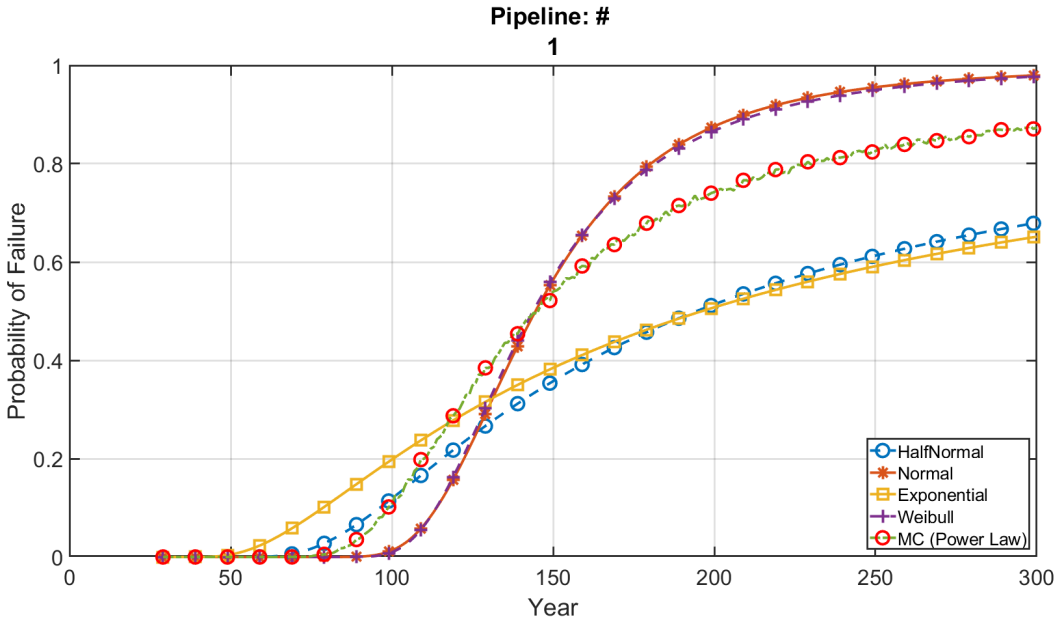
Pipeline: #
1
Probability of Failure
Year
HalfNormal
Normal
Exponential
Weibull
MC (Power Law)

(b)

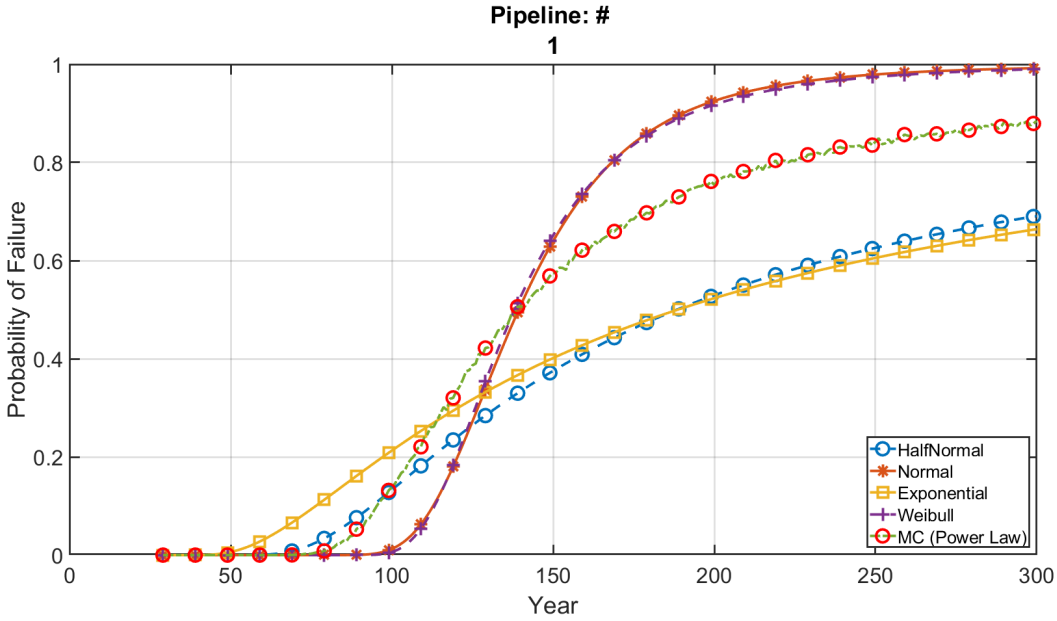

(c)

Figure 73. RSL of Updated Values using MCS for (a)30-inches, (b) 54-inches, (c) 60-inches RCSSPs

Table 18-Table 20 show the comparison between the estimated RSL for 30-, 54-, and 60-inches data respectively.

Table 18. Comparison of RSL Estimation Before and After BN for 30-inches data

30 inches		
Pipeline #	**Observed Data , Pf=0.1**	**Updated Data, Pf=0.1**
1	14	42
2	16	44
3	14	42
4	18	46
5	19	47
6	34	62
7	34	62
8	14	42
9	26	54
10	19	47
11	35	63
12	36	64
13	39	67
14	20	48
15	13	41
Prior	300	

Table 19. Comparison of RSL Estimation Before and After BN for 54-inches data

54 inches		
Pipeline #	**Observed Data , Pf=0.1**	**Updated Data, Pf=0.1**
1	70	99
2	64	94
3	59	88
4	69	98
5	59	87
Prior	300	

Table 20. Comparison of RSL Estimation Before and After BN for 60-inches data

60 inches		
Pipeline #	**Observed Data , Pf=0.1**	**Updated Data, Pf=0.1**
1	67	95
2	65	96
3	63	90
4	60	89
5	63	92
Prior	300	

It is concluded from the estimated RSL of the BN output that results are reasonable and realistic compared to data before BN (i.e., observed data from inspection). This can highlight the fact that BN accommodates the uncertainties of the data.

4.8.2 Gamma Distribution

According Table 3, the prior is set as Gamma distribution estimated from the previous study (Mahmoodian & Alani, 2014) using MLE methods with parameters as follows:

Shape = Normal (4.78,0.1)

Scale = Normal (0.425,0.1)

The scale is calculated as 0.17*t=0.17*28=4.78. The shape and scale values were deterministic, so the constant vitiation of 0.1 is used.

Posterior distribution is calculated using MCMC-MH algorithm with the following properties:

Iteration: 4000 with burn-in 25%.

Figure 74 shows the trace plots for the first pipeline # of 30-, 54-, and 60-inches pipes using 3 chains for 30 inches and 1 chain for 54- and 60-inch pipes. It shows that 3 chains converge and mix well, indicating a good sampling of the posterior distribution. All the trace plots for the rest of pipeline # are provided in *Appendix B* with 1 chain.

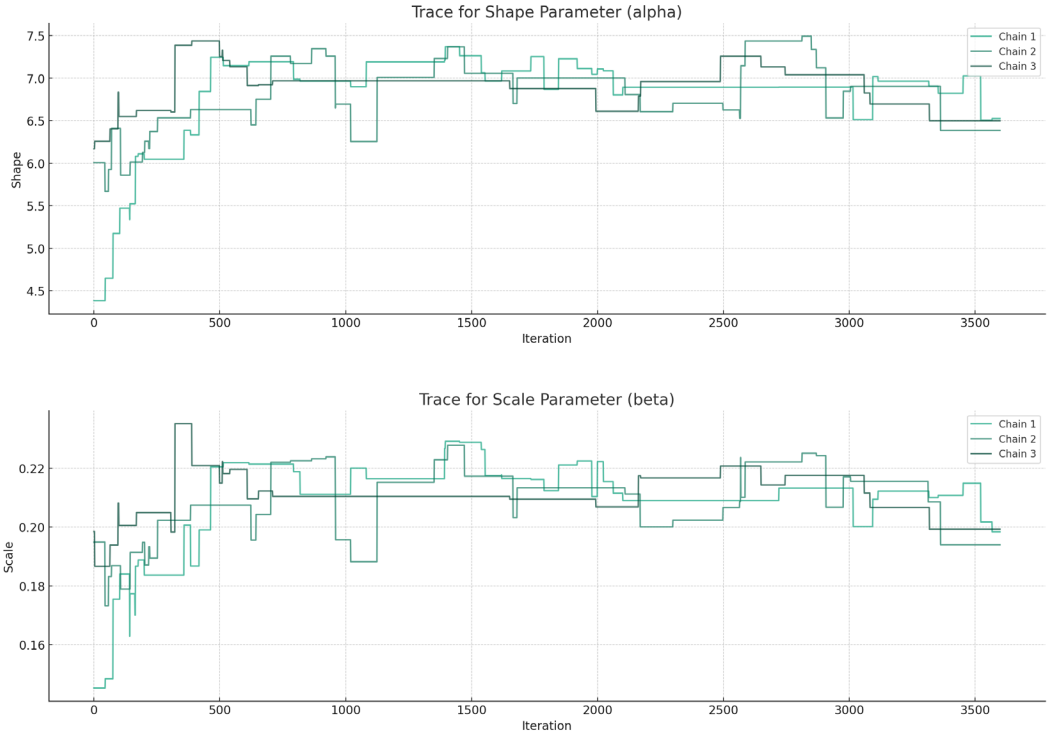

(a)

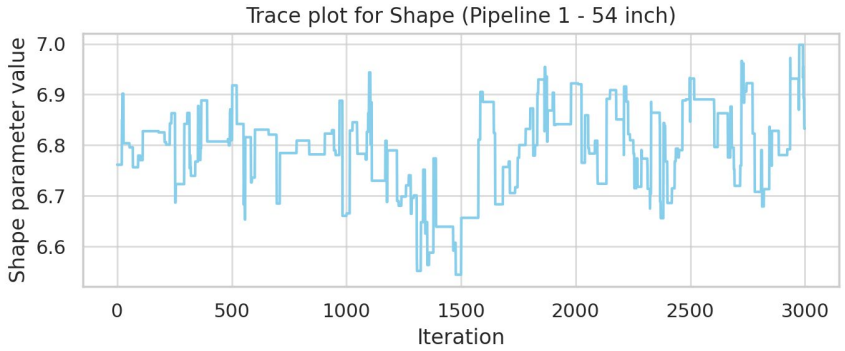

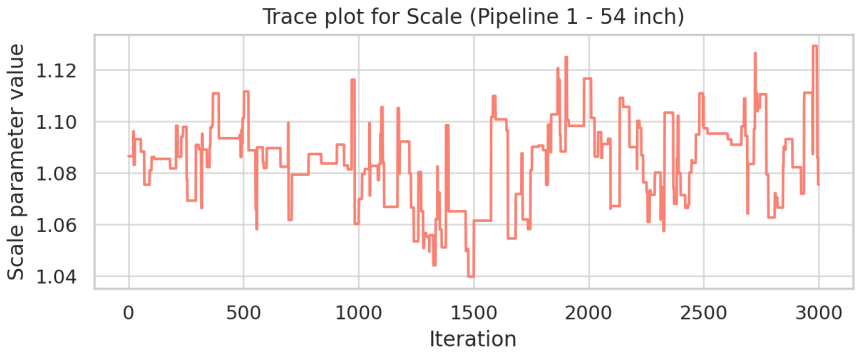

(b)

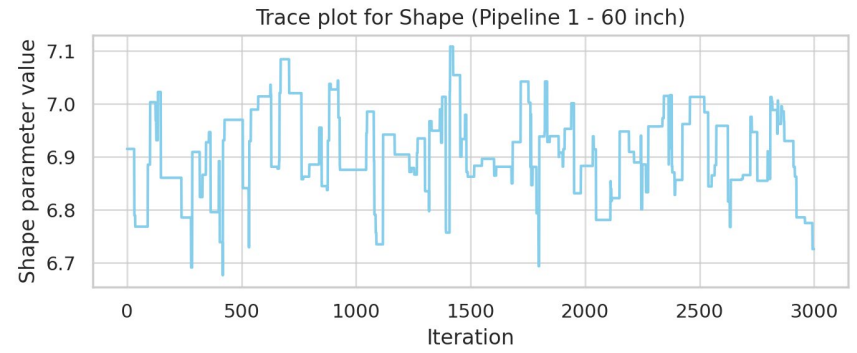

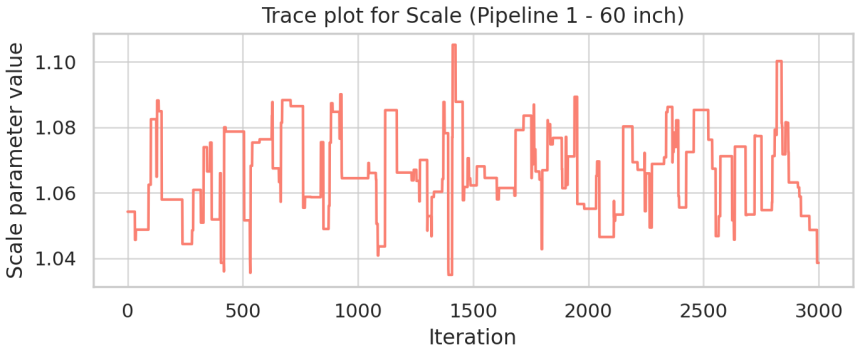

(c)

Figure 74. Trace Plots for Updated Posterior for the Gamma parameters Using BN for (a)30-inches, (b) 54-inches, (c) 60-inches.

Figure 75 shows the histograms for the posterior distributions of the of the shape and scale parameters of Gamma. All the histograms for the rest of pipeline # are provided in *Appendix B*.

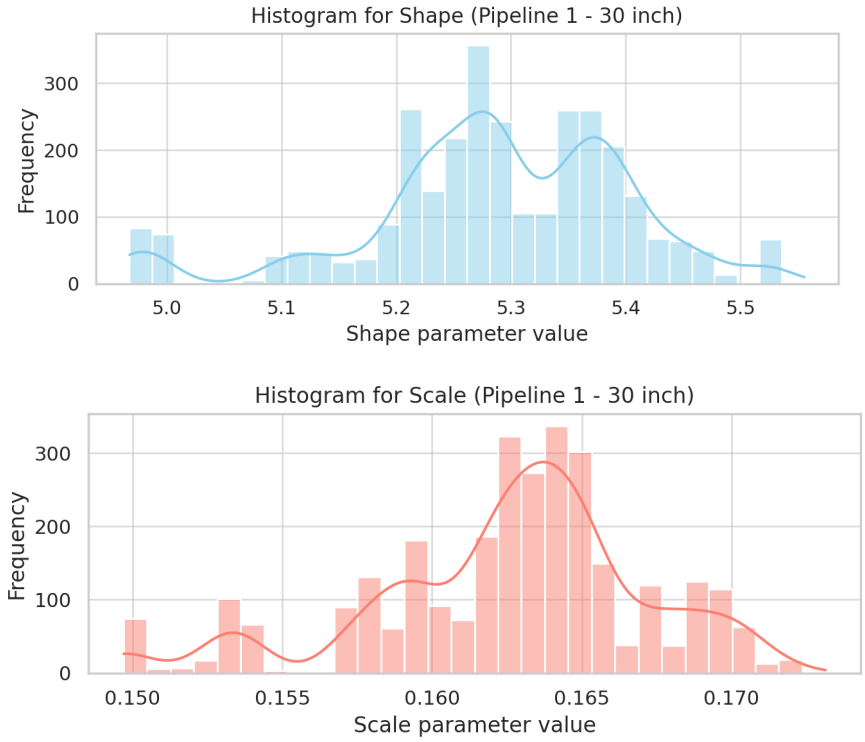
Histogram for Shape (Pipeline 1 - 30 inch)
Frequency
0
100
200
300
5.0
5.1
5.2
5.3
5.4
5.5
Shape parameter value
Histogram for Scale (Pipeline 1 - 30 inch)
Frequency
0
100
200
300
0.150
0.155
0.160
0.165
0.170
Scale parameter value

(a)

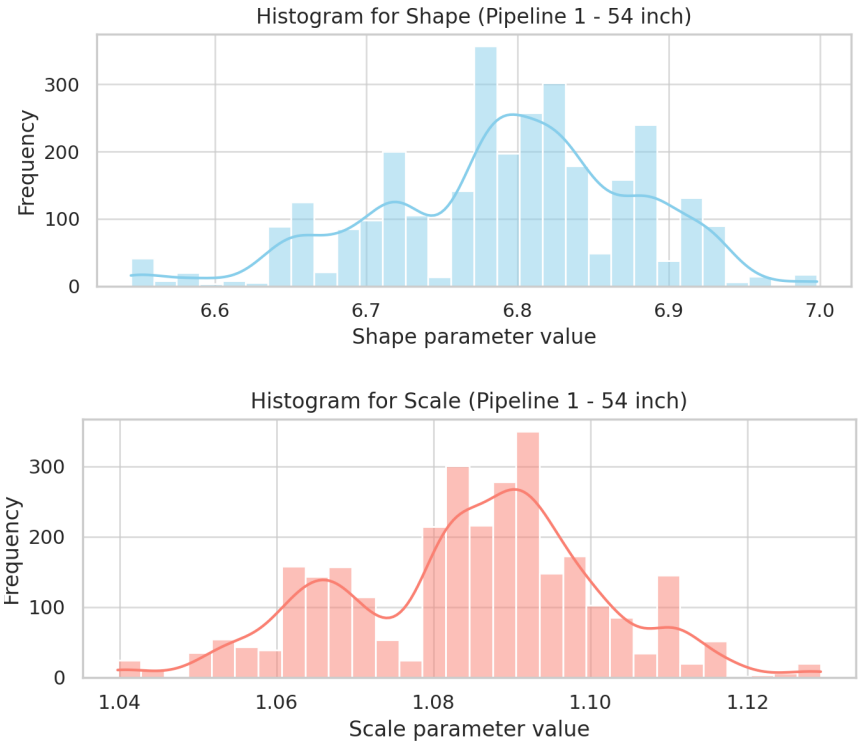
Histogram for Shape (Pipeline 1 - 54 inch)
Frequency
0
100
200
300
6.6
6.7
6.8
6.9
7.0
Shape parameter value
Histogram for Scale (Pipeline 1 - 54 inch)
Frequency
0
100
200
300
1.04
1.06
1.08
1.10
1.12
Scale parameter value

(b)

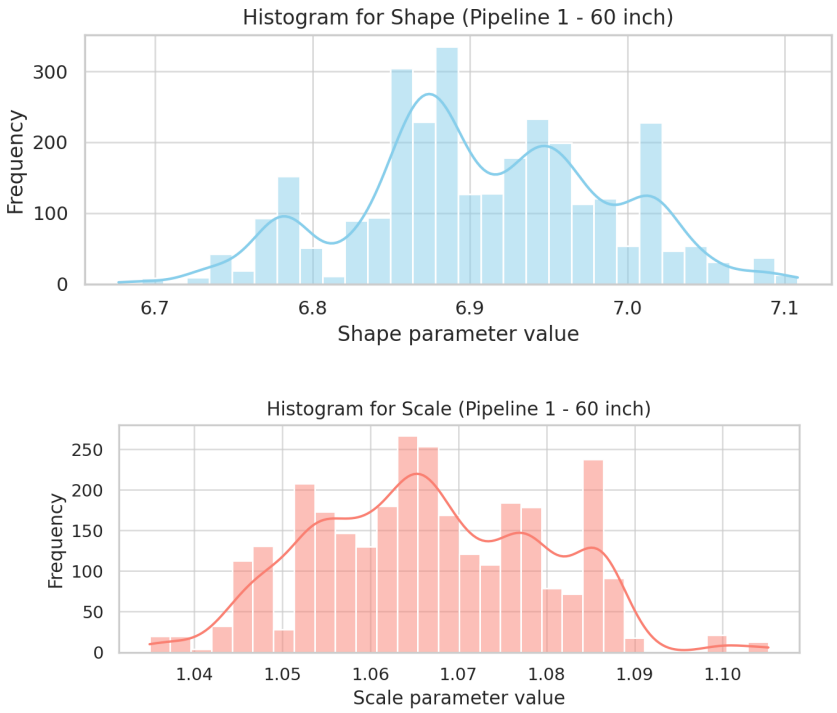

(C)

Figure 75. Histograms of Posterior Gamma Parameters Using BN for (a)30-inches, (b) 54-inches, (c) 60-inches.

Table 21-Table 23 show the results of the BN for posterior Gamma parameters for 30-, 54-, and 60-inch data respectively.

Table 21. Summary of Posterior Gamma Values for 30-inches RCSSPs

Pipeline #	Posterior Shape Mean	Posterior Scale Mean
1	5.313247709	0.163004697
2	5.883020264	0.219509266
3	5.357924392	0.17074237
4	4.945672467	0.208912113
5	5.221588584	0.229218918
6	5.247015927	0.402087269
7	4.82047434	0.378210333
8	5.562570148	0.181042525
9	4.523174435	0.269937055
10	5.157413364	0.220659049
11	4.422648003	0.35617798
12	5.128919797	0.421844733
13	5.013943495	0.453854988
14	5.346184351	0.250716326
15	5.903112497	0.173176496

Table 22. Summary of Posterior Gamma Values for 54-inches RCSSPs

Pipeline #	Posterior Shape Mean	Posterior Scale Mean
1	6.777538976	1.082588499
2	6.382523104	0.950214885
3	6.011790401	0.822110744
4	6.912801077	1.098740546
5	6.815187807	0.93042131

Table 23. Summary of Posterior Gamma Values for 60-inches RCSSPs

Pipeline #	Posterior Shape Mean	Posterior Scale Mean
1	6.902919028	1.06693709
2	6.149695007	0.930582012
3	6.386756412	0.917415599
4	6.239010447	0.868314513
5	7.4865035	1.080928817

4.8.2.1 RSL Comparisons for Update Gamma Distribution

RSL values are determined using MCS method (discussed in subsection 3.4.8.3). Figure 76 shows the comparison of the probability of exceedance results using the MCS for 30-, 54-, and 60-inch data.

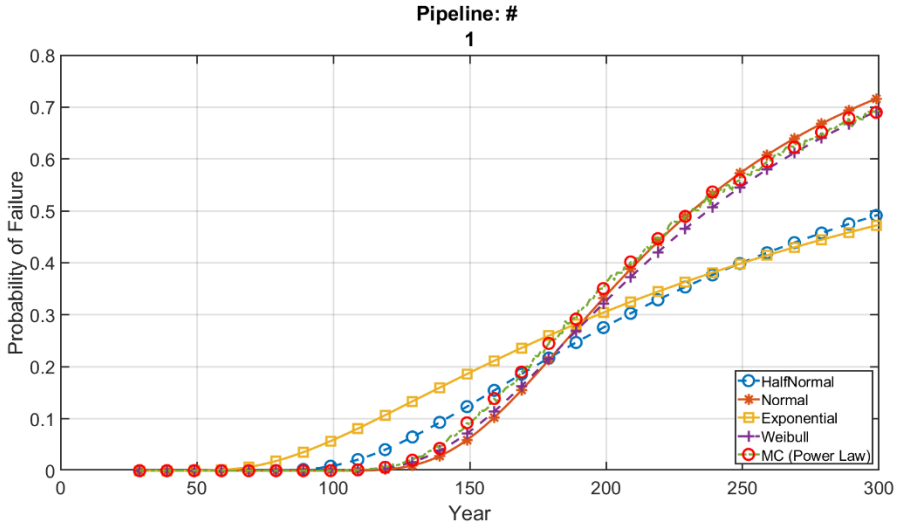

(a)

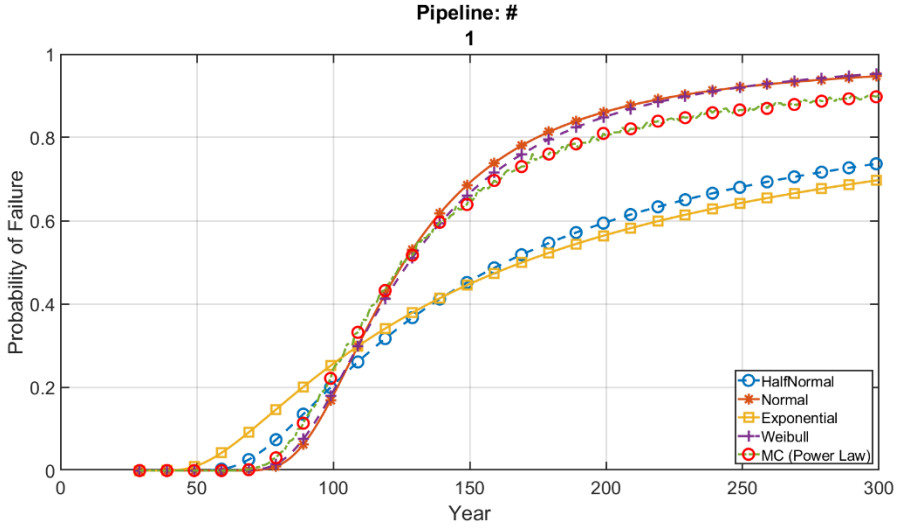

(b)

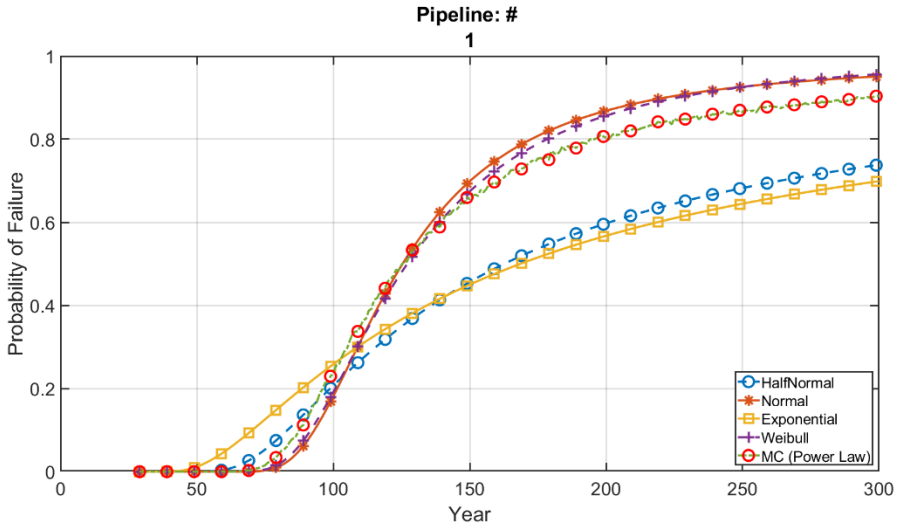

(c)

Figure 76. RSL of Updated Values using MCS for (a)30-inches, (b) 54-inches, (c) 60-inches RCSSPs

Table 24-Table 26 show the comparison between the estimated RSL using the probability of exceedance results (MCS) for 30-, 54-, and 60-inch data.

Table 24. Comparison of RSL Estimation Before and After BN for 30-inches data

30 inches		
Pipeline #	**Observed Data , Pf=0.1**	**Updated Data, Pf=0.1**
1	42	123
2	44	84
3	42	115
4	46	102
5	47	92
6	62	51
7	62	61
8	42	107
9	54	91
10	47	96
11	63	69
12	64	50
13	67	49
14	48	82
15	41	105
Prior	212	

Table 25. Comparison of RSL Estimation Before and After BN for 54-inches data

54 inches		
Pipeline #	**Observed Data , Pf=0.1**	**Updated Data, Pf=0.1**
1	70	59
2	64	72
3	59	87
4	69	57
5	59	67
Prior	212	

Table 26. Comparison of RSL Estimation Before and After BN for 60-inches data

60 inches		
Pipeline #	**Observed Data , Pf=0.1**	**Updated Data, Pf=0.1**
1	67	60
2	65	76
3	63	73
4	60	81
5	63	53
Prior	212	

In addition, the consistency of the estimated RSL is compared by constructing the confidence interval of the mean predicted RSL in three cases: observed data, Updated Weibull, Updated Gamma (with 95% confidence using Equation 30). Table 27-Table 29 compares the confidence intervals of RSL using *MCS* for 30-, 54-, and 60-inch data.

Table 27. Comparison of Confidence Intervals of RSL Values for 30-inch Data

30 Inches data			
Data	**Mean**	**Lower Bound**	**Upper Bound**
Observed	24.14285714	18.68945308	29.5962612
Updated Gamma	76	62.97069746	89.02930254
Updated Weibull	24.64285714	20.2014985	29.08421579

Table 28. Comparison of Confidence Intervals of RSL Values for 54-inch Data

54 Inches data			
Data	**Mean**	**Lower Bound**	**Upper Bound**
Observed	64.2	57.66502435	70.73497565
Updated Gamma	63.2	49.55863831	76.84136169
Updated Weibull	62.4	56.40647875	68.39352125

Table 29. Comparison of Confidence Intervals of RSL Values for 60-inch Data

60 Inches data			
Data	**Mean**	**Lower Bound**	**Upper Bound**
Observed	24.14285714	18.68945308	29.5962612
Updated Gamma	76	62.97069746	89.02930254
Updated Weibull	24.64285714	20.2014985	29.08421579

Figure 77 shows the boxplots of the estimated RSL for each pipeline diameter. the difference of lower bound and upper bound for updated Weibull values are less than *observed data* which led to more consistent results. However, updated Gamma values led to higher RSL.

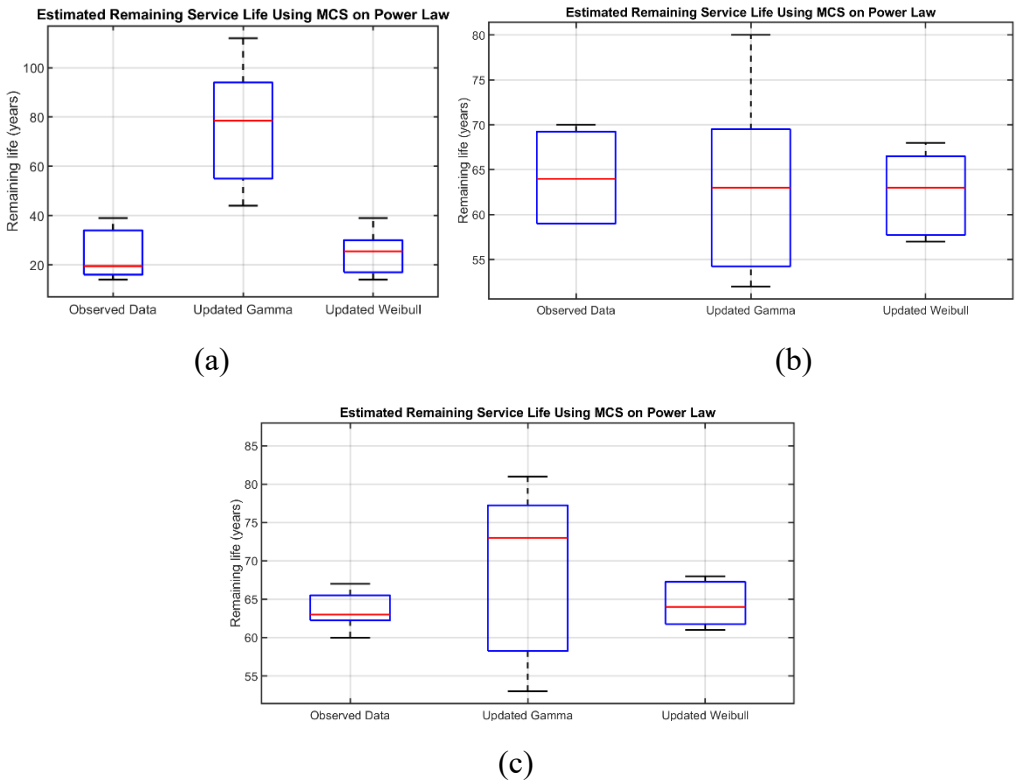

Figure 77. Box plots for Comparing the Confidence Intervals of RSL Values for (a) 30-inch data, (b) 54-inch data, (c) 60-inch data

CHAPTER 5. CONCLUSION AND FUTURE DEVELOPMENTS

5.1 Conclusion and Summary

The methodology is performed with minimal user-interference, using the proposed algorithm in MATLAB. Some Pipeline inspection companies have their own developed software that is proprietary and therefore, to the best of our knowledge details are not readily available to the scientific community. The present study proposes an automated data-driven algorithm for processing LiDAR inspection data and calculating the hydraulic properties, quantifying concrete erosion rate, and predicting the service life (RSL) of reinforced concrete sanitary sewer pipes (RCSSPs). The methodology is conducted on 8000 linear *ft* of RCSSPs. For the inspection outputs with 3D PCD, the processed PCD shows an accurate presentation of the inner concrete wall geometry of pipes; this is confirmed by overlaying the processed PCD on the CCTV image (in Figure 27). The results of the proposed distribution-fitting algorithm show that Half-normal distribution is the best-fit distribution for concrete erosion rate of RCSSPs calculated from 2D rings (in Figure 48); however, the predicted service life of RCSSPs using Half-normal distribution is close to the Weibull distribution values (in Figure 59). In addition, the predicted service life obtained using the algorithm proposed herein is more consistent than the results of a previous study using the same inspection data (in Figure 60). Furthermore, using Bayesian network (BN), the mean concrete loss for each pipeline # (M-M) is updated; the priors are selected from previous studies, and Weibull and Gamma likelihood functions are used separately as different case studies. The proposed methodology is verified by comparing the probability-of-failure plots and the predicted remaining service life (RSL) with those obtained by using MCS on Power law (Equation 22) and Pomeroy Equation 23 (in Figure 61 and Figure 62). In addition, as it is shown in Figure

77, the difference of lower bound and upper bound for updated Weibull values are less than observed data which led to more consistent results. However, updated Gamma values led to higher RSL. Finally, statistical methods including Single Variable Regression, Multi-Variable Regression, and Polynomial Regression models are utilized on the output of a proposed algorithm to estimate concrete erosion in the inner walls of RCSSPs. The regression models can be used to understand the relationship between the "Mean Loss (mm)" (the dependent variable) and other variables in the dataset (independent variables).

The proposed method provides a simple, but powerful tool for condition assessment of RCSSPs by coordinating the non-destructive (ND) inspection PCD; all is done with minimum user interference. These results could be presented in different scales based on the decision maker's judgment; it could be as small as a 1-inch ring, or as large as a 5-ft section or a whole line (M-M). Herein, the criteria for condition assessment of RCSSP is remaining service life (RSL); based on engineering judgement, the predicted service life could be calculated for different levels of acceptable risk P_a.

The results from different case studies in this paper can be used during the conceptual design stage to evaluate various design choices and to determine the impact that their implementation could have on their service life. The followings bullet points are the detailed conclusion of the results.

1- From the results for diameter and the cross-section deflection of the pipes (Section 4.2;Figure 29). The results certify the following highlights:

- Using the proposed framework, the inner diameter and cross-sectional deformation of the pipes are calculated consistently and accurately. The location of the anomalies such as uneven joints, and location of the blockage can be pinpointed with little user interference.

- The results of the proposed algorithm showed that the first ovality equation (Equation 11.a) provided by ASTM F-1216 (ASTM 2016) leads to a more reasonable and consistent calculation (Figure 31).
- The proposed framework allows for automated wall loss determination, without user interference that can be subsequently used for asset management purposes.
- From Figure 32 it showed that the proposed *KNN* method calculates the diameter and ovality of 2D rings more accurately than other methods such as Circle fitting and Ellipse fitting algorithms based on LS.

2-From the results of the algorithm, the mean concrete loss of different cases (i.e., the different zones of pipe circumference) was calculated. The results of different cases are compared using three different data assessment techniques, i.e., boxplots, probability plots, chi-square goodness-of-fit test. Based on the results, the following conclusions can be drawn:

- The results of the chi-square goodness-of-fit test (Table 4) illustrated statistically significant relationships between the mean concrete erosion of different case studies and the whole pipe circumference, especially sector 0^{o}-180^{o}; this is also certified by two visual inspection methods.
- The comparative (Figure 44) plots showed that the underlying behavior of concrete erosion for the 60^{o}-120^{o} pipe sector differed from other zones along the pipe circumference, which can be attributed to sulfide accumulation at the crown of the pipe.
- The results certified that eliminating some of the data in the filtering process of the PCD does not have an adverse effect on assessing the concrete wall erosion of RCSSPs. Since the filtering process is the only part that requires user interference, eliminating them reduced the processing time as well as the monetary resources.

- The results of the chi-square goodness-of-fit test in (Table 4) illustrated that there are statistically significant relationships between the mean concrete erosion of different cases and the whole pipe circumference. Meanwhile, the concrete erosion data for the case 0^{o} -180^{o} sector (of all five lines) had the closest values to the mean erosion of the whole pipe circumference. In addition, the two cases, 15^{o} -165^{o} and 30^{o} -150^{o}, are the next best options. Meanwhile, the chi-square goodness-of-fit test results matched the visual tests, e.g., the underlying distribution of the case: 60^{o} -120^{o} is different from other cases in line 1.

3-Comparing the results of RSL calculations for the method of the probability of exceedance, and X-intercept method (Section 3.4.5), it is concluded that:

•Among the six considered PDFs for distribution of wall erosion, "Method 1" (method of the probability of exceedance; *Section 3.4.10.1*) showed more consistency and depicted more rational life expectancy RSL compared to "Method 2" (method of X-intercept *Section 3.4.10.2*).

4-From the results of calculated hydraulic properties of pipe, overlays of a PCD on a corresponding CCVT image, results of the best distribution for concrete wall thickness loss data, and reliability-based prediction of the remaining service life (RSL) (for 1000 linear foot of large diameter RC sewer lines (54- and 60- inch)) using MCS and probability of exceedance method, and the results of a similar study, the following conclusions can be drawn:

- The overlay of the PCD and actual CCTV image corresponding to the seventh 5-ft section of Line 4 (Figure 27) certified that the LiDAR PCD can locate the water line, deposits at the haunches, and uneven joints accurately.

- The pie charts in Figure 49 (showing the results of the proposed distribution-fitting algorithm for all the rings of each ten lines (54- and 60-inch pipe)), confirmed that for most of the rings, the erosion rate data followed the Half-normal distribution (with zero mean). Figures 50-59 showed consistency between the Half-Normal and Weibull distributions.
- The results of box plots of RSL from the top 4 best distributions showed that assigning Exponential distribution led to lower RSL (about 12-13%); however, Normal distribution led to higher values of RSL (to 6%). More importantly, the Weibull and Half-normal distributions led to the same values.
- By comparing the confidence interval of the RSL calculated from the proposed method and a similar study (Figure 61) showed that the difference between each lower and upper bound is much smaller than the previous study (Moamaie, 2019), indicating that the results from the methodology proposed led to more consistent RSL.
- From the predicted RSL using 4 different reliability methods (shown in boxplots in Figure 63), it is illustrated that the X-intercept method led to larger RSL estimation than other methods; Estimated RSL from MCS on Power law (Equation 22) led to higher values than the Half-normal distribution results; however, RSL from MCS on Pomeroy model (Equation 23) aligned with the Half-normal distribution results.

5-From the results of statistical methods such as the Single variable Regression model, Multi-Variables Regression model, and Polynomial Regression model on the output of the proposed algorithm, it is concluded that:

- Results of Single variable regression model (Table 6-Table 8) showed that *Ovality* is the best variable to predict the *Mean concrete loss* with with lower RMSE.

- Results of Single variable regression on the properties of 30-inch pipes differed from 54- and 60-inch pipes. This is due to the imposed filtering phase on 54-60-inch data. The 30-inch inspection data are different 2D rings along the length of the pipe, however, the output of 54-60-inch inspection data are 3D PCDs for each 5-*ft* along the length of the pipe; the 2D rings are extracted from the 3D PCD using the proposed methods.
- From the heatmaps (correlation Matrices) (Figure 70) it is certified that the Mean loss does not have underlying correlation with the hydraulic parameters.
- From the results of Multi variable regression model:
    - Table 9 showed the best three-combination to predict the Mean Loss of 30-inch pipe is "Water Level (%): (*E*), Actual Radius (mm): (*B*), and Ovality: (*D*)."
    - Table 10 showed the best three-combination to predict the Mean Loss of 54-inch pipe is "Water Level (%): (E), Hydraulic Radius: (mm) (C), and Ovality: (D)."
    - Table 11 show the best three-combination to predict the Mean Loss of 60-inch pipe is "Water Level (%): (E), Actual Radius (mm): (B), Hydraulic Radius (mm) (C)."
    - The results show the combination "Water Level (%): (E), Actual Radius (mm): (B), Hydraulic Radius (mm): (C)" can predict the Mean Loss with reasonable RMSE.
- From the results of Polynomial regression model, it is concluded that Polynomial regression model did not improve the accuracy of the predictions comparing to Multi variable regression model. Table 13 showed that the combination "Water Level (%), Actual Radius (mm), Hydraulic Radius (mm)" can predict the Mean Loss. Meanwhile for 60-inch data, the predictions are more accurate that by Multi variable regression (15%).

6-From the results of BN on Weibull and Gamma likelihoods:

- Mean Loss values Updated by applying BN on Weibull prior led to lowest difference (difference of lower bound and upper bound) among other values: *observed data and updated Gamma.* So, BN on Weibull prior led to more consistent results. However, updated Gamma values led to higher values of RSL(Figure 77).

The result of the proposed approach is consistent, and reasonable with minimum user interference. Overall, the anticipated results can assist decision makers in prioritizing limited repair funding by providing a comprehensive, network-level, quantitative performance assessment of selected RC sanitary pipelines. The overall objective of this study is to develop an innovative, automated, and rational framework for condition assessment of transportation infrastructure in more specifically for RC sanitary pipelines.

5.2 Future Developments

Future developments of the proposed methodology will focus on the following:

1. In order to accurately calculate the Manning's equation (Equation 23), the Manning's roughness coefficient (MC) should be quantified more precisely; since LiDAR technology provides a high accuracy PCD, it is possible to calculate the Manning's roughness instead of using a constant value from the literature.

2.LiDAR data provides the accurate 3D presentation of the geometry of pipe; thus, it can determine some 3D properties of pipes such as bends, slope, and deflection (ovality) of pipes. However, the LiDAR is not able to capture the geometry of the pipes below the waterline. In addition, the 3D PCD shows scattering beyond 5 ft. length, which should be cut-off for post-processing purposes. These include some of the limitations of the LiDAR scanner used in the current study.

3. To calculate the remaining service life (RSL) of RCSSPs more accurately, many parameters need to be considered such as 1. environmental factors of pipelines such as humidity, temperature, etc., 2. mechanical properties of pipelines such as pipe diameter, initial ovality etc., 3. sewer material such as content of corrosive materials (sulfide and chloride content), and 4. information about the previous rehabilitation of the SSPs and type of rehabilitation (See Figure 78); e.g., in the inspected pipelines some of the RCSSPs has rehabilitated by a type of liners, but no information was available in the municipalities, therefore the pipes excluded from this study.

Therefore, future studies on other factors (such as effect of CIPP liner) that is associated with the corrosion of RC pipelines is suggested. Unfortunately, there is not enough data and information available for evaluating the effect of rehabilitation on the pipelines and on increasing the life expectancy of the pipes.

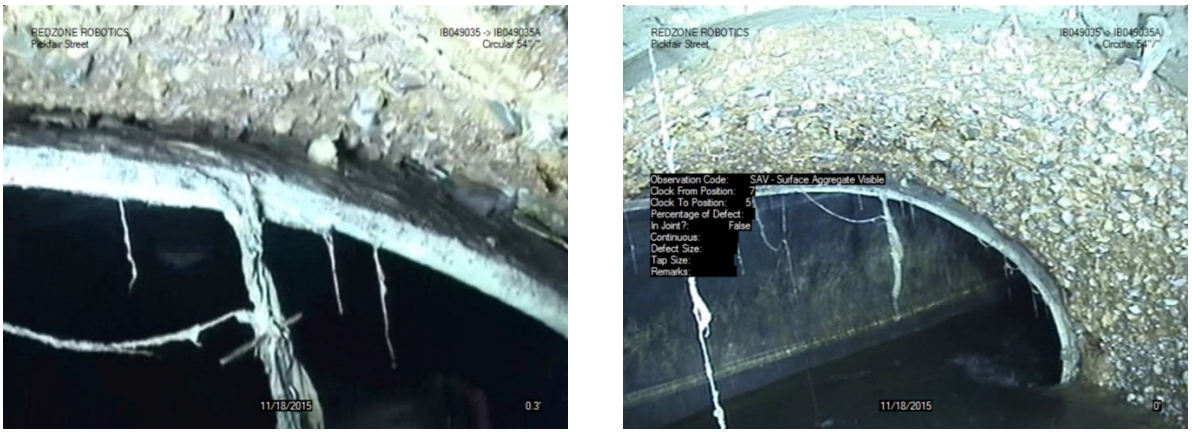

Figure 78. CIPP Liner Inside the RCSSPs

4. The loss of wall thickness is only a serviceability performance index and there are ultimate limit state indicators that affect the reliability of RCPs as well. In addition, from an asset management point of view, a risk assessment methodology for RCPs subjected to both environmental and external load effects, including both the probability and the consequences of exceedance of a performance criterion is more efficient and accurate.

5. It should be mentioned that LiDAR data captures the geometry of pipes above the flow line. Therefore, the proposed methodology is limited to detecting the anomalies above the flow line. Meanwhile, the effect of deposits below the flow on hydraulic properties of the pipe are accommodated by using probabilistic techniques.

REFERENCES

Abuhishmeh, K., & Hojat Jalali, H. (Forthcoming). Risk Assessment of Infrastructure Using a Modified Adaptive Neuro-Fuzzy System: Theoretical Application to Sewer Mains. *Journal of Pipeline System and Engineering Practice*. https://doi.org/https://doi.org/10.1061/JPSEA2/PSENG-1560.

Abuhishmeh, K. S. (2023). *Risk Assessment of Reinforced Concrete Sewer Pipes Under External Loading and Adverse Environmental Conditions Using Neuro-Fuzzy System* [Doctorate dissertation]. University of Texas at Arlington.

Ahammed, M., & Melchers, R. E. (1995). Reliability of Underground Pipelines Subject to Corrosion. *Journal of Transportation Engineering*, *120*(6). https://doi.org/10.1061/(ASCE)0733-947X(1994)120:6(989)

Ait Mokhtar, E. H., Chateauneuf, A., & Laggoune, R. (2016). Bayesian approach for the reliability assessment of corroded interdependent pipe networks. *International Journal of Pressure Vessels and Piping*, *148*, 46–58. https://doi.org/10.1016/j.ijpvp.2016.11.002

Al Asadi, M. (2018). *Algorithm Development For Sewer Pipe System Condition Assessment Using Multi-Sensor (MSI) Technology* [PhD Dissertations]. University of Texas at Arlington.

Altman, D. G. , & Bland, J. M. (1983). Measurement in medicine: the analysis of method comparison studies. *Journal of the Royal Statistical Society Series D: The Statistician*, *32*(3), 307–317.

Alzuhiri, M., Farrag, K., Lever, E., & Deng, Y. (2021). An Electronically Stabilized Multi-Color Multi-Ring Structured Light Sensor for Gas Pipelines Internal Surface Inspection. *IEEE Sensors Journal*, *21*(17), 19416–19426. https://doi.org/10.1109/JSEN.2021.3086415

Anbari, M. J., Tabesh, M., & Roozbahani, A. (2017). Risk assessment model to prioritize sewer pipes inspection in wastewater collection networks. *Journal of Environmental Management*, *190*, 91–101. https://doi.org/10.1016/j.jenvman.2016.12.052

Andrade, C. (2020). Linear propagation models of deterioration processes of concrete. *Corrosion Engineering, Science and Technology*, *vol.55,*(No.4,), pp.283–288. https://doi.org/10.1080/1478422X.2020.1750161

ASCE. (2022). *Infrastructure Report Card 2021*. https://infrastructurereportcard.org/wp-content/uploads/2020/12/National_IRC_2021-report.pdf

ASTM, F.-1216 – 16. (2016). *Standard Practice for Rehabilitation of Existing Pipelines and Conduits by the Inversion and Curing of a Resin-Impregnated Tube*. American National Standard.

Atique, F., & Attoh-Okine, N. (2018). Copula parameter estimation using Bayesian inference for pipe data analysis. *Canadian Journal of Civil Engineering*, *45*(1), 61–70. https://doi.org/10.1139/cjce-2017-0084

Bakry, I., Alzraiee, H., Kaddoura, K., El Masry, M., & Zayed, T. (2016). Condition Prediction for Chemical Grouting Rehabilitation of Sewer Networks. *Journal of Performance of Constructed Facilities*, *30*(6). https://doi.org/10.1061/(asce)cf.1943-5509.0000893

Barnwell, C., Doyle, W. P., & Gunn, C. L. (2009). LiDAR for Terrain Mapping on the Alaska Pipeline Corridor: A White Paper. *Alaska Natural Gas Transportation Projects, Office of the Federal Coordinator (OFC)*. https://www.arlis.org/docs/vol1/AlaskaGas/Paper/Paper_OFC_2009_LiDAR_TerrainMapping.pdf

Bizier, P. (2007). *Gravity Sanitary Sewer Design and Construction* (second). American Society of Civil Engineers.

Bradshaw, k. (2017). *San Antonio Express-News*. https://www.mysanantonio.com/news/local/article/West-Side-road-collapses-week-after-massive-10793869.php

Cheng, J. C. P., & Wang, M. (2018). Automated detection of sewer pipe defects in closed-circuit television images using deep learning techniques. *Automation in Construction, vol.95,* pp.155–171. https://doi.org/https://doi.org/10.1016/j.autcon.2018.08.006

Civil Crews. (2020). *Shapes of Sewer,Types of Sewer*. CivilCrews. https://civilcrews.com/shapes-types-of-sewer/

Clemens, F., Stanić, N., der Schoot, W. Van, Langeveld, J., & Lepot, M. (2015). Uncertainties associated with laser profiling of concrete sewer pipes for the quantification of the interior geometry. *Structure and Infrastructure Engineering, vol.11,* pp.1218–1239. https://doi.org/10.1080/15732479.2014.945466

Dahire, S., Tahir, F., Jiao, Y., & Liu, Y. (2018). Bayesian Network inference for probabilistic strength estimation of aging pipeline systems. *International Journal of Pressure Vessels and Piping*, *162*, 30–39. https://doi.org/10.1016/j.ijpvp.2018.01.004

Dang, L. M., Hassan, S. I., Im, S., Mehmood, I., & Moon, H. (2018). Utilizing text recognition for the defects extraction in sewers CCTV inspection videos. *Computers in Industry, vol.99,* pp.96–109. https://doi.org/https://doi.org/10.1016/j.compind.2018.03.020

De Belie, N., Monteny, J., Beeldens, A., Vincke, E., Van Gemert, D., & Verstraete, W. (2004). Experimental research and prediction of the effect of chemical and biogenic sulfuric acid on different types of commercially produced concrete sewer pipes. *Cement and Concrete Research*, *34*(12), 2223–2236. https://doi.org/10.1016/j.cemconres.2004.02.015

Dirksen, J., Clemens, F. H. L. R., Korving, H., Cherqui, F., Gauffre, P. Le, Ertl, T., Plihal, H., Müller, K., & Snaterse, C. T. M. (2013). The consistency of visual sewer inspection data. *Structure and Infrastructure Engineering, vol.9,*(No.3,), pp.214–228. https://doi.org/10.1080/15732479.2010.541265

Dong, S., Wang, D., Hui, E., Gao, C., Zhang, H., & Tan, Y. (2023). An Overview of the Application of Fiber-Reinforced Cementitious Composites in Spray Repair of Drainage Pipes. In *Buildings* (Vol. 13, Issue 5). MDPI. https://doi.org/10.3390/buildings13051119

Duran, O., Althoefer, K., & Seneviratne, L. D. (2003). Pipe inspection using a laser-based transducer and automated analysis techniques. *IEEE/ASME Transactions on Mechatronics*, *8*(3), 401–409. https://doi.org/10.1109/TMECH.2003.816809

Ebrahimi, M., Hojat Jalali, H., & Sabatino, S. (2023). Probabilistic condition assessment of reinforced concrete sanitary sewer pipelines using LiDAR inspection data. *Automation in Construction*, *150*. https://doi.org/10.1016/j.autcon.2023.104857

Ebrahimi, M., & Jalali, H. H. (2022a). Automated Condition Assessment of Sanitary Sewer Pipes Using LiDAR Inspection Data. *ASCE Pipeline Conference 2022*.

Ebrahimi, M., & Jalali, H. H. (2022b). Spatial Variability Effects of Wall Erosion on Assessment of Reinforced Concrete Sanitary Sewer Pipes (RCSSPs). *Tran-SET Conference 2022*.

Egger, C., Scheidegger, A., Reichert, P., & Maurer, M. (2013). Sewer deterioration modeling with condition data lacking historical records. *Water Research*, *47*(17), 6762–6779. https://doi.org/10.1016/j.watres.2013.09.010

Ékes, C. (2021). Inspecting Twin 42" Reinforced Concrete Pipes with Pipe Penetrating Radar Supplemented by LiDAR. In *Pipelines 2021* (pp. 236–241). https://doi.org/10.1061/9780784483602.027

Ékes, C., Neducza, B., & Henrich, G. (2011). B 302 GPR Goes Underground : Pipe Penetrating Radar. *North American Society for Trenchless Technology(NASTT)*. https://sewervue.com/papers/B-3-02_Final_Paper_GPR_Goes_Underground-Pipe_Penetrating.pdf.

Elmasry, M., Hawari, A., & Zayed, T. (2017). Defect based deterioration model for sewer pipelines using bayesian belief networks. *Canadian Journal of Civil Engineering*, *44*(9), 675–690. https://doi.org/10.1139/cjce-2016-0592

EPA. (1999). *Collection Systems O&M Fact Sheet Sewer Cleaning and Inspection*.

Feeney, C. S. , Thayer, S., Bonomo, M., & Martel, K. (2009). *Condition Assessment of Wastewater Collection Systems - White Paper*. https://nepis.epa.gov/Exe/ZyPDF.cgi/P1003ZQY.PDF?Dockey=P1003ZQY.PDF

Feng, Z., Horoshenkov, K. V, Tareq, M., Ali, B., & Tait, S. J. (2012). An Acoustic Method for Condition Classification in Live Sewer Networks. *World Conference on Nondestructive Testing(WCNDT)*. http://www.ndt.net/?id=12560

Foorginezhad, S., Mohseni-Dargah, M., Firoozirad, K., Aryai, V., Razmjou, A., Abbassi, R., Garaniya, V., Beheshti, A., & Asadnia, M. (2021a). Recent Advances in Sensing and Assessment of Corrosion in Sewage Pipelines. *Process Safety and Environmental Protection, vol.147,* pp.192–213. https://doi.org/https://doi.org/10.1016/j.psep.2020.09.009

Foorginezhad, S., Mohseni-Dargah, M., Firoozirad, K., Aryai, V., Razmjou, A., Abbassi, R., Garaniya, V., Beheshti, A., & Asadnia, M. (2021b). Recent Advances in Sensing and Assessment of Corrosion in Sewage Pipelines. In *Process Safety and Environmental Protection* (Vol. 147, pp. 192–213). Institution of Chemical Engineers. https://doi.org/10.1016/j.psep.2020.09.009

Gal, O. (2023). *fit_ellipse*. MATLAB Central File Exchange. https://www.mathworks.com/matlabcentral/fileexchange/3215-fit_ellipse. Retrieved November 21, 2023.. Retrieved November 21, 2023.

He, S., & Koizumi, A. (2013). Damage Discrimination Analysis with Quantification Theory for Sewage Pipe System. *Journal of Pipeline Systems Engineering and Practice, vol.4,*(No.1,), pp.11–16. https://doi.org/10.1061/(ASCE)PS.1949-1204.0000122

Hojat Jalali, H., & Ebrahimi, M. (2021). *Residual Life and Reliability Assessment of Underground RC Sanitary Sewer Pipelines under Uncertainty Final Report*. https://repository.lsu.edu/transet_pubs/126

Islander, R. L., Devinny, J. S., Mansfeld, F., Postyn, A., & Shih, H. (1991). Microbial Ecology of Crown Corrosion in Sewers. *Journal of Environmental Engineering, vol.117,*(No.6,), pp.751–770. https://doi.org/10.1061/(ASCE)0733-9372(1991)117:6(751)

Jackson, W., Dobie, G., MacLeod, C., West, G., Mineo, C., & McDonald, L. (2020). Error Analysis and Calibration for a Novel Pipe Profiling Tool. *IEEE Sensors Journal*, *20*(7), 3545–3555. https://doi.org/10.1109/JSEN.2019.2960939

Khaled Saleh Abuhishmeh. (2019). *Service Life Prediction and Risk Analysis of Reinforced Concrete Gravity Flow Pipes Using Reliability Theory* [Masters Thesis, University of Texas at Arlington]. https://rc.library.uta.edu/uta-ir/bitstream/handle/10106/28196/ABUHISHMEH-THESIS-2019.pdf?sequence=1%26isAllowed=y

Kramer, O. (2013). *K-Nearest Neighbors* (Vol. 51). Springer. https://doi.org/https://doi.org/10.1007/978-3-642-38652-7_2

Kumar, S. S., Abraham, D. M., Jahanshahi, M. R., Iseley, T., & Starr, J. (2018). Automated defect classification in sewer closed circuit television inspections using deep convolutional neural networks. *Automation in Construction, vol.91,* pp.273–283. https://doi.org/https://doi.org/10.1016/j.autcon.2018.03.028

Lambert, J., Carballo, A., Cano, A. M., Narksri, P., Wong, D., Takeuchi, E., & Takeda, K. (2020). Performance Analysis of 10 Models of 3D LiDARs for Automated Driving. *IEEE Access*, *8*, 131699–131722. https://doi.org/10.1109/ACCESS.2020.3009680

Leu, S. Sen, & Bui, Q. N. (2016). Leak Prediction Model for Water Distribution Networks Created Using a Bayesian Network Learning Approach. *Water Resources Management*, *30*(8), 2719–2733. https://doi.org/10.1007/s11269-016-1316-8

Lewis, P., Mc Elhinney, C. P., & McCarthy, T. (2012). LiDAR data management pipeline; from spatial database population to web-application visualization. *ACM International Conference Proceeding Series*. https://doi.org/10.1145/2345316.2345336

Li, D., Cong, A., & Guo, S. (2019). Sewer damage detection from imbalanced CCTV inspection data using deep convolutional neural networks with hierarchical classification. *Automation in Construction*, *101*, 199–208. https://doi.org/10.1016/j.autcon.2019.01.017

Li, R., Huang, H., Xin, K., & Tao, T. (2015). A review of methods for burst/leakage detection and location in water distribution systems. In *Water Science and Technology: Water Supply* (Vol. 15, Issue 3, pp. 429–441). IWA Publishing. https://doi.org/10.2166/ws.2014.131

Li, S.-X., Yu, S.-R., Zeng, H.-L., Li, J.-H., & Liang, R. (2009). Predicting corrosion remaining life of underground pipelines with a mechanically-based probabilistic model. *Journal of Petroleum Science and Engineering, vol.65,*(No.3,), pp.162–166. https://doi.org/https://doi.org/10.1016/j.petrol.2008.12.023

Liu, Y., Song, Y., Keller, J., Bond, P., & Jiang, G. (2017). Prediction of concrete corrosion in sewers with hybrid Gaussian processes regression model. *RSC Advances, vol.7,* pp.30894–30903. https://doi.org/10.1039/C7RA03959J

Mahmoodian, M., & Alani, A. (2014). Modeling Deterioration in Concrete Pipes as a Stochastic Gamma Process for Time-Dependent Reliability Analysis. *Journal of Pipeline Systems*

Engineering and Practice, vol.5,(No.1,), p.4013008. https://doi.org/10.1061/(ASCE)PS.1949-1204.0000145

Mahmoodian, M., & Li, C. Q. (2011). Service life prediction of underground concrete pipes subjected to corrosion. *Concrc - Proceedings of Concrete Solutions, 4th International Conference on Concrete Repair*. https://doi.org/10.1201/b11570-82

Makana, L. O., Shepherd, W. J., Tait, S., Rogers, C. D. F., Metje, N., Boxall, J. B., & Schellart, A. N. A. (2022). Future Inspection and Deterioration Prediction Capabilities for Buried Distributed Water Infrastructure. *Journal of Pipeline Systems Engineering and Practice*, *vol.13,*(No.3,), p.4022020. https://doi.org/10.1061/(ASCE)PS.1949-1204.0000656

Melchers, R. E. (Robert E.), & Beck, A. T. (2018). *Structural reliability analysis and prediction*.

Moamaie, P. (2019). *Remaining Service Life Estimation and Probabilistic Analysis of Reinforced Concrete Sewer Pipeline Systems* [Master's Thesis, University of Texas at Arlington]. https://rc.library.uta.edu/uta-ir/handle/10106/28601

Najafi, M. (2010). *Trenchless Technology Piping: Installation and Inspection*. The McGraw-Hill Companies, Inc. https://www.accessengineeringlibrary.com/content/book/9780071489287

Papoulis, A., & Pillai, U. (1991). *Probability, Random Variables, and Stochastic Processes*. McGraw-Hill .

Parker, C. D. (1951). *Mechanics of Corrosion of Concrete Sewers by Hydrogen Sulfide* (Vol. 23, Issue 12). https://www.jstor.org/stable/25031769

Pickard, S. K. (1983). Two-Stage" Bayesian Procedure for Determining Failure Rates from Experiential Data. In *IEEE Transactions on Power Apparatus and Systems* (Vol. 102, Issue 1).

Pishro-Nik, H. (2014). *Introduction to Probability, Statistics, and Random Processes*. Kappa Research, LLC.

Pleil, J. D. (2016). QQ-plots for assessing distributions of biomarker measurements and generating defensible summary statistics. *Journal of Breath Research, vol.10,*(No.3,), p.35001. https://doi.org/10.1088/1752-7155/10/3/035001

Pomerot, R. D. (1974). *Process Design Manual for Sulfide Control in Sanitary Sewerage Sewerage Systems*. https://nepis.epa.gov/Exe/ZyPURL.cgi?Dockey=2000ZE98.txt

Pomeroy, R. D., & Boon, A. G. (1990). The Problem of Hydrogen Sulphide in Sewers. *Clay Pipe Development Association,London, vol.2,*. https://www.cpda.co.uk/wp-content/uploads/2019/05/The-Problem-of-Hydrogen-Sulphide-in-Sewers.pdf

Redzone. (2021). *Redzone Robotics. Multi-Sensor Inspection*.

Ribas Silva, M. (1995). Study of biological degradation applied to concrete. *Transactions of the 13. International Conference on Structural Mechanics in Reactor Technology. v. 4*.

Romanova, A., Mahmoodian, M., & Alani, M. A. (2014). Influence and Interaction of Temperature, H2S and pH on Concrete Sewer Pipe Corrosion. *Nternational Journal of Civil, Architectural, Structural, Urban Science and Engineering*, *8*(6).

Saleh Abuhishmeh, K., & Hojat Jalali, H. (2023). Reliability Assessment of Reinforced Concrete Sewer Pipes Under Adverse Environmental Conditions: Case study for City of Arlington. *Journal of Pipeline Systems Engineering and Practice,*. https://ascelibrary.org/journal/jpsea2

Schuon, S., Theobalt, C., Davis, J., & Thrun, S. (2008). High-quality scanning using time-of-flight depth super resolution. *2008 IEEE Computer Society Conference on Computer Vision and Pattern Recognition Workshops*, pp.1–7. https://doi.org/10.1109/CVPRW.2008.4563171

Sevier, C. (2021). $1 trillion infrastructure bill. *ASCE*. https://infrastructurereportcard.org/congress-passes-historic-infrastructure-bill/

Sokolov, D. (2020). *Spherical coordinates. encyclopedia of mathematics*. Encyclopedia of Math. http://encyclopediaofmath.org/index.php?title= Spherical_coordinates&oldid=48774

Soltanianfard, M. A., Abuhishmeh, K., Hojat Jalali, H., & Shah, S. P. (2023). Sustainable concrete made with wastewater from different stages of filtration. *Construction and Building Materials*, *409*. https://doi.org/10.1016/j.conbuildmat.2023.133894

Sumith, YD. (2023). *Fast Circle Fitting using Landau Method*. MATLAB Central File Exchange. https://www.mathworks.com/matlabcentral/fileexchange/44219-fast-circle-fitting-using-landau-method

Tao, C. V. , & Hu, Y. (2002). Assessment of Airborne Lidar and Imaging Technology for Pipeline Mapping And Safety Applications. *Environmental Science*.

Teplý, B., Rovnaníková, M., Řoutil, L., & Schejbal, R. (2018). Time-Variant Performance of Concrete Sewer Pipes Undergoing Biogenic Sulfuric Acid Degradation. *Journal of Pipeline*

Systems Engineering and Practice, vol.9,(No.4,), p.4018013. https://doi.org/10.1061/(ASCE)PS.1949-1204.0000327

van Noortwijk, J. M., van der Weide, J. A. M., Kallen, M. J., & Pandey, M. D. (2007). Gamma processes and peaks-over-threshold distributions for time-dependent reliability. *Reliability Engineering and System Safety, 92,*(No. 12,), pp.1651–1658. https://doi.org/10.1016/j.ress.2006.11.00

Vogt, M., Rips, A., & Emmelmann, C. (2021). Comparison of iPad Pro®'s LiDAR and TrueDepth Capabilities with an Industrial 3D Scanning Solution. *Technologies*, *9*(2). https://doi.org/10.3390/technologies9020025

Water Management Manual. (2001). *Water resources research laboratory: Water measurement manual* . https://www.usbr.gov/tsc/techreferences/mands/wmm/WMM_3rd_2001.pdf

Wells, T., & Melchers, R. E. (2014). An observation-based model for corrosion of concrete sewers under aggressive conditions. *Cement and Concrete Research, vol.61-62,* pp.1–10. https://doi.org/https://doi.org/10.1016/j.cemconres.2014.03.013

Wells, T., & Melchers, R. E. (2015). Modelling concrete deterioration in sewers using theory and field observations. *Cement and Concrete Research, vol.77,* pp.82–96. https://doi.org/https://doi.org/10.1016/j.cemconres.2015.07.003

Wells, T., Melchers, R. E., & Bond, P. (2009). *Factors Involved in The Long-Term Corrosion of Concrete Sewers*.

Wu, J., Zhou, R., Xu, S., & Wu, Z. (2017). Probabilistic analysis of natural gas pipeline network accident based on Bayesian network. *Journal of Loss Prevention in the Process Industries*, *46*, 126–136. https://doi.org/10.1016/j.jlp.2017.01.025

Wu, L., Hu, C., & Liu, W. V. (2018). The sustainability of concrete in sewer tunnel—A narrative review of acid corrosion in the city of Edmonton, Canada. *Sustainability*, *vol.10 ,*(No.2 ,), p.517. https://doi.org/https://doi.org/10.3390/su10020517

Yin, X., Chen, Y., Bouferguene, A., Zaman, H., Al-Hussein, M., & Kurach, L. (2020). A deep learning-based framework for an automated defect detection system for sewer pipes. *Automation in Construction, vol.109,* p.102967. https://doi.org/https://doi.org/10.1016/j.autcon.2019.102967

Yin, X., Tianxin, M., Bouferguene, A., & Al-Hussein, M. (2021). Automation for sewer pipe assessment: CCTV video interpretation algorithm and sewer pipe video assessment (SPVA) system development. *Automation in Construction, vol.125,* p.103622. https://doi.org/https://doi.org/10.1016/j.autcon.2021.103622

APPENDIX A FITTING DIFFERENT DISTRIBUTIONS TO THE MEAN WALL THICKNESS LOSSES OF THE INSPECTED SEWER LINES

The methodology in this research measures a goodness of fit by comparing R^2 values for fitted line to QQ-plots of each all 10 pipelines (54- and 60-inch). Figure 79 shows the results for the distribution fitting algorithm, while Table 30 summarizes the R^2 values.

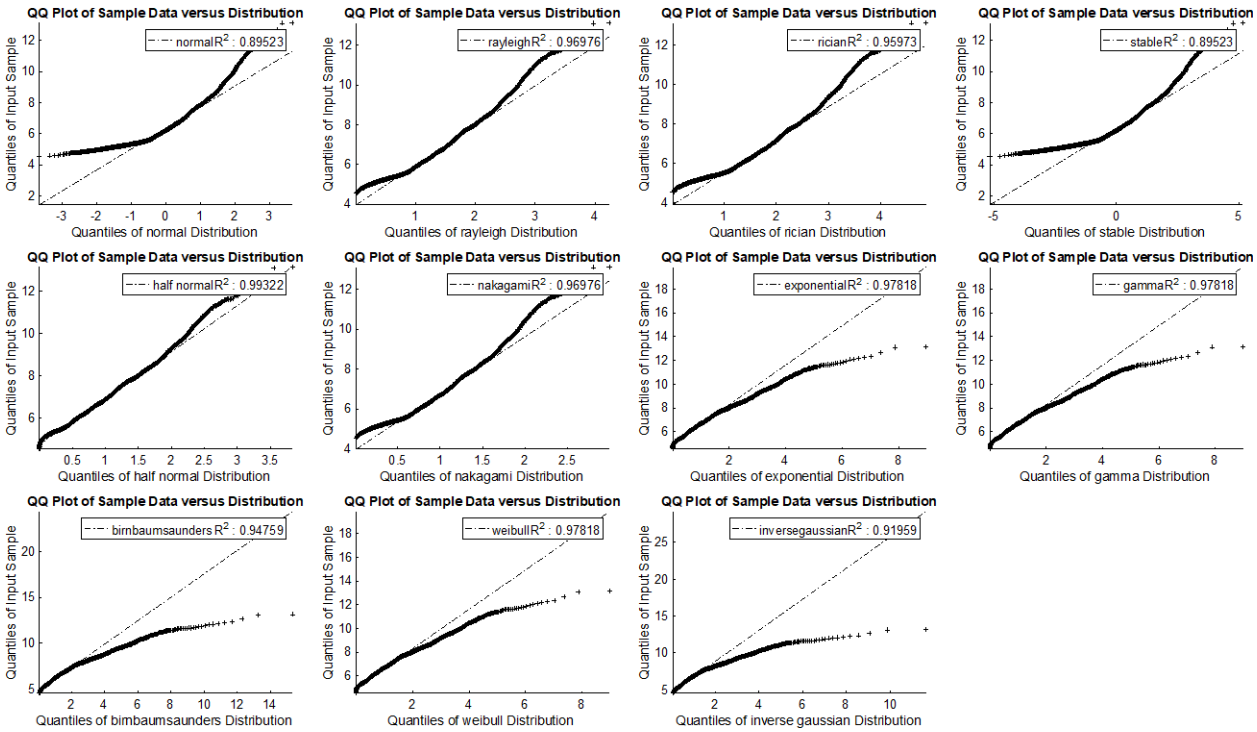

Line number: 1 ***(a)***

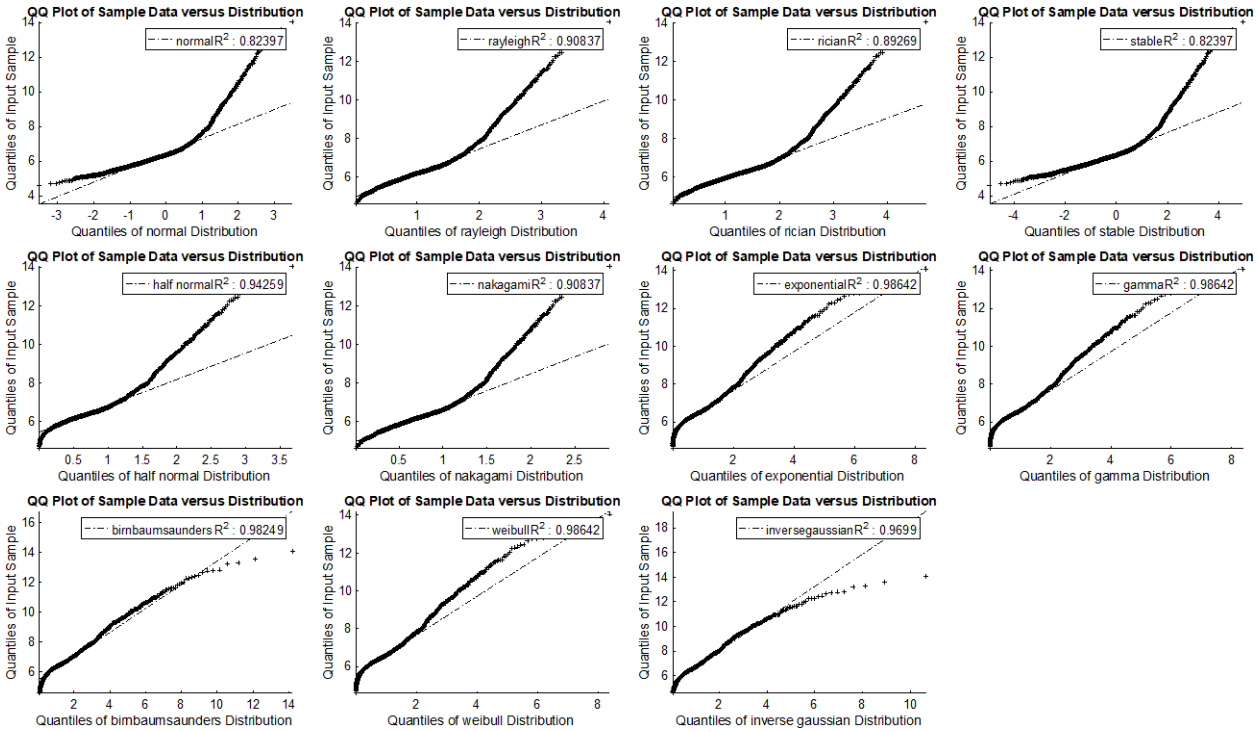

Line Number :2 ***(b)***

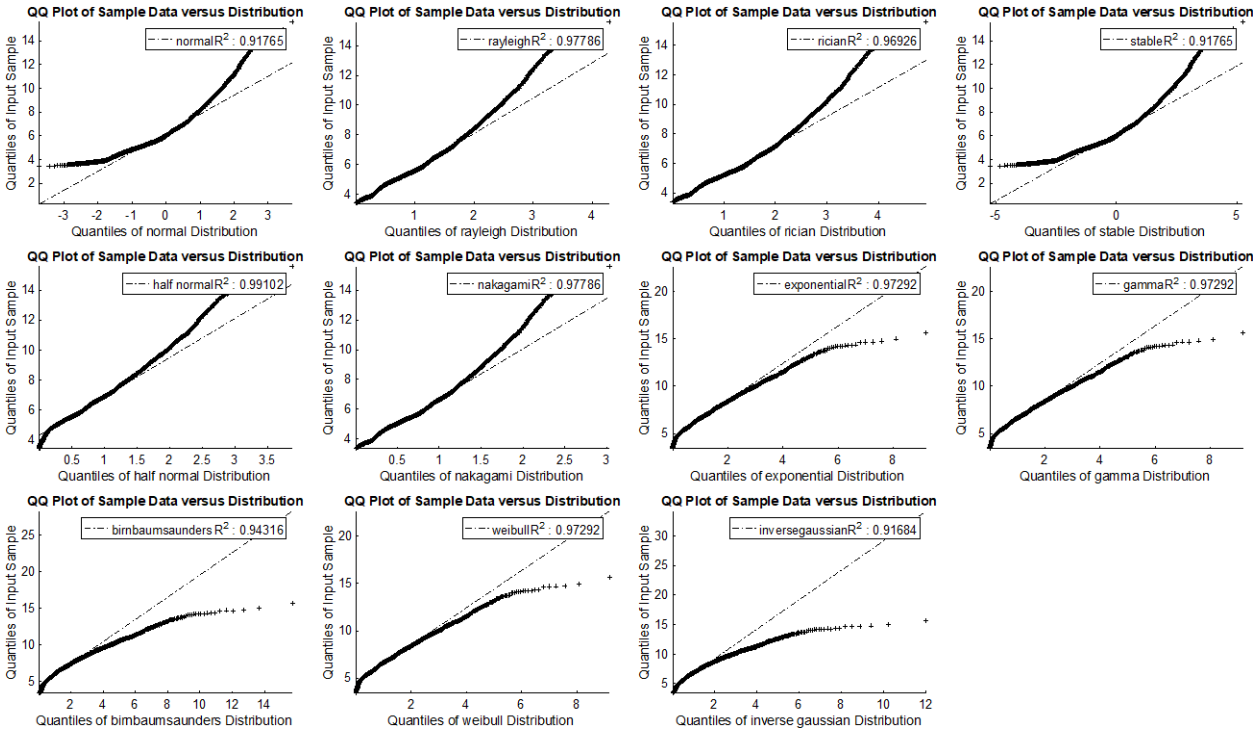

Line number: 3 ***(C)***

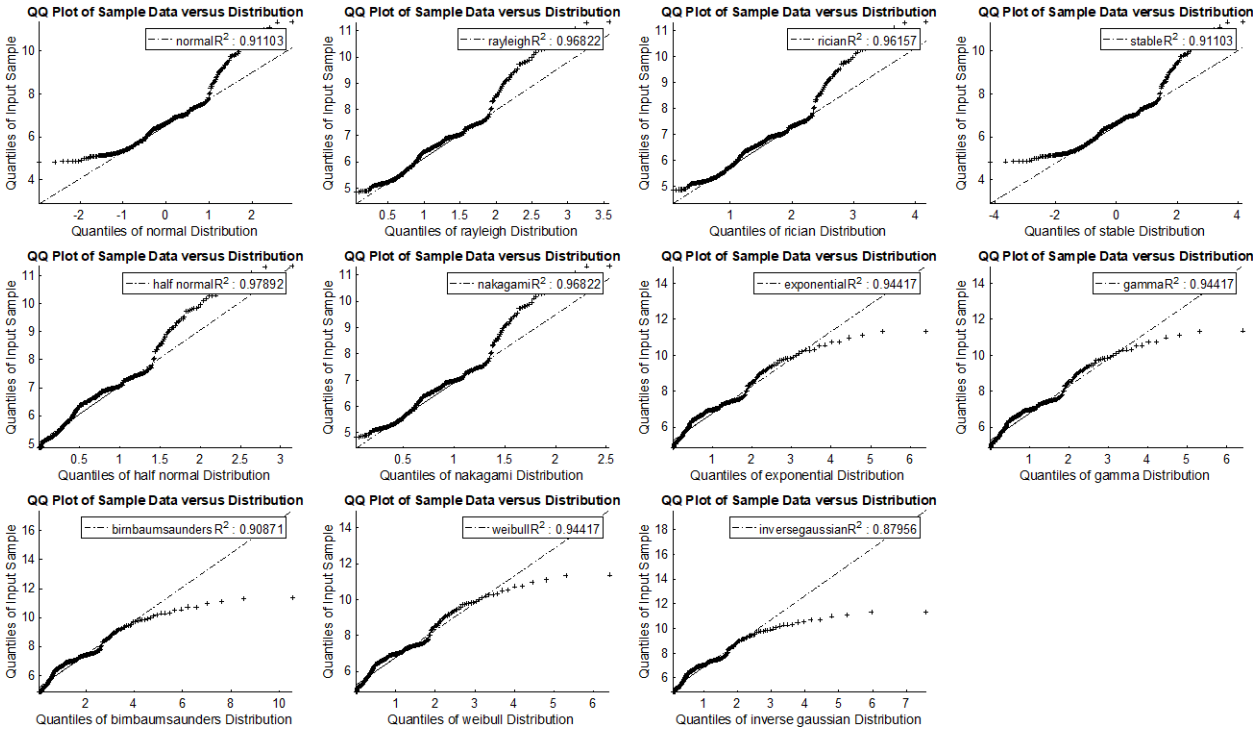

Line number: 4 ***(d)***

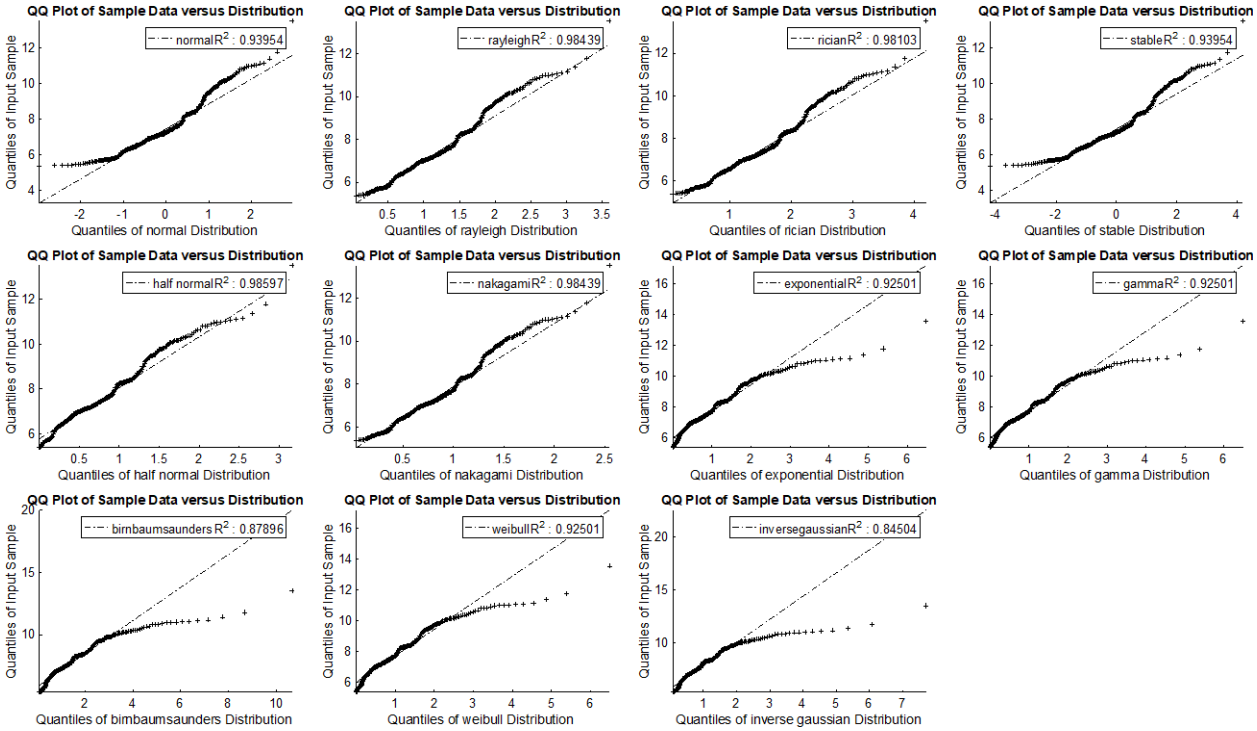

Line number: 5 ***(e)***

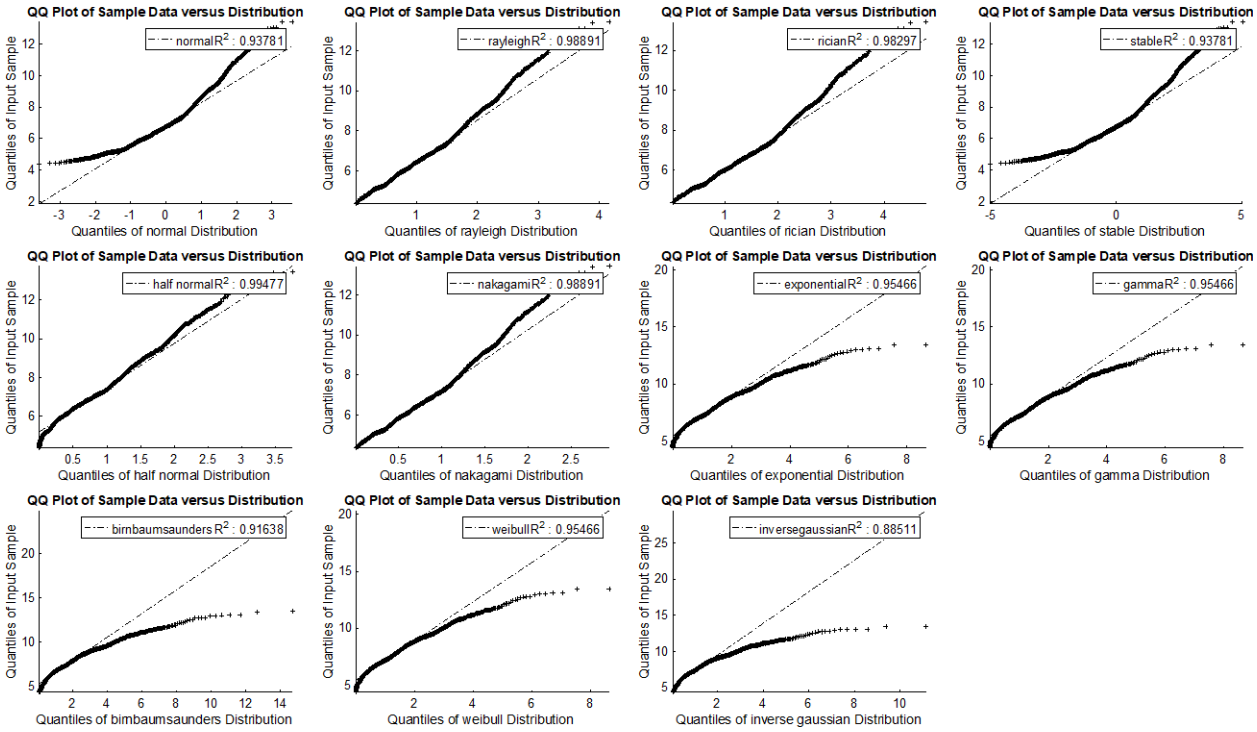

Line number: 6 ***(f)***

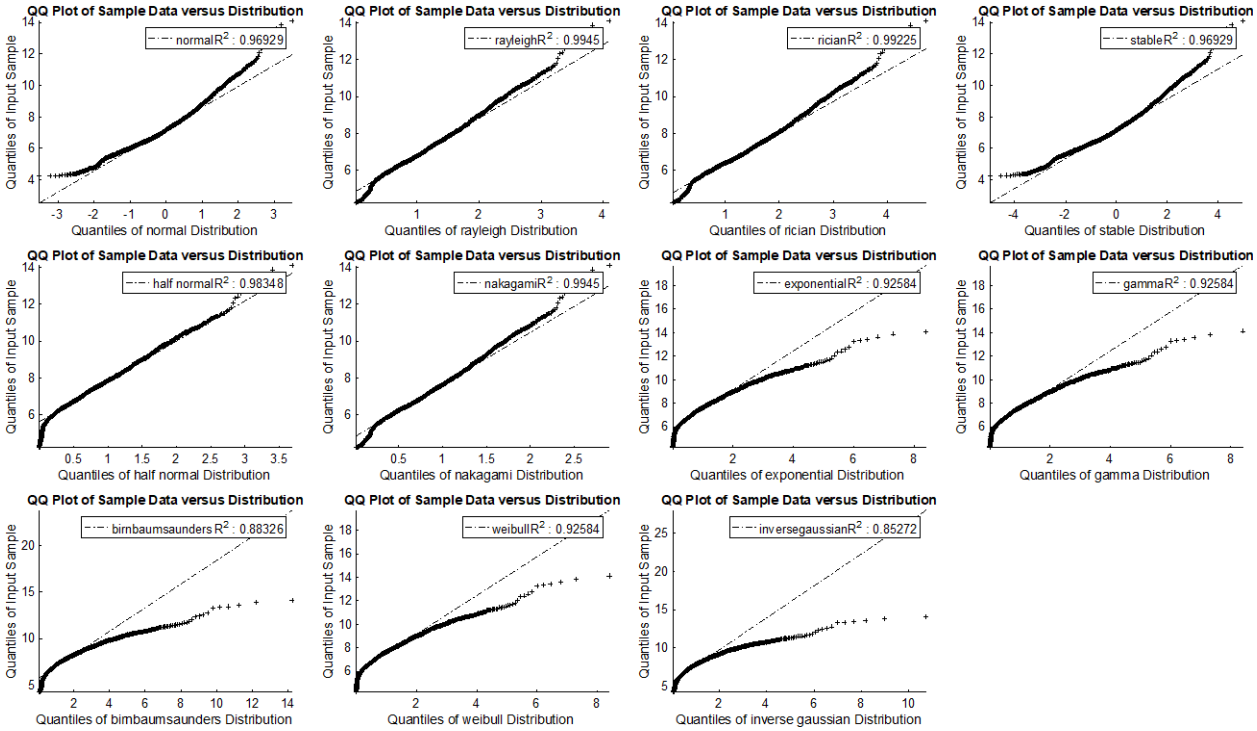

Line number: 7 ***(g)***

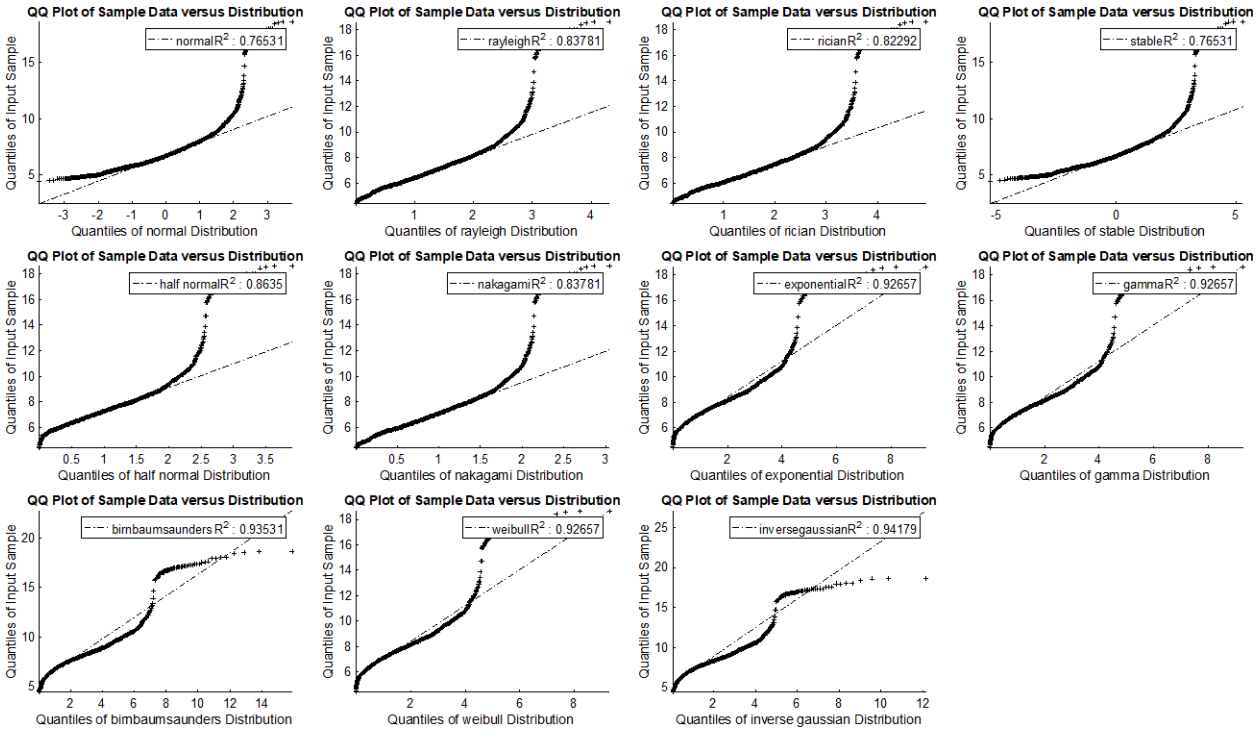

Line number: 8 ***(h)***

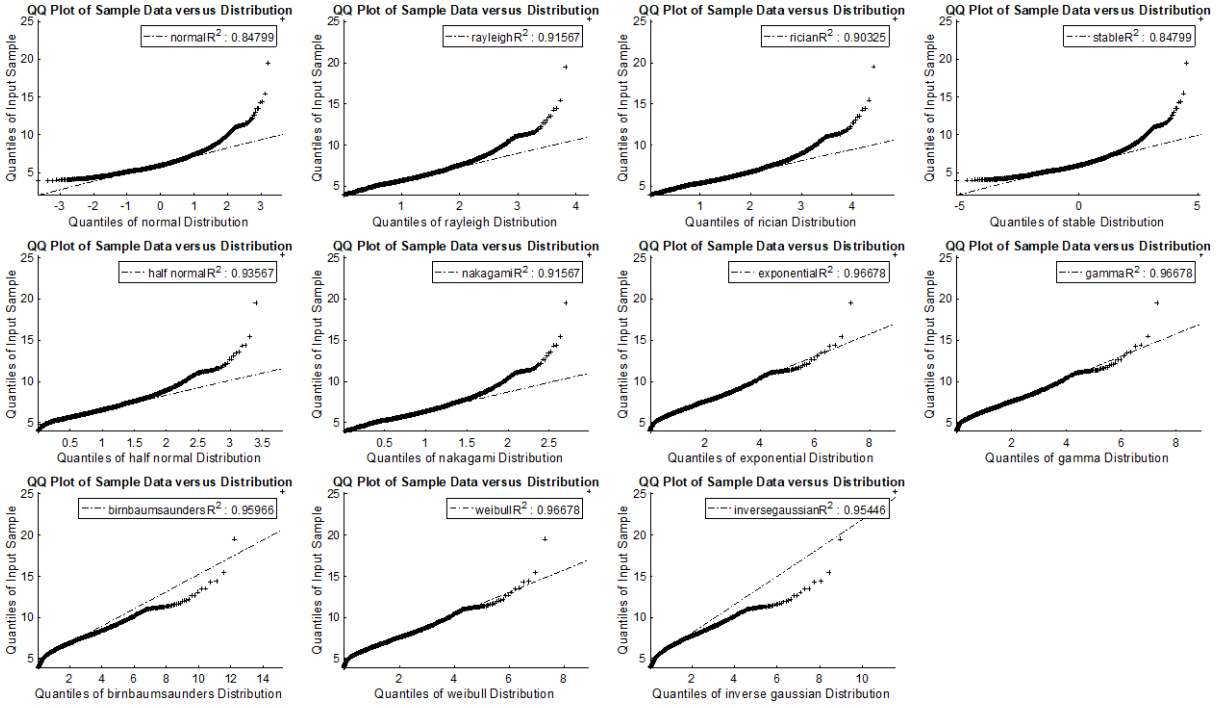

Line number: 9 ***(i)***

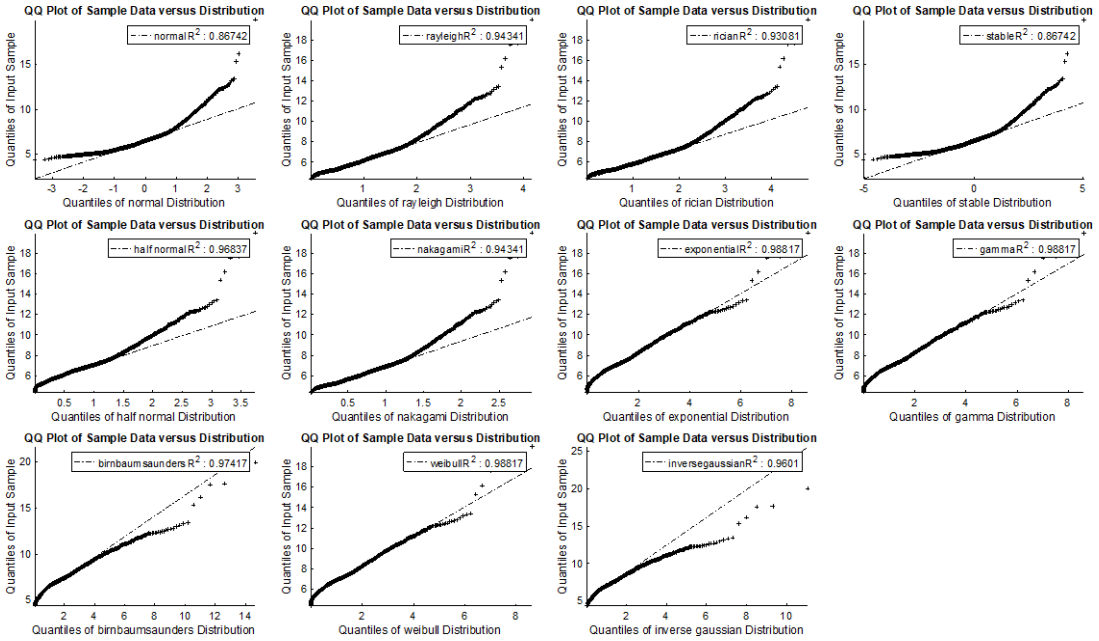

Line number: 10 ***(j)***

Figure 79. Results for fitting different distribution to the mean wall losses of 1-in rings and their R2 values for the first 10 pipelines, 54- and 60-inches.

Table 30. R2 values for different wall-thickness loss for four of the distribution for the mean wall losses of all 1-in rings of the first 10 selected pipeline

Line Number	Half Normal	Weibull	Normal	Exponential
1	0.9932178	0.978184	0.895234	0.97818362
2	0.9425863	0.986417	0.823965	0.98641707
3	0.9910176	0.97292	0.917648	0.9729201
4	0.9789172	0.944173	0.944173	0.94417268
5	0.9859686	0.925013	0.925013	0.92501281
6	0.9947731	0.954658	0.954658	0.95465812
7	0.9834837	0.925838	0.925838	0.92583791
8	0.8634997	0.926568	0.926568	0.92656845
9	0.9356701	0.966783	0.966783	0.96678305
10	0.9683671	0.988174	0.988174	0.98817363

APPENDIX B OUTPUTS OF BN

Figure 80-Figure 85 show the results from BN for updating the parameters of Weibull distribution,

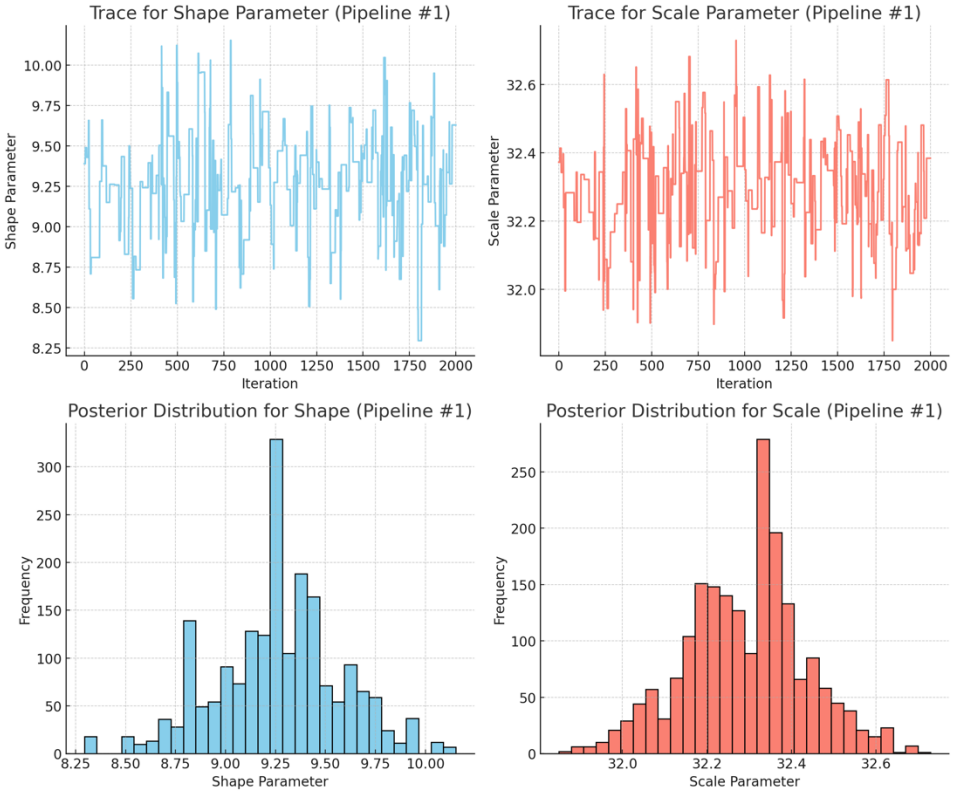

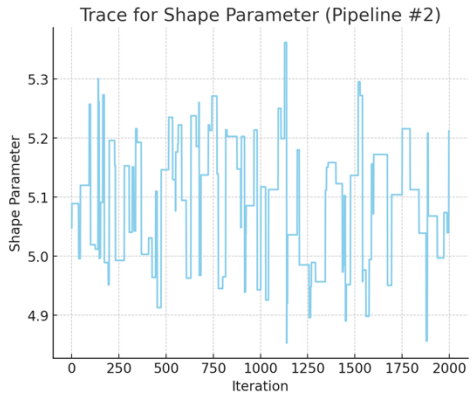
Trace for Shape Parameter (Pipeline #2)
Shape Parameter
Iteration

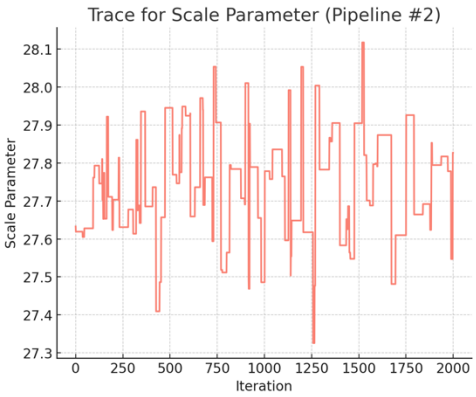
Trace for Scale Parameter (Pipeline #2)
Scale Parameter
Iteration

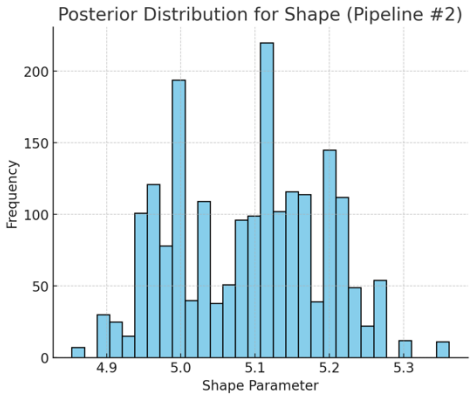
Posterior Distribution for Shape (Pipeline #2)
Frequency
Shape Parameter

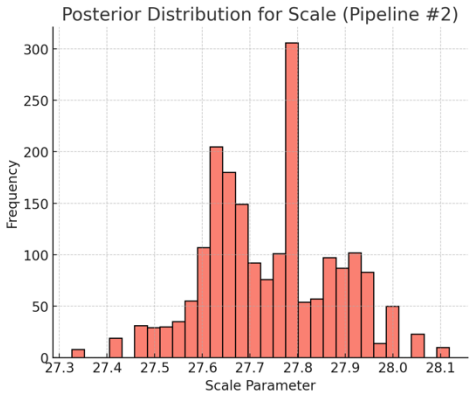
Posterior Distribution for Scale (Pipeline #2)
Frequency
Scale Parameter

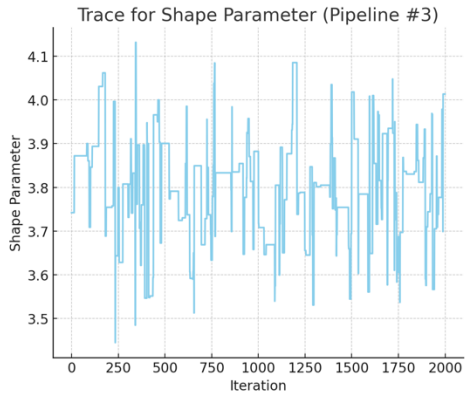
Trace for Shape Parameter (Pipeline #3)
Shape Parameter
Iteration

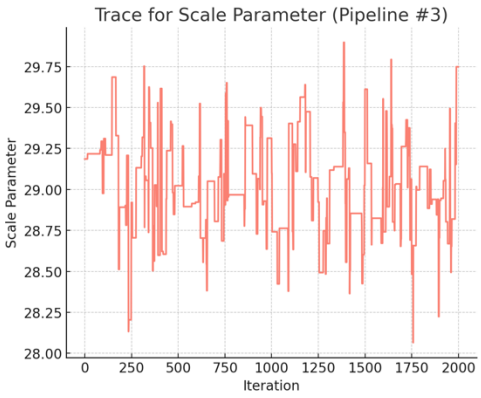
Trace for Scale Parameter (Pipeline #3)
Scale Parameter
Iteration

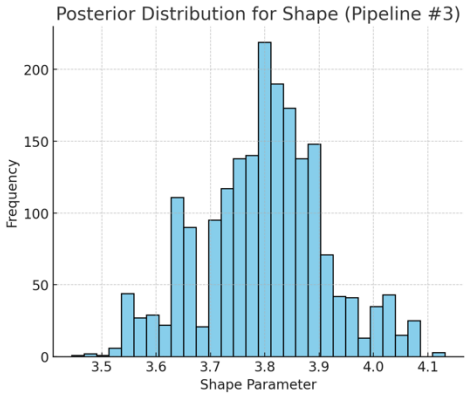
Posterior Distribution for Shape (Pipeline #3)
Frequency
Shape Parameter

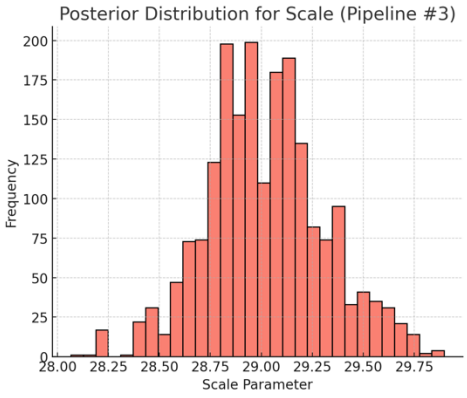
Posterior Distribution for Scale (Pipeline #3)
Frequency
Scale Parameter

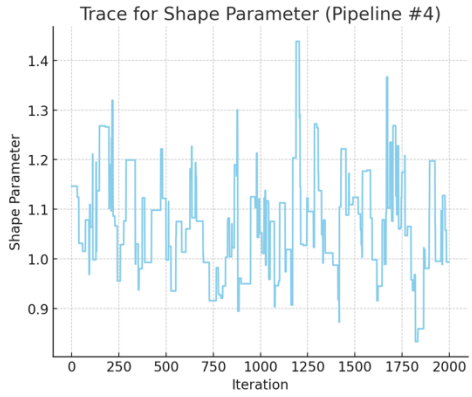
Trace for Shape Parameter (Pipeline #4)
Shape Parameter
Iteration

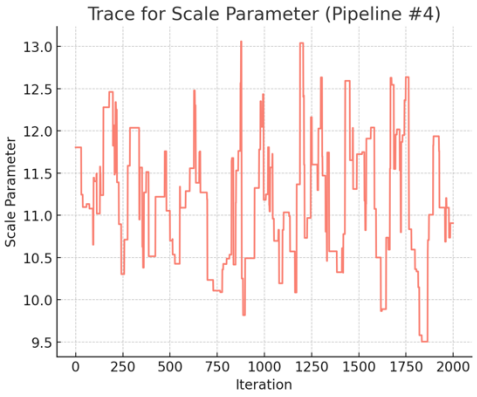
Trace for Scale Parameter (Pipeline #4)
Scale Parameter
Iteration

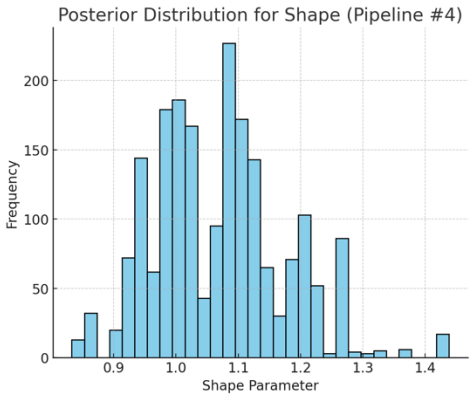
Posterior Distribution for Shape (Pipeline #4)
Frequency
Shape Parameter

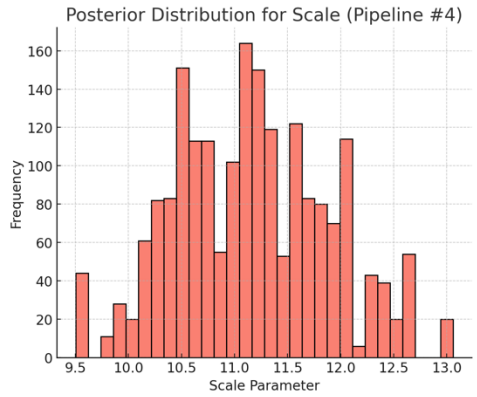
Posterior Distribution for Scale (Pipeline #4)
Frequency
Scale Parameter

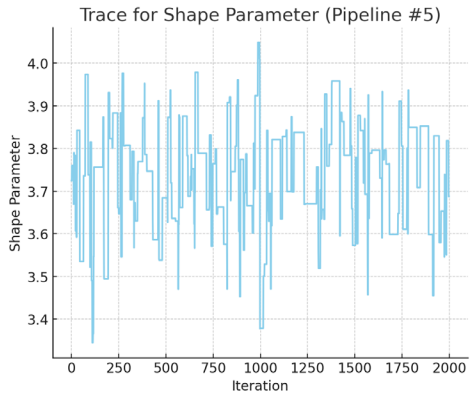
Trace for Shape Parameter (Pipeline #5)
Shape Parameter
Iteration

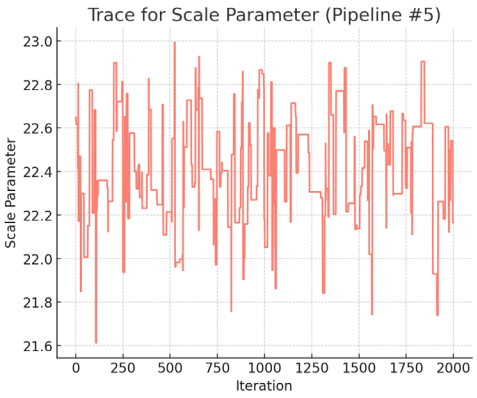
Trace for Scale Parameter (Pipeline #5)
Scale Parameter
Iteration

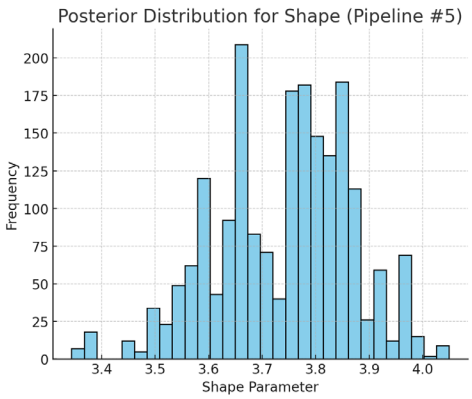
Posterior Distribution for Shape (Pipeline #5)
Frequency
Shape Parameter

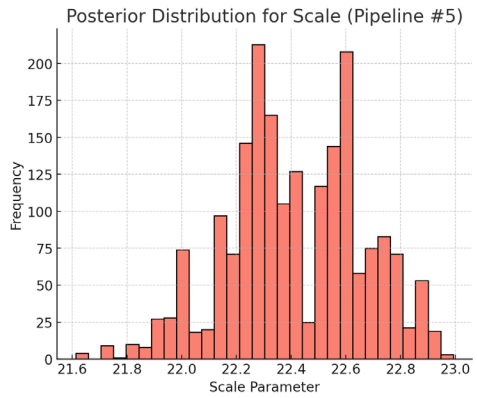
Posterior Distribution for Scale (Pipeline #5)
Frequency
Scale Parameter

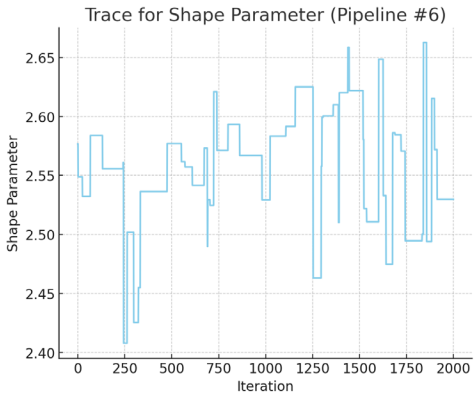
Trace for Shape Parameter (Pipeline #6)
Shape Parameter
Iteration

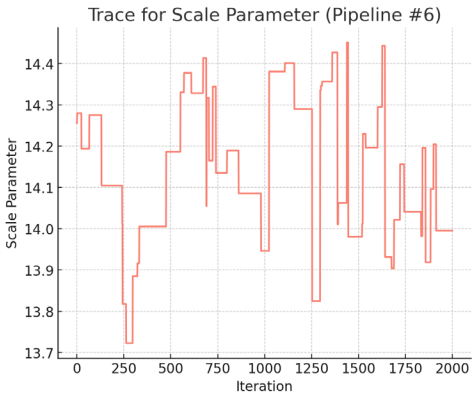
Trace for Scale Parameter (Pipeline #6)
Scale Parameter
Iteration

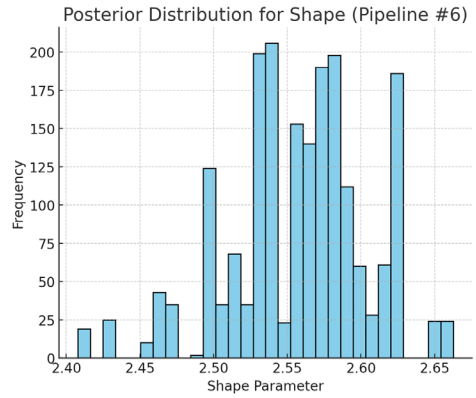
Posterior Distribution for Shape (Pipeline #6)
Frequency
Shape Parameter

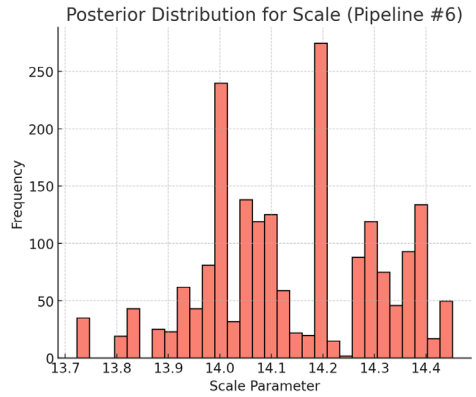
Posterior Distribution for Scale (Pipeline #6)
Frequency
Scale Parameter

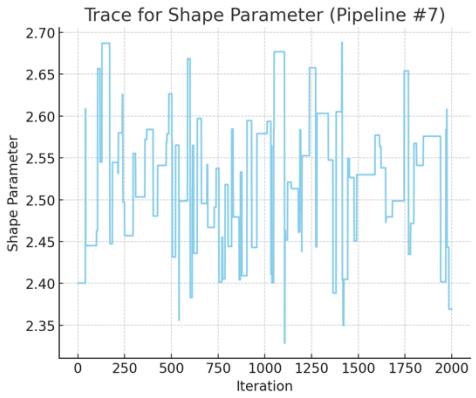
Trace for Shape Parameter (Pipeline #7)
Shape Parameter
Iteration

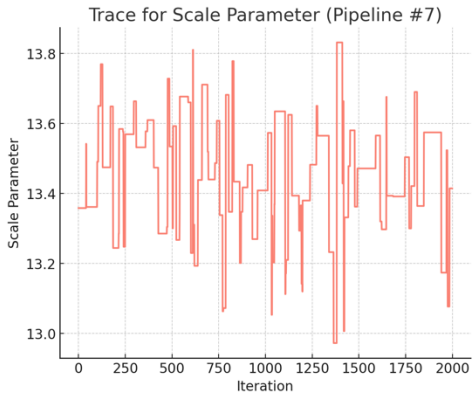
Trace for Scale Parameter (Pipeline #7)
Scale Parameter
Iteration

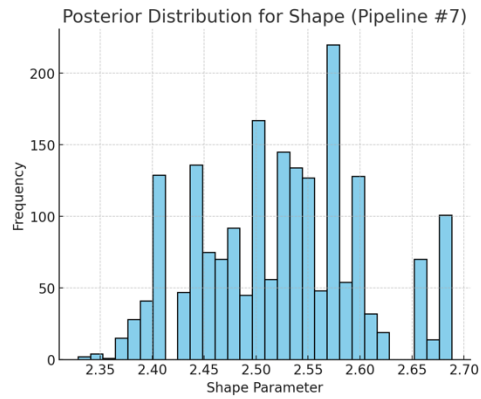
Posterior Distribution for Shape (Pipeline #7)
Frequency
Shape Parameter

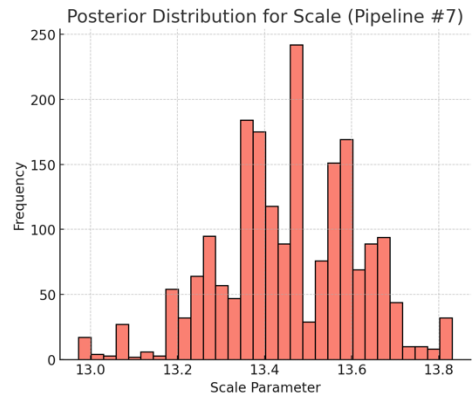
Posterior Distribution for Scale (Pipeline #7)
Frequency
Scale Parameter

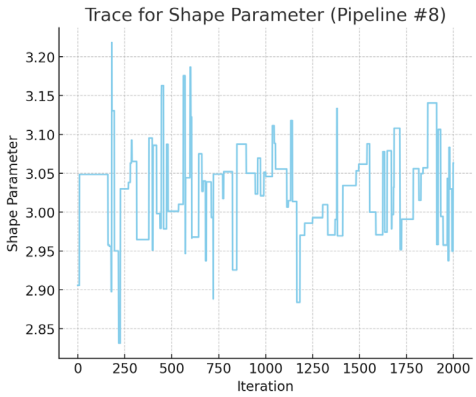
Trace for Shape Parameter (Pipeline #8)
Shape Parameter
Iteration

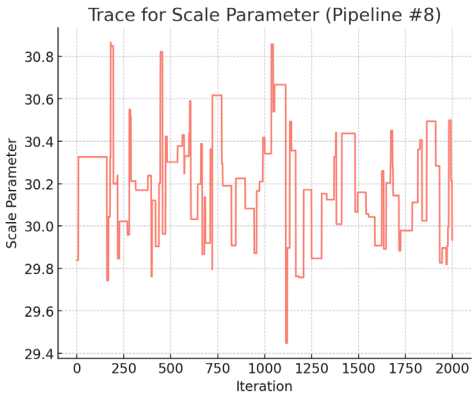
Trace for Scale Parameter (Pipeline #8)
Scale Parameter
Iteration

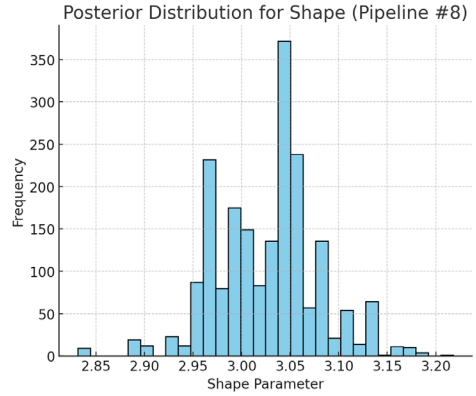
Posterior Distribution for Shape (Pipeline #8)
Frequency
Shape Parameter

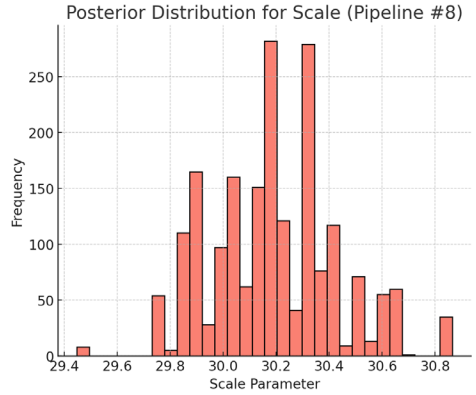
Posterior Distribution for Scale (Pipeline #8)
Frequency
Scale Parameter

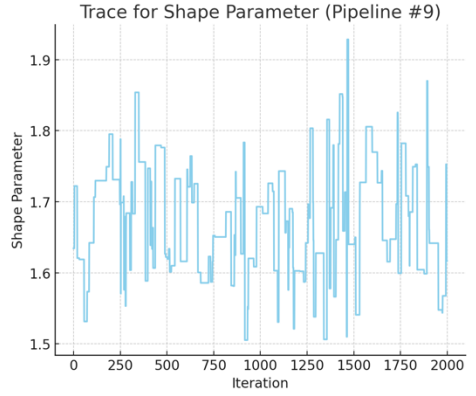
Trace for Shape Parameter (Pipeline #9)
Shape Parameter
Iteration

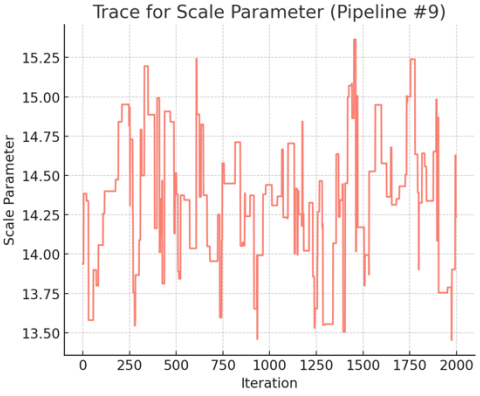
Trace for Scale Parameter (Pipeline #9)
Scale Parameter
Iteration

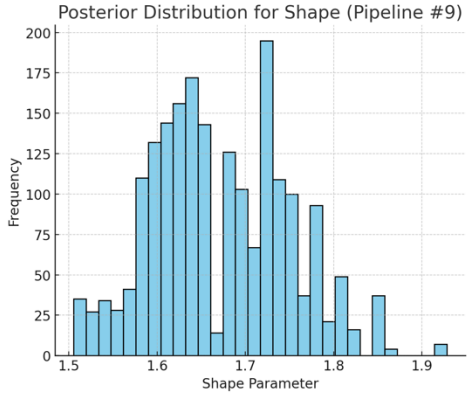
Posterior Distribution for Shape (Pipeline #9)
Frequency
Shape Parameter

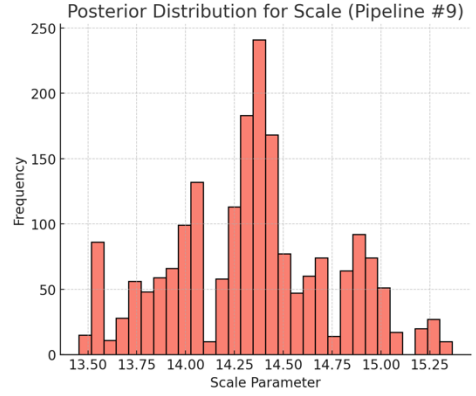
Posterior Distribution for Scale (Pipeline #9)
Frequency
Scale Parameter

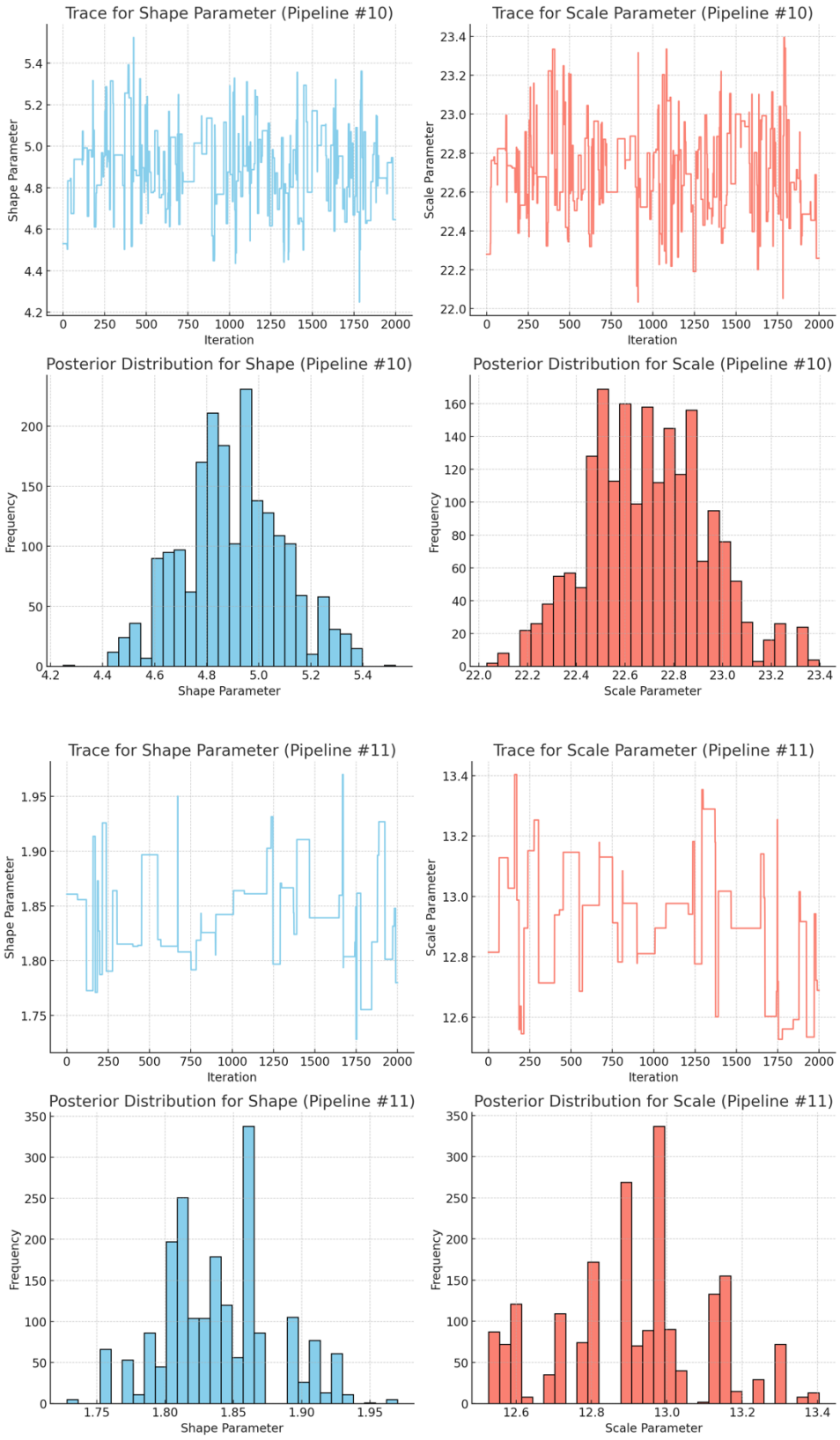
Trace for Shape Parameter (Pipeline #10)
Shape Parameter
Iteration
Trace for Scale Parameter (Pipeline #10)
Scale Parameter
Iteration
Posterior Distribution for Shape (Pipeline #10)
Frequency
Shape Parameter
Posterior Distribution for Scale (Pipeline #10)
Frequency
Scale Parameter
Trace for Shape Parameter (Pipeline #11)
Shape Parameter
Iteration
Trace for Scale Parameter (Pipeline #11)
Scale Parameter
Iteration
Posterior Distribution for Shape (Pipeline #11)
Frequency
Shape Parameter
Posterior Distribution for Scale (Pipeline #11)
Frequency
Scale Parameter

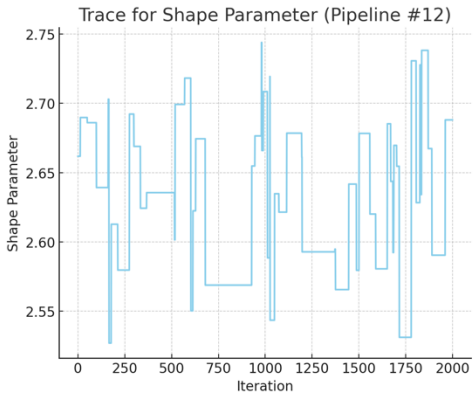
Trace for Shape Parameter (Pipeline #12)
Shape Parameter
Iteration

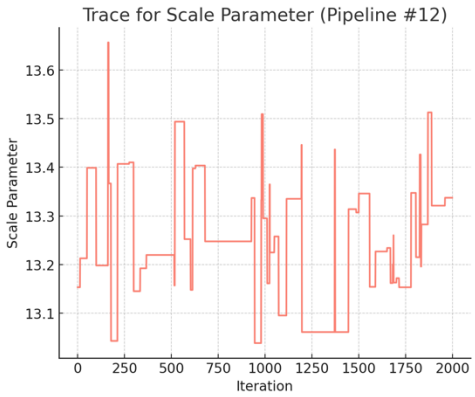
Trace for Scale Parameter (Pipeline #12)
Scale Parameter
Iteration

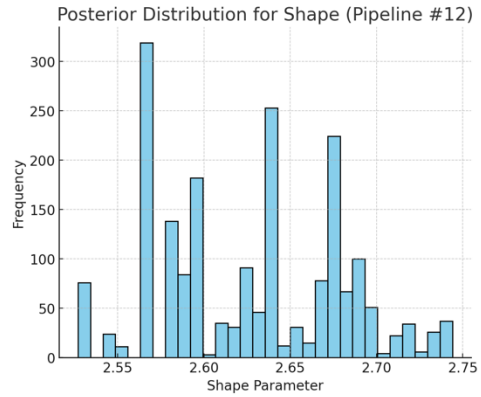
Posterior Distribution for Shape (Pipeline #12)
Frequency
Shape Parameter

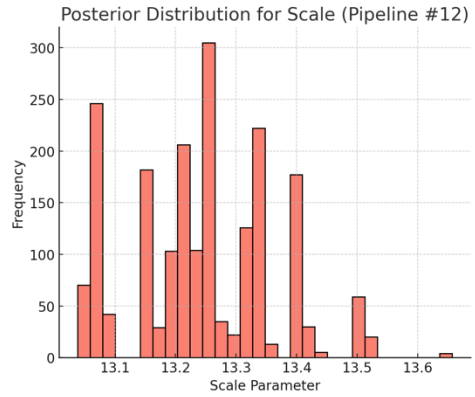
Posterior Distribution for Scale (Pipeline #12)
Frequency
Scale Parameter

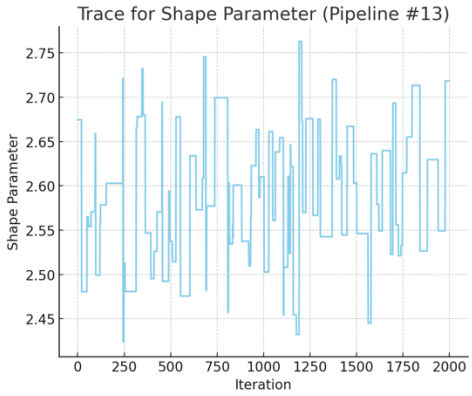
Trace for Shape Parameter (Pipeline #13)
Shape Parameter
Iteration

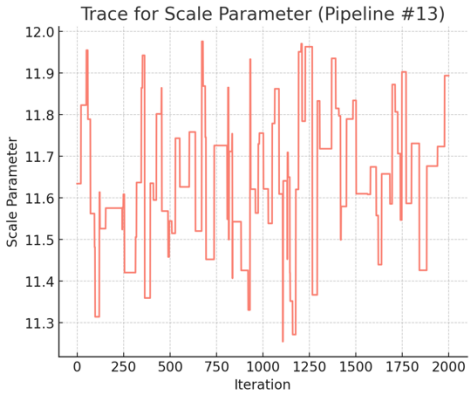
Trace for Scale Parameter (Pipeline #13)
Scale Parameter
Iteration

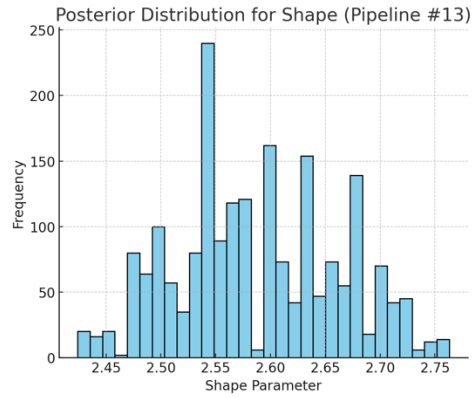
Posterior Distribution for Shape (Pipeline #13)
Frequency
Shape Parameter

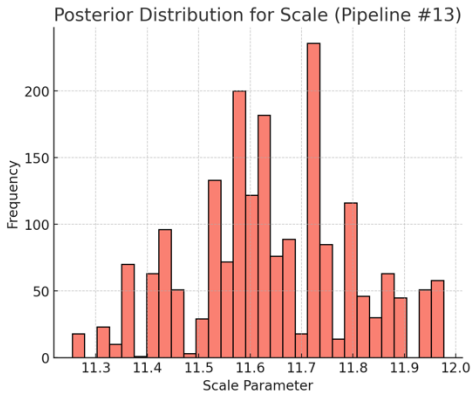
Posterior Distribution for Scale (Pipeline #13)
Frequency
Scale Parameter

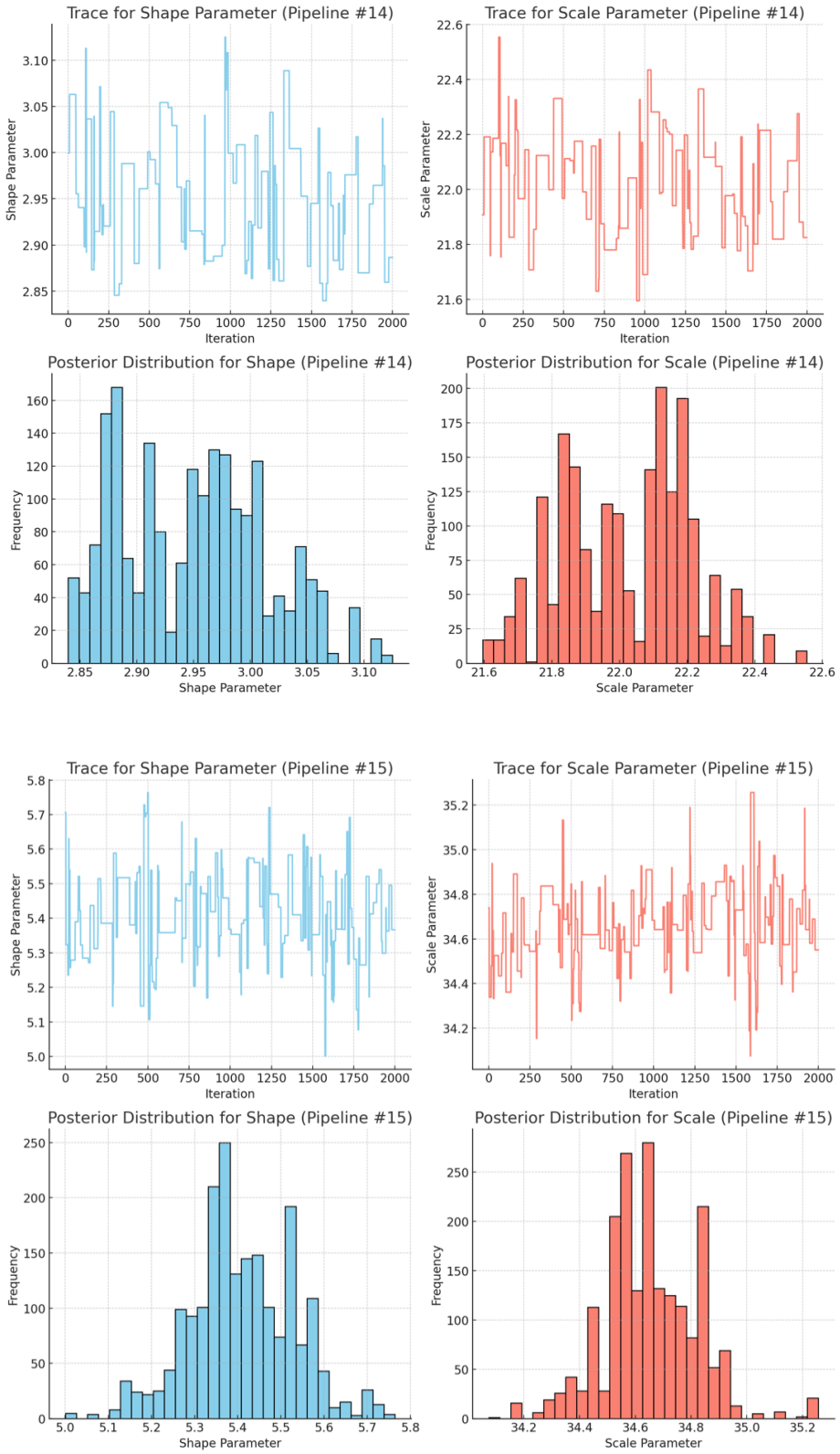

Figure 80. Trace Plots and Histograms of Updated Parameters from BN on Weibull Distribution for all pipeline # of 30-inches data

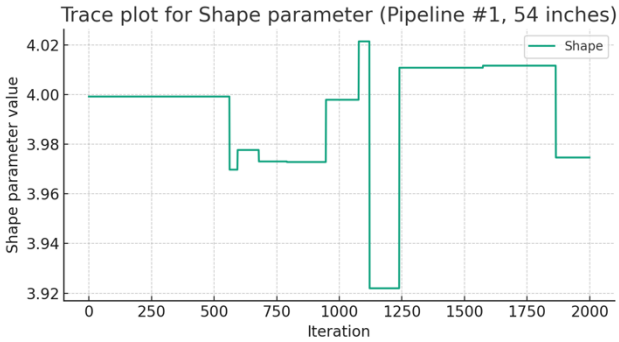
Trace plot for Shape parameter (Pipeline #1, 54 inches)
Shape
Shape parameter value
Iteration

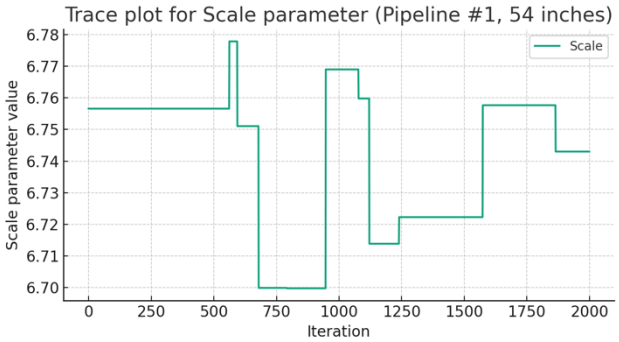
Trace plot for Scale parameter (Pipeline #1, 54 inches)
Scale
Scale parameter value
Iteration

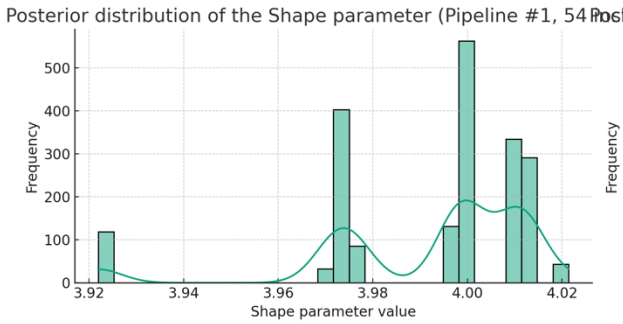
Posterior distribution of the Shape parameter (Pipeline #1, 54 inches)
Frequency
Shape parameter value

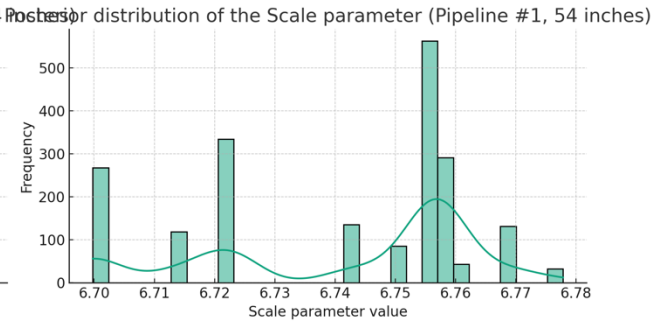
Posterior distribution of the Scale parameter (Pipeline #1, 54 inches)
Frequency
Scale parameter value

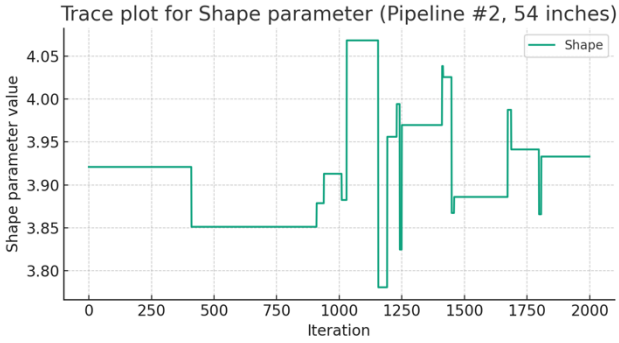
Trace plot for Shape parameter (Pipeline #2, 54 inches)
Shape
Shape parameter value
Iteration

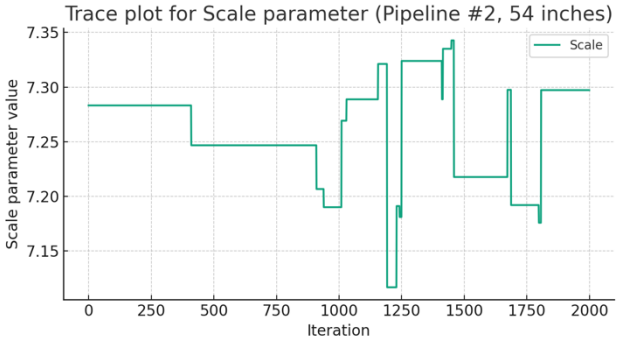
Trace plot for Scale parameter (Pipeline #2, 54 inches)
Scale
Scale parameter value
Iteration

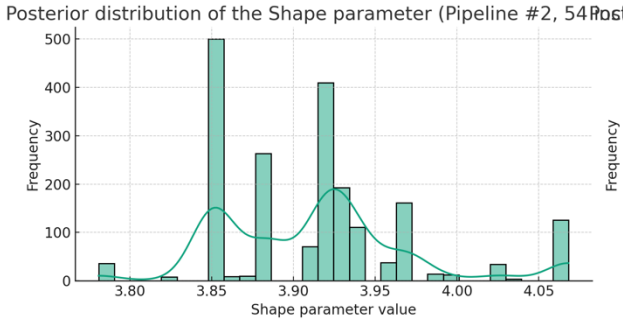
Posterior distribution of the Shape parameter (Pipeline #2, 54 inches)
Frequency
Shape parameter value

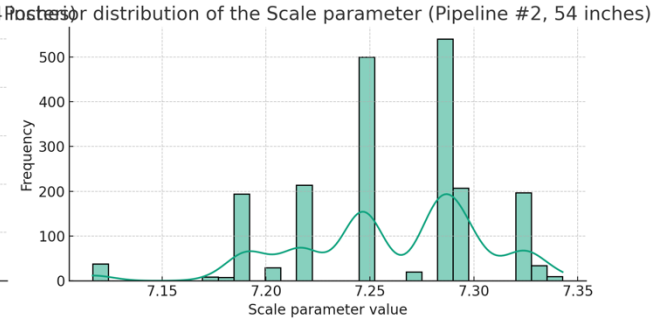
Posterior distribution of the Scale parameter (Pipeline #2, 54 inches)
Frequency
Scale parameter value

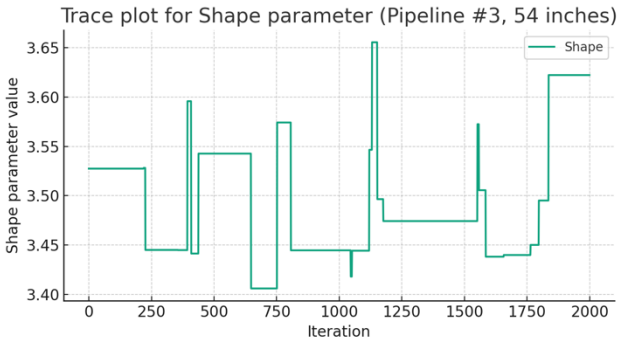
Trace plot for Shape parameter (Pipeline #3, 54 inches)
Shape
Shape parameter value
Iteration

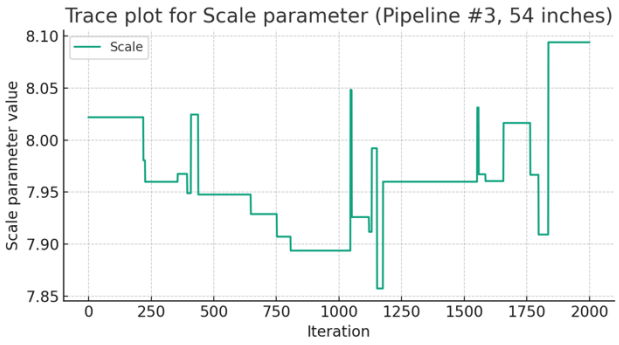
Trace plot for Scale parameter (Pipeline #3, 54 inches)
Scale
Scale parameter value
Iteration

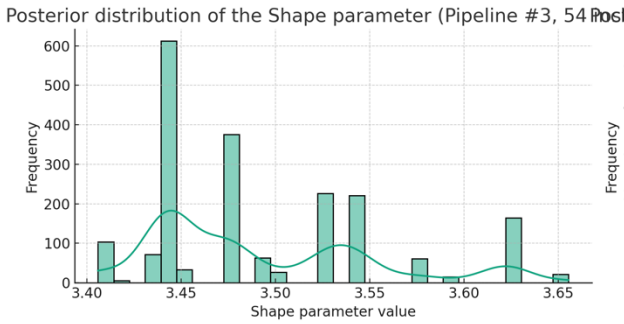
Posterior distribution of the Shape parameter (Pipeline #3, 54 inches)
Frequency
Shape parameter value

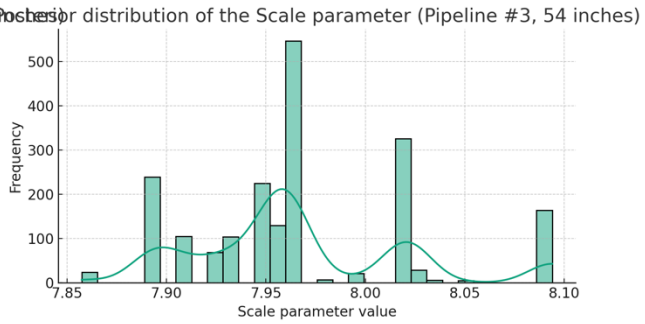
Posterior distribution of the Scale parameter (Pipeline #3, 54 inches)
Frequency
Scale parameter value

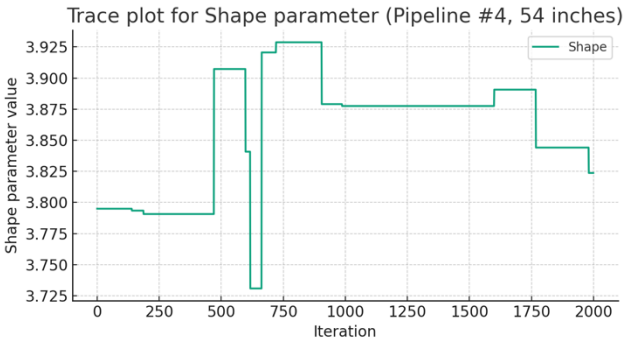
Trace plot for Shape parameter (Pipeline #4, 54 inches)
Shape
Shape parameter value
Iteration

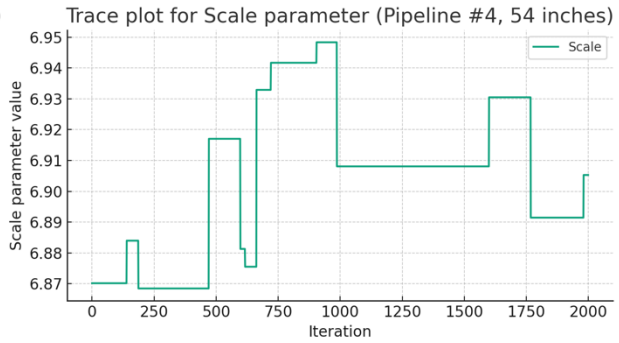
Trace plot for Scale parameter (Pipeline #4, 54 inches)
Scale
Scale parameter value
Iteration

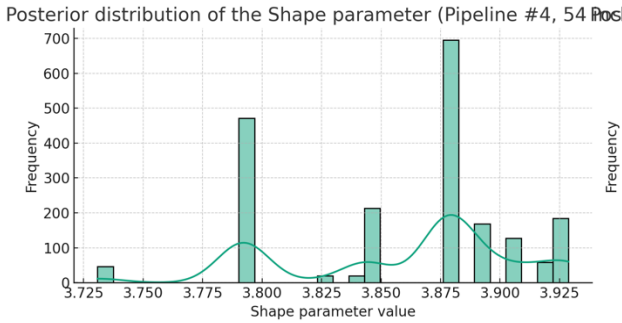
Posterior distribution of the Shape parameter (Pipeline #4, 54 inches)
Frequency
Shape parameter value

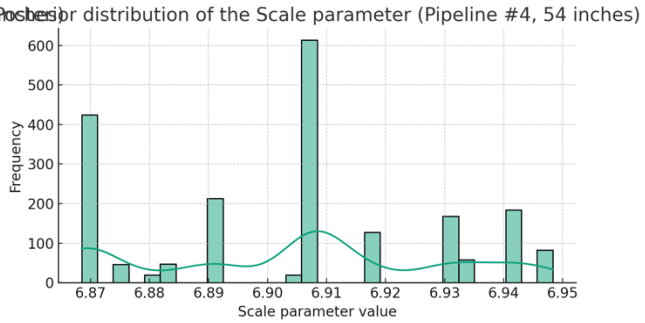
Posterior distribution of the Scale parameter (Pipeline #4, 54 inches)
Frequency
Scale parameter value

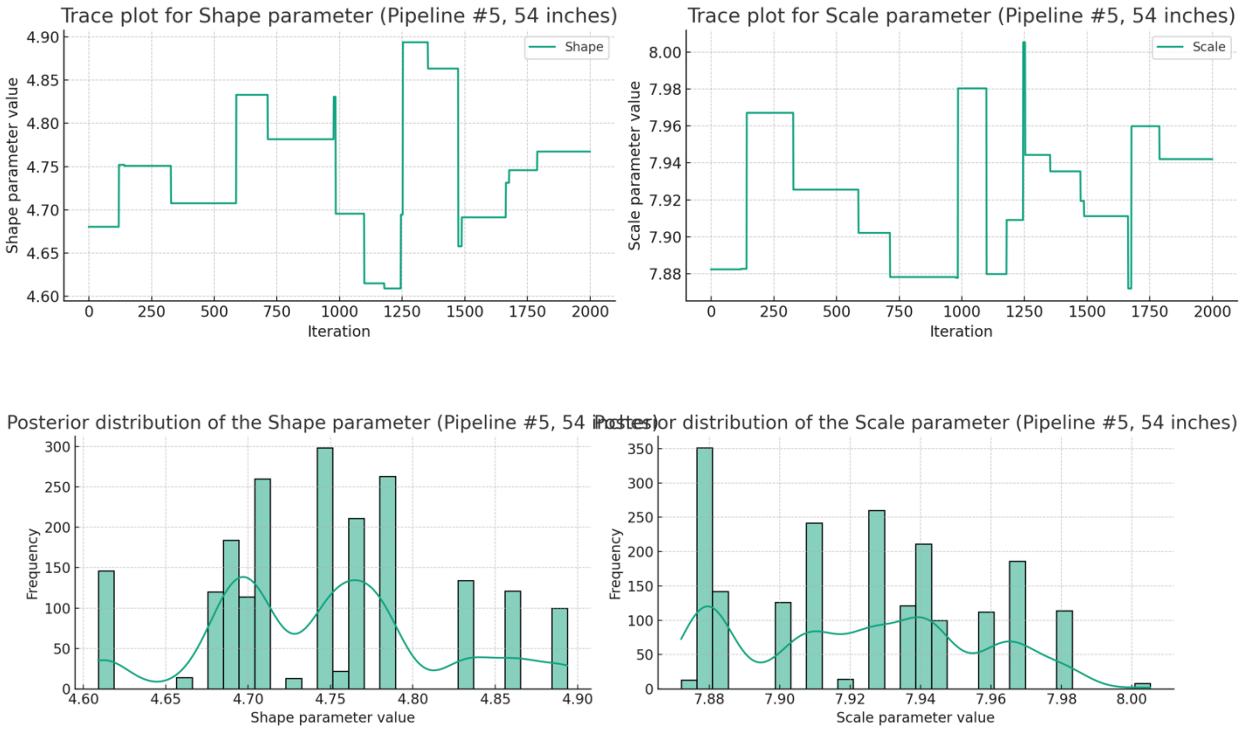

Figure 81. Trace Plots and Histograms of Updated Parameters from BN on Weibull Distribution for all pipeline # of 54-inches data

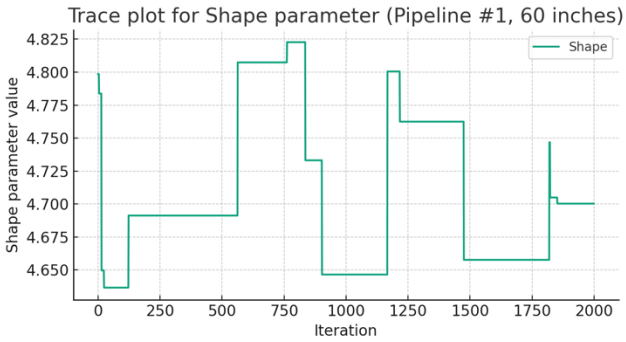
Trace plot for Shape parameter (Pipeline #1, 60 inches)
Shape
Shape parameter value
Iteration

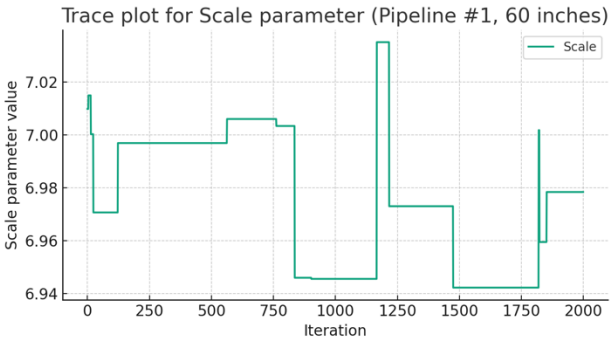
Trace plot for Scale parameter (Pipeline #1, 60 inches)
Scale
Scale parameter value
Iteration

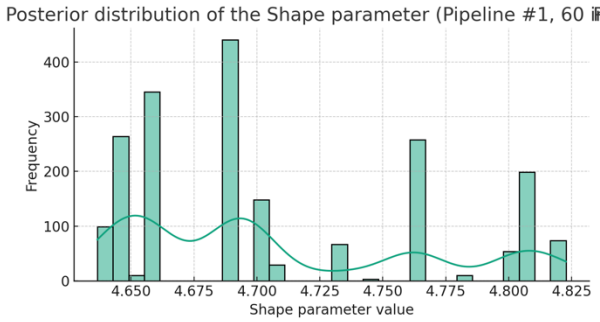
Posterior distribution of the Shape parameter (Pipeline #1, 60 inches)
Frequency
Shape parameter value

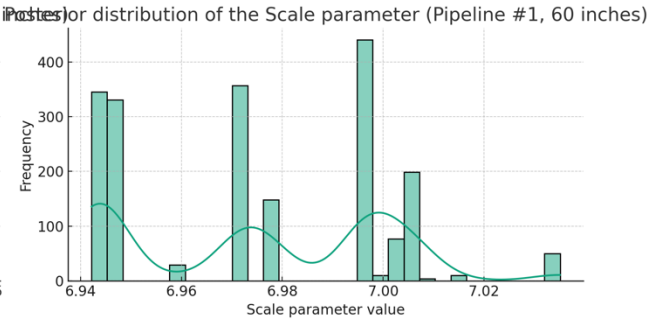
Posterior distribution of the Scale parameter (Pipeline #1, 60 inches)
Frequency
Scale parameter value

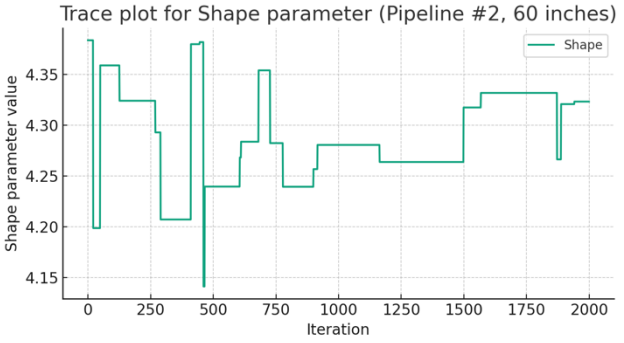
Trace plot for Shape parameter (Pipeline #2, 60 inches)
Shape
Shape parameter value
Iteration

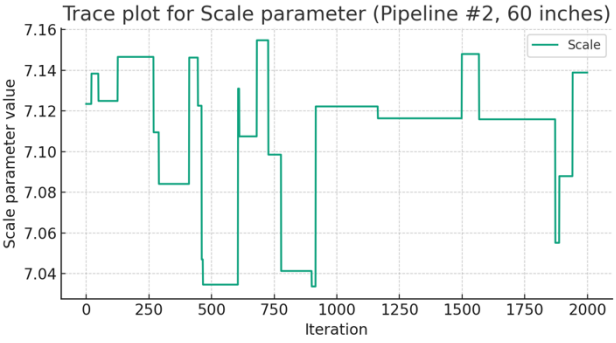
Trace plot for Scale parameter (Pipeline #2, 60 inches)
Scale
Scale parameter value
Iteration

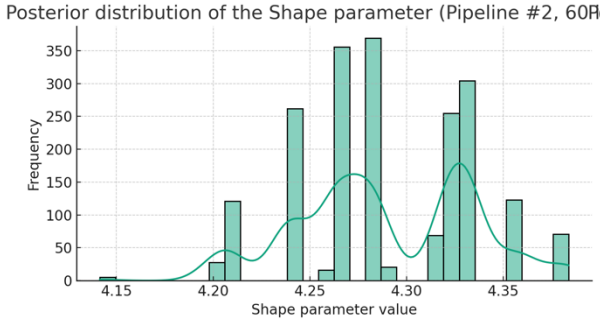
Posterior distribution of the Shape parameter (Pipeline #2, 60 inches)
Frequency
Shape parameter value

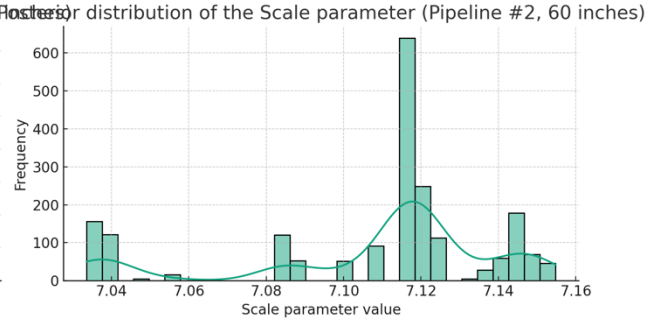
Posterior distribution of the Scale parameter (Pipeline #2, 60 inches)
Frequency
Scale parameter value

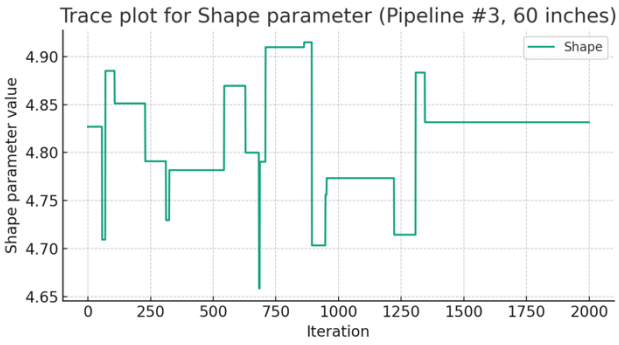
Trace plot for Shape parameter (Pipeline #3, 60 inches)
Shape
Shape parameter value
Iteration

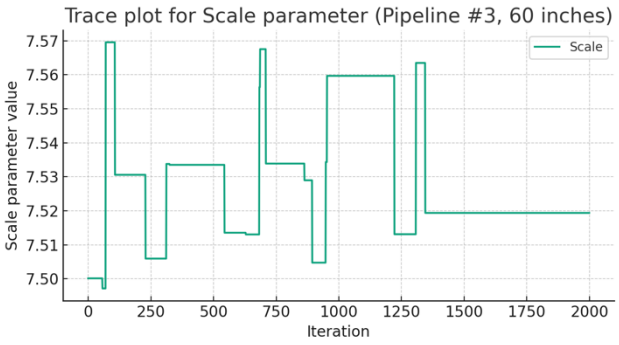
Trace plot for Scale parameter (Pipeline #3, 60 inches)
Scale
Scale parameter value
Iteration

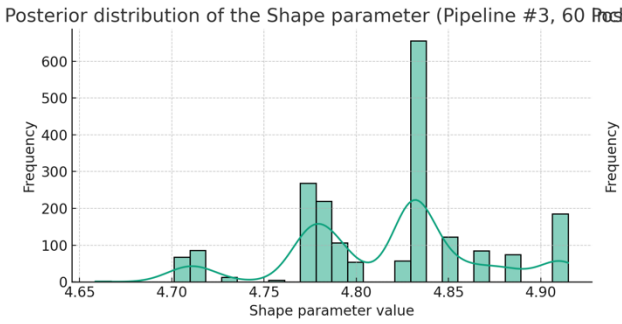
Posterior distribution of the Shape parameter (Pipeline #3, 60 inches)
Frequency
Shape parameter value

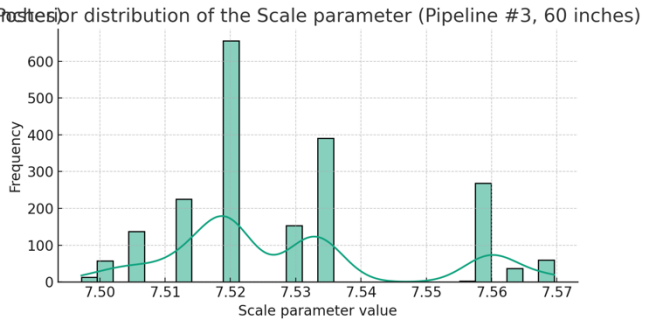
Posterior distribution of the Scale parameter (Pipeline #3, 60 inches)
Frequency
Scale parameter value

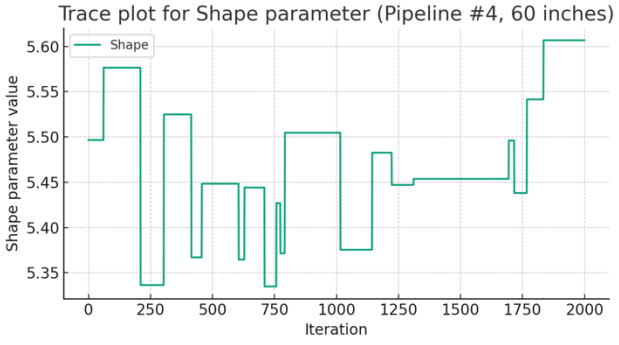
Trace plot for Shape parameter (Pipeline #4, 60 inches)
Shape
Shape parameter value
Iteration

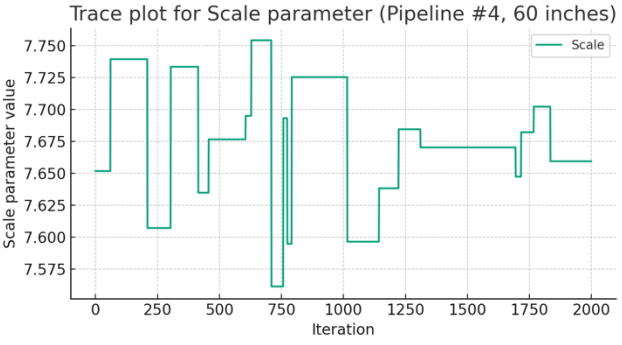
Trace plot for Scale parameter (Pipeline #4, 60 inches)
Scale
Scale parameter value
Iteration

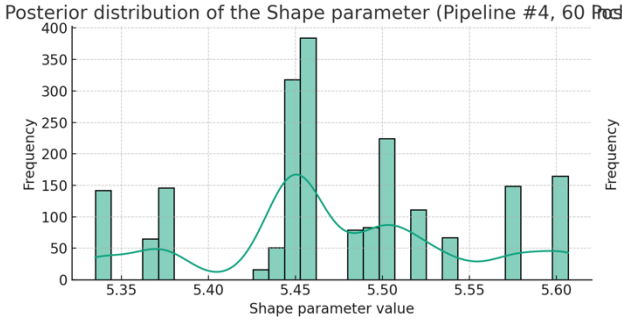
Posterior distribution of the Shape parameter (Pipeline #4, 60 inches)
Frequency
Shape parameter value

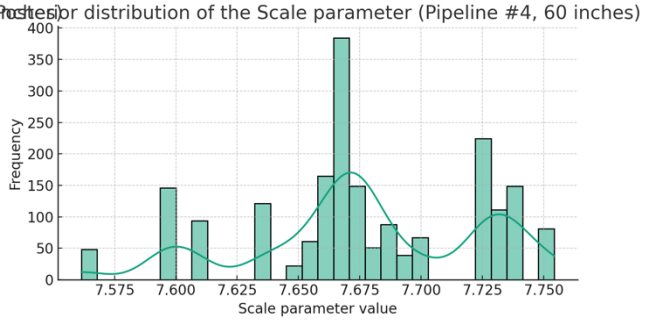
Posterior distribution of the Scale parameter (Pipeline #4, 60 inches)
Frequency
Scale parameter value

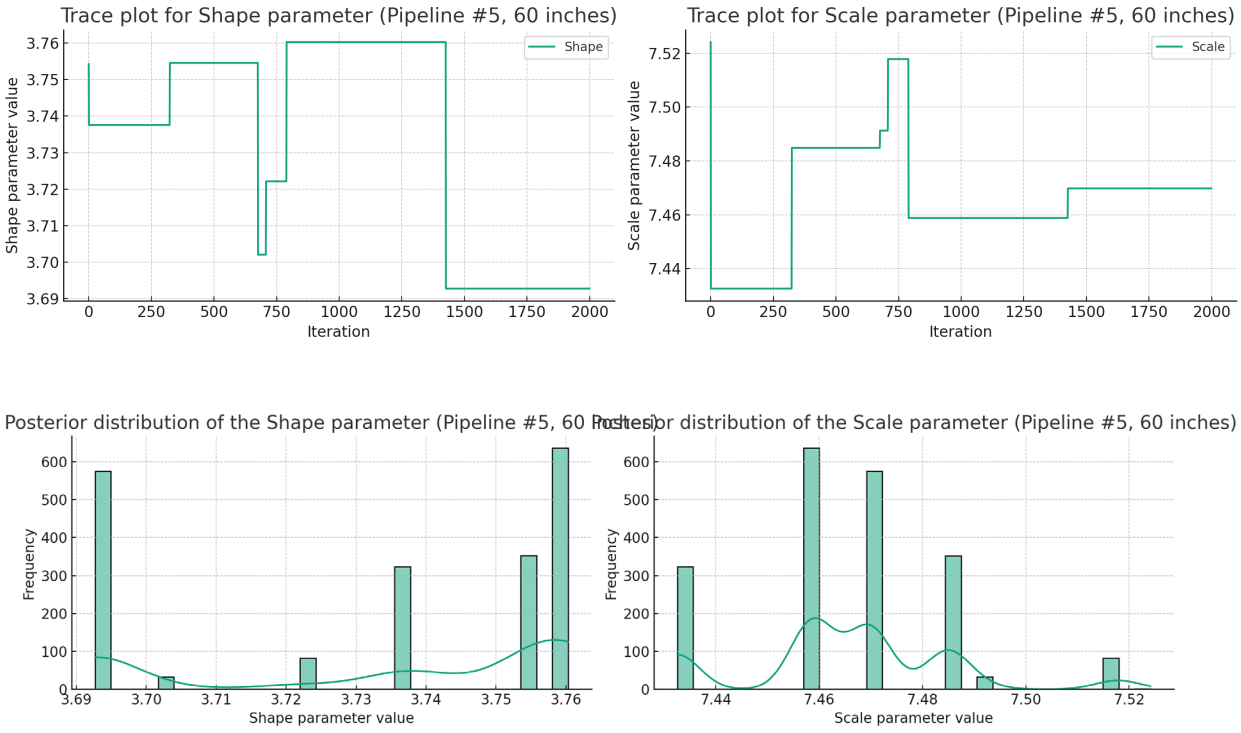

Figure 82. Trace Plots and Histograms of Updated Parameters from BN on Weibull Distribution for all pipeline # of 60-inches data

Figure 79-Figure 81 show the results from BN for updating the parameters of Gamma distribution,

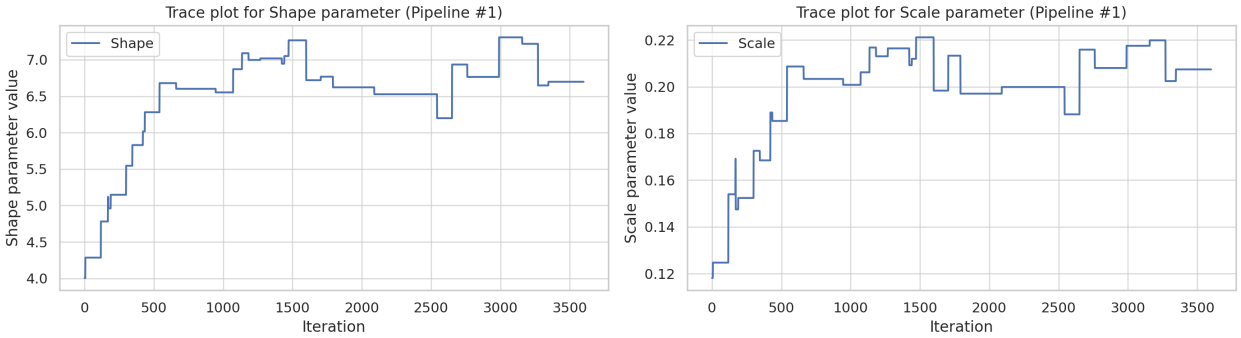

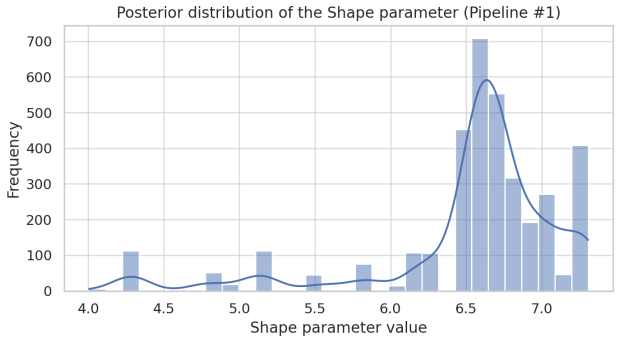
Posterior distribution of the Shape parameter (Pipeline #1)
Frequency
Shape parameter value

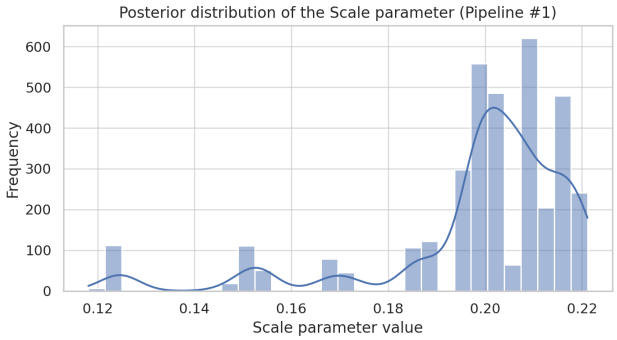
Posterior distribution of the Scale parameter (Pipeline #1)
Frequency
Scale parameter value

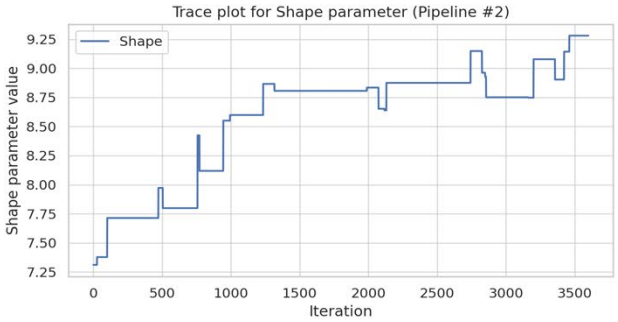
Trace plot for Shape parameter (Pipeline #2)
Shape
Shape parameter value
Iteration

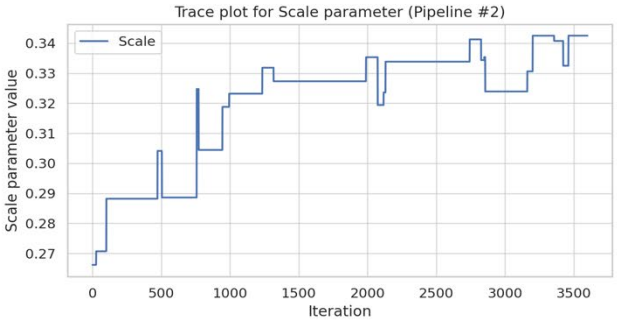
Trace plot for Scale parameter (Pipeline #2)
Scale
Scale parameter value
Iteration

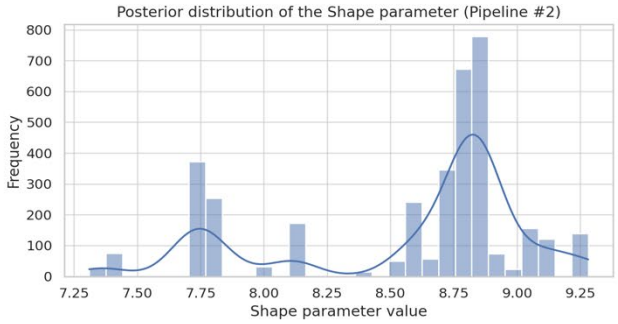
Posterior distribution of the Shape parameter (Pipeline #2)
Frequency
Shape parameter value

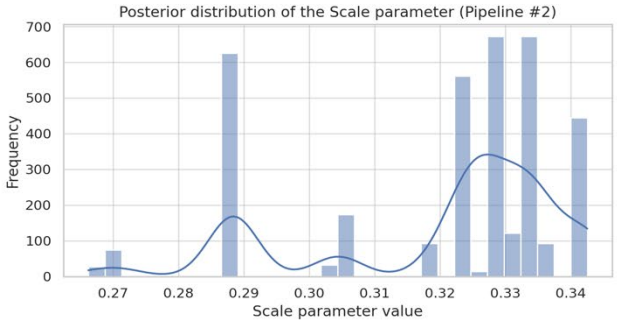
Posterior distribution of the Scale parameter (Pipeline #2)
Frequency
Scale parameter value

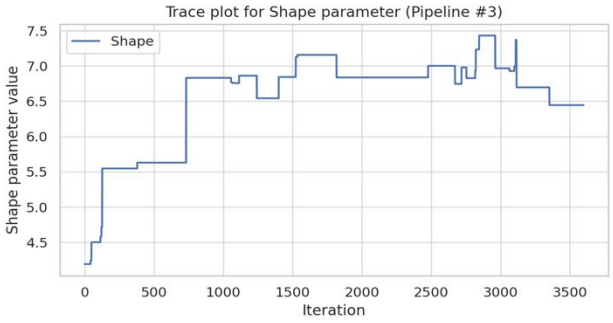
Trace plot for Shape parameter (Pipeline #3)
Shape
Shape parameter value
Iteration

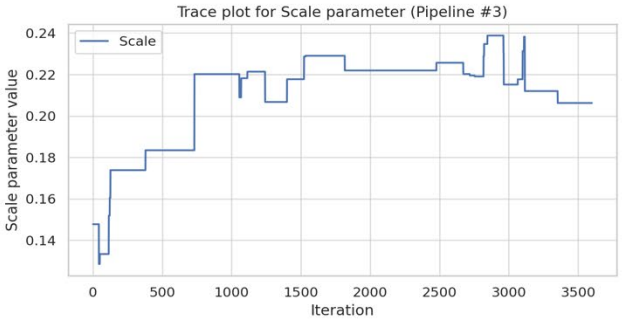
Trace plot for Scale parameter (Pipeline #3)
Scale
Scale parameter value
Iteration

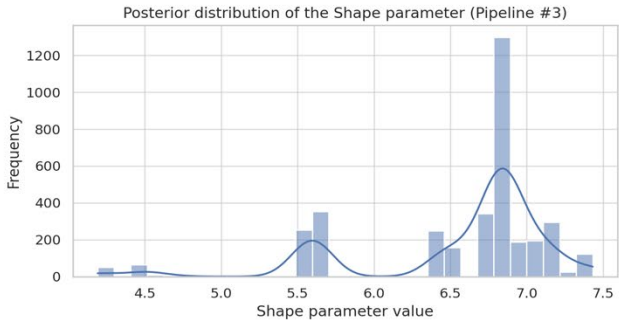
Posterior distribution of the Shape parameter (Pipeline #3)
Frequency
Shape parameter value

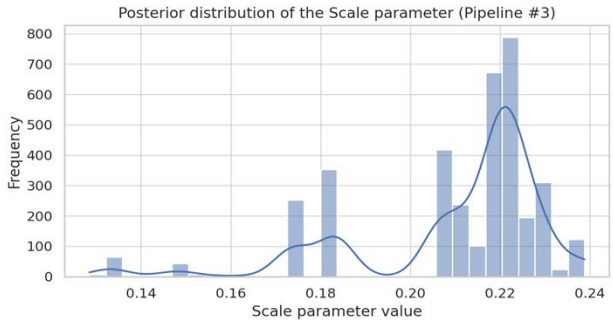
Posterior distribution of the Scale parameter (Pipeline #3)
Frequency
Scale parameter value

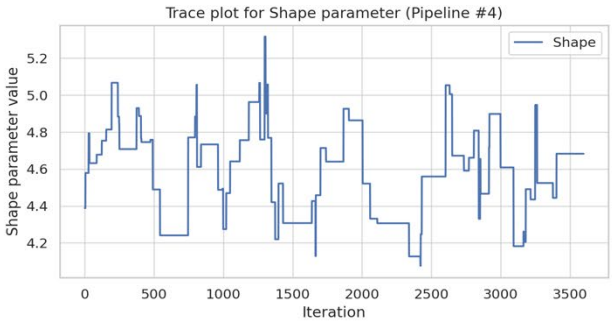
Trace plot for Shape parameter (Pipeline #4)
Shape
Shape parameter value
Iteration

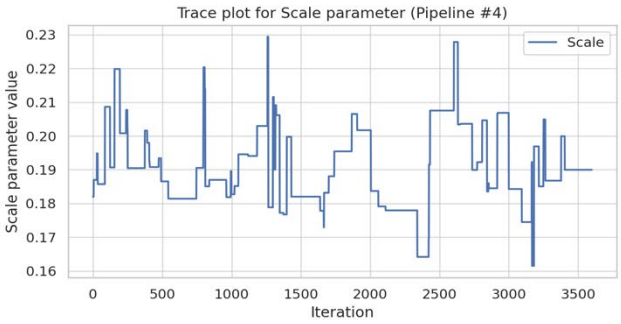
Trace plot for Scale parameter (Pipeline #4)
Scale
Scale parameter value
Iteration

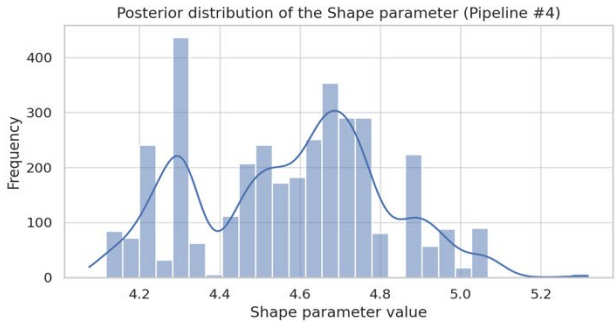
Posterior distribution of the Shape parameter (Pipeline #4)
Frequency
Shape parameter value

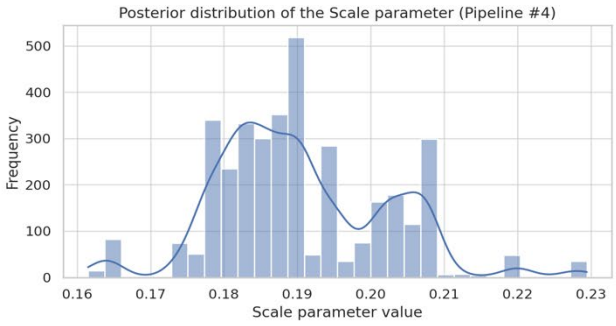
Posterior distribution of the Scale parameter (Pipeline #4)
Frequency
Scale parameter value

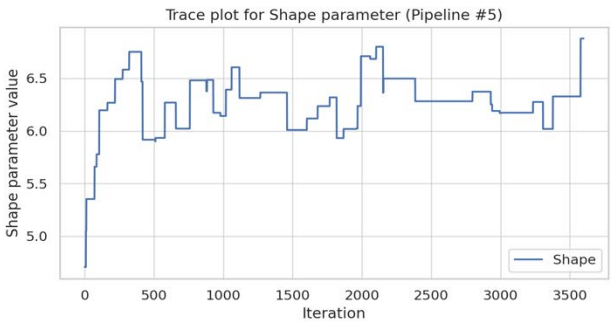
Trace plot for Shape parameter (Pipeline #5)
Shape
Shape parameter value
Iteration

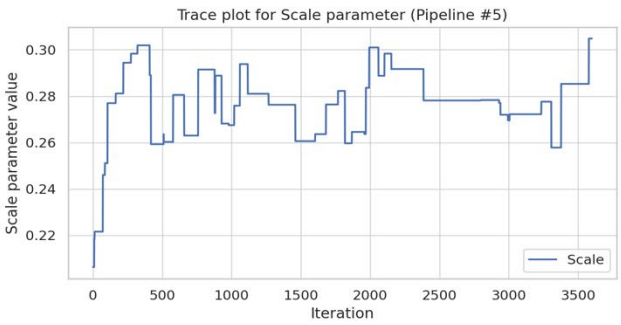
Trace plot for Scale parameter (Pipeline #5)
Scale
Scale parameter value
Iteration

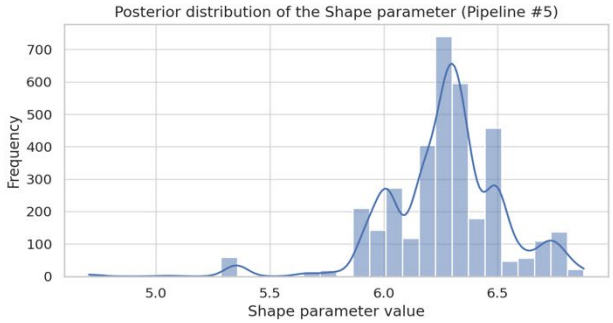
Posterior distribution of the Shape parameter (Pipeline #5)
Frequency
Shape parameter value

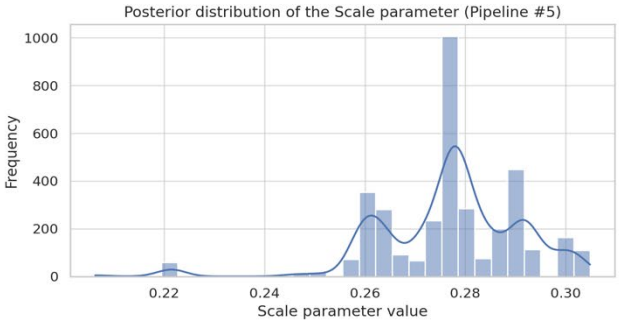
Posterior distribution of the Scale parameter (Pipeline #5)
Frequency
Scale parameter value

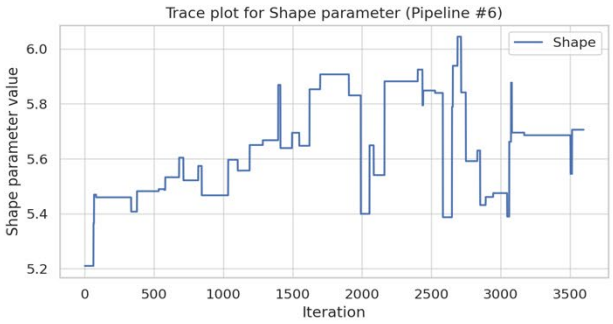
Trace plot for Shape parameter (Pipeline #6)
Shape
Shape parameter value
Iteration

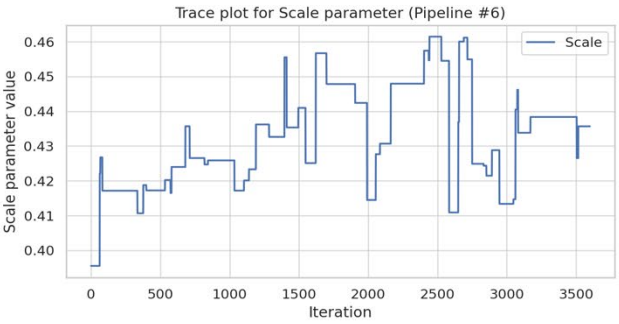
Trace plot for Scale parameter (Pipeline #6)
Scale
Scale parameter value
Iteration

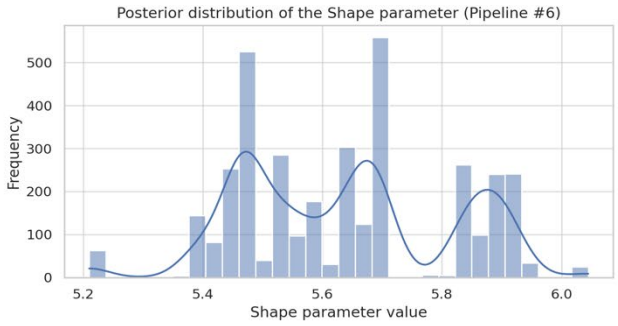
Posterior distribution of the Shape parameter (Pipeline #6)
Frequency
Shape parameter value

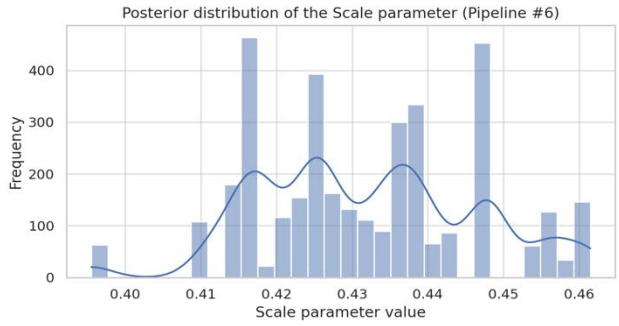
Posterior distribution of the Scale parameter (Pipeline #6)
Frequency
Scale parameter value

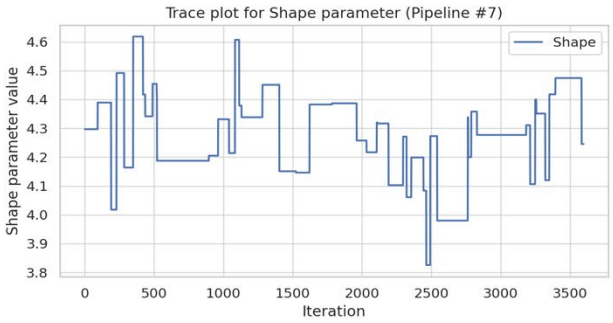
Trace plot for Shape parameter (Pipeline #7)
Shape
Shape parameter value
Iteration

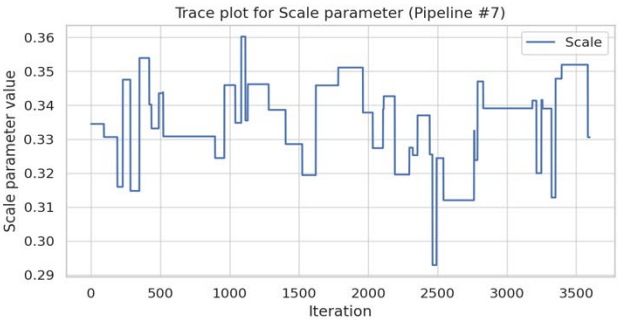
Trace plot for Scale parameter (Pipeline #7)
Scale
Scale parameter value
Iteration

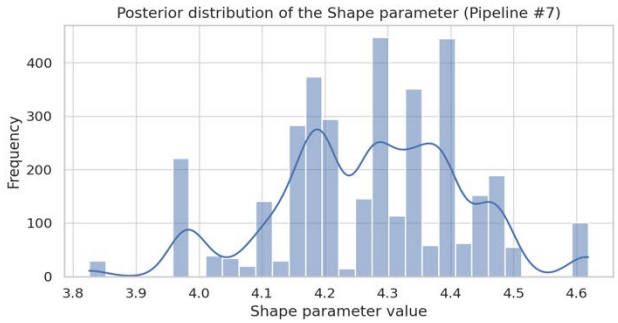
Posterior distribution of the Shape parameter (Pipeline #7)
Frequency
Shape parameter value

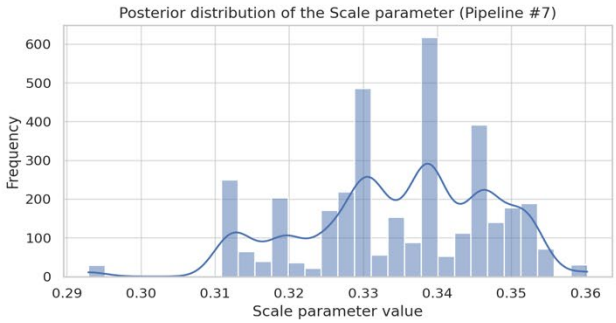
Posterior distribution of the Scale parameter (Pipeline #7)
Frequency
Scale parameter value

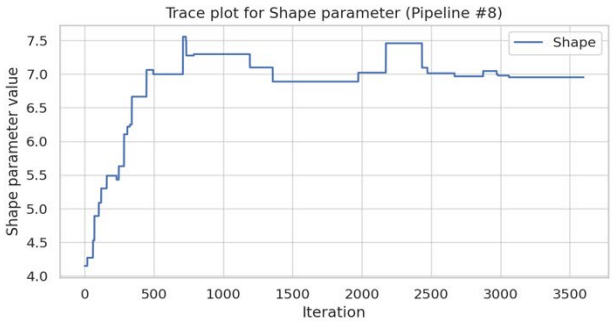
Trace plot for Shape parameter (Pipeline #8)
Shape
Shape parameter value
Iteration

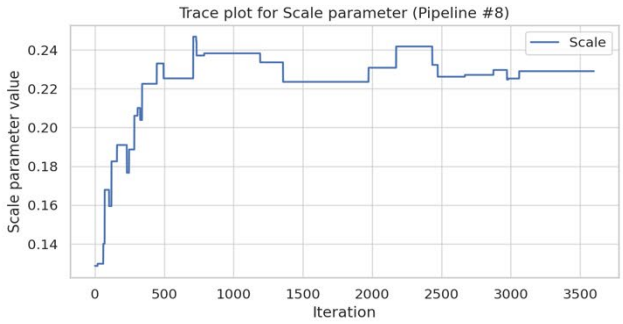
Trace plot for Scale parameter (Pipeline #8)
Scale
Scale parameter value
Iteration

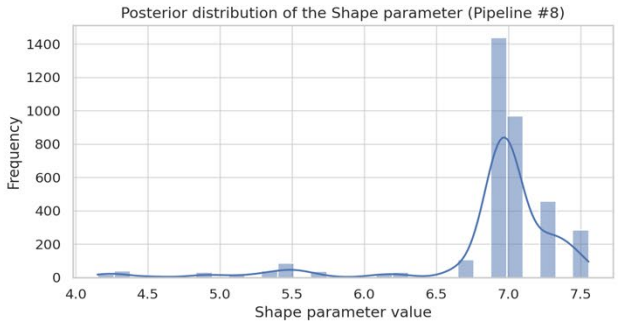
Posterior distribution of the Shape parameter (Pipeline #8)
Frequency
Shape parameter value

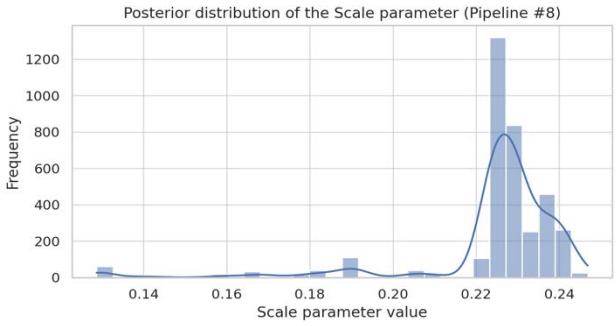
Posterior distribution of the Scale parameter (Pipeline #8)
Frequency
Scale parameter value

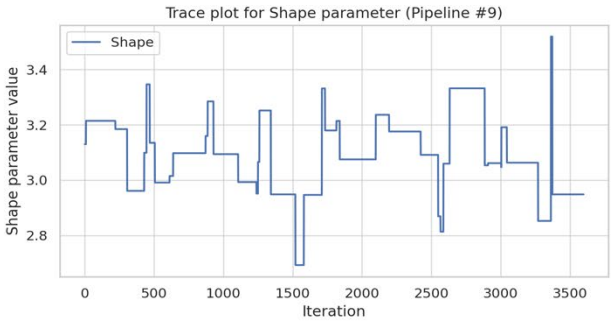
Trace plot for Shape parameter (Pipeline #9)
Shape
Shape parameter value
Iteration

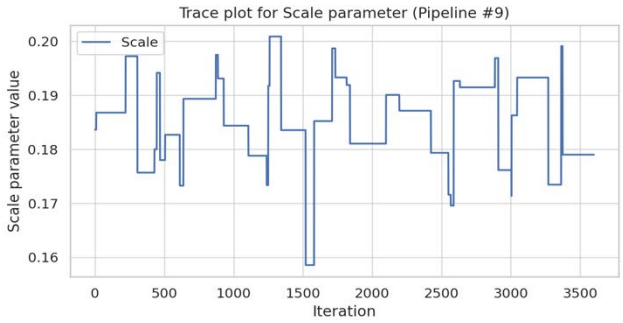
Trace plot for Scale parameter (Pipeline #9)
Scale
Scale parameter value
Iteration

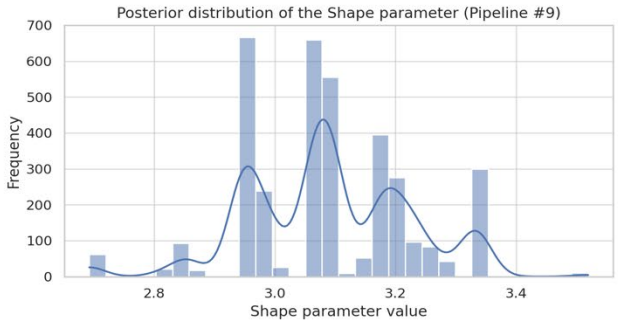
Posterior distribution of the Shape parameter (Pipeline #9)
Frequency
Shape parameter value

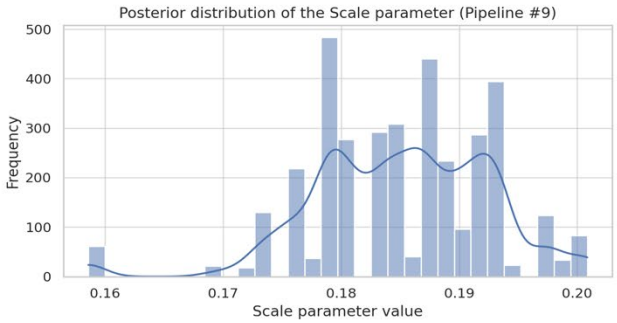
Posterior distribution of the Scale parameter (Pipeline #9)
Frequency
Scale parameter value

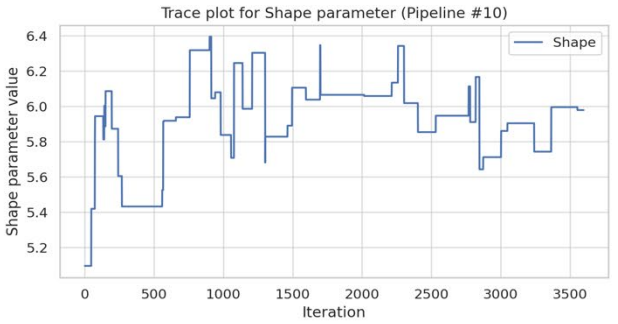
Trace plot for Shape parameter (Pipeline #10)
Shape
Shape parameter value
Iteration

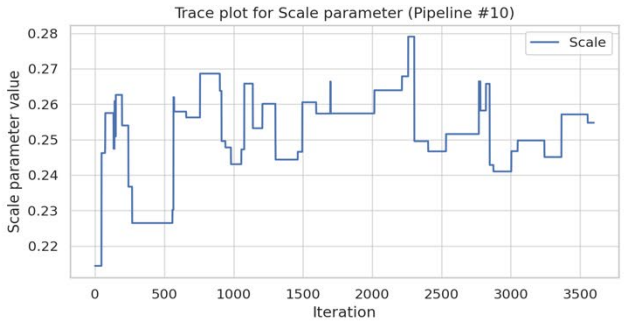
Trace plot for Scale parameter (Pipeline #10)
Scale
Scale parameter value
Iteration

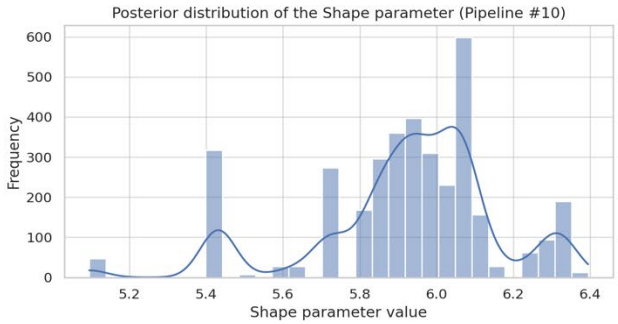
Posterior distribution of the Shape parameter (Pipeline #10)
Frequency
Shape parameter value

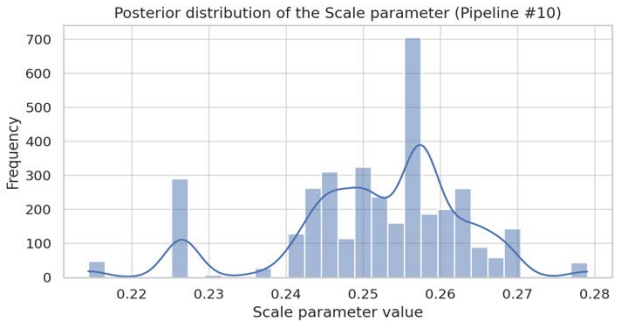
Posterior distribution of the Scale parameter (Pipeline #10)
Frequency
Scale parameter value

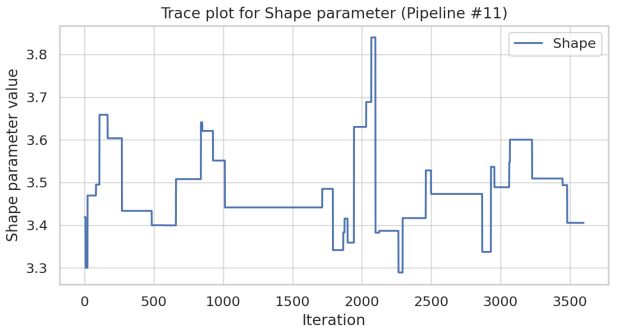
Trace plot for Shape parameter (Pipeline #11)
Shape
Shape parameter value
Iteration

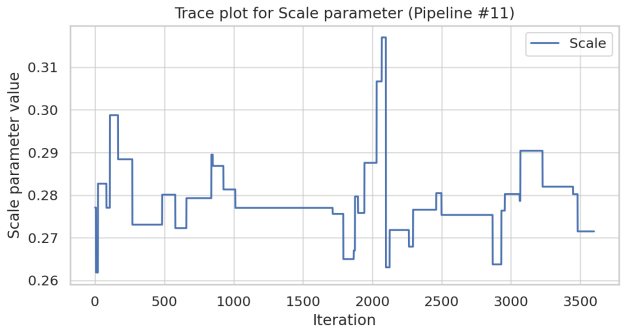
Trace plot for Scale parameter (Pipeline #11)
Scale
Scale parameter value
Iteration

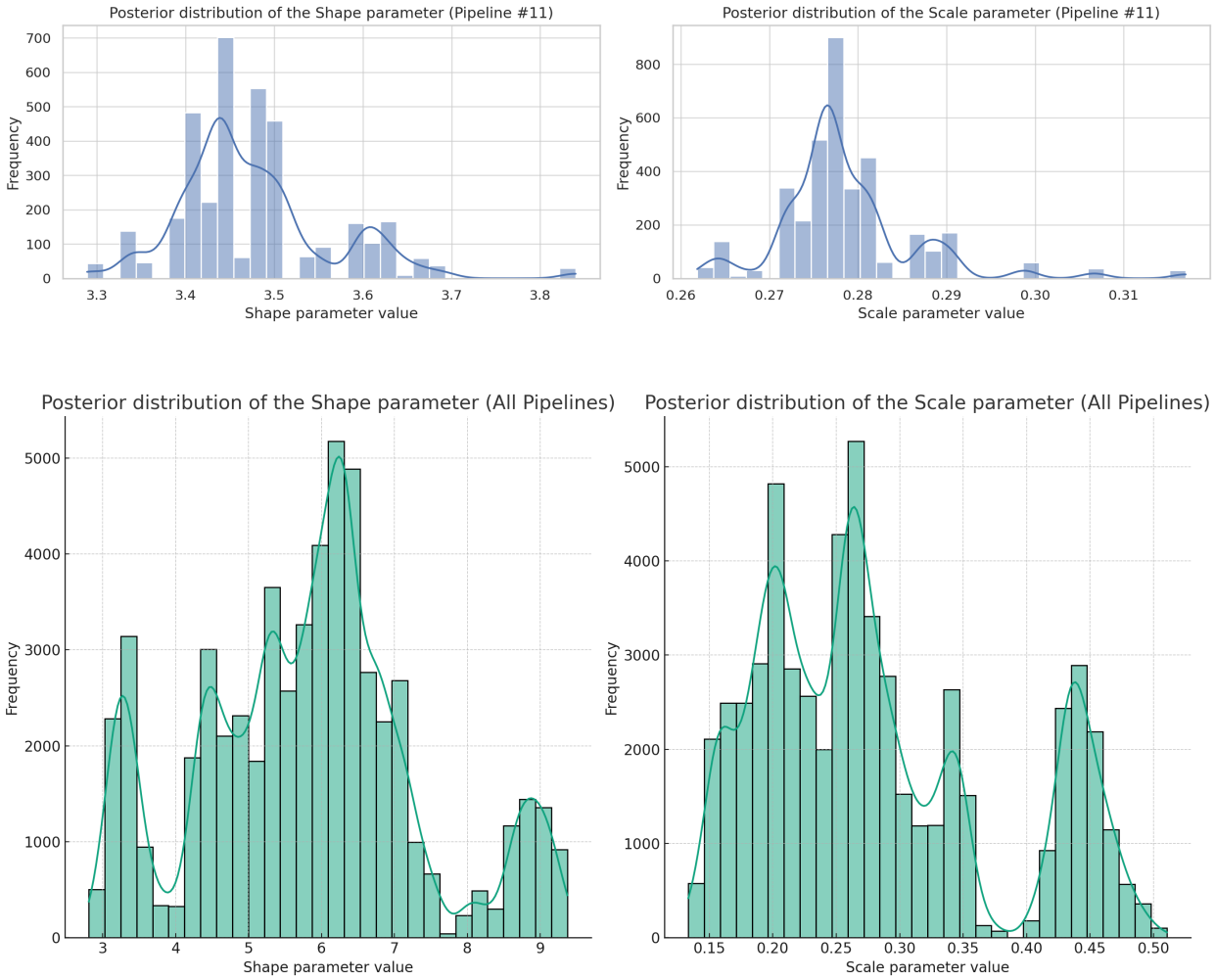

Figure 83. Trace Plots and Histograms of Updated Parameters from BN on Gamma Distribution for all pipeline # of 30-inches data

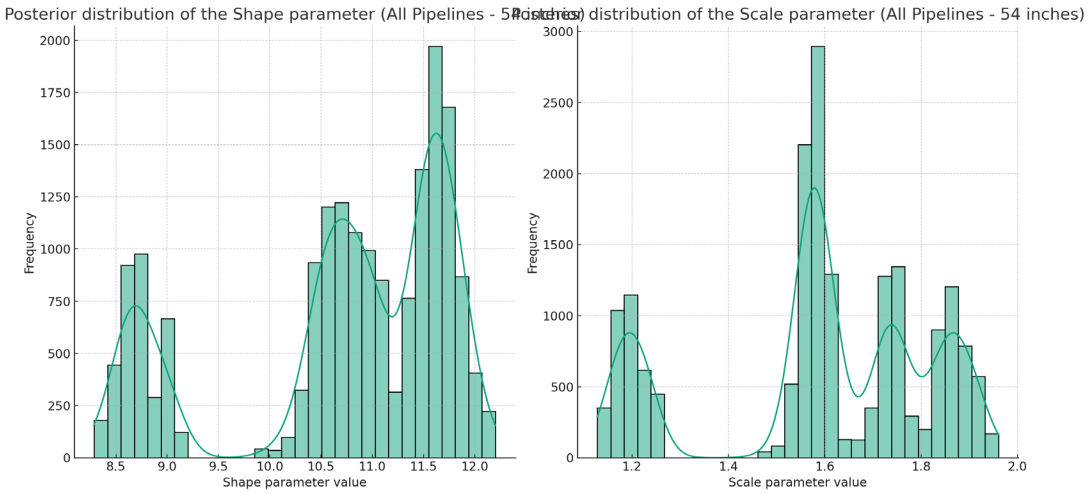

Figure 84. Trace Plots and Histograms of Updated Parameters from BN on Gamma Distribution for all pipeline # of 54-inches data

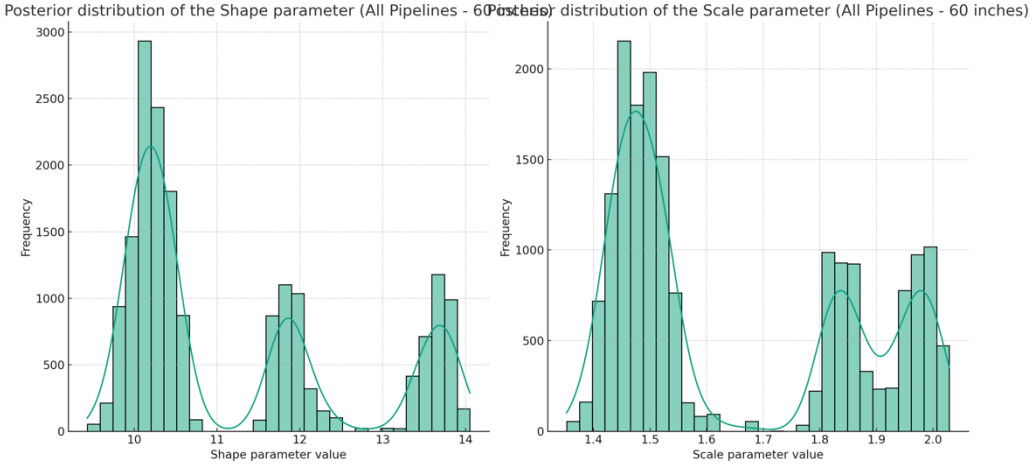

Figure 85. Trace Plots and Histograms of Updated Parameters from BN on Gamma Distribution for all pipeline # of 60-inches data

APPENDIX C – PROBABILITY CURVES FOR DIFFERENT METHODS ON THE UPDATED DATA USING BAYESIAN NETWORK

Figure 86 shows probability curves of different pipelines for 30-inche data of updated values from BN using Gamma distributions functions. Here, different methods are used: probability of exceedance method (discussed in subsection 3.4.10.1) using Half Normal Distribution, Normal Distribution, Exponential distribution, Weibull Distribution, and MCS method on Power law (Equation 22) for the updated values of BN.

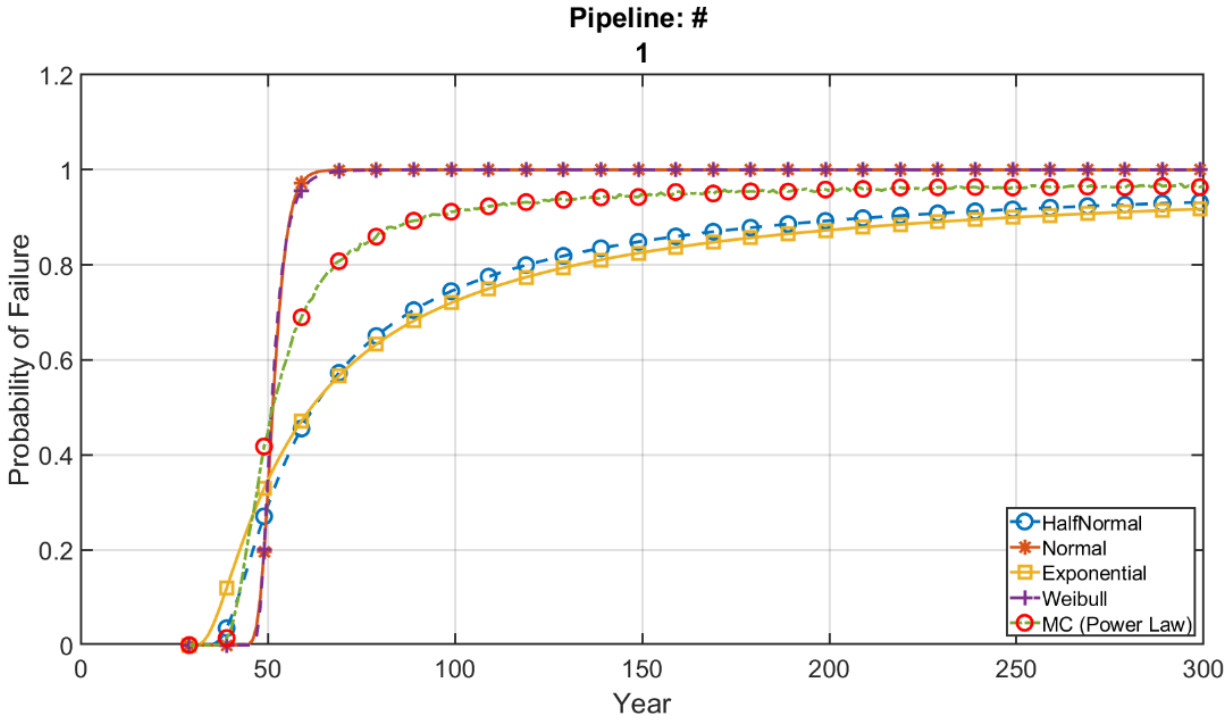

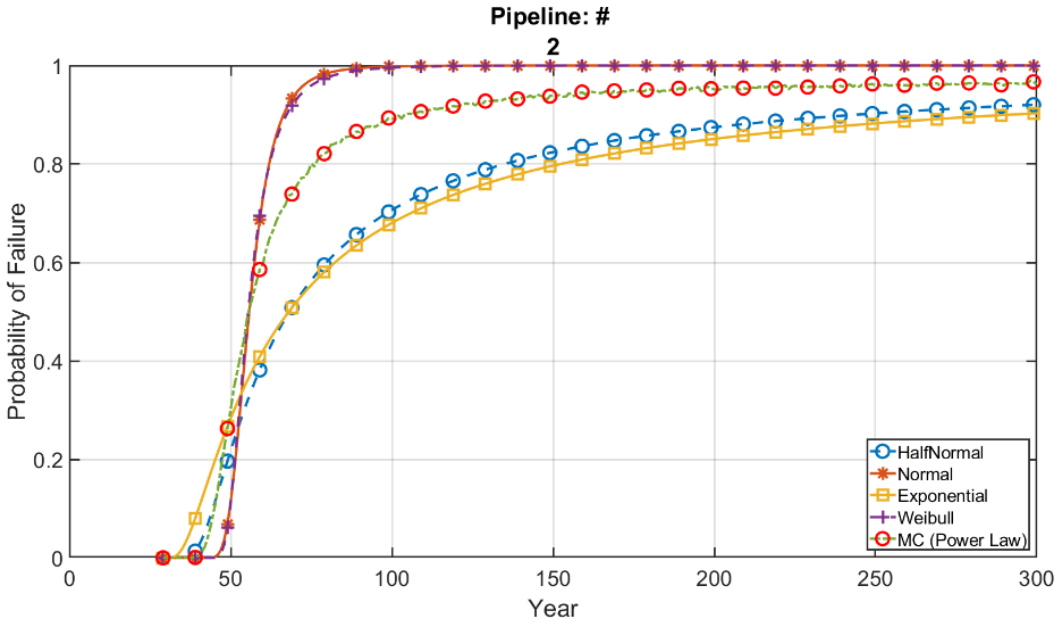
Pipeline: #
2
Probability of Failure
Year
HalfNormal
Normal
Exponential
Weibull
MC (Power Law)

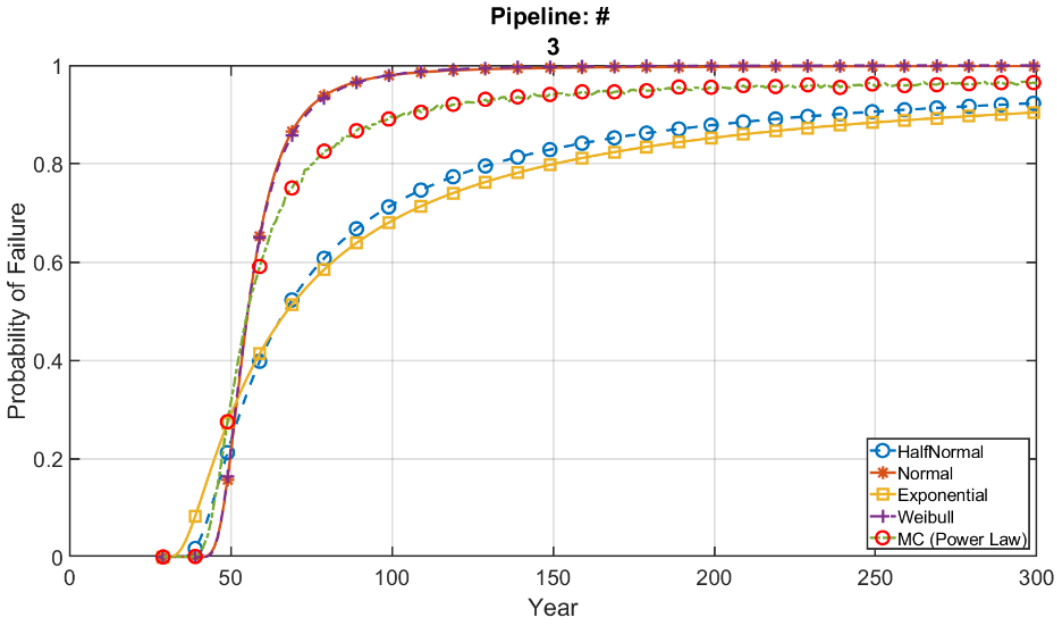
Pipeline: #
3
Probability of Failure
Year
HalfNormal
Normal
Exponential
Weibull
MC (Power Law)

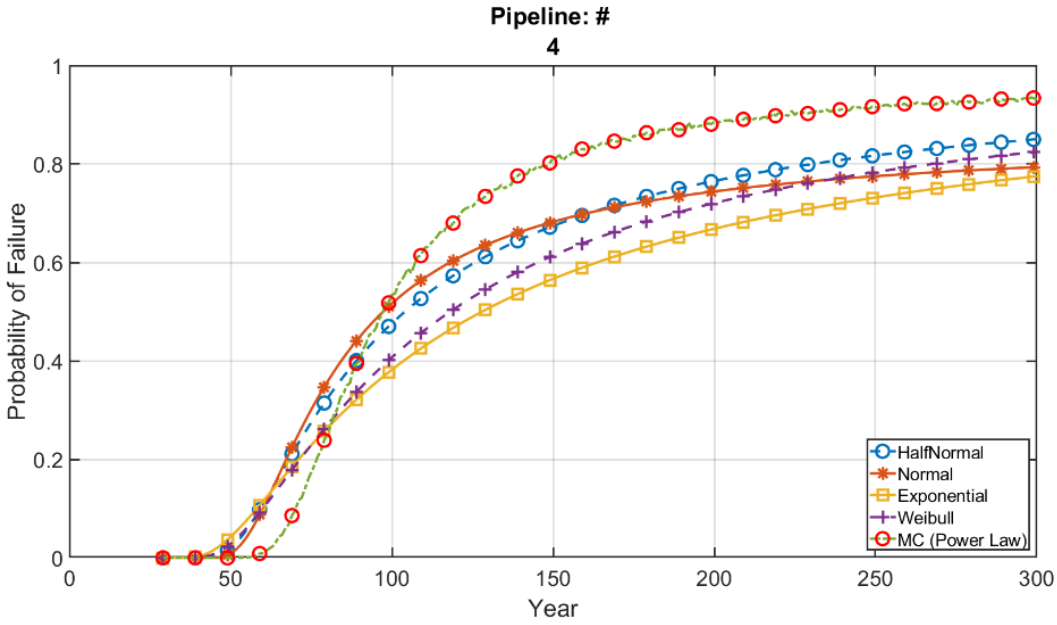
Pipeline: #
4
Probability of Failure
Year
HalfNormal
Normal
Exponential
Weibull
MC (Power Law)

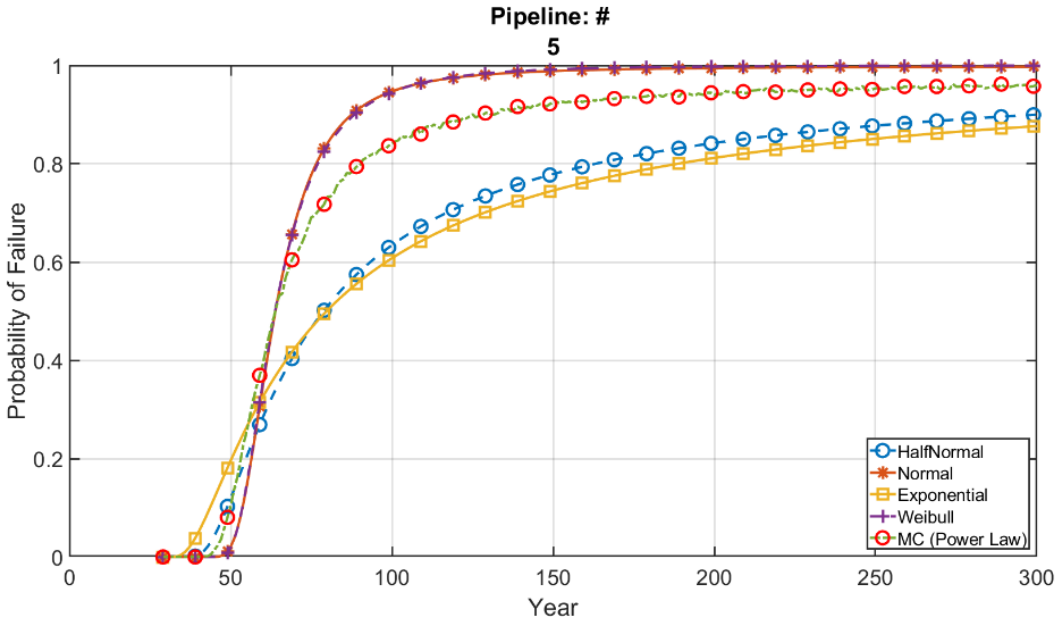
Pipeline: #
5
Probability of Failure
Year
HalfNormal
Normal
Exponential
Weibull
MC (Power Law)

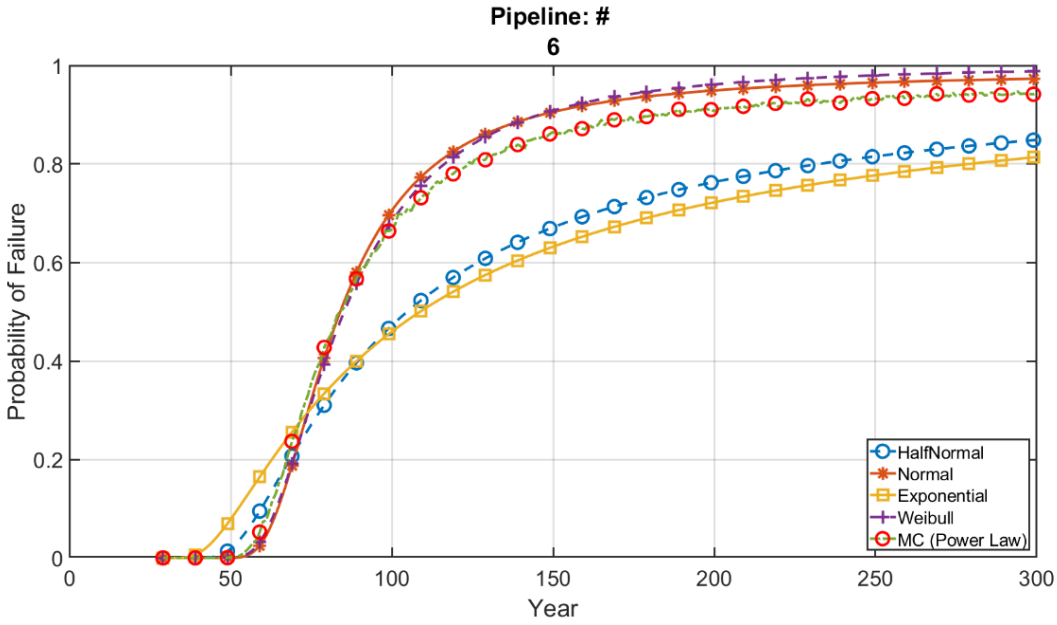
Pipeline: #
6
Probability of Failure
Year
HalfNormal
Normal
Exponential
Weibull
MC (Power Law)

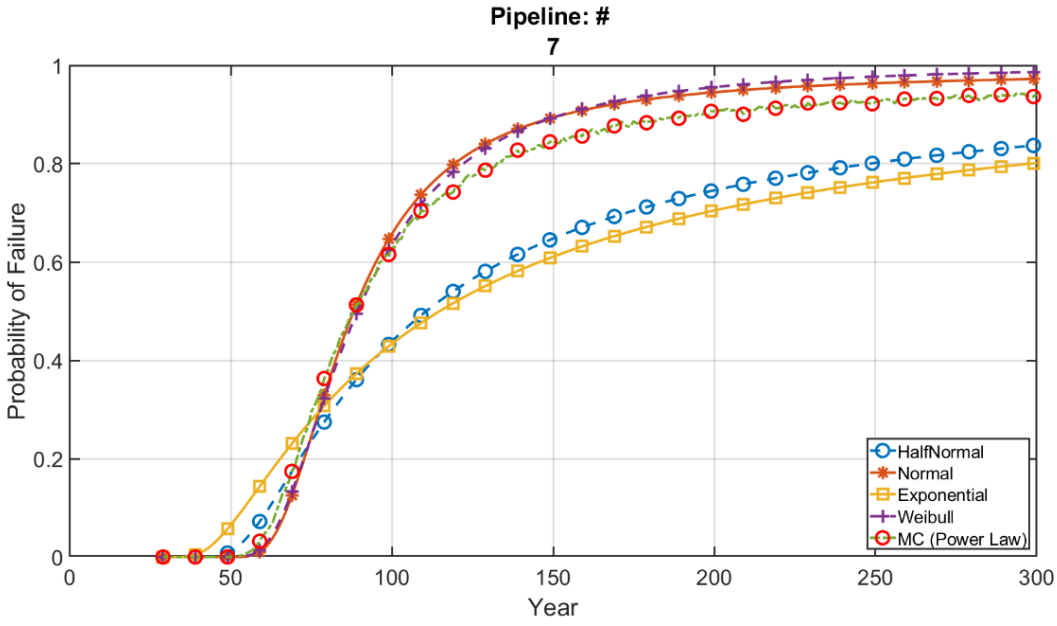
Pipeline: #
7
Probability of Failure
Year
HalfNormal
Normal
Exponential
Weibull
MC (Power Law)

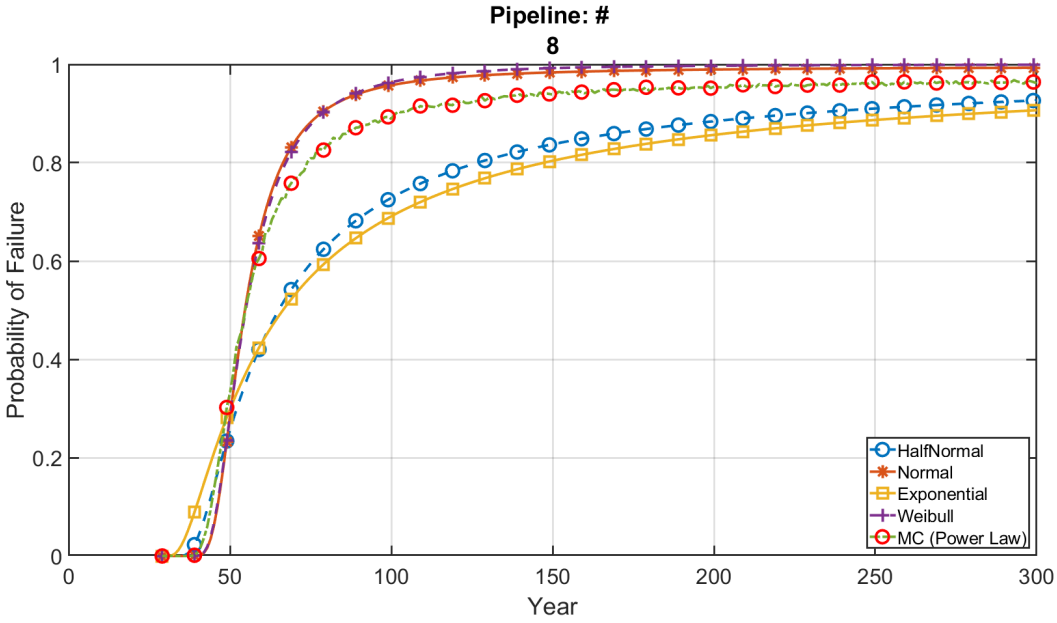
Pipeline: #
8
Probability of Failure
Year
HalfNormal
Normal
Exponential
Weibull
MC (Power Law)

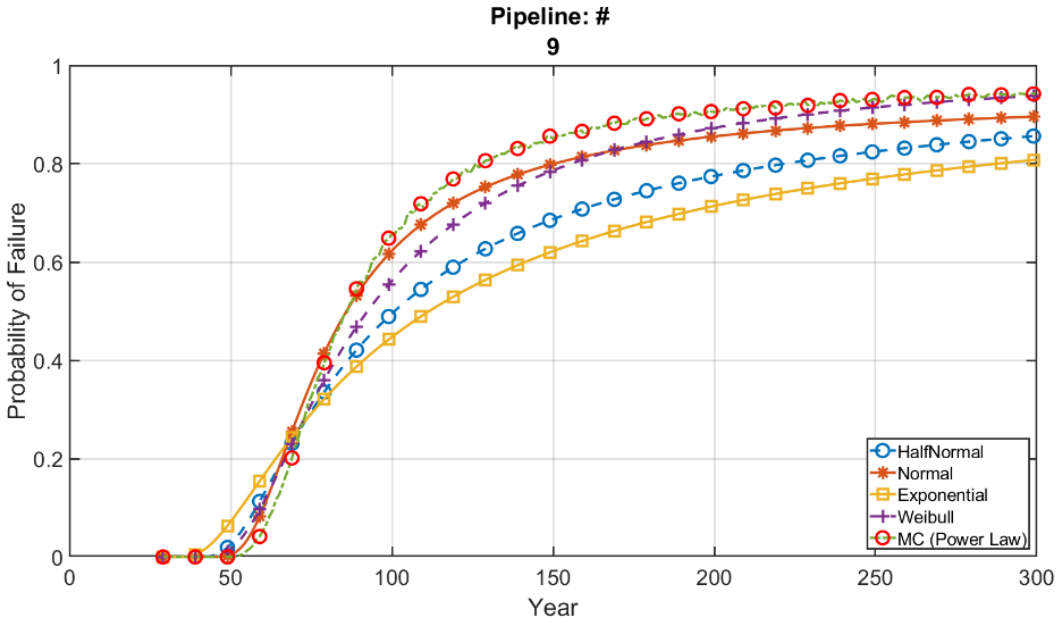
Pipeline: #
9
Probability of Failure
Year
HalfNormal
Normal
Exponential
Weibull
MC (Power Law)

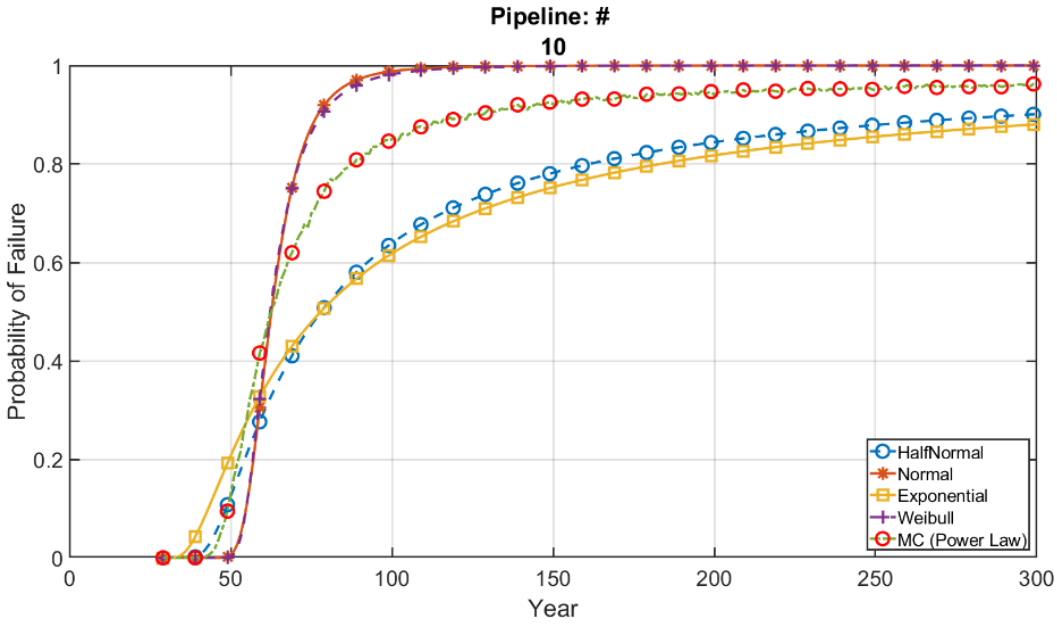
Pipeline: #
10
Probability of Failure
Year
HalfNormal
Normal
Exponential
Weibull
MC (Power Law)

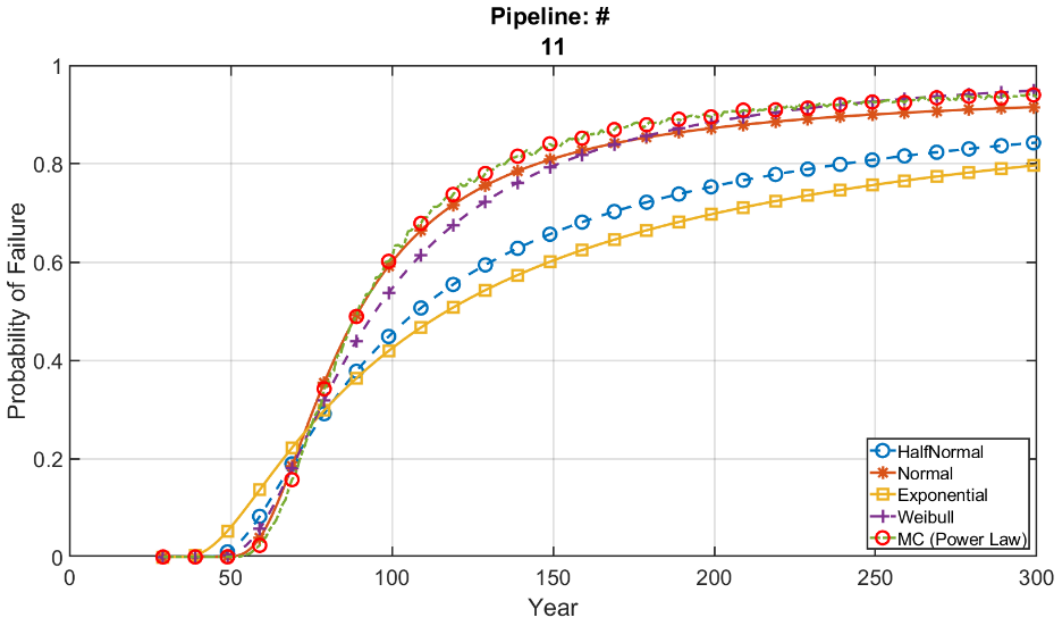
Pipeline: #
11
Probability of Failure
Year
HalfNormal
Normal
Exponential
Weibull
MC (Power Law)

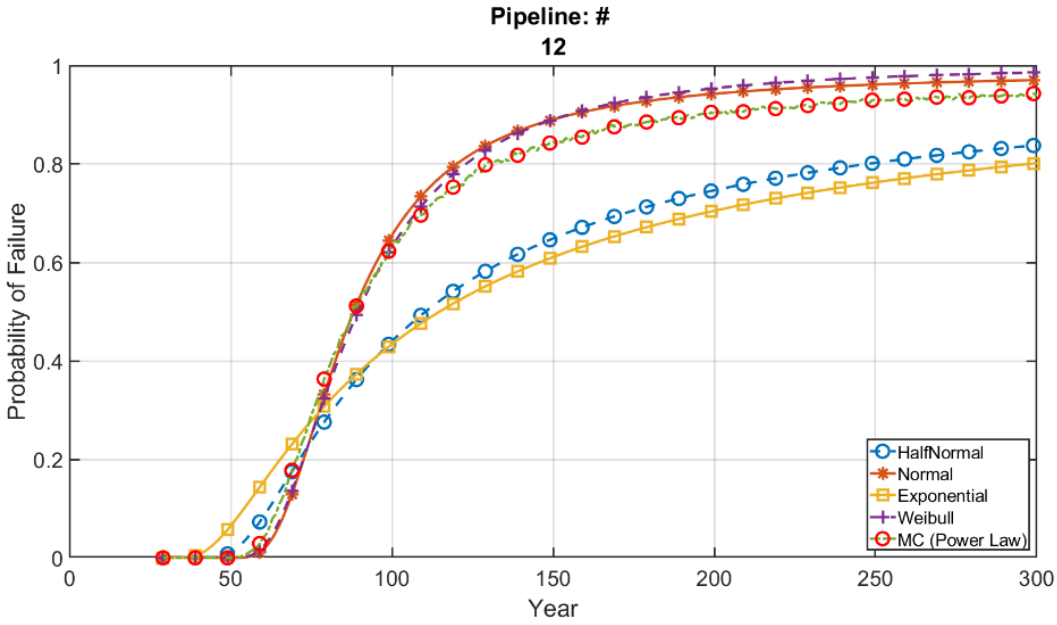
Pipeline: #
12
Probability of Failure
Year
HalfNormal
Normal
Exponential
Weibull
MC (Power Law)

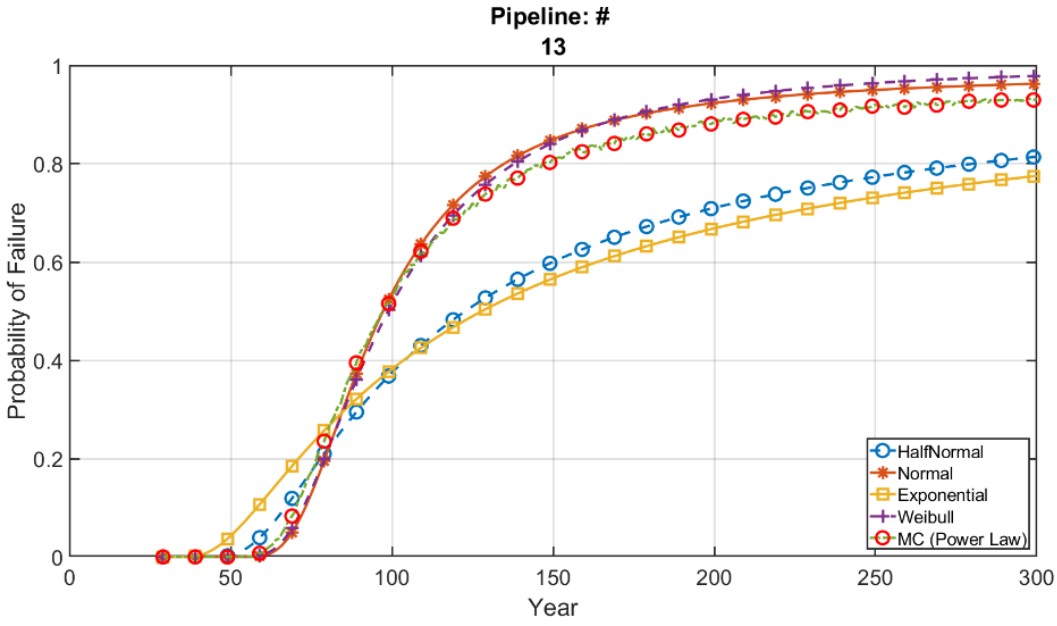
Pipeline: #
13
Probability of Failure
Year
HalfNormal
Normal
Exponential
Weibull
MC (Power Law)

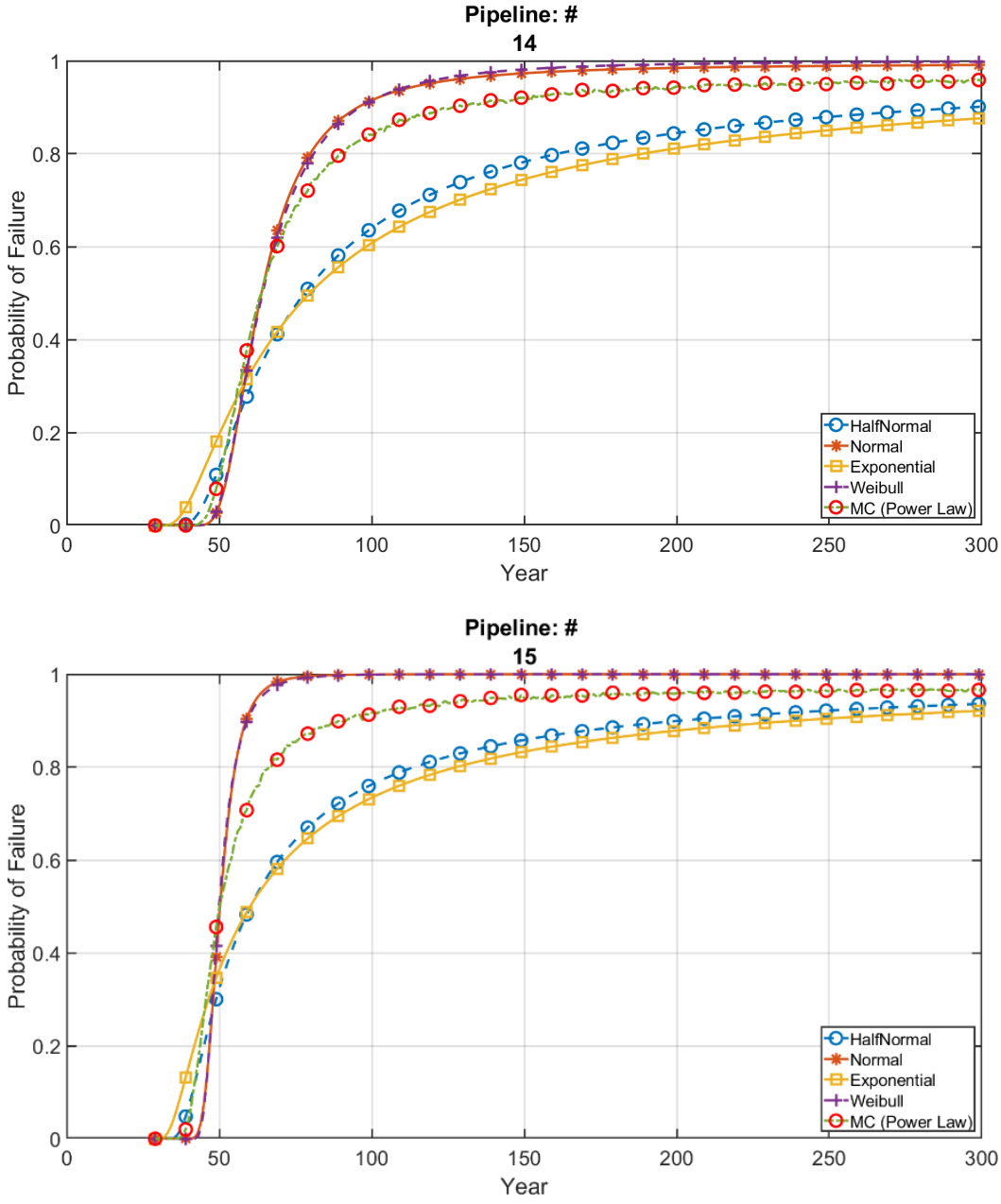

Figure 86. Probability Curves of 30-Inches Data on BN With Weibull Likelihood Functions

Figure 87 shows probability curves of different pipelines for 54-inche data.

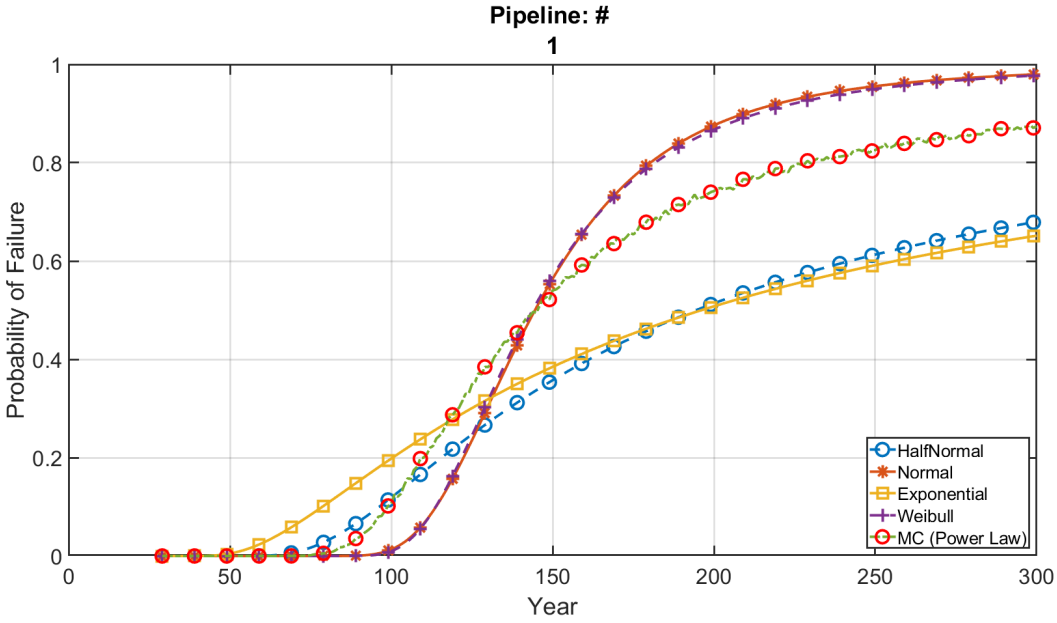
Pipeline: #
1
Probability of Failure
Year
HalfNormal
Normal
Exponential
Weibull
MC (Power Law)

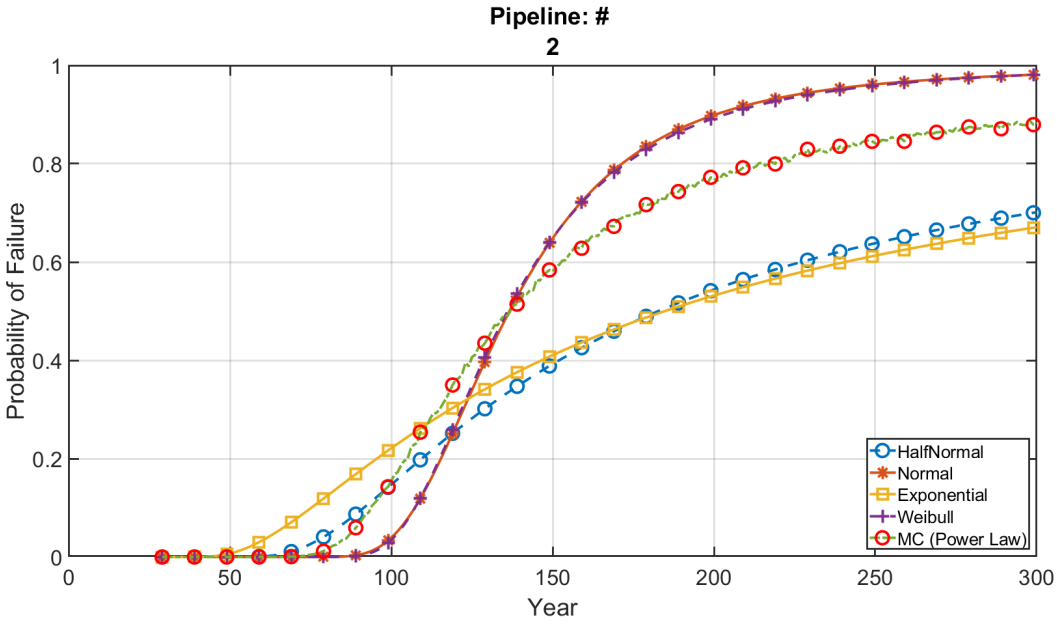
Pipeline: #
2
Probability of Failure
Year
HalfNormal
Normal
Exponential
Weibull
MC (Power Law)

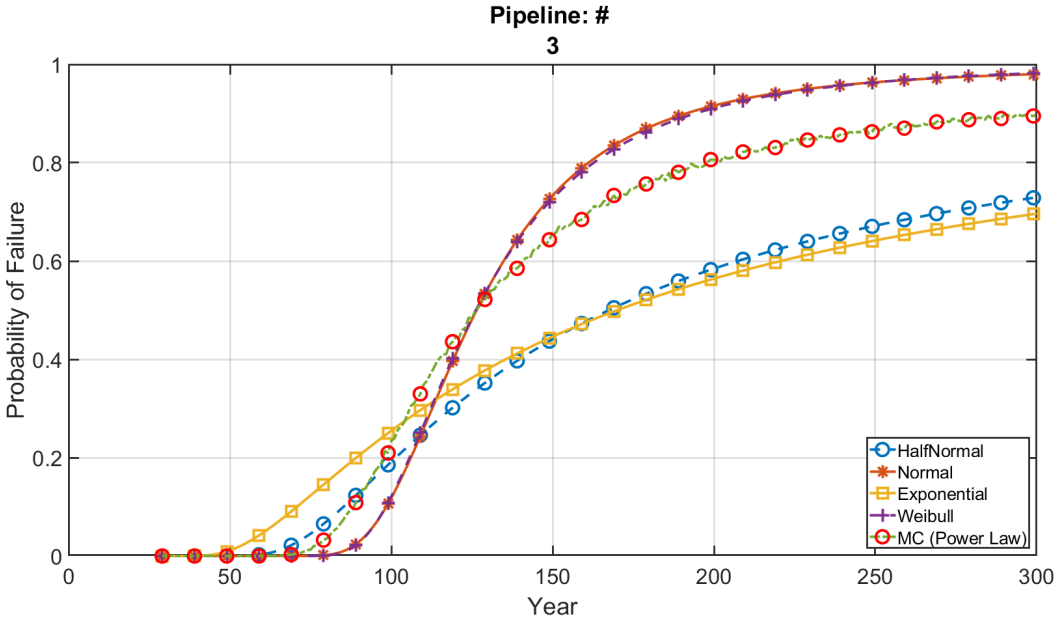
Pipeline: #
3
Probability of Failure
Year
HalfNormal
Normal
Exponential
Weibull
MC (Power Law)

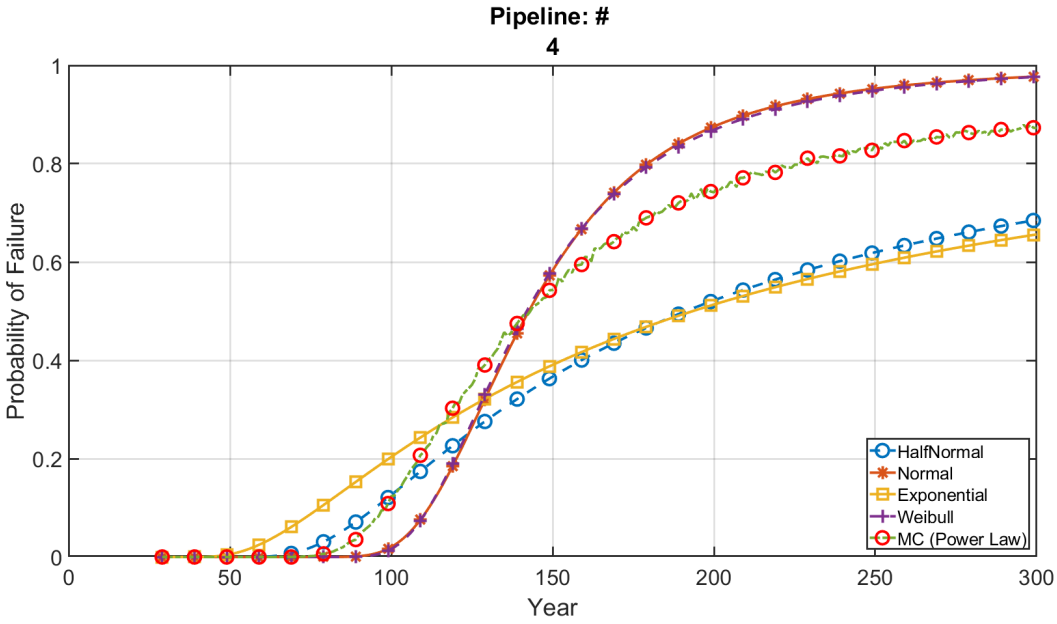
Pipeline: #
4
Probability of Failure
Year
HalfNormal
Normal
Exponential
Weibull
MC (Power Law)

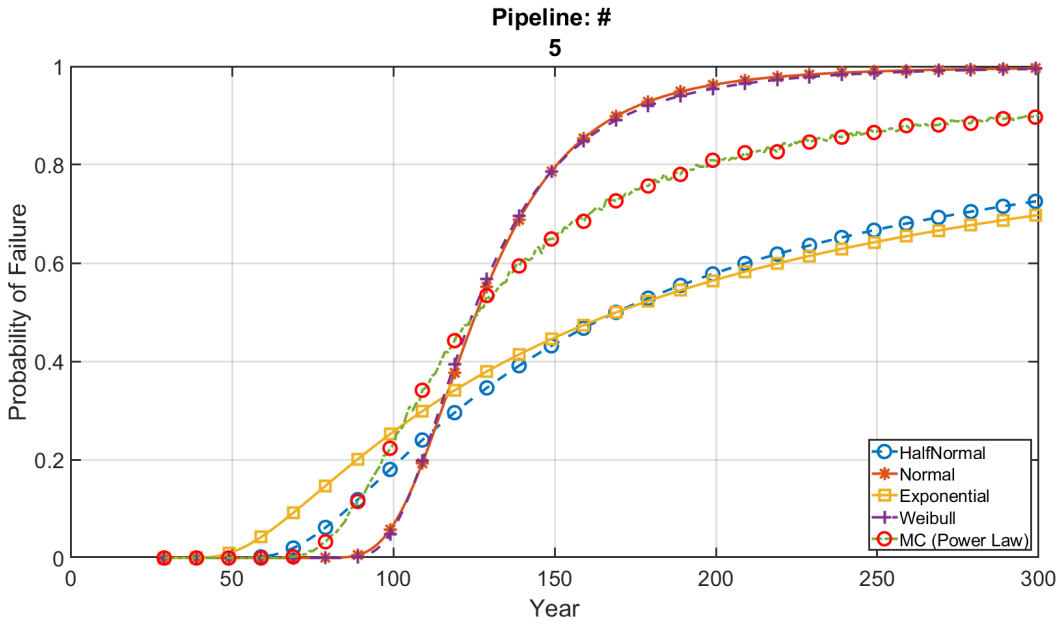

Figure 87. Probability Curves of 54-Inches Data on BN With Weibull Likelihood Functions

Figure 88 shows probability curves of different pipelines for 60-inche data.

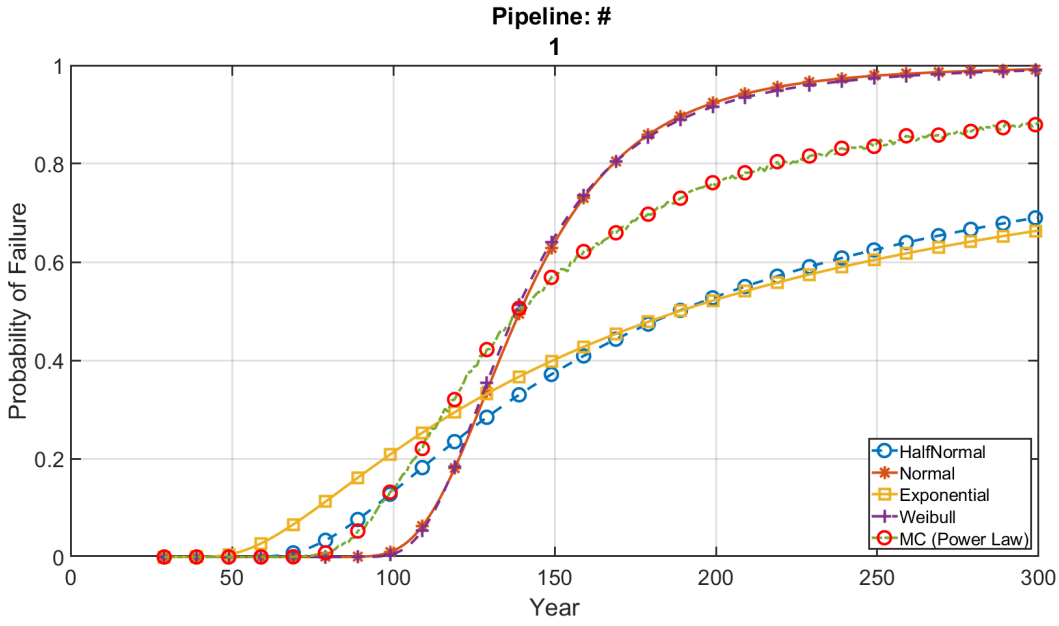

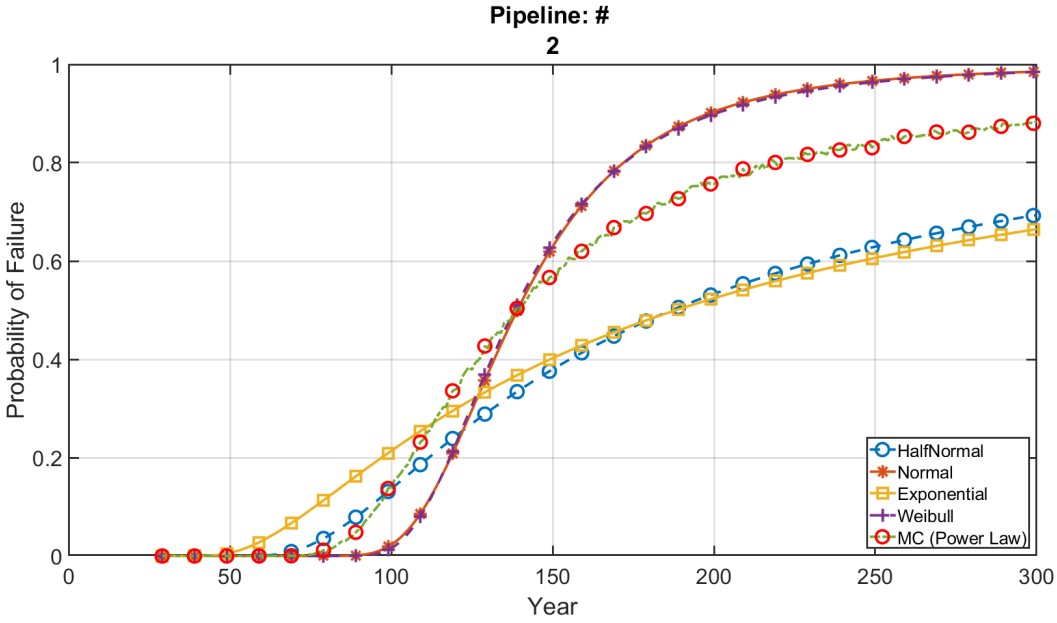
Pipeline: #
2
Probability of Failure
Year
HalfNormal
Normal
Exponential
Weibull
MC (Power Law)

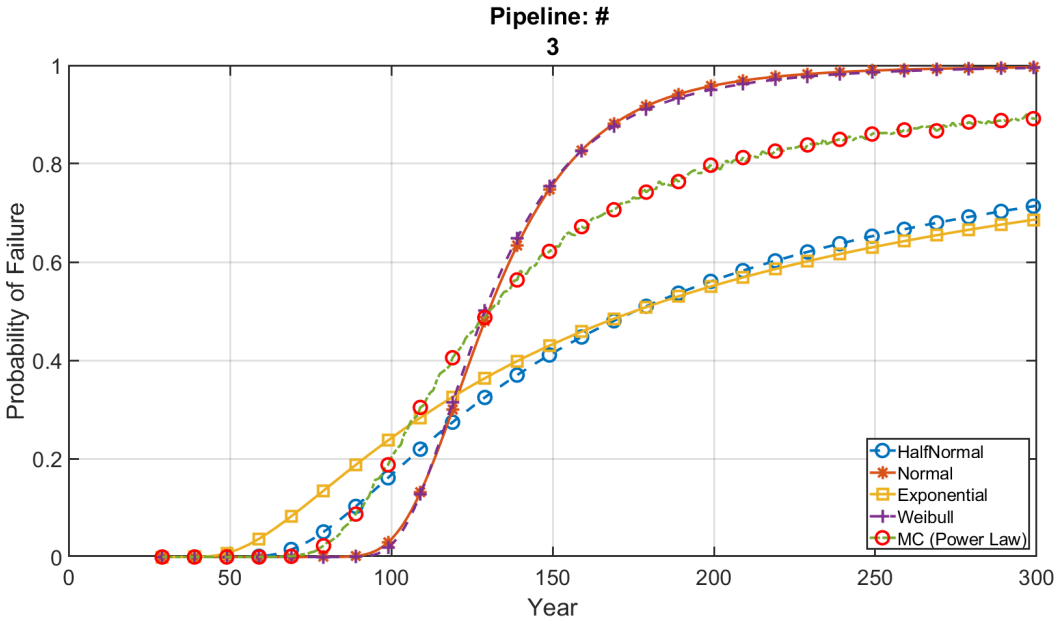
Pipeline: #
3
Probability of Failure
Year
HalfNormal
Normal
Exponential
Weibull
MC (Power Law)

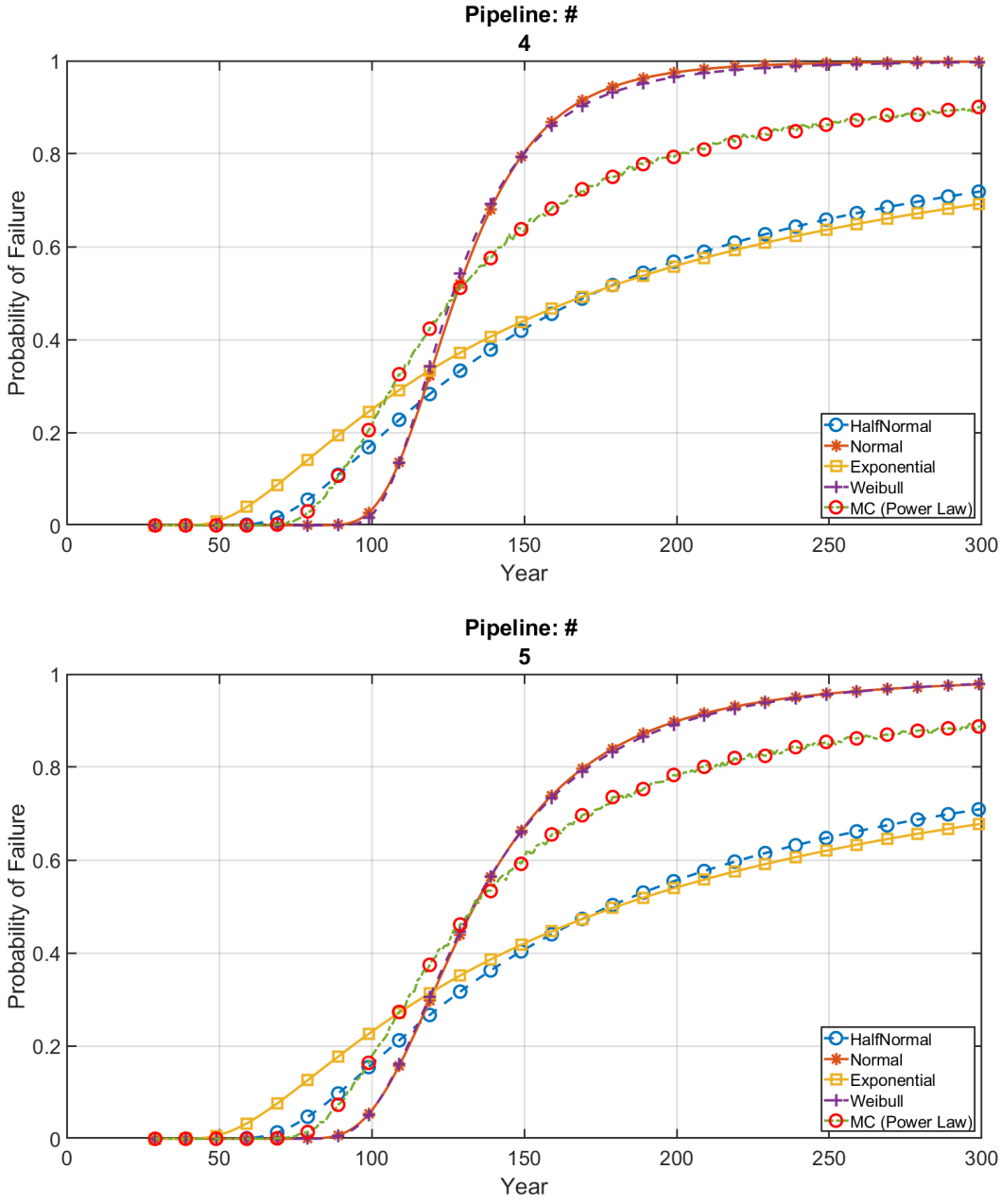

Figure 88. Probability Curves of 60-Inches Data on BN With Weibull Likelihood Functions

Figure 89 shows probability curves of different pipelines for 30-inche data on the updated Values of BN using Gamma distributions functions.

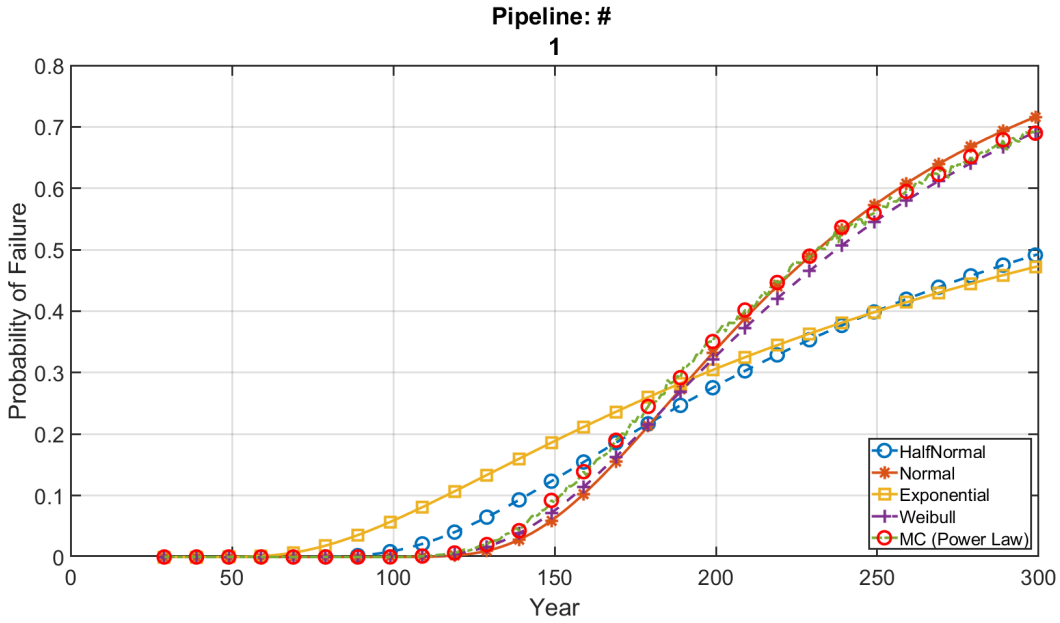

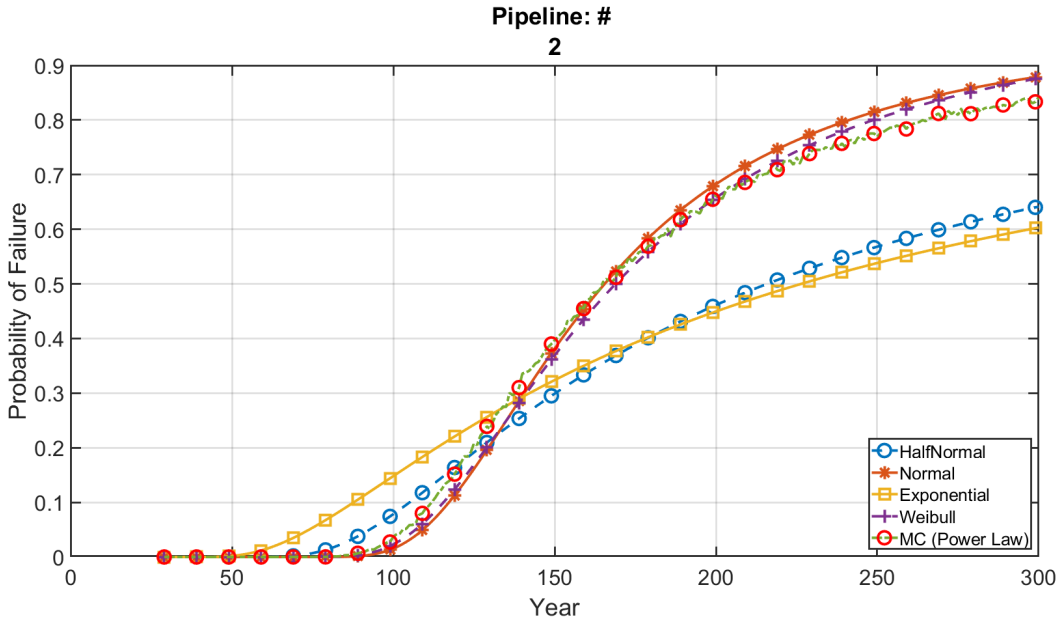

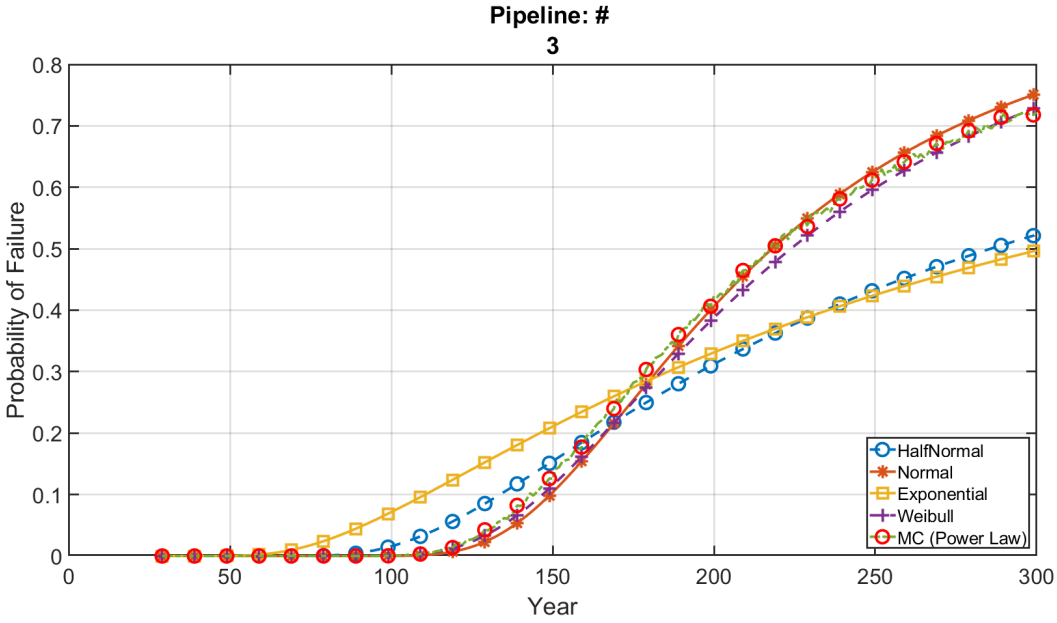
Pipeline: #
3
Probability of Failure
Year
HalfNormal
Normal
Exponential
Weibull
MC (Power Law)

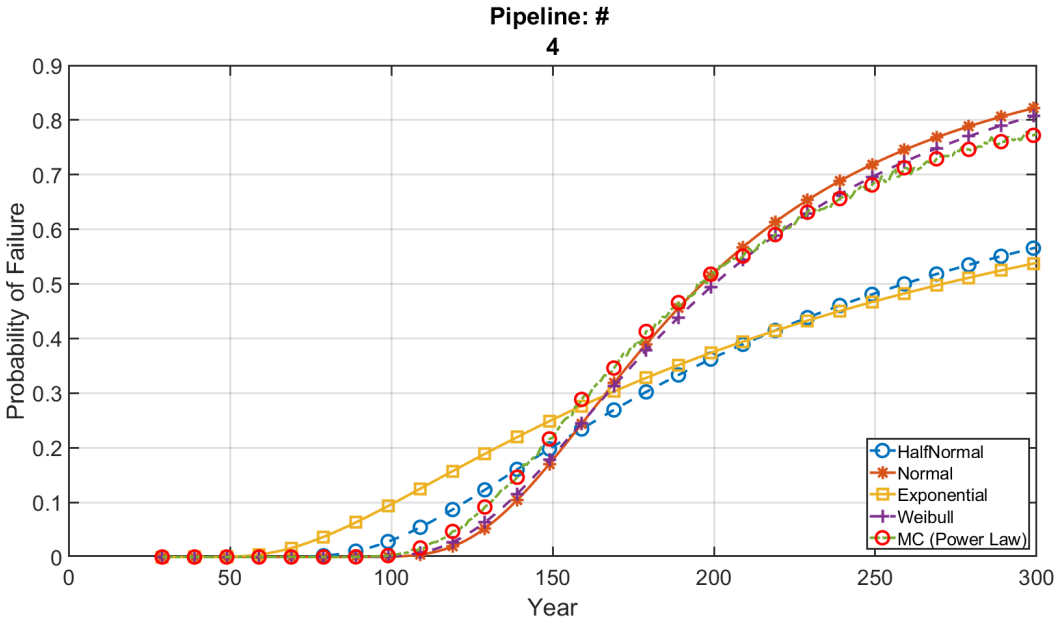
Pipeline: #
4
Probability of Failure
Year
HalfNormal
Normal
Exponential
Weibull
MC (Power Law)

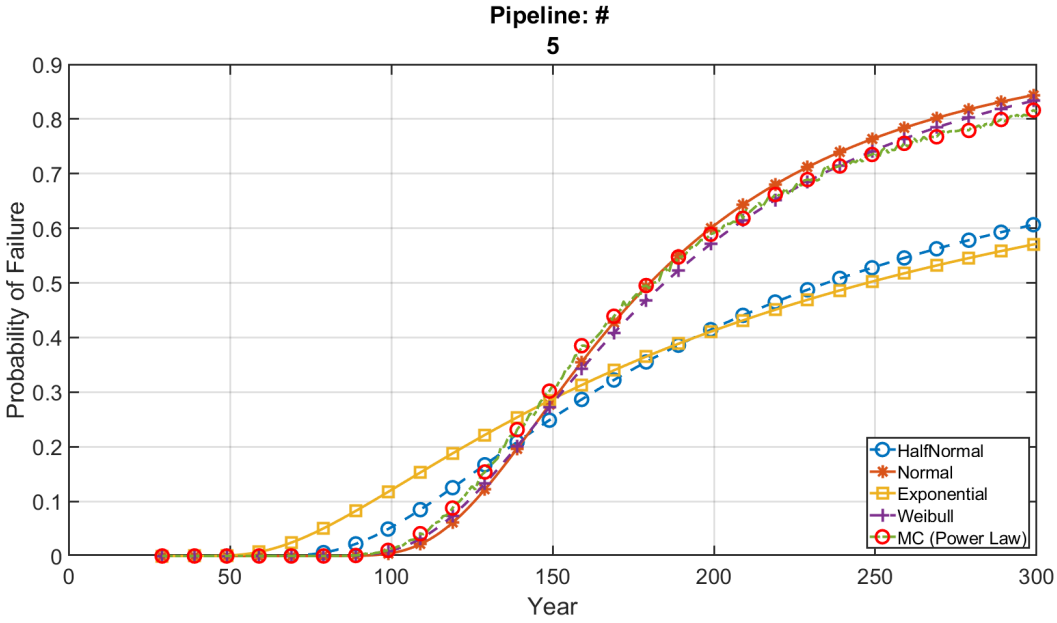
Pipeline: #
5
Probability of Failure
Year
HalfNormal
Normal
Exponential
Weibull
MC (Power Law)

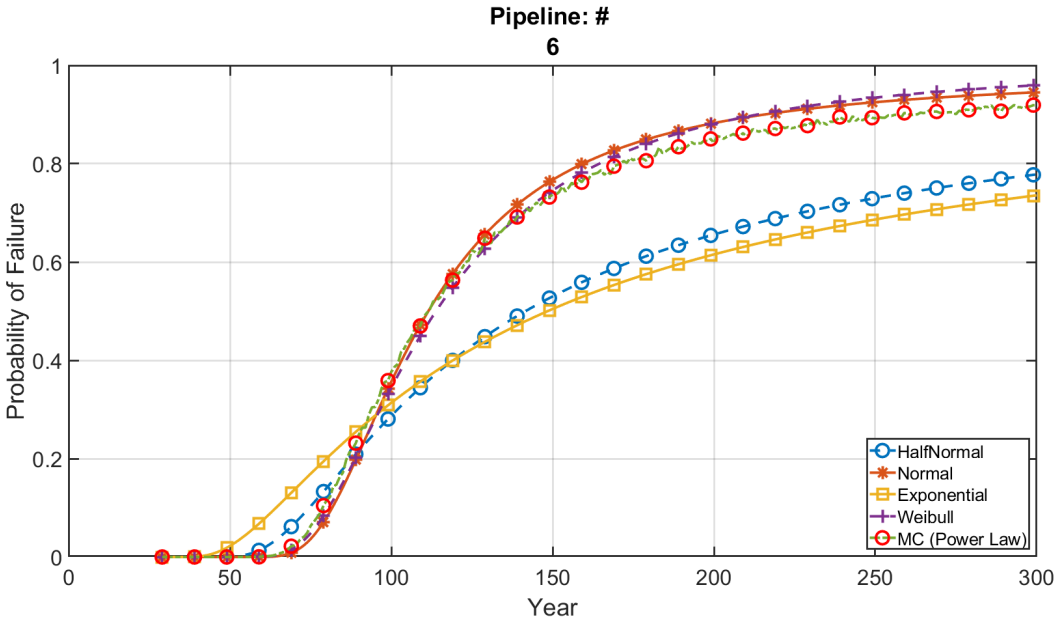
Pipeline: #
6
Probability of Failure
Year
HalfNormal
Normal
Exponential
Weibull
MC (Power Law)

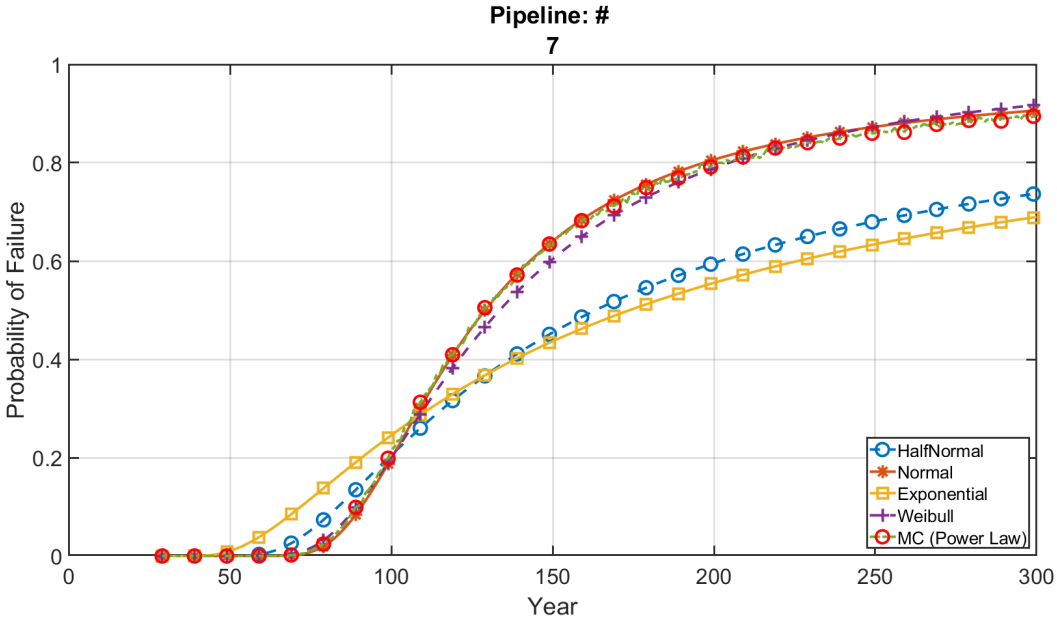
Pipeline: #
7
Probability of Failure
Year
HalfNormal
Normal
Exponential
Weibull
MC (Power Law)

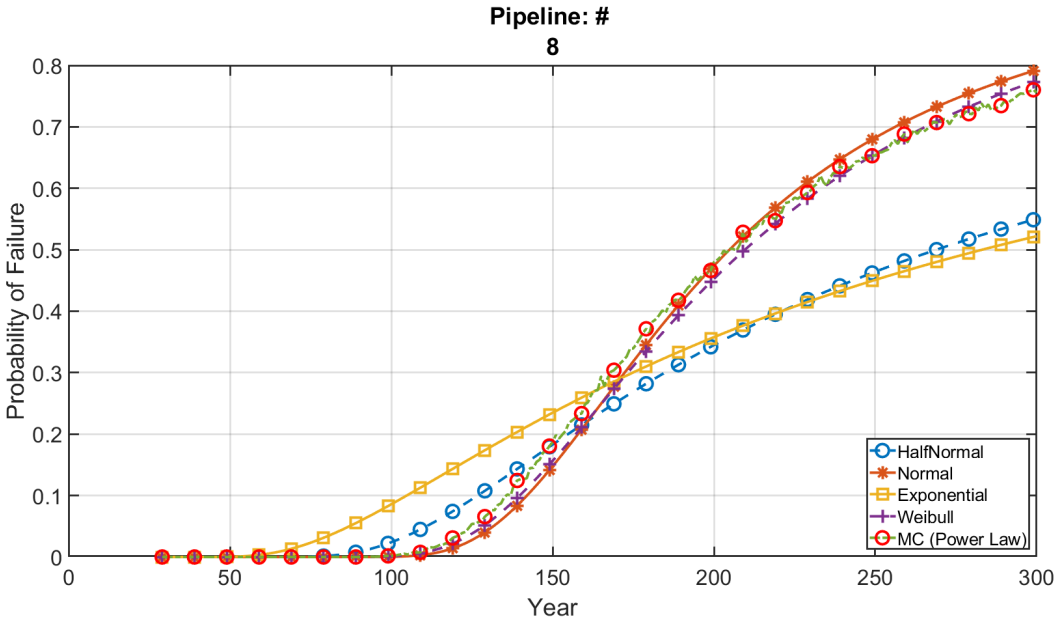
Pipeline: #
8
Probability of Failure
Year
HalfNormal
Normal
Exponential
Weibull
MC (Power Law)

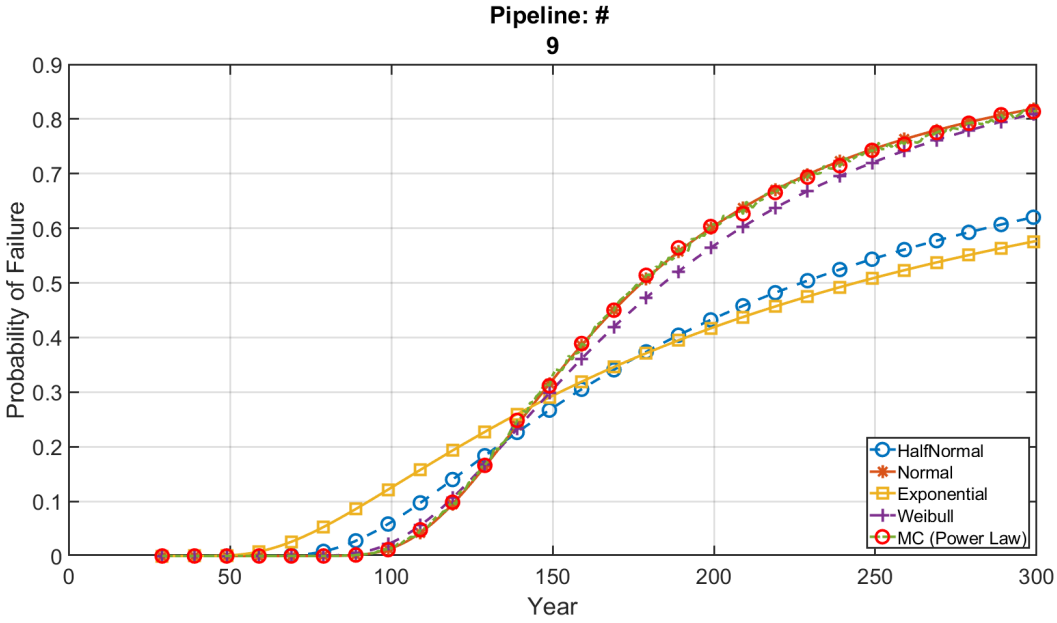
Pipeline: #
9
Probability of Failure
Year
HalfNormal
Normal
Exponential
Weibull
MC (Power Law)

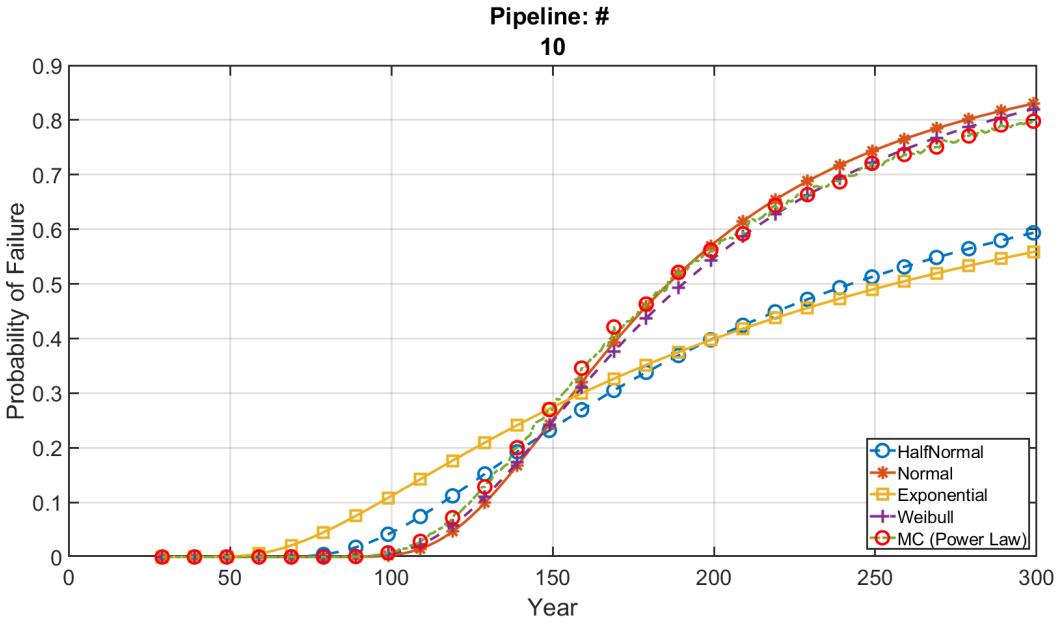
Pipeline: #
10
Probability of Failure
Year
HalfNormal
Normal
Exponential
Weibull
MC (Power Law)

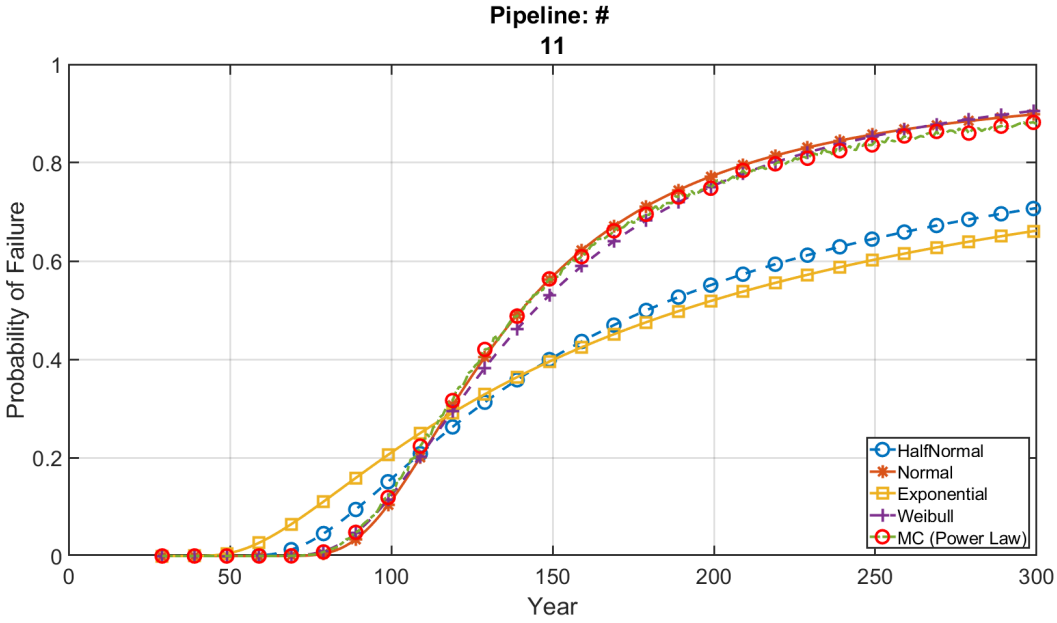
Pipeline: #
11
Probability of Failure
Year
HalfNormal
Normal
Exponential
Weibull
MC (Power Law)

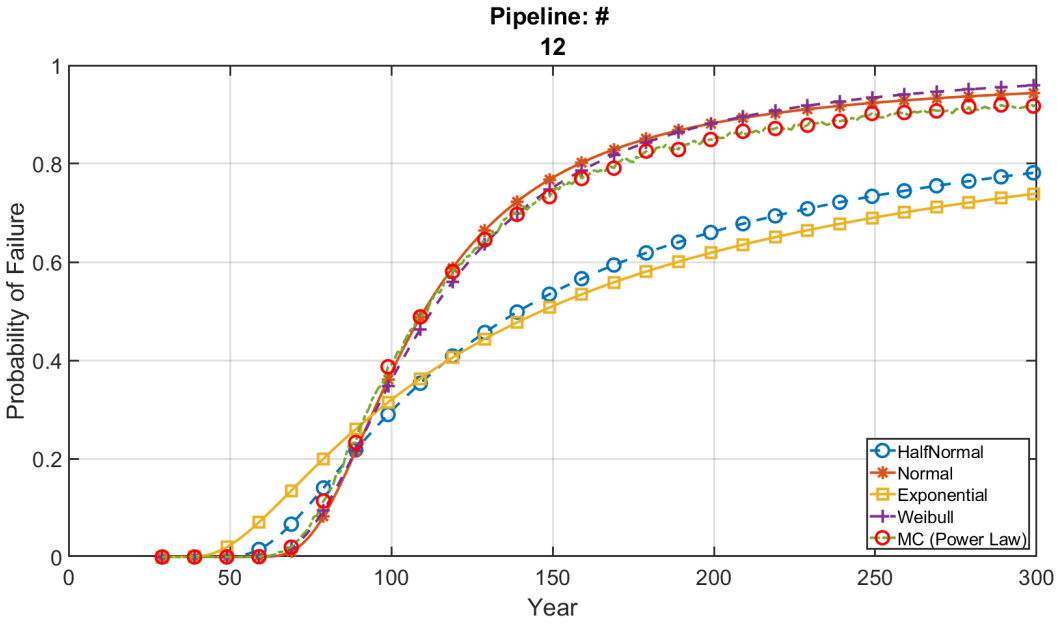
Pipeline: #
12
Probability of Failure
Year
HalfNormal
Normal
Exponential
Weibull
MC (Power Law)

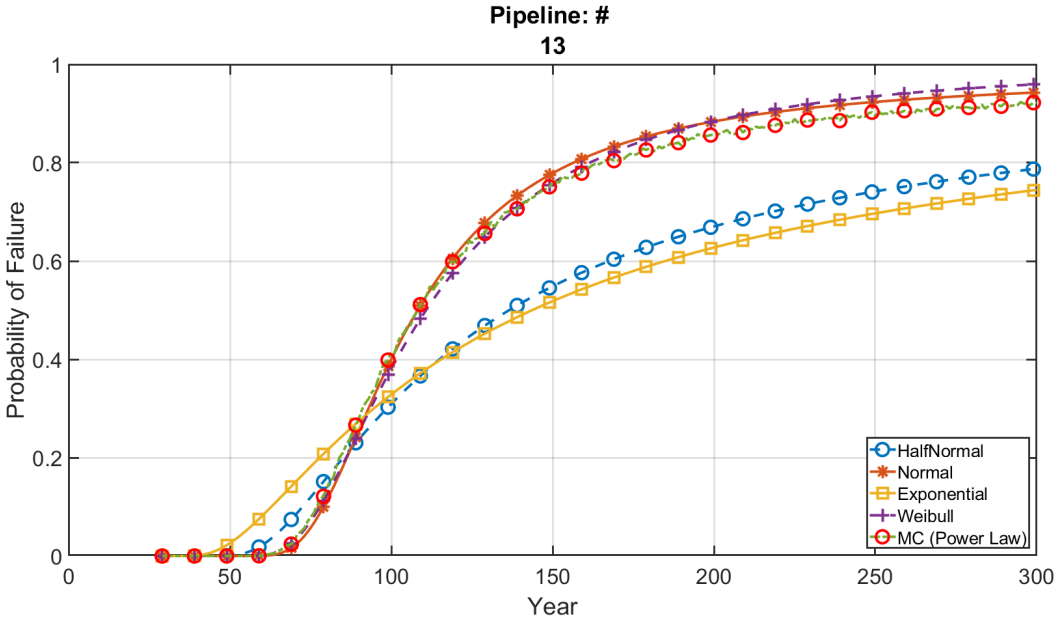
Pipeline: #
13
Probability of Failure
Year
HalfNormal
Normal
Exponential
Weibull
MC (Power Law)

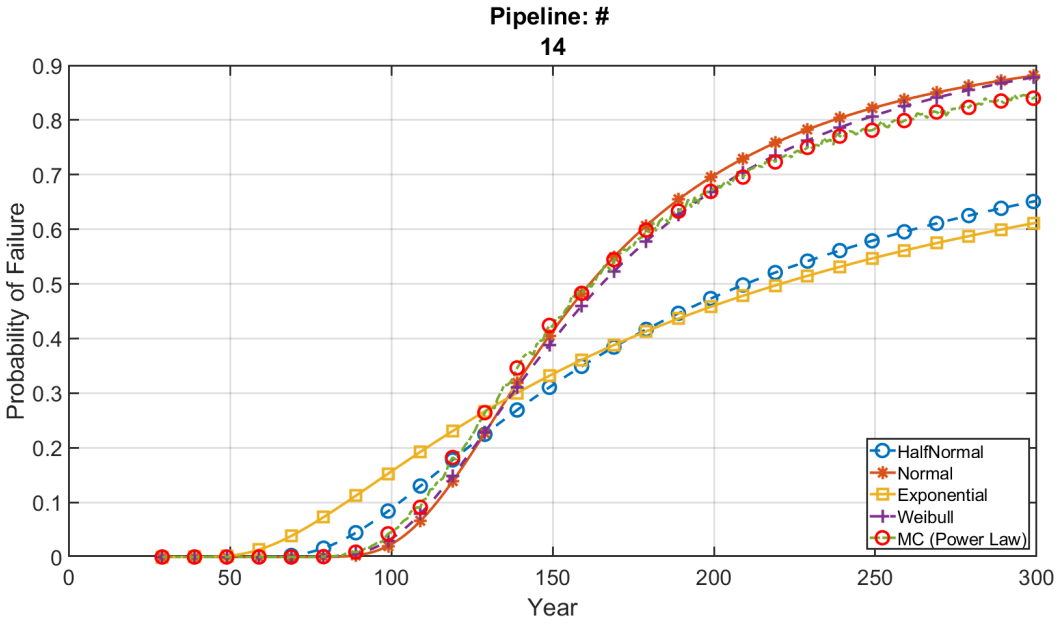
Pipeline: #
14
Probability of Failure
Year
HalfNormal
Normal
Exponential
Weibull
MC (Power Law)

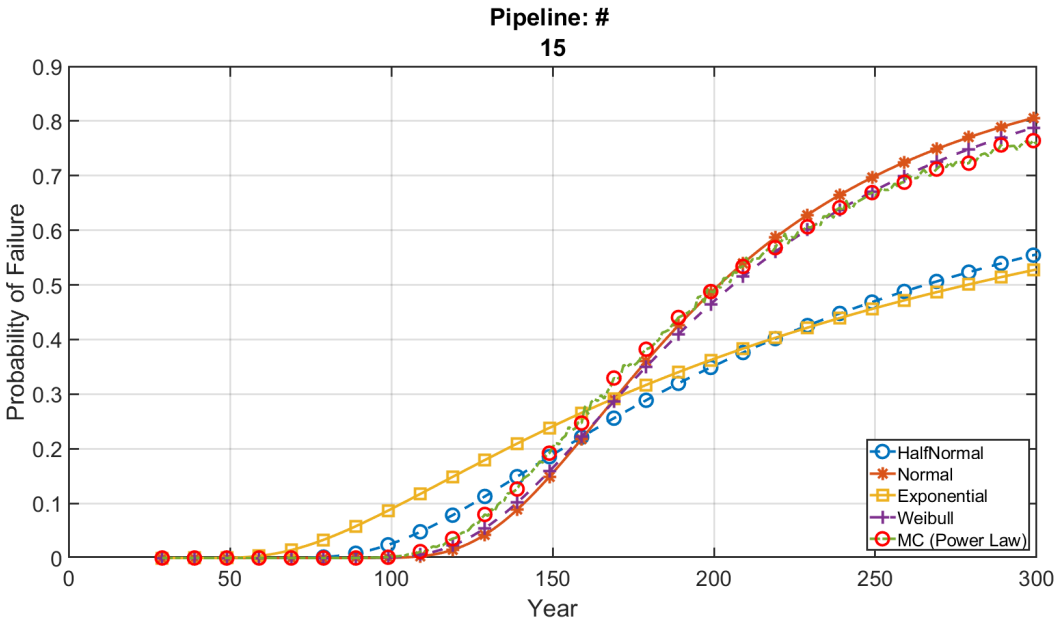

Figure 89.Probability Curves of 30-Inches Data on BN With Gamma Likelihood Functions

Figure 90 shows probability curves of different pipelines for 54-inche data.

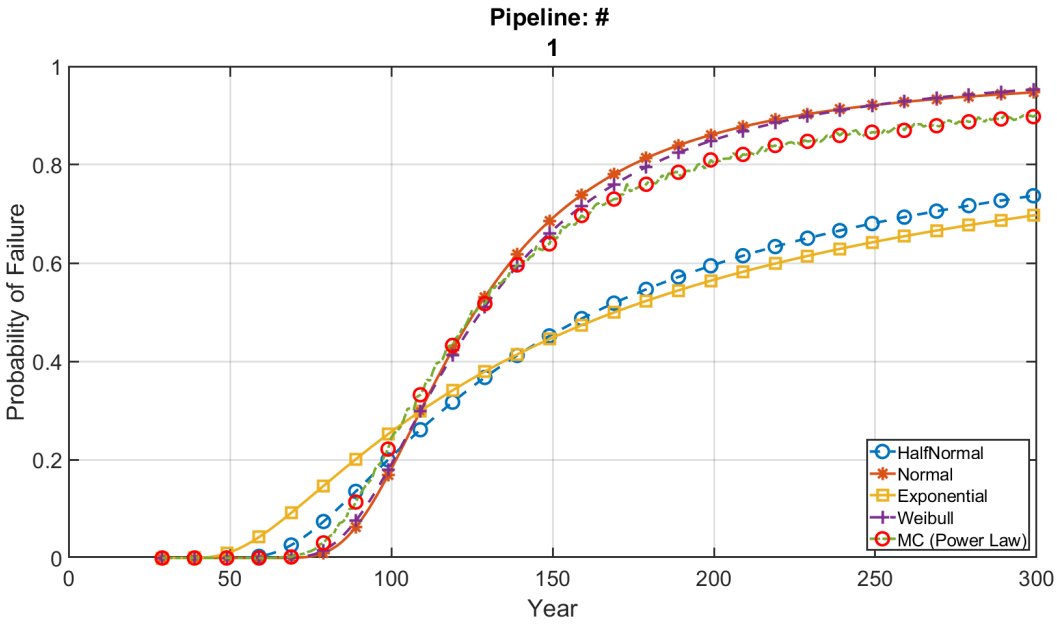

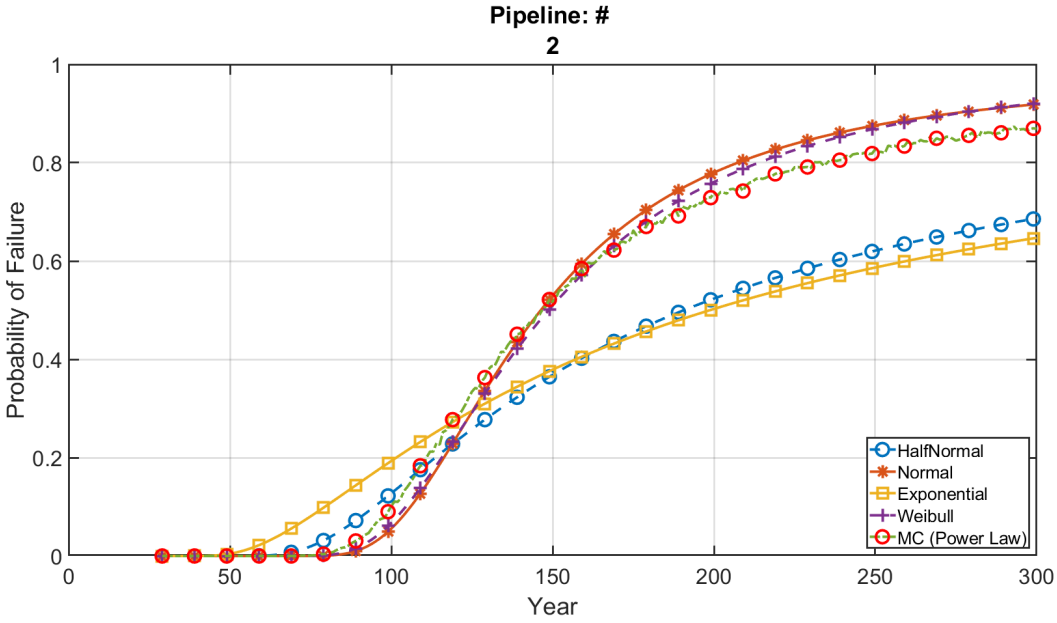
Pipeline: #
2
Probability of Failure
Year
HalfNormal
Normal
Exponential
Weibull
MC (Power Law)

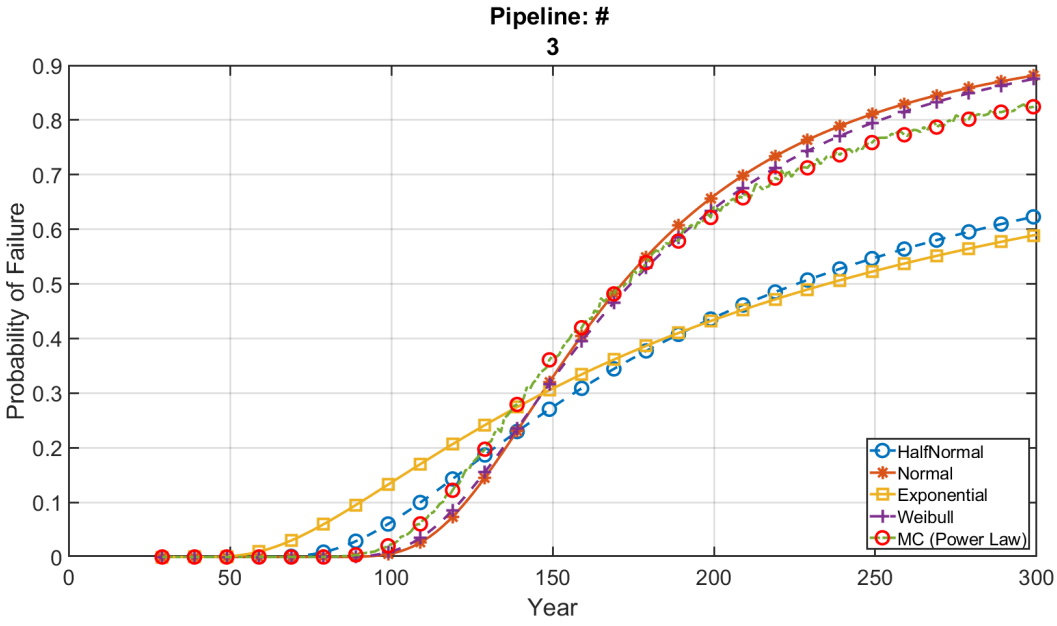
Pipeline: #
3
Probability of Failure
Year
HalfNormal
Normal
Exponential
Weibull
MC (Power Law)

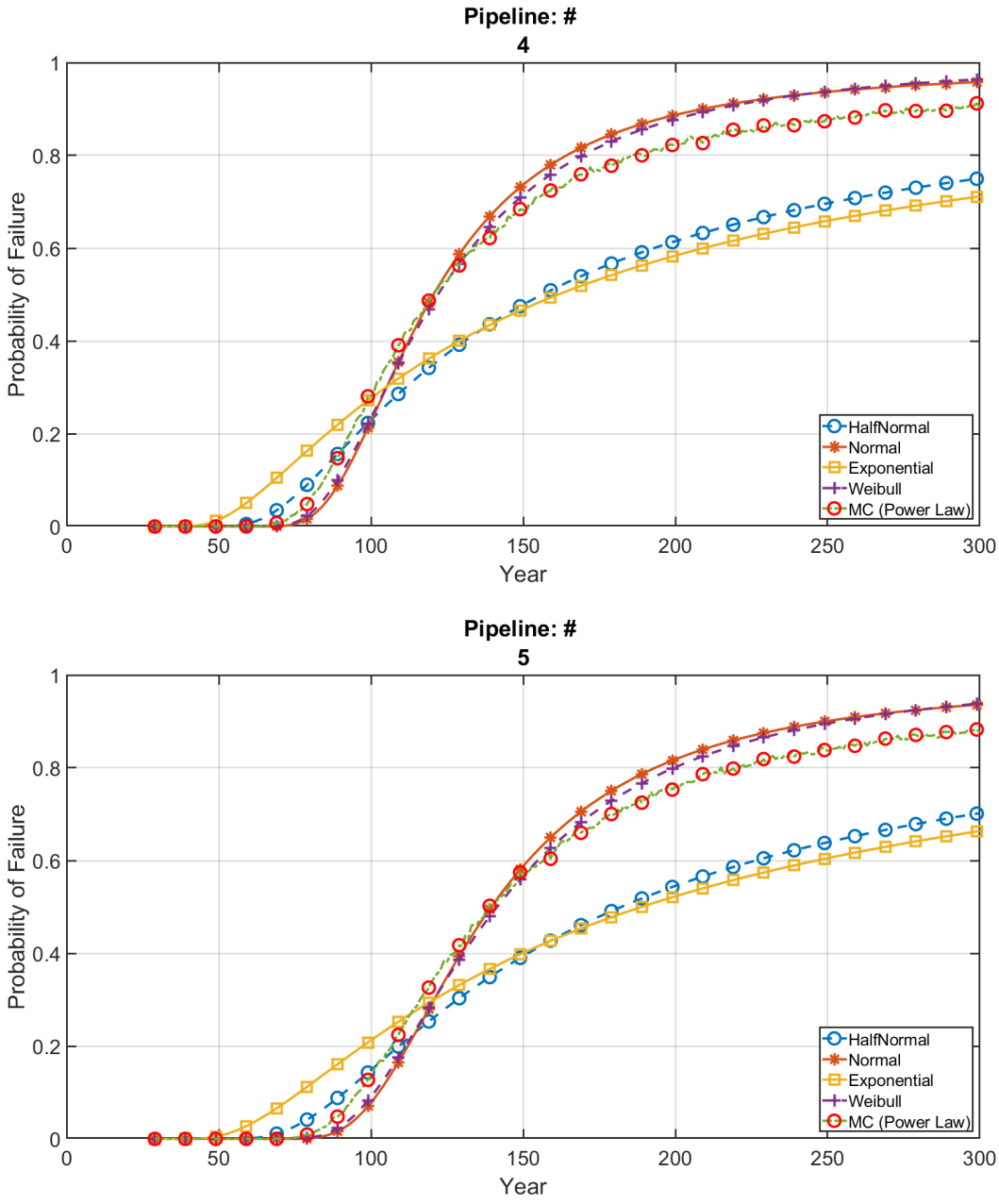

Figure 90. Probability Curves of 54-Inches Data on BN With Gamma Likelihood Functions

Figure 91 shows probability curves of different pipelines for 60-inche data.

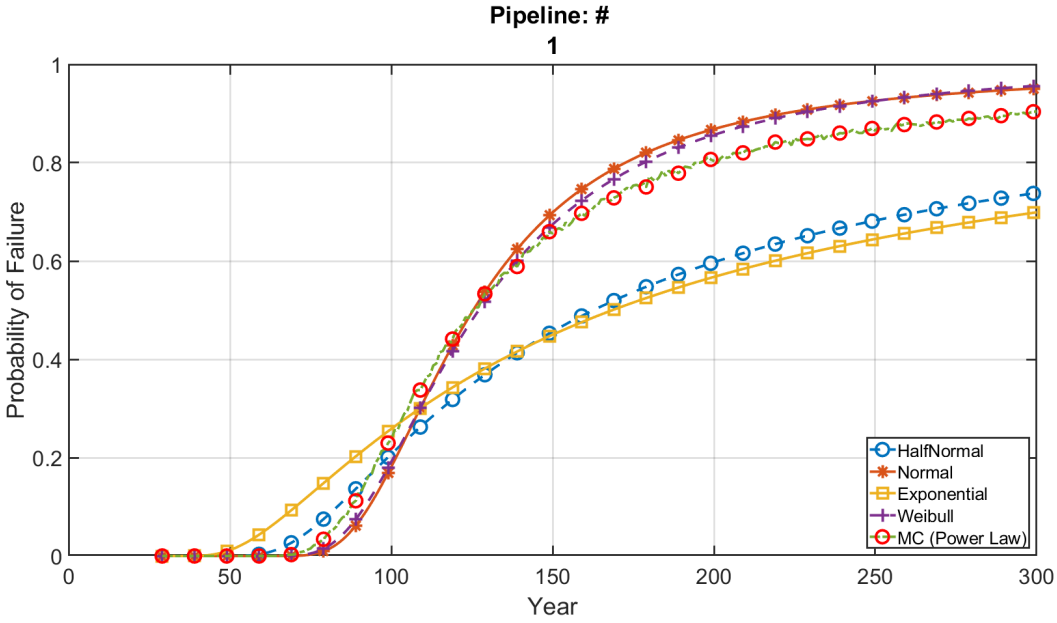
Pipeline: #
1
Probability of Failure
Year
HalfNormal
Normal
Exponential
Weibull
MC (Power Law)

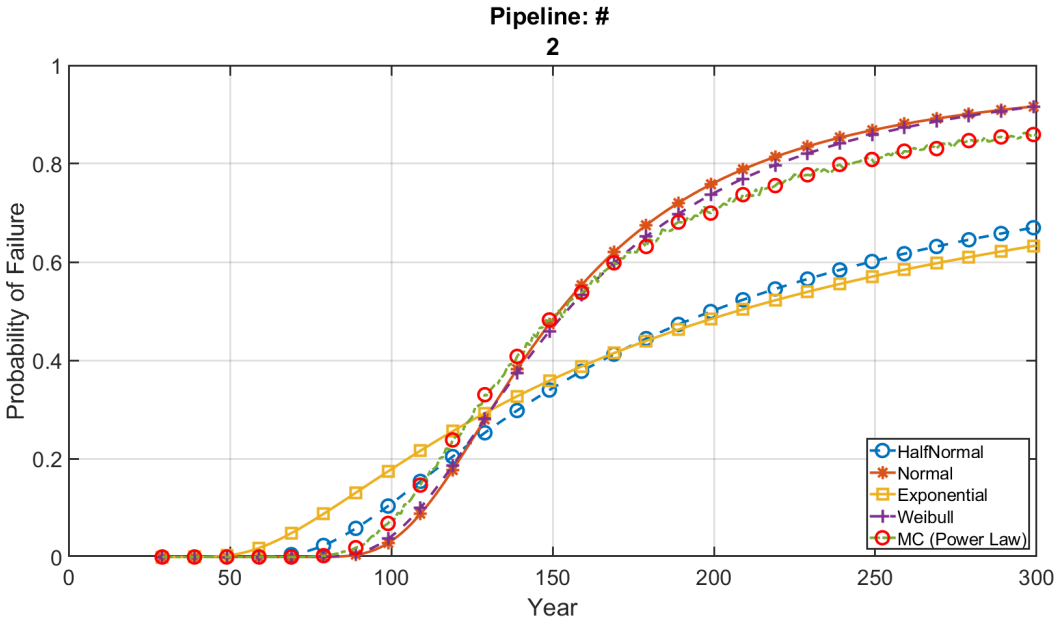
Pipeline: #
2
Probability of Failure
Year
HalfNormal
Normal
Exponential
Weibull
MC (Power Law)

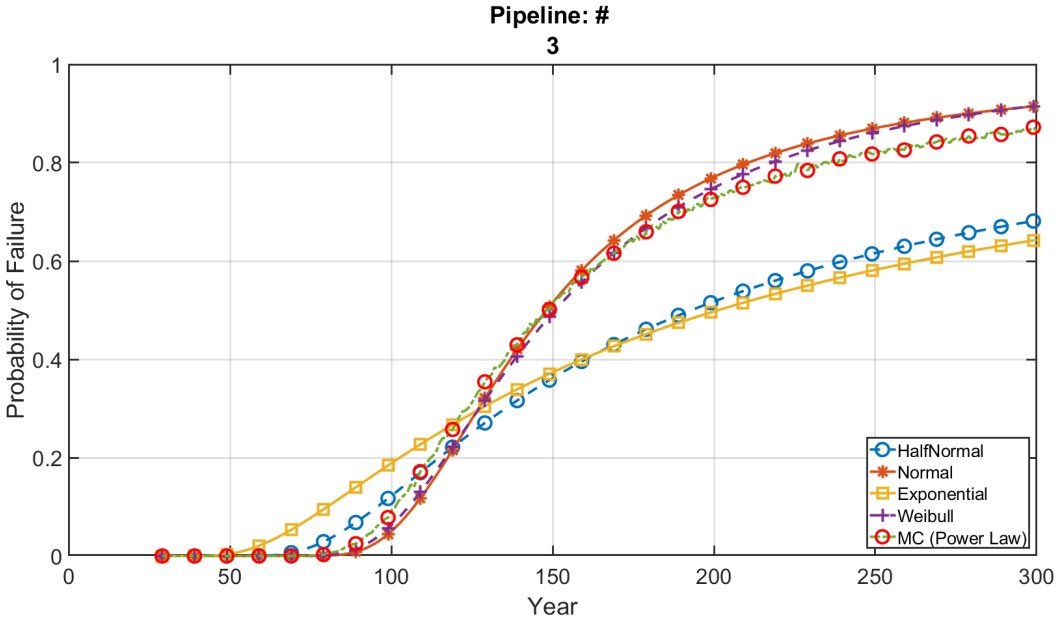
Pipeline: #
3
Probability of Failure
Year
HalfNormal
Normal
Exponential
Weibull
MC (Power Law)

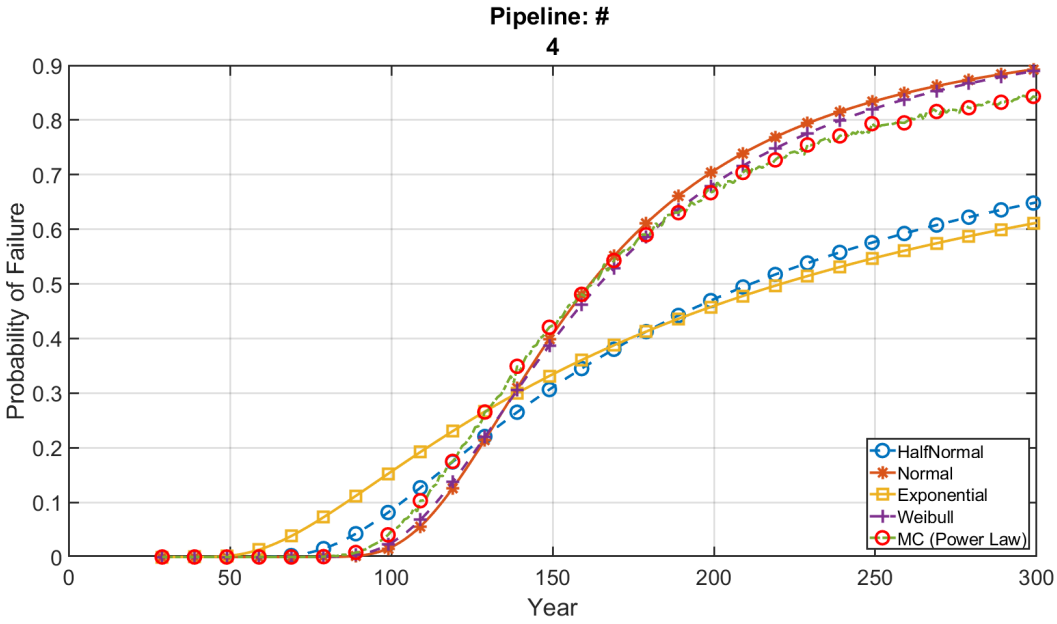
Pipeline: #
4
Probability of Failure
Year
HalfNormal
Normal
Exponential
Weibull
MC (Power Law)

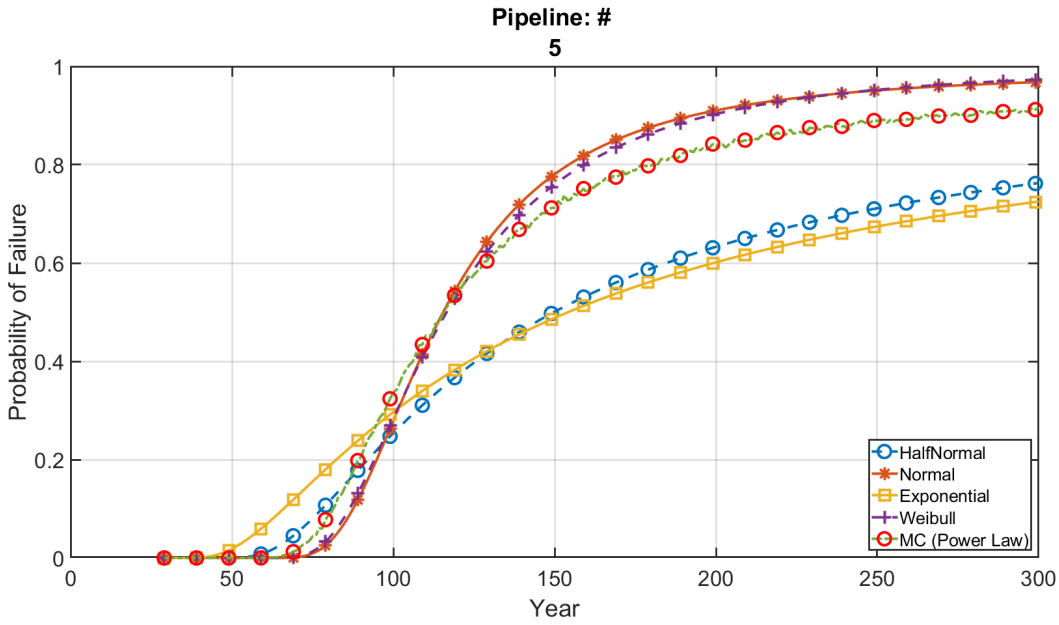

Figure 91. Probability Curves of 60-Inches Data on BN With Gamma Likelihood Functions